UNIVERSITÉ DU LUXEMBOURG

PhD-FSTC-2019-02
The Faculty of Sciences, Technology and Communication

DISSERTATION

Defence held on 22/01/2019 in Esch-sur-Alzette

to obtain the degree of

DOCTEUR DE L'UNIVERSITÉ DU LUXEMBOURG

EN PHYSIQUE

by

Finn BABBE
Born on 16 October 1989 in Husum (Germany)

OPTICAL ANALYSIS OF EFFICIENCY LIMITATIONS OF CU(IN,GA)SE_2 GROWN UNDER COPPER EXCESS

Dissertation defence committee

Dr. Susanne Siebentritt, dissertation supervisor
Professor, University of Luxembourg

Dr. Jürgen Christen
Professor, University of Magdeburg

Dr. Andreas Michels, Chairman
Professor, University of Luxembourg

Dr. Stephan Bücheler
Empa – Swiss Federal Laboratories for Materials Science and Technology

Dr. Daniele Brida, Vice Chairman
Professor, University of Luxembourg

CONTENTS

Abstract **7**

1 Introduction **9**

2 Fundamentals and Review **13**
2.1 Chalcopyrites . . . 13
2.1.1 Crystal structure . . . 14
2.1.2 Phase diagram . . . 14
2.1.3 Opto-electronic properties . . . 15
2.1.4 Intrinsic defects in chalcopyrites . . . 16
2.2 Solar cell devices . . . 17
2.2.1 PN-junction . . . 18
2.2.2 CIGS thin film solar cells . . . 21
2.2.3 Current voltage analysis . . . 25
2.3 Photoluminescence . . . 27
2.3.1 Basic principles . . . 27
2.3.2 Observable Transitions . . . 28
2.3.3 Defect spectroscopy by photoluminescence . . . 33
2.3.4 Defect Picture in Cu(In,Ga)Se_2 . . . 34
2.3.5 Quasi Fermi level splitting analysis . . . 36
2.3.6 Experimental Set up . . . 37
2.4 Absorber growth and preparation . . . 38
2.4.1 The deposition system . . . 38
2.4.2 Co-evaporation process used for $CuInSe_2$ . . . 40
2.4.3 Co-evaporation process used for Cu(In,Ga)Se_2 . . . 41
2.4.4 Cu-rich vs. Cu-poor composition . . . 43
2.5 Potassium fluoride post deposition treatment . . . 44
2.5.1 Post deposition treatment methods . . . 45
2.5.2 Effects of alkali PDT's on absorber layer and device characteristics 46

3 Potassium fluoride treatments of $CuInSe_2$ layers **49**
3.1 Ex-Situ post deposition treatment . . . 49
3.1.1 Preparatory steps and alkali deposition . . . 50
3.1.2 Results gathered on the best treated samples . . . 52
3.1.3 Interim conclusion . . . 56
3.2 In-situ post deposition treatment with etching step . . . 56

3.2.1 Process routine and treatment conditions . . . 57
3.2.2 Variation of the treatment duration . . . 57
3.2.3 Investigation of Cu-poor $CuInSe_2$ with KF PDT . . . 69
3.3 Summary potassium fluoride treatments . . . 71

4 Is there a third acceptor in CI(G)S? 73
4.1 Characteristics of the 0.9 eV peak in $CuInSe_2$ . . . 73
4.1.1 Excitation dependency . . . 74
4.1.2 Evaluation of the activation energy . . . 76
4.1.3 Influence of the growth conditions . . . 78
4.2 Comparison to $Cu(In,Ga)Se_2$ . . . 80
4.2.1 Influence and removal of interference . . . 80
4.2.2 Low gallium concentration . . . 81
4.2.3 Various gallium content . . . 82
4.3 Comparison to admittance measurements . . . 84
4.4 Effect of surface modification and deep PL . . . 86
4.4.1 Effect of potassium cyanide etching . . . 86
4.4.2 Effect of CdS deposition . . . 88
4.4.3 Deep luminescence in $CuInSe_2$ . . . 90
4.5 Summary and new defect picture . . . 91

5 The Optical Diode Factor 93
5.1 Diode factor of devices . . . 94
5.1.1 Classical determination from IV . . . 94
5.1.2 Determination by SunsVoc . . . 95
5.2 Theoretical derivation of the link between A and k . . . 96
5.2.1 Relationship in measurements . . . 97
5.3 Experimental Validation . . . 98
5.3.1 Relationship between k and the intensity dependence of the qFLs . . . 98
5.3.2 Comparison of power law exponent and diode factor . . . 99
5.4 Summary . . . 101

6 Quasi Fermi level splitting of $Cu(In,Ga)Se_2$ 103
6.1 Time dependent qFLs measurement . . . 103
6.1.1 Evaluation of the qFLs after etching . . . 104
6.1.2 Comparison of the initial qFLs . . . 105
6.2 Measurements on passivated absorber layers . . . 108
6.2.1 Comparison of qFLs on bare and CdS covered samples . . . 109
6.2.2 Enlargement of the data set . . . 110
6.2.3 Comparison of the qFLs and V_{OC} . . . 112
6.3 Summary . . . 114

7 Summary 117

8 Outlook 119

A Acknowledgments **121**

B Glossary **123**

C Calibrated PL and qFLs analysis **126**
C.1 Calibration of the measurement set up 126
C.2 Evaluation of the qFLs 127

D Additional information and data **132**
D.1 KF-PDT post deposition treatment of $CuInSe_2$ 132
D.2 Third Acceptor in $CuInSe_2$ 136
D.3 Reversibility of surface degradation 138

E List of publications and conference contributions **139**

Bibliography **159**

ABSTRACT

Solar cells made from the compound semiconductor Cu(In,Ga)Se_2 reach efficiencies of 22.9 % and are thus even better than multi crystalline silicon solar cells. All world records are achieved using absorber layers with an overall copper deficient composition, but Cu-rich grown samples have multiple favourable properties. However, especially losses in the open circuit voltage limit the device performance. Within this work these efficiency limitations of chalcopyrites grown with copper excess are investigated. The work has been divided into four chapters addressing different scientific questions.

(i) Do alkali treatments improve Cu-rich absorber layers?
The alkali treatment, which lead to the recent improvements of the efficiency world record, is adapted to $CuInSe_2$ samples with Cu-rich composition. The treatment leads to an improvement of the V_{OC} which originates roughly equally from an improvement of the bulk and the removal of a defect close to the interface. The treatment also improves the V_{OC} of Cu-poor samples. In both cases, the treatment increases the fill factor (FF) and leads to a reduction of copper content at the surface.

(ii) Is the V_{OC} limited by deep defects in Cu-rich Cu(In,Ga)Se_2?
A deep defect, which likely limits the V_{OC}, is observed in photoluminescence measurements (PL) independent of a surface treatment. The defect level is proposed to originate from the second charge transition of the Cu_{In} antisite defect (Cu_{In}(-1/-2)). During the investigation also a peak at 0.9 eV is detected and attributed to a DA-transition involving a third acceptor situated (135 ± 10) meV above the valence band. The A3 proposed to originate from the indium vacancy (V_{In}). Furthermore the defect was detected in admittance measurements and in Cu(In,Ga)Se_2 samples with low gallium content.

(iii) Is the diode factor intrinsically higher in Cu-rich chalcopyrites?
Cu-rich solar cells exhibit larger diode ideality factors which reduce the FF. A direct link between the power law exponent from intensity dependent PL measurements of absorbers and the diode factor of devices is derived and verified using Cu-poor Cu(In,Ga)Se_2 samples. This optical diode factor is the same in Cu-rich and Cu-poor samples.

(iv) Is the quasi Fermi level splitting (qFLs) of Cu-rich Cu(In,Ga)Se_2 absorber layers comparable to Cu-poor samples?
Measuring the qFLs of passivated Cu-rich and Cu-poor Cu(In,Ga)Se_2 samples, on average a 120 meV lower splitting is determined for Cu-rich samples. This difference increases with gallium content and is likely linked to a defect moving deeper into the bandgap, possibly related to the second charge transition of the Cu_{In} antisite defect.

Overall, samples with Cu-rich composition are not limited by the diode factor. However, a deep defect band causes recombination lowering the qFLs and thus the V_{OC}. This defect is not removed by alkali treatments. A key component to improve Cu-rich solar cells in the future, especially Cu(In,Ga)Se_2, will be to remove or passivate this defect level.

CHAPTER

ONE

INTRODUCTION

The anthropogenic climate change is one of the biggest challenges of the 21th century. In the Paris agreement of 2015 most countries of the world agreed to reduce CO_2 emission to restrict the global warming to below 2 °C [1]. Since power generation is responsible for roughly a third of all CO_2 emissions (34 % in the USA [2] and similar in industrial countries [3]), reducing emissions in this segment is an essential task to reach this goal. This reduction is possible with renewable energies like photovoltaic. The sun shines about 885 million terawatt hours (885×10^{12} kWh) of power onto the earth surface each year which is more than 6000 times the primary energy consumed by humankind [4]. Taking only sun rays hitting land masses into consideration it takes 5 hours to receive the energy humankind needs within a year [4].

The prices for solar modules have been dropping since 1975 on average by roughly 20 % each time the production was doubled, which was about every 2.5 years [5]. Due to this, the levelized cost of energy, which is a measure to compare different electricity generation methods, dropped strongly for photovoltaic installations within the last years and reached break even point with coal and other fossil fuels in Germany [6]. Solar energy is in most parts of the world a cost efficient way to generate electricity [5] and can be deployed in much shorter times compared to conventional power plants. Overall, photovoltaics is a great energy source that accounts for 17 % of newly installed power generation[1] in 2017 [7]. However, photovoltaic only accounts for about 1 % of the world wide generated electricity and contributes thus barely to the primary energy overall. A lot of work has to be done to make solar energy even more cost efficient and attractive for investors and politics.

Beside the mature technology of mono crystalline and multi crystalline silicon covering about 95 % of the commercial market, also compound semiconductors like copper indium gallium di-selenide ($Cu(In,Ga)Se_2$) can be used to manufacture solar cells. Research activities on the latter material started in the 1970's at the Bell laboratories on the ternary $CuInSe_2$ [8]. Tremendous research efforts over the past decades and key developments like sodium doping, gallium grading, and alkali treatments resulted in a current world record efficiency of 22.9 % [9]. $Cu(In,Ga)Se_2$ reaches higher efficiencies than the other thin film technologies like cadmium telluride (21.0 % [10], 22.1 % [11]) or amorphous silicon (10.2 % [10], 14.0 % [11]) and also higher efficiencies than polycrystalline silicon (22.3 % [10], [11]). It falls just short compared to the emerging perovskite technology (23.3 % [11]) which however still has stability issues. By alloying $CuInSe_2$ and $CuGaSe_2$, the quaternary $Cu(In,Ga)Se_2$ is formed which exist as a solid solution over the whole

[1] All renewables combined accounted for 49 % of the added power generation in 2017. [7]

[Ga]/([Ga] + [In])-range. By replacing indium and gallium with each other, the bandgap can be tuned between 1.0 eV and 1.7 eV.

The Cu(In,Ga)Se_2 semiconductor, also called chalcopyrite, is a versatile material which is phase stable even at strong deviations from the stoichiometric point. In general, two composition types are differentiated, namely Cu-poor composition with $[Cu]/([Ga] + [In]) < 1$ and Cu-rich conditions[2] with $[Cu]/([Ga] + [In]) \geq 1$. Both exhibit different opto-electronic properties which have been studied in the past with all kinds of measurement techniques. Overall, samples grown with copper excess show favourable properties in terms of crystal growth, charge carrier mobility [12][13], defect concentration [14], [15], Urbach energy [16] and similar quasi Fermi level splitting compared to Cu-poor [17]. However, when absorber layers are finished to solar cells, considerably lower efficiencies are reached using Cu-rich grown absorbers. Compared to devices made from Cu-poor absorbers, a large loss in open circuit voltage is observed which has been linked to recombination close to the interface [18]. In case of the ternary $CuInSe_2$ most of the loss can be recovered by treating the absorber surface after growth [19], but surface treatments are less effective in Cu(In,Ga)Se_2 [20].

The aim of this thesis is to investigate these efficiency limitations in the chalcopyrite systems and how they can be overcome with surface treatments. The main measurement technique used for this is photoluminescence. Photoluminescence measurements are contact free, non destructive, and can be done on bare absorbers. This allows the direct investigation of the absorber layer without possible influences of other layers in a device stack. From measurements at room temperature, the bandgap and the quasi Fermi level splitting (qFLs) can be derived [21]. By measuring at various temperatures down to 10 K, also the electronic defect structure of a semiconductor can be probed [22]. More details about this measurement technique are discussed in chapter 2. This chapter also discusses the compound semiconductor Cu(In,Ga)Se_2 and its properties in more detail and describes the solar cell device structure. Furthermore, the absorber growth processes will be presented, differences between Cu-rich and Cu-poor composition discussed, and a small literature review about alkali treatments given.

A keystone for the major efficiency improvements in the last five years (20.3 % [23] to 22.9 % [9]) was the treatment of Cu-poor absorber layer with alkali metals like potassium, rubidium, or caesium after growth. Although plenty studies investigated the influence of this treatment on Cu-poor absorber layers, no research effort was done with regard to Cu-rich samples. But applying it to Cu-rich absorbers is promising since the treatment is reported to form a Cu-deficient surface layer, similar to the previously mentioned surface treatments. Chapter 3 closes this gap and presents two process routes of a potassium fluoride post deposition treatment that can be applied to samples grown with copper excess by integrating an etching step into the procedure. The first one is an ex-situ treatment similar to [24] with alkali deposition and annealing in two separate steps. The second one is an in-situ treatment with an etching step which is closer related to the process leading to high efficiencies on Cu-poor samples [25], [26]. Especially the second route will be thoroughly investigated by electrical and optical measurement techniques, unveiling the effects of the treatment on both Cu-rich and Cu-poor $CuInSe_2$ absorber layers.

The doping density and other electrical properties are determined by intrinsic defects in Cu(In,Ga)Se_2. Over the past decades a comprehensive model about intrinsic defects emerged from experiments and theoretical calculations. In photoluminescence measurements one shallow donor and two shallow acceptors are commonly found in $CuInSe_2$ and

[2]Meaning a stoichiometric chalcopyrite and a secondary Cu_xSe phase after growth.

$CuGaSe_2$ [15], [27]–[29]. For $CuGaSe_2$, also a third acceptor was determined [30], [31] but could not be observed in $CuInSe_2$ [32]. However, for certain growth conditions a transition at 0.9 eV is observed in low temperature photoluminescence measurements on $CuInSe_2$. This transition is investigated in chapter 4 to clarify whether there is a third acceptor also in $CuInSe_2$ and $Cu(In,Ga)Se_2$. Part of this chapter also looks at luminescence coming from a comparable deep defect observed in $CuInSe_2$ at 0.8 eV in low temperature photoluminescence measurements. This defect possibly limits the device performance by lowering the V_{OC} because of recombination.

Another possible loss of power conversion efficiency are low fill factors which among other factors are caused by high diode factors. Since also Cu-rich solar cells suffer from high diode factors it is worth investigating here. The open circuit voltage of a device can be predicted from the quasi Fermi level splitting measured on bare or passivated absorber layers. In chapter 5, an approach will be discussed how this can also be done for the diode factor. The derived theory will be tested, using Cu-rich and Cu-poor $Cu(In,Ga)Se_2$ samples by investigating illumination dependent behaviour of the V_{OC} and of the quasi Fermi level splitting.

As mentioned before, samples grown Cu-rich have a lower device efficiency and especially suffer from losses in V_{OC}. In case of $Cu(In,Ga)Se_2$ [20] the treatment of the sample surface is much less effective than in $CuInSe_2$ [19]. This could be linked to the absorber properties, since in pure $CuInSe_2$ the quasi Fermi level splitting of Cu-rich and Cu-poor samples was shown to be similar on absorber layers [17]. In chapter 6, a follow up study is presented which investigates the quasi Fermi level splitting of bare and passivated $Cu(In,Ga)Se_2$ absorber layers with varying gallium content. The degradation in air will be studied in detail and the qFLs values of bare and passivated samples will be compared. At the end of the chapter the determined qFLs values are compared to the V_{OC} of finished devices. A summary of the gathered insights will be given in chapter 7 and an outlook in chapter 8.

CHAPTER

TWO

FUNDAMENTALS AND REVIEW

Within this thesis the chalcopyrite compound semiconductor $Cu(In,Ga)Se_2$ is used as the light absorbing layer. The properties and characteristics of this materials are discussed in section 2.1. To generate power from light absorption, generated charge carriers have to be separated. This can be achieved by combining a p-type and a n-type semiconductor to create an asymmetry within the system. The fundamentals of this so called pn-junction will be discussed in section 2.2. The same chapter will also illustrate and describe the stack of layers used in the solar cell devices, highlight possible recombination processes and discuss the band alignment.

A versatile and within this thesis widely used method for the characterization of absorber layers are photoluminescence measurements, which will be discussed in section 2.3. Possible observable transitions and their temperature as well as excitation dependance will be discussed, followed by an overview of the defect picture derived over the last decades for the ternaries $CuInSe_2$ and $CuGaSe_2$. Further, the determination of the quasi Fermi level splitting from photoluminescence measurement will be explained and the measurement set up described.

The molecular beam epitaxy system and the process routes used for sample growth will be discussed in section 2.4. Followed by a comparison of samples grown with copper excess and samples grown with a copper deficiency. In the last section recent developments and gathered insights regarding the post deposition treatment of absorber layers with alkali fluorides will be reviewed.

2.1 Chalcopyrites

The name chalcopyrite used to describe $CuInSe_2$ stems from the naturally found copper iron sulfide mineral ($CuFeS_2$) which has a the same structure. The usage of $CuInSe_2$ as an absorber layer started in the 1970's at the bell labs [8], [33]. The crystal structure of this material will be reviewed in the beginning of this section. Depending of the growth conditions, the material can form several different phases which will be discussed in section 2.1.2. By substituting indium atoms with gallium atoms the opto-electronic properties can be varied and especially the influence on the bandgap, as described in section 2.1.3, can be used to improve the solar cell efficiency. Afterwards possible defects will be examined and depicted in section 2.1.4.

2.1.1 Crystal structure

The crystal structure of chalcopyrites can be derived from the zincblende structure which is shown on the left in figure 2.1. The zincblende structure has a diamond structure but with alternating planes of a group III and group V elements (or of a group II and group VI elements). Those materials follow the Grimm-Sommerfeld rule [34], which means that they have on average 4 electrons per atom and thus form a crystal where each atom has four next neighboring atom in a tetrahedral coordination. To get the chalcopyrite structure from the given example, each Zn atom (group II) is replaced alternating with a Cu atom (group I) and a In atom (group III), like shown on the right side of figure 2.1. This replacement leads to a tetragonal distortion ($\eta = c/2a \neq 1$) meaning that the lattice constant c (11.616 Å) is not exactly twice the lattice constant a (5.784 Å) [35]. The distortion originates from the different bond length of Cu-Se and In-Se. Within this system it is possible to replace indium atoms by the smaller gallium atoms (same element group) to change the opto-electronic properties. A solid solution between $CuInSe_2$ and $CuGaSe_2$ exist over the whole compositional range. Besides alloying with gallium, also replacing selenium with sulfur is possible and also replacing copper with silver can be done [36].

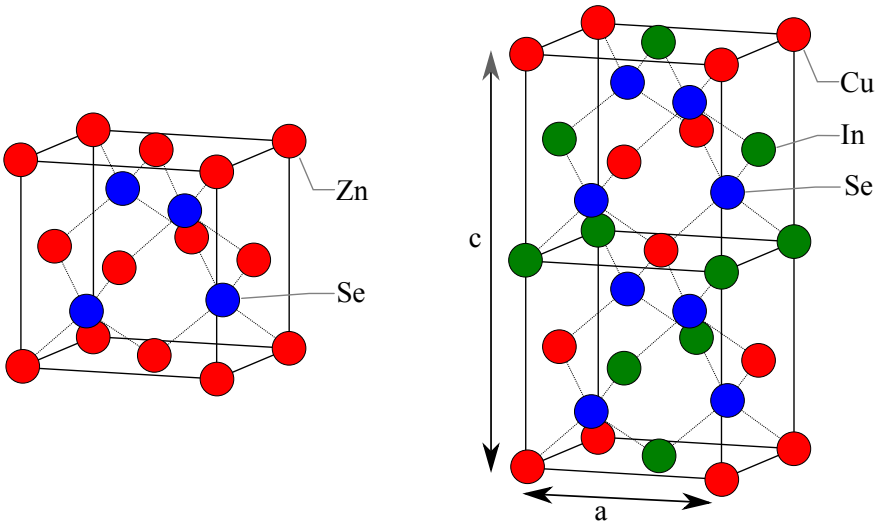

Figure 2.1: Left: Cubic unit cell of the of the zincblende structure. Right: Stacked tetragonal unit cell of the chalcopyrite crystal structure.

2.1.2 Phase diagram

The above describe phase is the so called α-phase. A key characteristics of it is that it can be formed over a wide compositional range. In figure 2.2, the pseudo binary phase diagram between In_2Se3 and Cu_2Se is depicted, showing various phases dependent on the temperature and the copper content. The stoichiometric point is at 25 % copper content. The α-phase is stable down to 22 % copper content at the growth temperature used in a co-evaporation process of about 550 °C. This high tolerance to copper loss can be explained by the formation of defect complexes consisting of two copper vacancies and an indium on copper antisite ($2V_{Cu}$-In_{Cu}) [37]. This complex is predicted to have a low formation energy, to be electrically inactive, and to stabilized the system [37]. For higher temperatures the δ-phase forms, which has a sphalerite structure (no ordering of Cu and In atoms). For very low copper contents and low temperatures the β-phase forms which is associated with

the so called order vacancy compound $CuIn_3Se_5$. For even lower copper contents also the γ-phase (not included in the graph) can form which has a composition of $CuIn_5Se_8$.

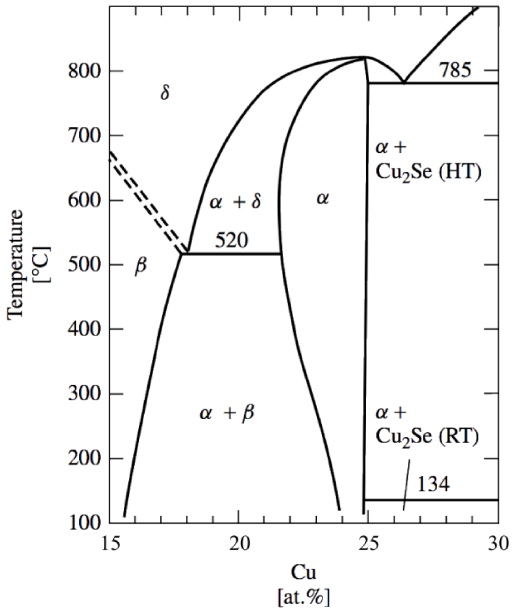

Figure 2.2: Pseudo binary In_2Se3-Cu_2Se phase diagram around the stoichiometric composition of $CuInSe_2$ at 25 % copper content with various phases, reprint from [38].

Moving in the other direction and above 25 % copper content, stoichiometric $CuInSe_2$ is formed in the α-phase together with Cu_xSe secondary phases, which take up excessive copper. In general those Cu_xSe phases form on top of the stoichiometric bulk [39] and are not enclosed within the stoichiometric phase. The Cu_xSe phases are highly conductive and shunt the solar cell if not etched away before device finishing. Samples grown under copper excess are denoted Cu-rich throughout this thesis, referring to the [Cu]/[In]-ratio after growth, although no real copper rich phase exist and they consist of a stoichiometric bulk and Cu_xSe phases. A really similar phase diagram has been shown for $CuGaSe_2$ [40] and it is comparable for the solid solution $Cu(In,Ga)Se_2$.

2.1.3 Opto-electronic properties

The ternary $CuInSe_2$ has a high absorption coefficient ($> 10^5\,cm^{-1}$) [41] and a direct bandgap E_G of about 1.02 eV, which increases by 0.2 meV K^{-1} with decreasing temperature. The refractive index is in the range of 3.1 and 2.6 for energies between 0.7 eV to 3 eV [42]. It should be noted here that the bandgap of absorber layers with Cu-poor composition is about 50 meV lower than in samples with Cu-rich composition. This difference can be explained by a coupled effect of the amount of copper vacancies V_{Cu} and of a lattice distortion [43]. When $CuInSe_2$ is alloyed with gallium, the unit cell shrinks and thus the bandgap increases. This change in the bandgap in $Cu(In_{1-x}, Ga_x)Se_2$ is not fully linear with gallium content (x) but follows a quadratic dependence. This bowing can be described by equation (2.1). The parameters used in the equation are $E_G^{CIS} = 1.02\,eV$, $E_G^{CGS} = 1.68\,eV$ and a bowing factor of $b = 1.67$ [42].

$$E_G^{CIGS} = x\,E_G^{CIS} + (1-x)x\,E_G^{CGS} - x(1-x)b \tag{2.1}$$

2.1.4 Intrinsic defects in chalcopyrites

The complex structure of $Cu(In_{1-x}, Ga_x)Se_2$ gives rise to a variety of different crystal defects that can be formed. Those play a key role in the performance of the material as an absorber in a solar cell and can be categorized in four classes [44].

1) Misalignment of a sole or several atoms can lead to dislocations or line defects.

2) An array of dislocation can lead to a planar defect. Examples for this are stacking faults, where the stacking order is abruptly changed, as well as grain boundaries, where the crystal orientation changes.

3) Three dimensional defects appear when part of the crystal is absent (void) or replaced by another material (inclusion).

4) Point defects are formed at a single lattice position and can be intrinsic or extrinsic. The investigated polycrystalline Cu(In,Ga)Se_2 thin films have grain sizes of a few micrometer and thus have a lot of grain boundaries, as shown in figure 2.6. Although grain boundaries (defect type 2) have a detrimental effect in other materials systems, they are benign in Cu(In,Ga)Se_2. Even though it is still under dispute if they even could be advantageous, it is agreed that they are not harmful. This can be attributed to the formation of a neutral barrier [45]. In good processes, inclusions do not play a role and also voids do not form. However, even for processes where voids are formed at the absorber-back contact interface, they were modeled to be benign or advantageous [46]. Intrinsic points defects play a big role since they are formed in high concentrations and thus determine the doping and the dominant recombination processes. Depending on the growth conditions, the formation of specific defects can be favoured or hampered leading to different doping densities [47] and even to a switch from p-type to n-type doping (only possible on epitaxial [13] or sodium free [47] samples). Within this work only polycrystalline Cu(In,Ga)Se_2 materials are investigated grown on soda lime glass which thus contain sodium. They always exhibit p-type doping in the order of $10^{16}\,cm^3$ which is in general higher in Cu-rich compositions than in Cu-poor compositions. Due to the different elements inside the crystal structure a large variety of point defects are possible, like:

1. **Vacancies** are missing atoms within the crystal structure, like V_{Cu}, V_{In}, V_{Ga}, V_{Se}
2. **Antisites** are atoms on the wrong lattice site, like Cu_{In}, Cu_{Ga}, In_{Cu}, Ga_{Cu}
3. **Interstitials** are atoms in between lattice sites, like Cu_i, In_i, Ga_i, Se_i
4. **Complexes** are combinations of the three defects above forming a new electronic state, like $2V_{Cu}$-In_{Cu}, Cu_i-Cu_{In}, Cu_i-V_{In}, Cu_i-$2V_{Cu}$, ect.

Also a large variety of defects have been observed experimentally by photoluminescence, cathodoluminescence, admittance, hall and other methods. However, the attribution of defect levels to point defects is not straight forward. The theoretical prediction of the formation of a defect is difficult since its formation enthalpy depends on the chemical potential of the species and thus on the growth condition. It furthermore depends on the Fermi level, which however depends on the charge carrier densities and thus on the charge state of the defect. All this leads to a complex interplay of parameters. Early calculation by Zhang, Wei and Zunger [48], gave first insights and predicted the copper vacancy V_{Cu} to have low formation energy and to be widely abundant in almost all compositions. Also the cation antisites were predicted to form rather easily, whereas selenium related antisites

could be excluded to form due to very high formation energies. Over the years the methods improved and especially usage of screened-exchange hybrid density functional theory of Heyd, Scuseria and Ernzerhof (HSE06) [49] improved the predicted formation enthalpies and defect energies. Although the values between different publications still differ [50]–[54], a more common picture evolved. The most likely formed points defects (V_{Cu}, Cu_{In}, Cu_i, Cu_{Ga}, In_{Cu}, Ga_{Cu}, V_{In}, V_{Se}) are shown in figure 2.3. The latest defect picture with the attribution of the point defects to experimental data is presented in section 2.3.4.

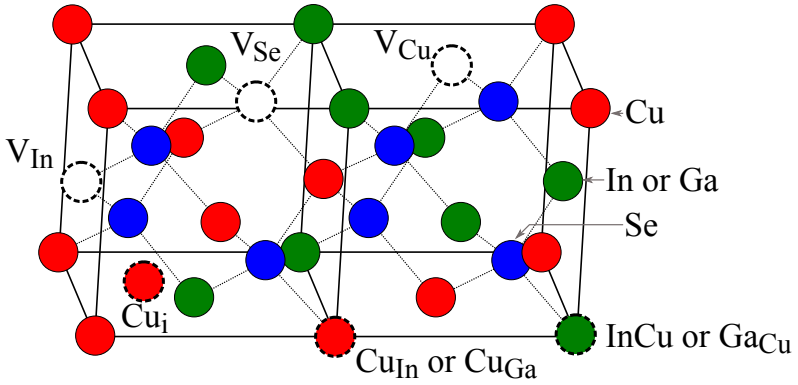

Figure 2.3: Tetragonal unit cell of the chalcopyrite crystal structure with possible intrinsic point defects.

2.2 Solar cell devices

The function of a solar cell device is to generate charge carries by absorbing light and to separate them spatially, so that a voltage builds up at the terminals that can used to power an electrical load. For this purpose a material is needed which can absorber light in the visible range and in which the lifetime of the excited charge carrier is long enough to allow a spatial separation. A good material for this are semiconductors, since the energy gap between the valence band and the conduction band makes absorption possible but hinders the recombination due to the lack of continuous states. To separate the generated charge carriers an asymmetry in the system is needed, which can be achieved by combining two semiconductors with different types of doping. The investigated solar cells within this thesis are made from n^+p junctions, where a p-type semiconductor is in contact with a n-type semiconductor with a much higher doping. The basics of the pn junction will be discussed in section 2.2.1. To form a real solar cell more layers are needed than the two semiconductors forming the pn junction. In section 2.2.2 device structures used in literature are presented as well as the layer stack used within this work. Subsequently the band alignment and possible loss mechanism are discussed. The characterization of solar cells with current voltage measurements will be discussed in section 2.2.3. The presented statements are based in case of the junctions formations and the derivation of the Shockley equation on the books of Würfel [55] and Sze [56]. In case of the device structure and current voltage analysis the explanations follow the books of Scheer and Schock [36] as well as of Luque and Hegedus [57].

2.2.1 PN-junction

The asymmetry in a photovoltaic device is generally introduced by a pn junction. Two types of junctions are differentiated, namely homo junctions and hetero junctions. In a homo junction, the doping within one material is changed laterally by introducing different dopants leading to a junction within one material. In a hetero junction two different semiconductors are combined. To reduce the complexity in the derivation of the necessary formulas, a homo junction will be used exemplary, although hetero junctions are used in thin film solar cells.

On the left side of figure 2.4 the energy scheme of a p-typed doped and an n-typed doped semiconductor are depicted. The distance of the conduction band edge E_C to he vacuum level is given by the sum of the electron affinity χ and external electric field $-e\Phi$ (electric potential). The distance between the conduction band edge E_C and the valence band edge E_V is the bandgap E_G. Adding the work function W_A (or chemical potential) to the electronic potential gives the energetic position of the Fermi level E_F (or the electro chemical potential). The Fermi level position depends on the doping concentration of acceptors N_A and the density of states at the valence band edge N_V. It defines where the occupation probability of an electronic state is $1/2$ according to the Fermi-Dirac distribution. Respectively, the same is valid for n-type semiconductors where E_F is defined by the doping concentration of donors N_D and the density of states at the conduction band edge N_C. With increasing doping concentration the Fermi level moves closer to the respective band edge. For solar cells non degenerately doped semiconductor are used meaning that the Fermi level is inside the bandgap and at least $3k_BT$ away from the respective band edge ($E_V + 3k_BT < E_F < E_C - 3k_BT$), with the Boltzmann constant k_B and the temperature T. In this case also the Boltzmann approximation is valid simplifying some calculations.

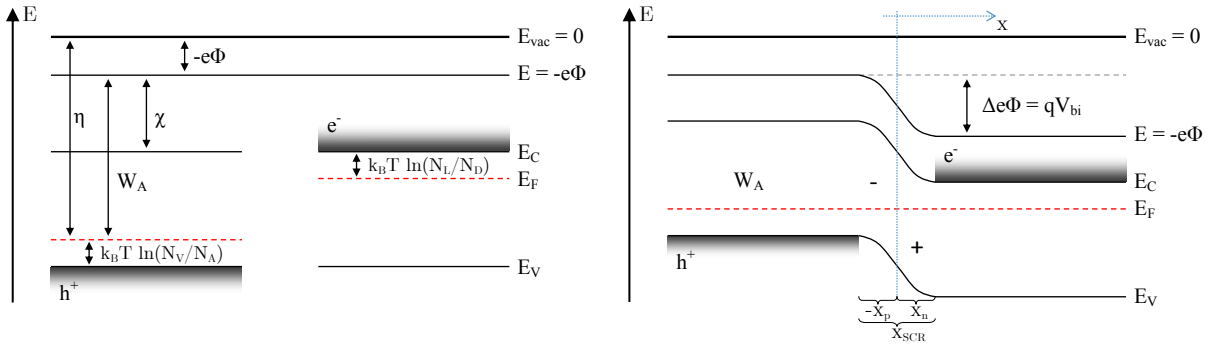

Figure 2.4: Left: Schematic energy diagram of p-type and a n-type doped semiconductor. Right: Energy diagram of a pn homo junction. Adapted from [58].

If a p-type semiconductor and a n-type semiconductor are joint together, the electrons from the p-type semiconductor diffuse into the n-type semiconductor and holes from the n-type semiconductor into the p-type semiconductor due to the gradient in concentration. The majority charge carriers from each side recombine at the interface, leaving charged ions in their respective original semiconductor side. These fixed positive and negative charges in the former neutral region built up an electrostatic potential, which is opposing the diffusion of the respective majority charge carriers. In thermal equilibrium the forces from diffusion, which can also be described in chemical potential differences, and the electric potential cancel each other out leading to a flat electro chemical potential E_F. The

electric potential which builds up is called build in voltage V_{bi}. Since the semiconductor is in equilibrium, the product of the charge carrier densities at each point is given by the intrinsic charge carrier density and can be described by equation (2.2).

$$np = n_i^2 = N_{\mathrm{C}} N_{\mathrm{V}} \exp(-E_{\mathrm{G}}/(k_{\mathrm{B}}T)) \tag{2.2}$$

The extension of the space charge region (or depletion width) into the respective side x_{p} and x_{n} depends on the doping densities of both semiconductors. Assuming a total ionization of the dopants in both semiconductors, an abrupt junction, and a box like distribution of the ionized dopants, the charge neutrally tells us that the relative widths are defined by equation (2.3).

$$N_{\mathrm{A}} x_{\mathrm{p}} = N_{\mathrm{d}} x_{\mathrm{n}} \tag{2.3}$$

When the Poisson equation, which links the electrostatic potential to the charge density, is integrated twice (find details in [56]) the width is found to be given by equation (2.4) with ϵ_{r} being the dielectric constant and ϵ_0 being the vacuum permittivity.

$$x_{\mathrm{SCR}} = \sqrt{\frac{2\epsilon_{\mathrm{r}}\epsilon_0}{q}\left(\frac{1}{N_{\mathrm{A}}} + \frac{1}{N_{\mathrm{D}}}\right) V_{\mathrm{bi}}} \xrightarrow{N_{\mathrm{D}} >> N_{\mathrm{A}}} \approx \sqrt{\frac{2\epsilon_{\mathrm{r}}\epsilon_0}{q\, N_{\mathrm{A}}} V_{\mathrm{bi}}} \tag{2.4}$$

In Cu(In,Ga)Se_2 thin film solar cells the p-type absorber layer has a much lower doping than the n-type doped window/buffer double layer. Due to this the space charge region nearly fully extends into the absorber layer and the electric potential only drops in the absorber layer. With $N_{\mathrm{D}} >> N_{\mathrm{A}}$ the space charge region width calculation can be simplified as indicated in equation (2.4). If an external voltage is applied the electric potential across the pn junction changes ($\Delta\Phi = V_{\mathrm{bi}} - V$) and with this the space region width. Since later admittance measurements are partly used within the script it should be noted, that it is possible to assign a capacitance to the space charge region. This can be done assuming an ideal plate capacitor with the charge $Q = q\, N_{\mathrm{A}}$ and the distance x_{SCR}. The capacitance is then given by equation (2.5). More details about capacitance based measurement techniques can be found in [59].

$$C_{\mathrm{SCR}} = \frac{dQ}{dV} = \sqrt{\frac{q\epsilon_{\mathrm{r}}\epsilon_0}{2}\frac{N_{\mathrm{A}}}{V_{\mathrm{bi}} - V}} \tag{2.5}$$

PN junction under illumination

When the pn junction is illuminated with light with sufficient energy ($E_{\mathrm{h}\nu} > E_{\mathrm{G}}$), excess charge carriers (Δn and Δp) are generated. Since the description of the charge carrier density of the electron and holes it not possible with one Fermi level anymore, quasi Fermi levels are introduced for electrons and holes. The charge carrier density is then given by equation (2.6) assuming that the semiconductors are not degenerately excited.

$$n = N_{\mathrm{C}} \exp\left(\frac{E_{\mathrm{C}} - E_{\mathrm{F,n}}}{k_{\mathrm{B}}T}\right) \qquad p = N_{\mathrm{V}} \exp\left(\frac{E_{\mathrm{V}} - E_{\mathrm{F,p}}}{k_{\mathrm{B}}T}\right) \tag{2.6}$$

The product of the charge carrier densities now depends on the local splitting of the quasi Fermi levels as shown in equation (2.7). This quasi Fermi level splitting (qFLs) describes the local chemical potential and thus the maximal extractable energy.

$$np = n_i^2 \exp\left(\frac{E_{\mathrm{F,n}} - E_{\mathrm{F,p}}}{k_{\mathrm{B}}T}\right) \tag{2.7}$$

If the temperature is constant, it can be shown that the local current density is defined by the gradient of the quasi Fermi level and the carrier density as depicted in equation (2.8) for electrons and holes respectively, with the electron mobility μ_{n} and hole mobility μ_{p}.

$$J_{\mathrm{n}}(x) = \mu_{\mathrm{n}} n \frac{dE_{\mathrm{F,n}}}{dx} \qquad\qquad J_{\mathrm{p}}(x) = \mu_p p \frac{dE_{\mathrm{F,p}}}{dx} \tag{2.8}$$

For a homogenous materials (no variation in electron affinity χ, bandgap E_{G}, or density of states) the current of holes and electrons can be expanded to equation (2.9). Here the Einstein-Smoluchowski relation ($D = \mu k_{\mathrm{B}}T/e$) is used to calculate the diffusion constants D_{n} and D_{p}. The first term describes the diffusion current, which for electrons goes from the n-type semiconductor into the p-type semiconductor (right to left in figure 2.5). The second term describes the drift current from the p-type into the n-type semiconductor for electrons. The drift and diffusion current of holes are directed into the respective opposing direction.

$$J_{\mathrm{n}}(x) = eD_{\mathrm{n}} \frac{dn}{dx} - e\mu_{\mathrm{n}} n \frac{d\Phi}{dx} \qquad\qquad J_{\mathrm{p}}(x) = -eD_{\mathrm{p}} \frac{dp}{dx} - e\mu_{\mathrm{p}} p \frac{d\Phi}{dx} \tag{2.9}$$

The total current of charge carriers is now defined by the summation of the electron current density and the hole current density ($J_{\mathrm{total}} = J_{\mathrm{n}}(x) + J_{\mathrm{p}}(x)$). With this knowledge three cases for an illuminated pn junction are compared, as depicted in figure 2.5. For the illumination a flat generation profile is assumed leading to a uniform excitation of charge carriers across the semiconductors. The generated excess charge carriers (Δn and Δp) and especially the strong relative increase of minority carriers lead to an enhanced drift current. If both contacts are connected without a load and thus no applied voltage, the quasi Fermi level for holes in the p-type semiconductor has to be the same as the quasi Fermi level for electrons in the n-type semiconductor as depicted in 2.5 (a). Due to the excess charge carriers a considerable drift current is flowing across the junction, which depends on the illumination conditions and is called short circuit current. If a small forwards bias is applied to the junction all energy levels on the n-type side move up respectively to the p-type side as shown in 2.5 (b). The drift current does not change considerable by this, but due to the lower energy barrier for the majority charge carriers the diffusion current increases. This is the case in which solar cells are operated. If the applied forward bias is increased further, the diffusion current increases exponentially, due to the reduce potential barrier. At some point, drift and diffusion cancel each other out and no current is flowing 2.5 (c). In this case the quasi Fermi levels for holes and electrons are flat but split due to the illumination. The applied voltage needed for this is called open circuit voltage. This condition can also be reached if the contacts are not connected or no contacts exist. The electric potential in those cases is generated by the build up of charge carriers form the drift current, which are not extracted.

The overall charge transport across a pn junction can be described when three coupled differential equations are solved. Those "semiconductor equations", first described by van Roosbroeck [60], include one continuity equation for electrons, one continuity equation for holes, and a Poisson equation. From rigorous derivation and multiple simplifications the Shockley equation can be derived, as shown in [36] and [61]). Assuming that the photo current is voltage independent and that it can be superimposed with the diode current, equation (2.10) is derived.

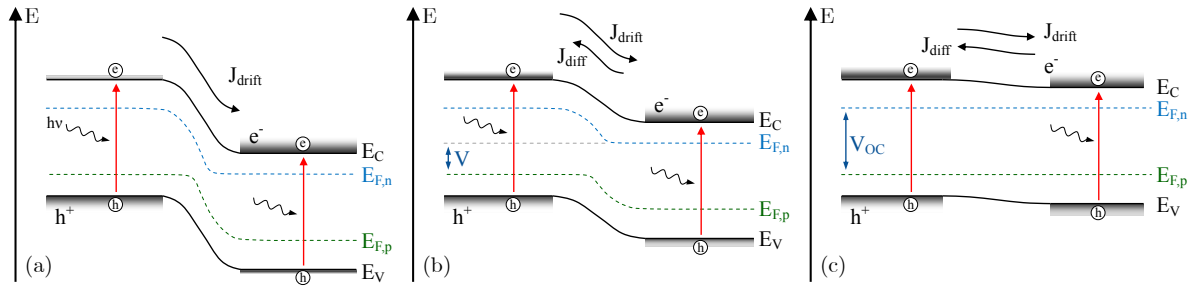

Figure 2.5: Schematic band diagram of an illuminated pn junction under (a) short circuit conditions and (b) under small forward bias and (c) with applied open circuit voltage. Based on [58].

$$J(V) = J_0 \left[\exp\left(\frac{qV}{A\, k_\mathrm{B} T} \right) - 1 \right] - J_\mathrm{SC} \tag{2.10}$$

It describes the current across a junction as a function of the applied voltage and depends on the saturation current density J_0, the diode ideality factor A, the Boltzmann constant k_B, the temperature T, and the photo current J_SC. When the junction is not illuminated and a reverse bias is applied, charge carriers are still excited thermally. Those excited charge carriers lead to a small drift current across the junction which is the saturation current density J_0. The diode ideality factor A has in general a value between 1 and 2 and gives an indication on how close the device is to an ideal diode ($A = 1$). The value depends on the injection level, defects, recombination (dependent on type and location), and will be discussed in more detailed in section 5.1.

2.2.2 CIGS thin film solar cells

Although in theory only a pn junction is needed to separate charge carriers, a solar cell device needs more components to extract charge carriers. In case of Cu(In,Ga)Se_2 solar cells a layer stack as shown schematically on the left in figure 2.6 is used within the thesis. On the right side of figure 2.6 a cross section scanning electron image of a solar cell is shown. A brief historical sketch about milestones in the Cu(In,Ga)Se_2 research and the development of the device structure can be found in [36]. An overview about recent progress can be found in [62]. In the following first common methods and materials for the solar cell fabrication are discussed. Afterwards the process used for device fabrication used within this work is outlined.

Over the last 3 decades the highest efficiencies were reached by a broad range of methods and materials [33], [63]–[66]. For the substrate predominately soda lime glass (SLG) is used which has a similar expansion coefficient to $CuInSe_2$ which reduces the build up of stress during cooling after film growth. Furthermore, it contains considerable amounts of sodium (Na). During growth this diffuses through the molybdenum back contact into the growing absorber layer and improves the crystal growth and enhances the solar cell performance [33], [67], [68]. However, also the usage of flexible substrates like stainless steel or flexible polyimide foil is possible and the cells made on those substrates reach efficiencies above 20 % [69].

The back contact is made of a 500 nm to 1000 nm thick layer of molybdenum (Mo) sputtered onto the substrate. Other metals have been test previously, but mostly showed poor performance [70].

On top of the back contact the absorber layer is grown. The most common absorber deposition techniques are co-evaporation [26] and a combination of sputtering of precursor layers and annealing them [71]. The absorber layer are typically between 2 µm and 3 µm thick and are deliberately manufacture with a double gallium gradient leading to a larger bandgap at the front and back contact. Especially the grading towards the back minimizes recombination and thus increases the V_{OC} [72]. At the beginning of the growth process excess selenium is evaporated to aid the formation of a $MoSe_2$ surface layer at the back contact. This layer is proposed to form a quasi-ohmic contact between absorber and metal [73] and to give a small spike in the conduction band alignment reducing recombination [73], [74].

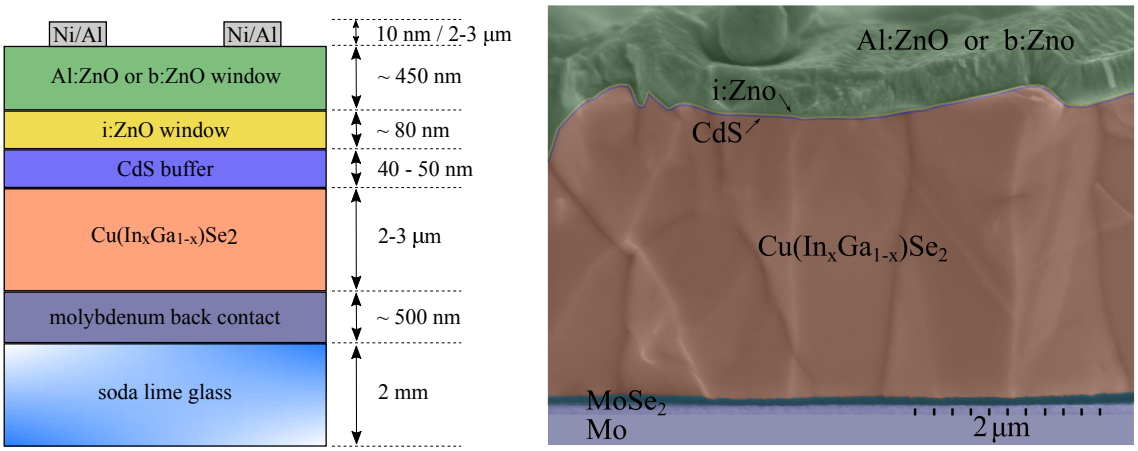

Figure 2.6: Schematic stack and cross section scanning electron image of a $Cu(In,Ga)Se_2$ solar cell.

After growth the absorber layer is covered with a buffer layer. Predominately a roughly 50 nm thick cadmium sulfide layer (CdS) is used which is deposited by wet chemical bath deposition. Due to the deposition method a full coverage of the absorber surface is possible despite the low thickness. The CdS growth is characterized by pseudo epitaxial growth, due to the small lattice mismatch to $CuInSe_2$ and the cleaning affect of the ammonia in the chemical solution [33]. Although not needed to form a solar cell and partly absorbing the light in the short wavelength region, the CdS layer improves efficiency. It has a favourable band alignment with the absorber layer leading to a spike like configuration [39] and it protects the absorber from damage inflicted by the succeeding sputtering of the window layer [75]. Furthermore, in literature it is speculated that the in-diffusion of Cd into the first few nanometer of the absorber layer helps the formation of a good hetero contact [76]–[78]. Several other buffer layers [Zn(O,S), In_2S_3, (Zn,Mg)O, (Zn,Sn)O] have been investigated [33], [63], [65], [79] seeking to get rid of the toxic and rare cadmium and reduce parasitic absorption in the short wavelength region. Very promising results have been recently shown by Solar Frontier [71], [80] showing a record cell with 22.8 % efficiency (in-house measurement) with a zinc oxysulfide buffer [Zn(O,S)].

In the next step the transparent front contact, the window layer, is deposited. Commonly a double layer of intrinsic zinc oxide and an aluminum doped zinc oxide (AZO) is used deposited by sputtering. Both the CdS and the intrinsic ZnO have a rather high resistivity and thus increase the series resistance in the solar cell. However, due to the low conductivity, areas with lower quality are screened limiting their detrimental effect on the cell performance [81]. Other options for the window layer are boron doped zinc oxide, hydrogenated indium oxide, or indium zinc oxide which have been successfully

implemented [63]. To enhance the carrier collection a metal grid is deposited on the absorber in the last step. The enhanced carrier collection outweighs the losses from the shading of the opaque grids.

In the world record cells CdS is replaced by Zn(O,S) and intrinsic ZnO is replaced by (Zn,Mg)O to reduce the parasitic absorption in the short wavelength region [26], [71]. All this different materials and process routes show the variety of the cell system and possibilities for future developments.

Device processing of the investigated solar cells

The samples investigated throughout this work are all polycrystalline samples grown by co-evaporation on molybdenum covered soda lime glass. For $CuInSe_2$ and $Cu(In,Ga)Se_2$ two different growth processes are used which are described in more detail in section 2.4.2 and section 2.4.3. The $CuInSe_2$ absorbers are typically about 3 µm thick whereas the $Cu(In,Ga)Se_2$ are in general with $\sim$2.2 µm a bit thinner. Before the deposition of the buffer layer, each absorber is etched in a potassium cyanide (KCN) solution. This is necessary for absorber grown with a final Cu-rich composition to remove the conductive Cu_xSe layer formed at the absorber surface. The etching is done in 10 wt% KCN in water solution for 5 min for Cu-rich samples. It removes all Cu_xSe secondary phases as well as possible oxides formed during storage or transfer [82], [83]. Although not necessarily needed since no Cu_xSe is formed during growth, also Cu-poor samples are etched for 30 s in 5 wt% KCN solution to removes residual oxides [17]. Directly after etching the absorber layer is covered with a 50 nm thick CdS buffer layer, which is deposited by wet chemical bath deposition. The process used for the deposition is originally based on [75] but was adapted to our needs. The reaction takes place at a constant temperature of 67 °C for 4 min to 6 min until a turbidity is observed in the solution. The reactants used in the solution are cadmium sulfate (2 mmol), thiourea (50 mmol), ammonia (1.5 mol) and de-ionized water.

Similar to literature a double layer of intrinsic and doped zinc oxide is used as window layer and deposited by sputtering. For most $Cu(In,Ga)Se_2$ samples a double layer of intrinsic zinc oxide and an aluminum doped zinc oxide (AZO) is used, since they were mostly made in the beginning of my doctoral studies. Later the baseline process changed and from there on the samples are finished with a window layer consisting of a double layer made of again intrinsic ZnO and nominally undoped zinc oxide layer deposited under an additional plasma near the substrate (bZnO). The latter one has the same resistivity compared to AZO but a higher mobility, which leads to a higher transparency in the infrared region [84]. The grids used to enhanced the carrier collection are deposited by electron beam evaporation and consist of around 10 nm of nickel to improved adhesion and 2 µm of aluminum.

Band alignment

The layer stack discussed above, gives rise to a more complicated band diagram than for a simple pn junction. The different doping densities, electron affinities, and bandgaps of the layers result in the band diagram shown in figure 2.7. The junction is depicted under illumination in open circuit condition, leading to split but flat quasi Fermi levels. Between the conduction band of the absorber and the CdS buffer layer an offset to higher energies is observed, which is called spike configuration. From the buffer layer to the window layer a cliff like configuration is seen. The same terminology is used for band offsets in the valence

band, where only cliff like offsets are observed. The spike like behaviour of the CdS in the conduction band depends on the gallium content of the Cu(In,Ga)Se_2 absorber. The band offset changes to a cliff like behaviour for bandgaps above 1.35 eV [85], since the inclusion of gallium shifts the conduction band upwards. In general a spike like configuration is favourable for the cell performance since it reduces interface recombination without blocking the current as long it is not too high (>0.4 eV) [86], [87]. The electrons can cross the barrier imposed by the spike by thermionic emission. A cliff like behaviour on the other hand strongly limits the possible device performance due to enhanced recombination.

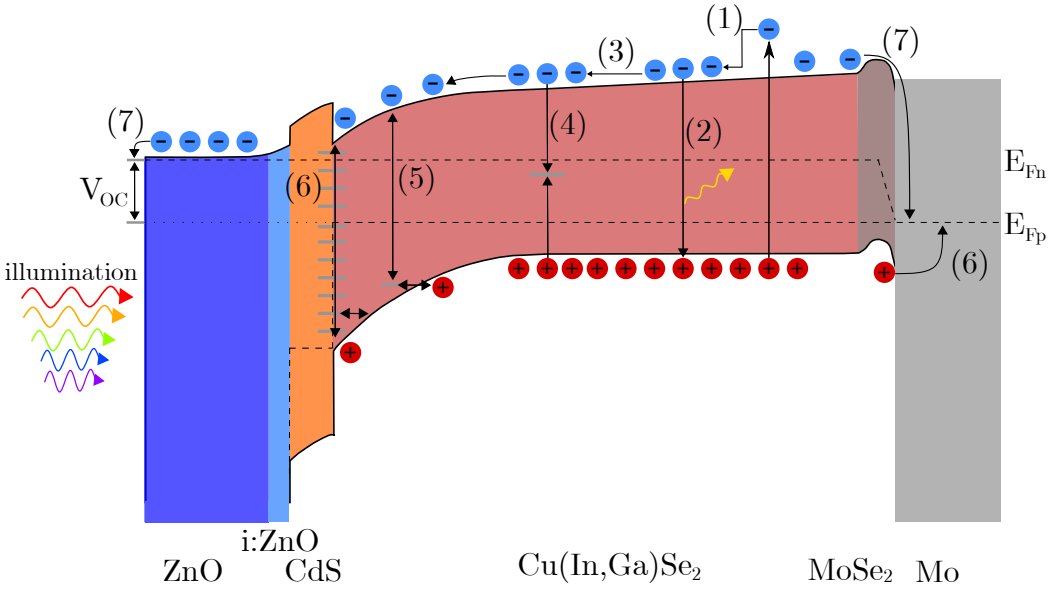

Figure 2.7: Schematic band alignment of a common Cu(In,Ga)Se_2 solar cell under illumination and open circuit condition. Various loss mechanisms are also depicted with (1) thermalization loss, (2) radiative recombination (not a loss), (3) transport losses (see text), (4) defect recombination, (5) recombination in the space charge region, (6) interface recombination, and (7) contact recombination. Grey horizontal lines depict defect states.

Within the graph also possible loss mechanisms are depicted. Everything starts by the generation of an electron hole pair by absorbing a photon coming through the window layer. The excited carrier thermalize to the band edges within picoseconds under the emission of phonons (1). The magnitude of this loss depends on the bandgap of the semiconductor and the energy of the absorbed photon. A possible way to minimize this loss is the usage of multi junction solar cells [57]. While diffusing in the absorber layer, the generated electron might recombine radiatively with a majority charge carrier (2). This process is unavoidable and is thus not really a loss. The impact of this is negligible on the device performance.

A low minority carrier lifetime and limited diffusion can lead to a reduced carrier collection (3). However, for the investigated samples this is a minor effect. The recombination involving a (deep) defect (4) is called Shockley-Read-Hall recombination (SRH) and can be reduced by lowering the defect density. Recombination (5) summarizes recombination within the space charge region which includes SRH recombination and tunnel enhanced recombination. The latter one is especially important in samples with high doping densities, like Cu-rich chalcopyrites, since this leads to strong bend bending towards the buffer layer. In this case tunneling enhanced recombination can be an efficient recombination path [12]. Recombination path (6) depicts recombination via interface defect states. Also included

in the picture are contact losses (7) which are especially important when the absorber has no grading towards the back since the absorber-molybdenum interface has a comparable high recombination velocity [72].

2.2.3 Current voltage analysis

The most widely used technique for the characterization of pn-junctions and solar cell devices is the measurement of the current as a function of the applied voltage (IV). This measurement is generally done both in the dark and under illumination. The illumination conditions are tuned to be close to $100\,\mathrm{mW\,cm^{-2}}$ with an air mass 1.5 spectrum (AM1.5) [88], roughly representing the average power density and spectrum in southern Europe. It should be noted here that for the illumination in the beginning of the dissertation a cold halogen lamp was used. The mismatch of the spectrum of the lamp and the AM1.5 spectrum makes comparisons between in-house measurements and literature complicated. To compare in between samples with similar bandgap however, it is a valid method. Later a solar simulator was used, which spectrum is closer to the AM1.5 spectrum.

An ideal solar cell as described by equation (2.10) can be described in an equivalent circuit consisting of a power source and a diode in parallel, as depicted on the left in figure 2.8. However, a $Cu(In,Ga)Se_2$ solar cell has more layers than the pn-junction as described in section 2.2.2 and plenty of loss mechanism are possible. To account for this the equivalent circuit is extended. To include possible shunt paths across the absorber layer or low quality areas a resistance is put in parallel to the two existing components, which is called shunt resistance or parallel resistance R_{Sh}. Furthermore, the contacts are not perfect and have a limited conductivity. To account for this another resistance is added in series R_{S}. Part of the applied voltage now drops across this resistance reducing the voltage across the diode.

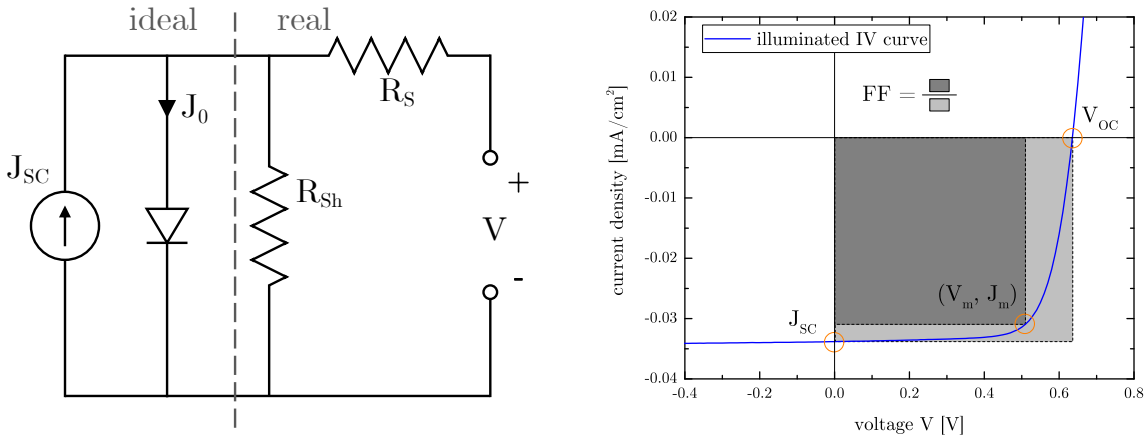

Figure 2.8: Left: Equivalent circuit of a solar cell device including a power generation source, a diode, the shunt resistance R_{Sh} and the series resistance R_{S}. Right: Exemplary current voltage curve of a chalcopyrite solar cell. Indicated are also key quantities like J_{SC} ,V_{OC} and fill factor (see text for details).

Adding those extension to equation (2.10), gives equation (2.11), which now describes a real devices. For more complex systems also a second diode could be added to the equation, but will not be done within this work.

$$J(V) = J_0 \left[\exp\left(\frac{q(V - JR_\mathrm{S})}{A\,k_\mathrm{B}T} \right) - 1 \right] + \frac{(V - JR_\mathrm{S})}{R_\mathrm{Sh}} - J_{SC} \tag{2.11}$$

From an illuminated current voltage measurement, like shown on the right of figure 2.8, characteristics like V_OC, J_SC and efficiency η can be directly assessed. The multiplication of current and voltage gives the extractable power. The efficiency is defined by the maximum electrical power output divided by the power of the illumination used (equation (2.12)). The voltage and current at the maximal power output (V_m and J_m) are used to define the fill factor ($FF = V_\mathrm{m}J_\mathrm{m}/V_\mathrm{OC}J_\mathrm{SC}$). Simplified the FF is a measure on how round the curve is in the fourth quadrant. The maximal achievable value depends on the bandgap and is roughly 0.87 for the investigated bandgap region of 0.95 eV to 1.3 eV [89].

$$\eta = \frac{J_\mathrm{m}\,V_\mathrm{m}}{P_\mathrm{ill}} = \frac{J_\mathrm{SC}\,V_\mathrm{SC}\,FF}{P_\mathrm{ill}} \tag{2.12}$$

By fitting the IV curve with equation (2.11) also parameters like A, J_0, R_S, and R_Sh can be determined. For the fitting an orthogonal regression is used to account for the strongly varying slopes in forward and reverse bias. Within this thesis the IV fitting program *ivfit* developed by the energy center of the Netherlands (ECN) will be used, see also [90]. Rearranging equation (2.11) for the voltage using open circuit conditions (meaning: $J(V) = 0$), equation (2.13) can be derived.

$$V_\mathrm{OC} = \frac{A\,k_\mathrm{B}T}{q}\,\ln\left(-\frac{V_\mathrm{OC}}{R_\mathrm{Sh}\,J_0} + \frac{J_\mathrm{SC}}{J_0} \right) \approx \frac{A\,k_\mathrm{B}T}{q}\,\ln\left(\frac{J_\mathrm{SC}}{J_0} \right) \tag{2.13}$$

For the investigated samples it can be assumed that $V_\mathrm{OC}/R_\mathrm{Sh}$ is much smaller than J_SC and can thus be neglected in equation (2.13). The saturation current density J_0 has a temperature activated characteristic, which can be described by $J_0 = J_{00}\exp(E_\mathrm{A,rec}/A\,k_\mathrm{B}T)$ [36], with the reference current density J_{00} and the activation energy of the main recombination path $E_\mathrm{A,rec}$. Using this expression the above formula can be rewritten to equation (2.14).

$$V_\mathrm{OC} = \frac{E_\mathrm{A,rec}}{q} - \frac{A\,k_\mathrm{B}T}{q}\,\ln\left(-\frac{J_{00}}{J_\mathrm{SC}} \right) \tag{2.14}$$

From this equation it can be concluded that the activation energy of the main recombination path can be extracted, when the V_OC is plotted over the temperature and extrapolated to 0 K [91]. Such a fit is commonly done in the range between 280 K and 320 K to be close to working temperature but also have enough data points for the fit [92].

For the fit it is assumed that the diode factor is temperature independent in this region and that J_{00}, which is weakly temperature dependent, is constant. In case of Cu-rich samples those assumptions are not always true and have to be treated with caution.

If the recombination takes place in the bulk or within the space charge region (2 and 4 in figure 2.7), the activation energy is equivalent to the bandgap. This is in general the case for Cu-poor $CuInSe_2$ and $Cu(In,Ga)Se_2$ devices [18]. If recombination happens near or at the interface (5 and 6 in figure 2.7), the determined activation energy will be smaller than the bandgap, which is observed for Cu-rich devices [18]. The detailed reasons for this are in general rather complicated but two examples will be figuratively explained in the following. An interface often has a high density of defects, which are spread over a wide range of energies. Those states can trap a charge carrier which then recombines non radiatively over the spread out defect energies. The activation energy for this process is well below the bandgap due to the comparable small energy difference

between defect states. In the second example a highly doped semiconductor is assumed. Due to the high doping the space charge region will be narrow leading to strong band bending, which promotes tunnel enhanced recombination. In this case for example a hole can tunnel into a comparable deep defect state and recombine from there with an electron. The activation energy is then defined by the bandgap subtracted by the defect energy. A more detailed discussion about recombination processes and the activation energy of the main recombination channel can be found in [36], [92], [93]. Details about the set up for current voltage measurements and the set up for temperature dependent current voltage measurements can be found in [94] and [95].

2.3 Photoluminescence

Photoluminescence describes the emission of photons from a solid that is disturbed from its thermal equilibrium by the illumination of light with sufficient energy. The emitted light is generated when an electron transitions from an higher occupied electronic state into a lower unoccupied stated. The investigating of the spectrum of the emitted light allows direct insight into the electronic structure of semiconductors. This methods will be widely used in the following and should therefore be discussed. The basic principles are described in the beginning, followed by a more detailed description of observable transitions. In section 2.3.3 methods will be described which allow to identify the different observable transitions from excitation intensity and temperature dependent measurements. Section 2.3.4 will give a brief overview over the current defect picture derived over the years from various experiments and theoretical calculations. In section 2.3.5 absolute calibrated measurements are introduced which can be used to extract the quasi Fermi level splitting from room temperature measurements. At the end the experimental set up used for all measurements is described. A more detailed discussion about photoluminescence transition can be found in the book of Yu and Cadonda (chapter 7) [44]. A review about intrinsic point defects in $CuInSe_2$ and $Cu(In,Ga)Se_2$ can be found in [22]. Details and background information about the theory of the chemical potential of radiation used for the evaluation of the quasi Fermi level splitting can be found in the publications of Würfel [21], [55]. A practical guide about photoluminescence measurements of $Cu(In,Ga)Se_2$ absorber and their interpretation is given by Unold and Gütay [96].

2.3.1 Basic principles

Each body with a temperature above 0 K emits black body radiation. If a semiconductor is furthermore disturbed from thermal equilibrium by the illumination with light of sufficient energy, electron hole pairs are generated. Due to the gap in energetic states those charge carriers have to recombine radiatively under the emission of a photon taking up the energy difference. The emitted light is called photoluminescence and can give insights on the electronic structure of the semiconductor. The whole process of absorption and emission can be divided into several steps:

1. A semiconductor initially in thermal equilibrium is illuminated by light. Photons with sufficient energy ($E_{ph} > E_G$) excite electrons from the valence band across the bandgap into the conduction band leaving a free hole in valence band. Directly after the excitation (10^{-14} s) the charge carriers reflect the excitation spectrum.

2. The generated charge carriers thermalize under the emission of phonons to the band edges in the matter of picoseconds and towards a quasi-thermal-equilibrium distribution. This distributions of the charge carriers is independent of the excitation spectrum, enabling measurements with monochromatic excitation equivalent to the photon flux from the sun.

3. In the last step the charge carriers recombine radiatively emitting a photon with an energy corresponding to the energy difference of the involved states. [1]

2.3.2 Observable Transitions

Depending on the temperature and the crystal quality of the investigated semiconductor, various optical transitions from different energetic states can be observed in a measured photoluminescence spectrum. The most common transitions observed in photoluminescence experiments are shown in figure 2.9. The dominating transition changes with the temperature. At room temperature shallow defects are ionized making band-to-band transitions the primary transition. At lower temperatures (<200 K) defect and excitonic related transitions can be observed. The different transitions and their temperature and excitation dependent behaviour will be examined in greater detail the following.

Band-to-Band Recombination

The radiative recombination of excess free charge carriers from band to band (BB-transition) in general prevails at elevated temperature (>200 K). At those temperatures shallow defects are ionized due to thermal re-emission of the captured charge carriers to the respective band and excitons are dissociated by thermal energy due to their small bindings energies (<10 meV). In a perfect semiconductor without tailing or deep defects the shape of the emission profile $I_{\mathrm{PL}}(E)$ for energies above the bandgap E_{G} is given by equation (2.15), with the Boltzmann constant k_{B} and the temperature T.

$$I_{\mathrm{PL}}(E) \propto (E - E_{\mathrm{G}})^{1/2} \exp\left(\frac{-(E - E_{\mathrm{G}})}{k_{\mathrm{B}}T}\right) \tag{2.15}$$

The shape of the emission spectrum is determined by the square-root like density of states at the edges, represented by the left term, and the Boltzmann distribution of their occupation, represented by the right term. The position of the peak maximum, determined from the derivative, is with $E_{\mathrm{G}} + k_{\mathrm{B}}T/2$ slightly above the bandgap. Estimating the bandgap from the maximum of a photoluminescence spectrum is thus possible, but caution has to be taken when semiconductors with high doping or sub bandgap absorption and thus also sub bandgap emission are investigated. Especially the latter can shift the maximum of the photoluminescence peak towards lower energies [97], [98]. The room temperature

[1] It should be noted here that also non radiative recombination is possible and dominates at room temperature. For good Cu(In,Ga)Se_2 absorber layers, giving solar cells with above 17 % efficiency, below 1 % of all generated charge carriers pairs recombine radiatively.

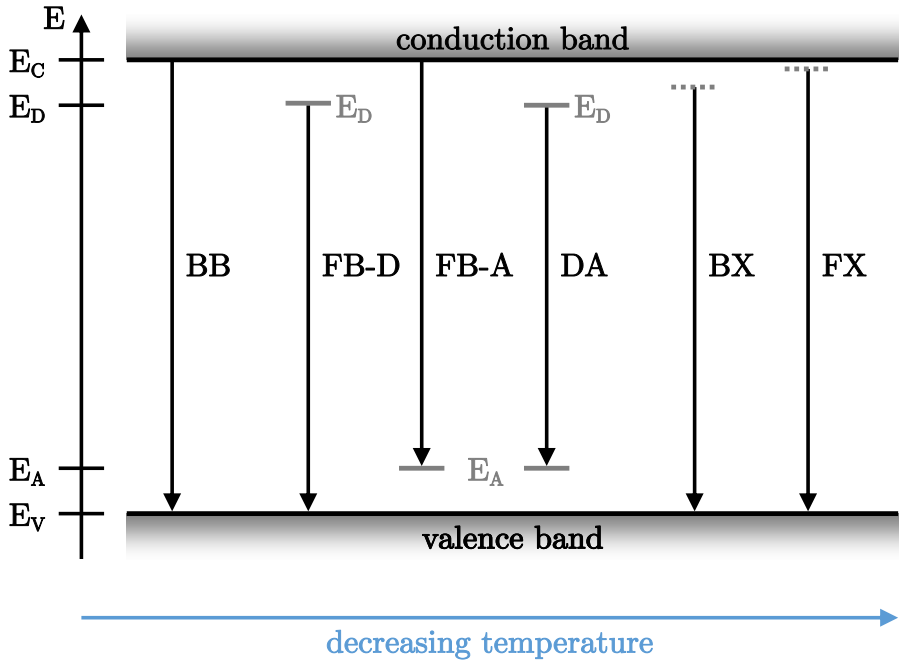

Figure 2.9: Schematic illustration of optical transitions commonly observable in photoluminescence experiments. Shown are band-to-band (BB), free-to-bound involving a donor (FB-D), free-to-bound involving an acceptor (FB-A), donor-acceptor-pair (DA), bound excitonic (BX), and free excitonic (FX) transitions. The probability of the different transition depends on the temperature as indicated by the blue arrow.

photoluminescence peak of Cu(In,Ga)Se_2 samples is in general close to being symmetric due to tail states and can approximated with a Gauss curve.

If the lifetime of the charge carriers is not too short and the charge carriers in the bands thus have the time to reach a quasi equilibrium, the luminescence flux outside of the material can be described by Planck's generalized law given in equation (2.16). This equation links the emitted luminescence per energy interval $Y_{PL}(E)$ to the absorptivity $A(E)$, the temperature T, and the splitting of the quasi Fermi levels of the electrons and holes ($\Delta\mu = \mu_C - \mu_V$). It was derived by Würfel [21], [55] looking at the detailed balanced of emission and radiation, assuming a lambertian surface, a homogenous illumination, and a homogenous material.

$$Y_{PL}(E) = \frac{1}{4\pi^2\hbar^3c^2} \cdot \frac{A(E)E^2}{\exp\left(\frac{(E-\Delta\mu)}{k_BT}\right) - 1} \tag{2.16}$$

Free-to-Bound Recombination

The probability of re-emitting trapped charge carriers into the bands reduces with decreasing temperature. The recombination of a free charge carrier in the conduction band with a trapped carrier in an acceptor state is called free-to-bound transition (FB-transition). Likewise a transition from a bound electron to a free hole can occur. The energy of the emitted photon is defined by the bandgap subtracted by the binding energy of the defect state. Yet, an additional term of $k_BT/2$ has to be added to account for the distribution of free carriers in the respective band edge. With increasing temperature the energy of the transition thus follows the bandgap and this second term as show in equation (2.17). Since

the translation symmetry of the crystal is broken by the defects states, trapped charge carriers can recombine with the charge carriers regardless of the wave vector.

$$h\nu_{\mathrm{FB}} = E_{\mathrm{G}}(T) - E_{\mathrm{A/D}} + k_{\mathrm{B}}T/2 \tag{2.17}$$

Donor-Acceptor-Pair Recombination

It is not unusual for a semiconductor to contain both donors and acceptors. In equilibrium some of the electrons from the donors will recombine with the holes from the acceptors, leaving both ionized donors and ionized acceptors in the semiconductor. Those kind of materials are called compensated, since the effective doping is reduced. Under illumination generated excess charge carriers can be trapped by those ionized defects forming neutral defect centers. When a trapped electron recombines radiatively with a trapped hole it is called donor-acceptor pair transition (DA-transition). The energy of the emitted photon in this case is not only defined by the bandgap subtracted by the two respective binding energies, but also the Coulomb interaction of the ionized defects states has to be considered. The reason for this is that the initial state has two neutral defects whereas the final state has two ionized defects with lower energy because of the Coulomb attraction. The Coulomb energy E_{C} depends on the distance r between the two involved defects, the dielectric constant ϵ_r and the vacuum permittivity ϵ_0. The energy of the emitted photon is thus given by equation (2.18). It should be noted here that tunneling is part of every DA-transition, since the involved defects are not located at the same site. With increasing temperature a small blue shift of the transition is observed, due to the recombination of donor and acceptors which are closer together. This can be explained by the fact, that the probability of re-emission to the band of a trapped carrier increases with the temperature and that the involved tunneling step is more likely for short distances. In the case of thermally emptied defects the recombination of pairs in close proximity will dominate [99].

$$h\nu_{\mathrm{DA}} = E_{\mathrm{G}}(T) - E_{\mathrm{A}} - E_{\mathrm{D}} + e^2/\left(4\pi\epsilon_r\epsilon_0 r\right) \tag{2.18}$$

The fact that the energy of the photon depends on the distance of the involved defects can be used to identify DA-transitions. For instance by increasing the excitation density and thus the number of excess charge carriers, the number of occupied defects states will increase and by this reduce the average distance between the acceptor and donor involved in a DA-transition. Therefore the energy of the emitted photon shifts to higher energy which is a characteristic of DA-transition, as will be discussed in section 2.3.3.

Phonon Coupling

When a defect is involved in the optical transition that exhibits a strong electron-phonon coupling, the observed peak can be shifted or distorted. For shallow defects the wave function is usually delocalized, leading to a low electron density at the defect. In this case the influence of a charge transition is small onto the neighboring atoms, leading to a weak electron-phonon interaction. On the other hand deep defects are usually highly localized, leading to a high electron density at the defect. In this case a charge transition can displace neighboring atoms, causing them to rearrange locally, which can shift the electron potential spatially. The emission from this shifted potential depends on the magnitude of the shift itself and the phonon modes. The emission can be best described with a configuration coordinate diagram. Since within this work only defects that have a weak

electron-phonon interactions are investigated, the discussion about details is cut short here, but details can be found in [100] and [101]. For transition with a weak electron-phonon coupling a main peak and several replicas of this peak at lower energies are observed. The main peak has the highest intensity and is the zero-phonon line which does not involve any phonon interaction. The position of the n-th side peak is shifted by the phonon energy as described in equation (2.19).

$$h\nu_n = h\nu_0 - n \cdot E_{\text{Phonon}} \tag{2.19}$$

For weakly coupled transitions the intensity of the replicas decreases with the number of involved phonons. The relative peak height of the n-th phonon replica (I_n) to the main peak (I_0) is given by equation (2.20). The parameter S is called Huang-Rhys factor and can be understood as the average number of phonons involved in the transition.

$$I_n = I_0 \exp(-S)\,\frac{S^n}{n!} \tag{2.20}$$

The electron-phonon coupling is called weak when $S < 1$. In this case the zero-phonon line has the highest intensity. For larger Huang-Rhys factors ($S \geq 1$) the electron-phonon coupling is called strong. In this case the highest intensity is observed for one of the replicas, strongly distorting the measured spectrum. Identifying the zero phonon line in this case can be tricky. Especially when the peak width of the different replicas is larger than the phonon energy (the spacing between peaks).

Excitonic Recombination

At low temperatures (<70 K) the formation of excitons is expected in photoluminescence experiments on high quality semiconductors. Those excitons consist of an electron-hole pair bound together by Coulomb interaction. They can only be observed at low temperatures when the thermal energy is lower than the binding energy ($k_{\text{B}}T < E_{\text{Ex}}$) and hence they do not dissociate. Additionally, high quality materials have to be used, since the presence of local electrical field caused by defects and impurities also dissociates excitons. Two types of excitons are distinguished depending on the binding energy [44]. Frenkel excitons occur in materials with small dielectric constants leading to strong Coulomb interactions, binding energies in the range of several 100 meV and small extension (usually within one unit cell). The second type are Wannier-Mott excitons, which prevail in most semiconductors. A large dielectric constants and a low effective mass of electrons, as in the case of Cu(In,Ga)Se_2, lead to a weakly bound electron-hole pair which is delocalized over several unit cells. Two types of types of Wannier-Mott excitons are observable in Cu(In,Ga)Se_2.

1) Free Exciton The binding energy of a free exciton can be described by the hydrogen model and is given by equation (2.21). For the mass the reduced electron-hole mass is used ($1/m_r = 1/m_e + 1/m_h$), with the electron mass m_e and the hole mass m_h. Most of the constants can be summarized using the Rydberg energy $R_y = m_0\, e^4/(2\hbar^2 4\pi^2\epsilon_0^2) \approx 13.6\,\text{eV}$. Furthermore, only in very pure crystals quantum numbers n larger than 1 can be observed. Setting it to 1 and using the Rydberg energy leads to the simplifications made in the equation.

$$E_{\text{FX,n}} = \frac{m_r\, e^4}{2\hbar^2(4\pi\epsilon_0\epsilon_r)^2}\,\frac{1}{n^2} = R_y\frac{m_r}{m_0\epsilon_r^2} \tag{2.21}$$

Using the experimentally determined reduced mass for $CuInSe_2$ of $m_r/m_0 = 0.095$ [102] and $\epsilon_r = 13.6$ [103] a binding energy of 7 meV can be calculated. This binding energy is slightly above the experimental value of 5.1 meV found in [28] but well inline with other experimental determined values of 7 meV [104] and 7.5 meV [105]. The transition energy of free excitonic transitions (FX) is given by the bandgap E_G subtracted by the binding energy and follows the temperature dependance of the bandgap.

2) Bound Exciton If donors and acceptors are present in the semiconductor then the excitons are attracted by those impurities by van der Waals interaction. The binding energy of the exciton increases when bound to an impurity, making the formation likely. The additional binding energy is proportional to the ionization energy of the defect, as described by Haynes rule [22], [106], [107]. In general binding to neutral as well as charge defects is possible, but the former is morel likely since it results in a higher binding energy of the exciton. The annihilation of free excitons (FX) and bound excitons (BX) is depicted in figure 2.9 by using a virtual state, that does not exist, close to the conduction band to express the energy released.

Photoluminescence from compensated semiconductors

If the investigated material has a high density of acceptors and donors which are in the same order of magnitude, the semiconductor becomes compensated with a net doping density lower than the doping density. The statistical distribution of the defects within the lattice leads to a distortion of the band structure due to electrostatic potential fluctuations originating from the fixed space charges. With the fluctuations of the band edges FB- and DA-transitions with significant smaller energy become possible [22], [96], [108]. The energy range possible for DA-transitions via tunnel enhanced recombination leads to an asymmetrical broadening of the photoluminescence peak towards lower energies. Also the average transition energy reduces with potentials fluctuations shifting the peak position to lower energies. Since the maximum DA-transition energy is still defined by the vertical transition with negligible tunneling, the high energy side of the peak is defined by the temperature broadening as given in equation (2.15). The broadening towards lower energies can be used to determine an average depth of the fluctuation, also described as band tails.

In general, all $Cu(In,Ga)Se_2$ samples with a Cu-poor composition exhibit potential fluctuations and thus a broad asymmetric peak in low temperature photoluminescence measurements [12], [22]. With increasing excitation density it is possible to screen part of the potential fluctuation. Hence, shifts of the peak position of above 10 meV/decade are observed with excitation. With increasing temperature and constant low excitation, the maximum of the broad photoluminescence peaks shifts toward lower energies. This can be explained by a re-distribution of carriers within the potential wells. With increasing thermal energy it is possible for the carriers to move into a lower energetic well, leading to reduction of the energy difference. For increasing temperatures the probability of trapped carriers to get emitted to the band increases, favouring the transition between electron hole pairs in close proximity. Due to this a blue shift similar to the one observed in DA-transitions of uncompensated materials, is detected for even higher temperatures. Although a few Cu-poor samples are analysed by low temperature photoluminescence measurements, the evaluation of band-tails and compensated samples is not a key component of this work. A more detailed discussion about potential fluctuations in compensated semiconductors can be found in [22], [96], [108].

2.3.3 Defect spectroscopy by photoluminescence

A distinction between the possible optical transitions can be achieved by looking at the peak position and luminescence intensity dependent on the excitation density and the temperature. The peak shift with temperature has been discussed for each transition above and is summarized in table 2.1.

Table 2.1: Temperature dependance and excitation density dependance of various luminescence transition including excitonic (EX), free-to-bound (FB), donor-acceptor transition (DA) as well as DA in the presence of strong potential fluctuations (PF).

Transition	**Temperature dependence**		**Excitation density dependence**	
type	Peak energy	PL intensity	Peak energy	PL intensity
EX	follows E_G	$E_\mathrm{A} = E_\mathrm{EX}$	constant	$1 < k < 2$
FB	follows $k_\mathrm{B}T/2$ and E_G	$E_\mathrm{A} = E_\mathrm{defect}$	constant	$k < 1$
DA	small blue shift	$E_\mathrm{A} = E_\mathrm{defect}$	few meV/decade	$k < 1$
PF	first red than blue shift	$E_\mathrm{A} = E_\mathrm{defect}$	$> 8\,\mathrm{meV}$/decade	$k \approx 1$

The luminescence intensity in general quenches with increasing temperature, since the thermal energy is large enough to dissociate excitons or to thermally empty defect states. The decay of the luminescence intensity Y_PL can be described by equation (2.22) [22], with C_1 and C_2 being proportionality constants and $E_{\mathrm{A},1}$ and $E_{\mathrm{A},2}$ the respective activation energies. Since a thermal emission of the charge carriers into the band is assumed, also a factor of $T^{3/2}$ is included to account for the temperature dependence of the effective density of states at the band edges [96]. In case of excitonic emission, the term $[C_2\,T^{3/2}\exp(-E_{\mathrm{A},2}/k_\mathrm{B}T)]$ is omitted. This is also the case for free-to-bound transitions since only one charge carriers is thermally emitted.

$$Y_\mathrm{PL}(T) = \frac{1}{1 + C_1\,T^{3/2}\exp\left(-\frac{E_{\mathrm{A},1}}{k_\mathrm{B}T}\right) + C_2\,T^{3/2}\exp(-E_{\mathrm{A},2}/k_\mathrm{B}T)} \tag{2.22}$$

For donor-acceptor pair transitions the activation energy of the donor and the acceptor can be obtained. The activation energy gained at low temperatures corresponds to the shallower defect state, since it thermally empties first. However, caution has to be taken when the proportionality constants do not have the same order of magnitude. In this case fitting the model gives unreasonable low activation energies of the shallower defect state ($< 5\,\mathrm{meV}$), which also influences the second activation energy. To get better results for the second activation energy in this case, the fitting is best be done with a fixed activation energy $E_{\mathrm{A},1}$ of zero [109]. Caution also has to be taken when deep defects are present with a high electron and hole capture cross section, as they can cause abrupt thermal quenching via non radiative recombination leading to an overestimation of the determined activation energy [110].

Complementary excitation dependent measurements can be used to identify optical transition. The shift of the peak position can be described using the empirical equation (2.23) with the excitation density I_Exc, the original position $E_\mathrm{PL}(I_0)$, and the shift per decade β. The energy of the emitted photon in a donor-acceptor pair transition

depends on the distance of the two involved defects due to the Coulomb interaction. The shift of the peak position with excitation follows an S-shape over several orders of magnitude excitation [111], [112] and the maximal blue shift can be estimated to be about 7 meV in $CuInSe_2$ using the already introduced values for the effective mass and ϵ_r [96]. In experimental measurements where only a limited range of illumination conditions can be investigated, commonly shifts of 1 meV/decade to 6 meV/decade are observed for donor-acceptor pair transitions in $CuInSe_2$ [15] and $CuGaSe_2$ [14].

$$E_{\mathrm{PL}}(I_{\mathrm{Exc}}) = E_{\mathrm{PL}}(I_0) + \beta \log\left(I_{\mathrm{Exc}}/I_0\right) \tag{2.23}$$

If the band edges are distorted by potential fluctuations, the shift with excitation of DA-transition will be higher, easily exceeding 10 meV. The peak positions of excitons and free-to-bound transitions do not depend on the excitation.

In general, the luminescence intensity follows the power law dependency with the excitation shown in equation (2.24) derived from the rate equations [113]. From those calculations a power law exponent k between 1 and 2 for both free excitons and bound excitons for several orders of magnitude excitation is expected. For donor-acceptor pair transitions and free-to-bound transition a k value below 1 is derived.

$$Y_{\mathrm{PL}} \propto I_{\mathrm{Exc}}^{k} \tag{2.24}$$

Later it was shown that this linear behaviour is not always true and that the slope in log-log plot of the photoluminescence intensity over the excitation density can change, especially when deep defects are involved [114]. Recent calculations and thoroughly derivation from the rate equations show that the slope indeed changes depending on the excitation in steps of 0.5 [115] (for example from 1 to 0.5).

In experiments the excitation dependance is mostly measured over 1 or 2 orders of magnitude and thus not enough to measure the whole transition between different slopes. The commonly measured values between multiples of 1/2 can thus be interpreted as transition regions between two slopes. Another insight of this publication is that with the contribution of deep defects it is also possible for FB and DA-transition to have k values of 3/2 for low excitation densities [115].

In case of samples disturbed by potential fluctuations, commonly a power law exponent just below 1 is observed. Overall, in most cases the old attribution of k-values can still be used to distinguish between excitonic transitions ($k > 1$) and defect related transitions ($k < 1$). Caution has to be taken when investigating samples with strong band tailing (like kesterites). Here the main transition exhibits a k value of nearly perfectly 1 [116]. An overview of the temperature and intensity dependance of the different optical transition is given in table 2.1.

2.3.4 Defect Picture in Cu(In,Ga)Se_2

A comprehensive model about intrinsic defect in the ternaries $CuInSe_2$ and $CuGaSe_2$ was developed and refined over the years. With various methods like photoluminescence [14], [15], [22], [29], [117], cathodoluminescence [29], [31], admittance [118] and Hall measurements [13], [119]–[121] defects energies were measured and compared. With the introduction of the screened-exchange hybrid density functional theory of Heyd, Scuseria and Ernzerhof (HSE06) [49] into the theoretical calculation of point defects and defects clusters in chalcogenides the calculated formation energies and activation energies improved. Although the values of calculated values still differ between publications [50]–[54] a more

common picture evolved within the last few years. A good review about the defects reported over time can be found in [22] and an updated review about the current state of knowledge can be found in [101], [122].

Great similarities are found in the defect spectra between $CuInSe_2$ and $CuGaSe_2$ and it was shown that there is a smooth transition between both [29]. Photoluminescence spectra of $Cu(In_{1-x}, Ga_x)Se_2$ samples grown under low copper excess measured at 10 K usually consist of several distinct peaks [14], [15], which can be attributed to excitonic luminescence as well as donor-acceptor pair transition. Experiment and theory agree that the shallowest acceptor A1 is most likely related to the copper vacancy (V_{Cu}) with an activation energy of 40 meV for $CuInSe_2$ and 60 meV for $CuGaSe_2$. The involved shallow donor in the donor-acceptor pair transitions has an activation energy of 10 meV both in $CuInSe_2$ and $CuGaSe_2$ and is attributed to the indium on copper antisite (In_{Cu}) and/or the copper interstitial (Cu_i), depending on the growth conditions. Also widely observed is a second donor-acceptor pair transition, involving the same donor. The activation energy of the second acceptor (A2) is with 60 meV for $CuInSe_2$ and 100 meV for $CuGaSe_2$, higher compared to A1. Although calculated as a deeper acceptor in theory ($\approx$ 150 meV) this acceptor is attributed to the copper on indium antisite (Cu_{In}) or the copper on gallium antisite (Cu_{Ga}) respectively. This attribution is related to the observation that the photoluminescence intensity of the DA2 transition increases, with increasing copper excess during growth.

Other parts of the defect picture are still under debate. A third peak in photoluminescence measurements of $CuGaSe_2$ samples at 1.58 eV was attributed to a phonon replica of the second donor acceptor pair transition (DA2) [14]. Later cathodoluminescence measurements [31] and spatially resolved photoluminescence measurements [30] showed that this peak is a superposition of a phonon replica of the DA2 transition and another DA-transition, likely from the known shallow acceptor into a third acceptor with an activation energy of 130 meV. From theoretical calculation it is not possible to attributed this third acceptor to an intrinsic point defect. Because of this several defect complexes have been proposed to be the origin of this defect level [50], [54]. From the finding in $CuGaSe_2$, a third acceptor was also postulated for $CuInSe_2$, but spatially resolved photoluminescence measurements show no evidence of a third DA-transition at 0.94 eV in $CuInSe_2$ [32].

For epitaxial $CuInSe_2$ samples a donor with an activation energy of 100 meV was shown by hall measurements [123] and it has been attributed to be related to the selenium vacancy V_{Se} (possibly in a complex V_{Se}-V_{Cu}) [51], [122]. The fact that it is not observable in photoluminescence can be explained by the calculated amphoteric nature of the defect and the switch from a donor to an acceptor under illumination.

Two deep defect bands ($<$530 meV and $<$390 meV) below the conduction band have been shown by photoluminescence in $CuGaSe_2$ [124], which could fit to two electron traps found by modulated photo current and capacitance junction techniques [118]. One of these bands has been attributed to the gallium on copper antisite Ga_{Cu} in correspondence with theoretical calculations [50], [125].

The growth on soda lime glass leads to a considerable in-diffusion of sodium into the absorber layer [67] (up to 0.1 % atomic percent). Alternatively it is added intentionally after the absorber growth on sodium free substrates [126]. Both methods increase the device performance but are also known to change the doping density measured in devices. This raises the question if the sodium atoms form extrinsic defect states in the bandgap. However, no experimental proof for this has been found. Additionally recent calculation show that sodium is likely to form electrically inactive sodium on copper antisites (Na_{Cu}) [127]. The

change in doping density can be explained by a secondary effect of the Na_{Cu} antisite, which forms during growth but is not stable during cooling. This leads to an out-diffusion of sodium from the bulk (migration to the grain boundaries where it is mostly detected in atom probe studies [128]–[130]), leaving copper vacancies V_{Cu} which are acceptors and thus increases the doping density.

2.3.5 Quasi Fermi level splitting analysis

When a luminescence spectrum is calibrated to yield absolute values of photons/s/cm^2, it can be used to extract the quasi Fermi level splitting. To calibrate the set up several steps are needed, that are described in the appendix in section C.1. There are different approaches to evaluated the quasi Fermi level splitting from calibrated measurements, but all rely on Planck's generalized law (equation (2.16)). If the optical constants and the absorptivity are known for the investigated material, Planck's generalized law can be directly applied. Since this is generally not the case, different methods using various simplifications are used.

A comprehensive method is fitting the whole spectrum with a numerical approximation, as shown by Katahara and Hillhouse [97]. This methods can give insights about the temperature, the quasi Fermi level splitting, the bandgap, and potential fluctuations. It properly describes data with moderate signal to noise ratio. However, for the fitting two parameters defined by integrals have to be numerically approximated, making the method computational heavy. Furthermore, this methods tends to overestimate the temperature by several 10 K, which leads to an underestimation of the quasi Fermi level splitting. Due to those drawbacks this method will not be used. Instead a more basic approach is taken, described in the following.

Considering only the high energy wing of the emission peak at sufficiently high energies ($E > E_G + 0.1\,\mathrm{eV}$), the absorptivity can be approximated to be unity ($A(E) \approx 1$). Additionally it is assumed that the term $(E-\Delta\mu)/k_B T$ in the denominator of equation (2.16) is much larger than 1, justifying that the latter one can be neglected. Taking the logarithm of Planck's generalized law including those simplification and rearranging it, equation (2.25) is derived. The constants in Planck's generalized law ($1/4\pi^2\hbar^3c^2$) have a value of $9.88 \times 10^{22}\,\mathrm{eV^{-3}\,s^{-1}\,cm^{-2}}$ and are commonly abbreviated with C or with 10^{23}. Multiplied with the squared energy E^2 this matches with the unit of the photoluminescence flux, making it possible to take the logarithm of a dimensionless number.

$$\ln\left(\frac{Y_{PL}(E)}{C\,E^2}\right) = -\frac{E-\Delta\mu}{k_B T} \tag{2.25}$$

With this formula it is possible to determine the temperature from the slope and the quasi Fermi level splitting from the intercept of a linear fit through the high energy wing of the semi-logarithmically plotted photoluminescence spectrum. A more detailed description and an example can be found in section C.2 in the appendix. In summary, this method can be easily applied and gives the desired quasi Fermi level splitting. It should be noted here that the method assumes a homogenous semiconductor with constant quasi Fermi levels, which is not the case for $Cu(In,Ga)Se_2$ samples grown by a 3-stage process. Furthermore, the method is susceptible to low signal-to-noise ratios and to background signals in the photoluminescence spectra. The reason for this is the strong influence of the slope of the linear fit onto the extracted quasi Fermi level splitting, which is about $2.4\,\mathrm{meV\,K^{-1}}$. A more detailed discussion about errors of the fitting routine can be found in section C.2.

Since the emitted photoluminescence does not depend on the excitation wavelength used, it is possible to adjust the excitation flux to have the same number of photons as the semiconductor would absorb during the illumination with an AM1.5 solar spectrum. For this adjustment the bandgap of the investigated materials has to be known. The calibration process for the excitation flux and the determination of the equivalent suns is discussed in section C.2.

2.3.6 Experimental Set up

All photoluminescence measurements are carried out in a home built set up, which is sketched in figure 2.10. For excitation monochromatic light of either an argon ion laser (514 nm) or a laser diode (600 nm) is used. On the optical pathway to the sample position, the unwanted modes and wavelengths inside the laser light are removed with a combination of long-pass, short-pass, and bandpass filters. This is especially important for the argon ion laser since the argon gas also emits other wavelengths. Furthermore, neutral density filters mounted in a filter wheel can be used to attenuated the laser power from optical density 0 (OD0) to optical density 4 (OD4). The beam is guided through an aperture in the first collecting mirror onto the sample position. The radius of the Gaussian spot size there is about one millimeter ($r_{\mathrm{Ar}} \approx 1.1\,\mathrm{mm}$ and $r_{\mathrm{diode}} \approx 1.3\,\mathrm{mm}$). A lens can optionally be flipped into the beam path focusing the light down to about 80 µm to increase the excitation density.

The collection of emitted light is done by an off-axis parabolic mirror which is two inch wide and has focal length of 101.6 mm. The rather long focal length reduces the numerical aperture and with this the angle of acceptance which reduces the portion of the emitted photons that can be collected. However, this is needed to fit a cryostat in front of the collecting mirror. A second mirror with the same size is used to focus the collected light of the first mirror onto an multi-mode optical fiber. The focal length of the second mirror is with 152.4 mm higher to reduce the half angle and avoid losses coupling the light into the fiber. The reflectance profile of the metallic mirrors is flat over a wide wavelength range, minimizing errors by chromatic aberration. In contrast to a confocal configuration it is possible to align and optimize excitation path and collection path independently from each other.

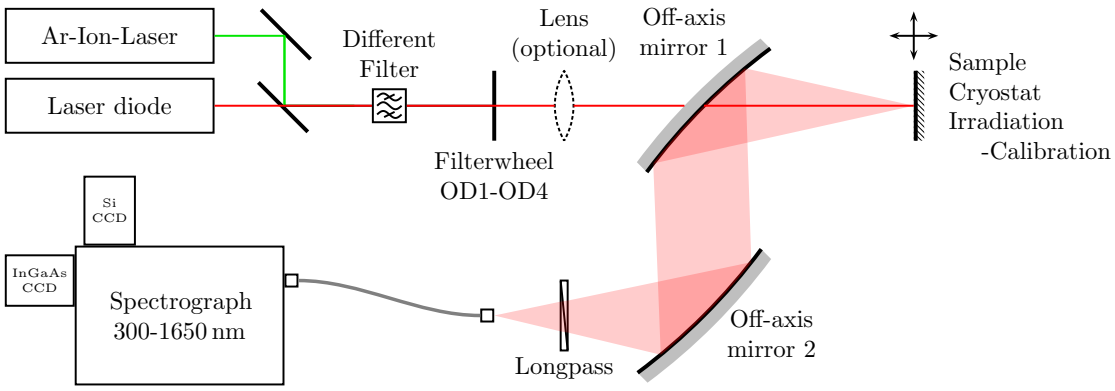

Figure 2.10: Sketch of experimental setup used for all photoluminescence experiments.

After the light is collected, it is guided by the fiber into a monochromator where it is spectrally resolved and detected by either a Si-CCD camera (300 nm to 1100 nm) or

an InGaAs-array detector (800 nm to 1600 nm). For all measurements a grating with 100 lines/mm was used giving a spectral resolution of about 15 nm with a multi-mode fiber with a width of 550 µm. For higher resolution (but lower signal) a multi-mode optical fiber with a width of 200 µm was used, leading to a spectral resolution of about 6 nm. In front of the fiber a long-pass filter is used the cut out the reflection of the laser light from the sample surface out of the signal. This is necessary to avoid any damage to the sensitive detectors since the intensity of the emitted photoluminescence is orders of magnitude smaller than the reflected laser light. More details about the design and construction of the experimental set up can be found in [101].

Each spectrum consist of counts measured per pixel. Each pixel can be linked to the wavelength from the angle of the grating. To give the Y-axis (counts) a physical unit and to correct for the transmission/reflection properties of all optical components in the collection path a spectral correction function is multiplied with the raw spectrum. This correction function is determined by measuring spectrum of a halogen lamp reflected from a spectralon surface, which has a spectrally flat and Lambertian reflection profile. By dividing the measured spectrum by the known spectrum of the lamp, the spectral correction function is calculated. After spectral correction each spectrum is in relative units of photons/(s cm^2nm). For further fitting and data treatment, each spectrum is transferred into energy space using the Jacobian transformation, which takes the difference in energy spacing into account [131]. To get the absolute flux a multiplicative calibration factor is needed. It can be derived from the determination of the laser profile, the laser power at the sample position and the spectrum measured from a reflected laser spot. Details about all correction steps and the experimental process to determine the calibration factor can be found in section C.1 in the appendix.

2.4 Absorber growth and preparation

This section covers the molecular beam epitaxy system used for the growth by co-evaporation of all investigated samples. The $CuInSe_2$ samples are grown with a 1-stage process which is discussed in section 2.4.2. For $Cu(In,Ga)Se_2$ samples, a more elaborated process with three evaporation stages is used which will be discussed in more detail in section 2.4.3. Within this work samples are distinguished with regard to there copper content after growth into Cu-rich samples (grown with copper excess) and Cu-poor samples (grown with a copper deficiency). The differences and similarities in the opto-electronic properties of both compositions are discussed in section 2.4.4.

2.4.1 The deposition system

All in this manuscript investigated absorber layers are grown in a Veeco Gen930 molecular beam epitaxy systems which is sketched in figure 2.11. Since the absorber layers are grown on soda lime glass substrates covered with polycrystalline molybdenum, the growth is non epitaxial leading to polycrystalline absorber layers. Hence the set up will be referred to as physical vapour deposition (PVD) system to avoid misconceptions.

The center piece of the PVD is the growth chamber which is vacuum pumped by a turbo molecular pump. In combination with liquid nitrogen cooling, pressures of below 10^{-8} mbar are reached during growth. The cryopanel at the backside acts as a particle trap catching materials which are not deposited on the substrates. Copper, indium, and gallium are evaporated from separate effusion cells by heating them above their respective melting

point. Each cell has a heating filament at the base to heat up the material and second filament at the top to avoid deposition there and to ensure a homogenous evaporation profile. The elemental beam flux can be controlled by adjusting the base temperature. The selenium is evaporated from a valved cracking source. Here selenium is melted in a crucible which is sealed with a needle valve. The flux depends on the selenium temperature and the opening of the valve. Furthermore, the evaporated selenium vapour passes through a cracking tube which can be heated to 1000 °C. The higher temperature is used to split up the most likely gaseous species of Se_8 into smaller, more reactive cluster like Se_2 [132], [133]. All evaporation sources are equipped with separate shutters enabling to switch the deposition on and off within a couple of seconds.

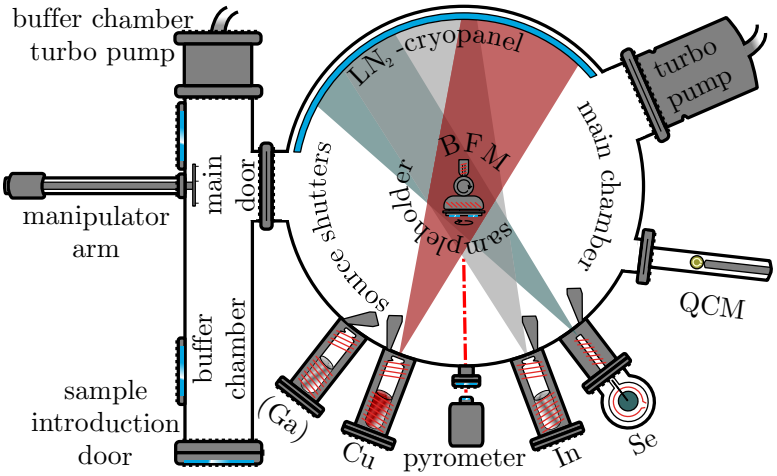

Figure 2.11: Schematic of the PVD system used for absorber preparation, reprint from [95]. To use the system for post deposition treatments furthermore a KF source was added to the system.

The flux variation is quite small in between days when the same base temperatures are used. Nevertheless, several characterization tools for checking the flux and growth rate are incorporated in the main chamber. Namely those are QCM, BFM, EIES, and pyrometer which will be discussed in more detail in the following.

A quartz crystal micro balance (QCM) can be introduced into the chamber for the measurement of the deposition rate of copper, indium and gallium. The piezoelectric crystal changes is vibration frequency depending on the thickness of the crystal. Since frequencies can be measured reliable and precise even tiny changes in the thickness caused by the metals deposited on top of the crystal can be measured. Knowing the density of the deposited material as well as the ratio of the acoustic impedance of the material and of the crystal, it is possible to calculate the deposited thickness. Although in theory this method could also be used for selenium, in practice this is not possible. The interplay from selenium with previously deposited copper leads to the formation of Cu_xSe which has a much lower density compared to copper alone leading to rapid expansion and the destruction of the crystal.

A second characterization tool is the beam flux monitor (BFM) which is an ionization gauge. Electrons are emitted from a heated filament (cathode) that are accelerate towards a positively charged helical grid (anode). When the electrons collide with gaseous molecules/atoms positive ions are formed. If this happens within the helical grid, those ions are collected by a second cathode giving a small current. In case of a constant filament to grid voltage and constant electron emission current, the rate of ionization is

directly proportional to the density of molecules or atoms and thus the pressure. Using a BFM, measurements of the chamber pressure but also of particle fluxes directed at the ionization gauge are possible. However, since the measured flux depends on the geometry of the incoming flux, the molecular species, and the background pressure, only relative measurements are possible. Due to this, it is also not possible to translate the fluxes into growth rates. Nevertheless, it is possible to compare relative between process days.

A further tool to characterized fluxes installed inside the main chamber is the electron impact emission spectroscopy (EIES) flux sensor. Although separate measurements for all elements should be possible simultaneously, only for selenium reliable values could be determined. It is thus only used as a complementary tool to quantify the selenium flux.

A pyrometer with a detection range of 2 µm to 2.6 µm is used to optically measure the temperature of the sample surface during the absorber growth. Furthermore, the interference effect caused by the thin films grown to the measured signal are used to control the thickness deposited in the later discussed 3-stage process.

A common operating day of the PVD starts with the cooling of the main chamber with liquid nitrogen. Afterwards the sources are heated up to evaporation temperature. During this time the sample holder which can hold up to four substrates with a size of 2.54 cm x 2.54 cm is loaded into the buffer chamber. Then the evaporation rates of Cu, In and Ga are measured by QCM and BFM and adjusted to the target flux. Subsequently the Se flux is measured with BFM and EIES. When all fluxes are measured, the sample holder is transferred into the growth chamber. With the sample holder in place a growth recipe is started, which automatically conducts predefined actions like controlling the substrate temperature or opening/closing shutters. During the growth process the substrate holder is constantly rotated to improve the homogeneity of the deposition. Two different growth processes are used for $CuInSe_2$ and $Cu(In,Ga)Se_2$ samples which are described in section 2.4.2 and section 2.4.3. When the growth process is finished after about two to three hours, the sample holder is transferred back into the buffer chamber and likely a second sample holder is mounted for a second process. Since cooling the chamber, heating up the sources, and measuring the fluxes takes already about 3 to 4 hours, usually only two or three growth processes per day are done.

2.4.2 Co-evaporation process used for $CuInSe_2$

For the growth of all investigated $CuInSe_2$ samples a basic single stage (1-stage) process is used. In this process all constituent are evaporated at the same time with constant fluxes. The process is schematically depicted in figure 2.12. The temperature values given in the figure and in the following text are set point temperatures of the substrate heater. The temperatures at the substrate surface measured with the pyrometer are below those values. To avoid any deposition on the substrate holder during idling, it is constantly heated to at least 200 °C.

In the beginning of the process the selenium source is opened and the temperature of the substrate holder is ramped up quickly up to 500 °C with the other sources still being closed. The selenium is already evaporated to aid the formation of a thin $MoSe_2$ layer which in literature is argued to form an ohmic contact between the absorber layer and the back contact [134]. Subsequently the temperature is ramped up further with a lower rate to 550 °C to avoid temperature overshooting. Afterwards the shutter of copper and indium are opened and the absorber layer is grown. The temperature is further increased

to 590 °C after 10 min to aid the crystallization. For the rest of the deposition process the temperature is kept constant. The growth ends by cutting the supply of copper and indium and cooling the sample holder down to 300 °C while still under selenium flux. This is done to avoid the loss of selenium from the formed absorber layer, which would otherwise evaporate because of its high vapour pressure [135], [136]. Below 300 °C the Se supply is cut and sample is cooled down to 200 °C before it gets taken out of the growth chamber.

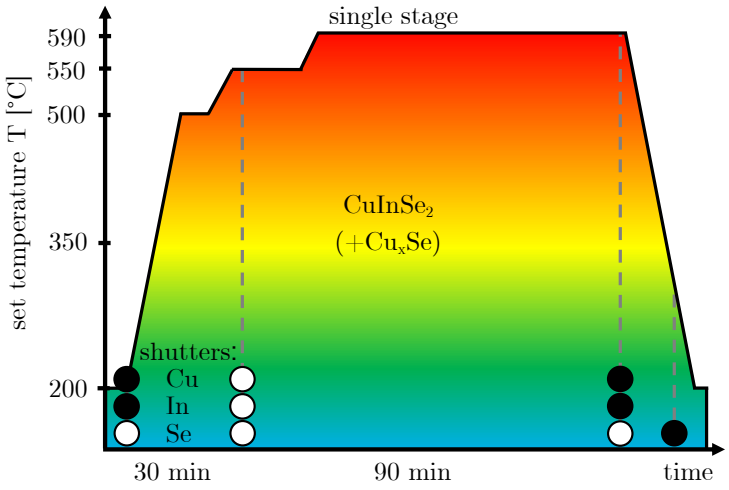

Figure 2.12: Schematic growth process used for the formation of $CuInSe_2$ absorber layers. Drawn is the temperature profile over time. Furthermore added is the status of the shutter in front of the sources indicating whether the deposition is on (white) or off (black).

The final [Cu]/[In]-ratio of the absorber layers depends mainly on copper and indium flux. However, also the selenium flux changes the composition [137]. By changing the selenium fluxes from low to high condition the [Cu]/[In]-ratio can be reduced from 1.5 down to 1.2 using constant copper and indium fluxes. In general low selenium over pressures are preferred since they give the highest efficiencies when the samples are grown under copper excess [137]. In case of copper deficient samples the selenium overpressure used has a negligible effect on the device performance. The thickness of the grown absorber varies between processes but is in general about 3 µm for both Cu-rich and Cu-poor composition.

2.4.3 Co-evaporation process used for $Cu(In,Ga)Se_2$

For $Cu(In,Ga)Se_2$ samples a more complex process is used with three different evaporation stages, first presented by Gabor et al. [138]. It has two advantages compared to the 1-stage process. Firstly, during the process the [Cu]/([Ga] + [In])-ratio changes due to the alternating evaporation of copper and indium+gallium. This allows also samples with a final overall Cu-poor composition to go through an intermediate Cu-rich phase which leads to an enhanced grain size and a better device performance [72], [139]. Secondly, a double gallium gradient through the absorber thickness with a gallium enrichment at the front and the back is achieved. The increased bandgap towards the molybdenum back contact reduces interface recombination enhancing the V_{OC} by up to 80 mV [72], [140]. The grading towards the front is proposed to have a similar but less pronounced effect.

A slightly adapted growth process compared to [138] is used for the investigated samples which is depicted in figure 2.13. It starts of with a high temperature step (500 °C) which is used to clean molybdenum surface from residual surfactants. In the 1-stage process

presented before this cleaning is done automatically in the beginning of the process due to the high temperatures used. In the three stage process a temperature of 350 °C is used during the first stage which might not be enough to get rid of the adsorbants. After this cleaning step of about 20 min the sample holder is cooled down to the before mention temperature.

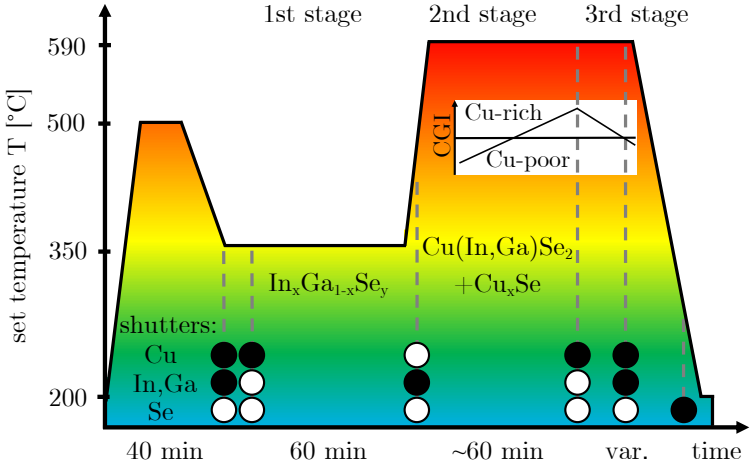

Figure 2.13: Schematic growth process used for the formation of $Cu(In,Ga)Se_2$ absorber layers. Drawn is the temperature profile over time. Furthermore added is the status of the shutter in front of the sources indicating whether the deposition is on (white) or off (black). The white inset represents the [Cu]/([Ga] + [In])-ratio during the end of the second stage and during the third stage.

Similar to the 1-stage process only selenium is supplied for a few minutes before the deposition starts to promote the formation of a thin $MoSe_2$ layer. The actual first stage of the process starts by switching the indium and gallium flux on by opening the shutters of the sources. In this stage a $(In_xGa_{1-x})_2Se_3$ precursor layer is grown at a comparable low temperature which helps to improve the homogeneity. In total about 90 % of the overall indium and gallium is deposited during this stage. The duration is generally around 60 min and depends on the fluxes used and the target thickness. After the desired thickness is reached, the indium and gallium shutter are closed and the temperature is ramp up to 470 °C.

The second stage starts by opening the copper shutter and a further increase of the substrate temperature to 590 °C. The supplied copper forms together with the precursor layer the $Cu(In,Ga)Se_2$ chalcopyrite. In the course of the second stage, the [Cu]/([Ga] + [In])-ratio increases until a value of roughly 1.4 is reached. Moving into the Cu-rich regime helps the recrystallization [141] and increases the grain size. The start of the formation of the secondary Cu_xSe layer can be tracked by an increase in the power needed to heat the substrate holder. Due to the metallic nature of the secondary phase, the emissivity is higher compared to the $Cu(In,Ga)Se_2$ layer and leads to a stronger heat dissipation. When the desired CGI ratio is reached, the copper supply is switched of.

In the third stage again indium and gallium are supplied. By varying the length of this last stage the final composition can be chosen. Selecting a long duration of the third stage (> 10 min) results in a final Cu-poor composition since all excess Cu_xSe is reused to form the chalcopyrite. Short durations on the other side (< 9 min) give samples with Cu-rich composition, as still secondary phases are present. Overall duration between 4 min and 24 min were used. When the desired composition is reached, the flux of indium and

gallium is switched off and the samples are cooled down under selenium atmosphere. Also in this process the selenium supply is stopped below 300 °C and after reaching 200 °C the samples are taken out. While the CGI depends on the length of the third stage, the [Ga]/([Ga] + [In])-ratio depends on the indium and gallium flux. The final composition of the absorber layer is measured by energy dispersive X-ray spectroscopy (EDX) using an acceleration voltage of 20 kV .

2.4.4 Cu-rich vs. Cu-poor composition

The $Cu(In_{1-x}, Ga_x)Se_2$ chalcopyrite is a versatile material that can be grown under various conditions as briefly described in section 2.1.2. Within this work samples with an overall copper deficiency ([Cu]/([Ga] + [In]) < 1) and samples grown with copper excess ([Cu]/([Ga] + [In]) ≥ 1) after growth will be distinguished. The former will be denoted as Cu-poor and the latter as Cu-rich. It should be noted here that no real phase with excess copper exist and that samples grown under copper excess consist of a stoichiometric absorber layer and Cu_xSe secondary phases, which are etched away before cell processing. Although closely related, both composition exhibit different optical and electrical properties which are discussed in the following.

The current state of the art $Cu(In,Ga)Se_2$ solar cell are made with a Cu-poor composition reaching efficiencies above 20 % [9], [25], [26]. The latest improvement were facilitated by a post deposition treatment with heavy alkalis, as discussed in section 2.5. Compared with that, samples grown under copper excess do not reach efficiencies above 10 % [20], [142]. A large contribution to the lower efficiencies in samples grown Cu-rich is the lower open circuit voltage. The loss in V_{OC} originates from recombination close to the interface, as temperature dependent current voltage measurements reveal, whereas samples with Cu-poor composition are not limited by recombination close to the interface [18].

Looking at the phase diagram, it is obvious that the large stability region on the Cu-poor side can only exist due to the formation of large numbers defects. The two most likely formed defects are the copper vacancy V_{Cu} (A1) and indium on copper antisite In_{Cu} (D), which form a shallow acceptor and a shallow donor (see also section 2.3.4). It is assumed that they are partly passivated by the formation of an electrical inactive defect complex (In_{Cu}-$2V_{Cu}$), but likely not all of them. The recombination of the remaining free carriers leads to fixed charges and fluctuating potentials. This can be best seen in low temperature photoluminescence measurements, where a broad asymmetric peak is observed for samples grown Cu-poor [12], [14], [15].

Although the potential fluctuations are screened at room temperature, the large number of ionized defects will deteriorate transport properties within a grain. This assumption is supported by Hall measurements where the majority carrier mobility is lower in Cu-poor samples than in Cu-rich ones [12], [13]. Another indication for worse transport properties is the lower carrier collection efficiency in Cu-poor samples [143]. Looking at the low temperature spectra of samples grown under Cu-excess on the other side, several defined peaks are observed which are related to different defect transitions. Even excitonic luminescence can be observed, showing the high crystal quality. Higher mobilities and collection efficiencies are determined for this composition [143].

In general polycrystalline $CuInSe_2$ samples grown under copper excess exhibit large grains up to a few micrometer (see figure D.1 in the appendix). Samples grown Cu-poor in a 1-stage process are normally characterized by smaller grains (see figure D.2 in the appendix). For high efficient solar cells multi-stage processes are used, including a stage

where the absorbers is Cu-rich to aid the formation of large crystals, as described in section 2.4.3. The apparent doping density in samples grown under Cu-excess determined by capacitance measurements are general in the range of $\approx 4 \times 10^{16}\,\mathrm{cm}^3$ [12]. When the copper content is lowered below stoichiometry this value drops towards $\approx 1 \times 10^{16}\,\mathrm{cm}^3$, which can be explained the higher number of compensating donor defects reducing the net-doping.

When photoluminescence measurements are carried out on bare $CuInSe_2$ absorber layers, similar initial quasi Fermi level splitting values are found for both composition [17]. Though, when exposed to air, the interaction with oxygen leads to an enhanced surface recombination decreasing the photoluminescence yield [17] (radiative recombination) and lowering the minority carrier lifetime [144]. The measured drop in quasi Fermi level splitting is 3x stronger and 10x faster in Cu-poor samples compared to Cu-rich samples (polycrystalline $CuInSe_2$) [17]. A possible way to reverse this surface degradation is a short etch (30 s) in KCN, fully restoring the as grown qFLs [17]. A second way to restore the surface, is the storage of the sample in ultra high vacuum, as shown in section D.3 in the appendix[2]. From room temperature photoluminescence also the sub bandgap absorption in form of Urbach tails can be investigated, which is linked to potential fluctuations. Investigations show a strong increase of the Urbach energy from 11 meV to up to 17 meV when reducing the copper content below stoichiometry [16]. A recent study shows that the V_{OC} loss is directly linked to magnitude of the Urbach energy, it should be thus as small as possible [146].

Summarizing, samples grown with copper excess show a lot favourable properties in terms of crystal growth, charge transport, defect concentration and Urbach energy. However, they show considerably lower efficiencies and V_{OC}. The lower open circuit voltage in $CuInSe_2$ is linked to recombination close to the interface, which has been recently proposed to caused by a selenium related defect that is induced by the necessary KCN etching [147]. In $CuInSe_2$ it is possible to remove this defect by surface treatment like KF-Se [148], Se [147], or In-Se [19]. With the latter one, even comparable efficiencies to Cu-poor $CuInSe_2$ are possible. In $Cu(In,Ga)Se_2$ it is not possible to increase the efficiency of Cu-rich samples to values reached in Cu-poor samples with a Ga-Se treatment [20].

2.5 KF PDT on CIGS - literature review

Within the last 5 years tremendous success in improving the efficiency of $Cu(In,Ga)Se_2$ solar cells has been achieved, increasing the device performance of small devices from 20.3 % [23] to up to 22.9 % [9], [26]. This increase is mainly facilitated by a newly developed alkali treatment after the growth process. This method was initially developed to supply sodium to absorber layer grown on alkali free substrates like polyimide [69], [126] to utilize the positive effect of sodium on the cell performance [67]. The use of potassium or other alkali metal was assumed to have similar effects compared to sodium since earlier studies with alkali precursor layers (NaF, KF, CsF) showed similar improvements in the device performance for all alkalis [149]. Combining the post deposition treatment (PDT) of sodium fluoride (NaF) with a post deposition of potassium fluoride (KF) on samples grown on polyimide foil a new world record for all $Cu(In,Ga)Se_2$ technologies at that time was achieved [25]. After this the KF-PDT was also used in high temperature growth processes

[2]This possibility shows that unlike assumed, no chemically bound indium oxide is formed at the surface [145], but that the oxygen is only physisorbed to the surface and is able to desorb again.

on soda lime glass leading to continuously increasing new world record efficiencies [9], [80], [150], [151]. Using even heavier alkali elements like rubidium and caesium for the PDT similar or even higher efficiencies can be reached [26]. The following sections will discuss two different methods on how the PDT can be done. Afterwards the effect of the alkali treatment on the absorber layer and the finished device will be briefly discussed. A recent review about the incorporation of alkali metals can be found in [152]. A more detailed picture about the effects reported in literature can be found in the review article of Muzillo [130].

2.5.1 Post deposition treatment methods

There are several ways how alkalis can be introduced into the absorber layer. For all investigated samples a high temperature co-evaporation process is used for the growth of the absorber layer using soda lime glass. The combination of both leads to an inherent introduction of sodium into the absorber. Other methods to include sodium into the absorber layer are 1) growing on a sodium doped molybdenum layer [153], 2) adding a sodium fluoride (NaF) precursor layer on top of the molybdenum back contact [154], 3) evaporating NaF during the growth process [155], and 4) evaporating NaF after the growth process [126]. The influence of the fluorine on the absorber layer remains unknown but seems to be at least not detrimental. The fluorine is not detected by secondary ion emission spectroscopy (SIMS) measurements[3] within the layers after the growth. Currently it is assumed that it forms SeF_6 together with the excessive selenium which then desorbs from the absorber surface [156]. Alternatively it could be the case that it accumulates at the surface and is washed away before the buffer layer deposition. All methods for the introduction of sodium have been shown to improve the device performance, but highest efficiencies are reached using soda lime glass and a high temperature process [157].

Potassium can be added using the same methods. As discussed before PDT's with KF leads among with RbF to the highest efficiencies [9], [26], [80][4] and are the only method investigated within this thesis. Depending whether the treatment takes place inside or outside the growth chamber, two different process routes are differentiated. The former is called "in-situ" and the latter "ex-situ". Adapted versions of both will be used.

In-Situ potassium fluoride treatment

This PDT routine was first described by Chirila et al. [25] and is composed of the following steps. After the growth of the $Cu(In,Ga)Se_2$ absorber layer by either co-evaporation or precursor annealing, the sample is cooled down to an intermediate temperature between 350 °C and 400 °C [25], [150]. At this temperature a low flux of KF is evaporated under selenium atmosphere for 10 min to 20 min. Afterwards the samples are cooled down to room temperature, washed by de-ionized water or ammonium hydroxide and further processed by adding the buffer and window layers. Part of this work is to transfer this PDT to absorber layers grown under copper excess and study its effects. However, Cu-rich grown samples form a Cu_xSe secondary phase at the absorber surface, which impedes the direct treatment of the sample surface. Due to this, the process is altered for this type of samples to remove the secondary phase before the post deposition treatment as described in section 3.2.1.

[3] SIMS has low detection threshold for fluorine and is able to detect smallest amount of it.

[4] It should be noted here that treatments with rubidium fluoride reach similar efficiencies [26].

Ex-Situ potassium fluoride treatment

The alkali treatment can also be done in two steps, as first shown by Pistor et al. [24]. In this routine the alkali metal (KF) is deposited in a separate tool and afterwards incorporated under selenium atmosphere into the absorber. The process has been shown to improve the V_{OC} and leads to similar changes at the sample surface as the in-situ process. However, a strong drop in fill factor caused by an increased series resistance prevents gains in efficiency of the devices. The details about the adapted process will be discussed in section 3.1.1.

2.5.2 Effects of alkali PDT's on absorber layer and device characteristics

Plenty of studies have been published on the effects of treatments with alkalis and a recent literature review can can be found in [130]. The results vary depending on the alkali metal used, on the method of introducing the alkali metal to the absorber layer, and also on the specific process parameters used like temperature and flux [130], [158]. Since only soda lime glass substrates and the alkali metal potassium will be used throughout this thesis, the review here will be narrowed down to those specific conditions.

The key component of the PDT is the enhanced device performance. This increase is mainly driven by a higher open circuit voltage. A minor positive effect is regularly observed in an increased fill factor. The influence on the short current density differs between publications and depends on the device finishing. It was reported that the KF PDT enhances the deposition of CdS [25], [150], leading to thicker CdS layers and more parasitic absorption and thus reduces J_{SC}. However, this effect on the CdS deposition process can also be used to an advantage. The changed CdS deposition process allows to deposit even thinner CdS layers without losses in V_{OC} leading to improvement in the J_{SC} [25], [150].

Those phenomenological changes of the device parameters are explained by two main observation. These are on the one side the creation of a surface layer with a different composition and on the other side an ion exchange in the whole absorber altering the electronic properties. Investigating the sample surface after the treatment with KF, a copper depleted layer is detected by XPS [24], [25], [159], [160] consisting of potassium indium gallium and selenium. The gallium content within this layer is still under discussion and is reported to be still observable on the one side [161], [162] or completely depleted on the other side [25], [158], [163], likely dependent on the process. Because of the elemental composition, the surface layer is also referred to as KIS or KIGS layer. This layer can smoothly cover the whole absorber surface [25], [160] or can be structured [158], [159], [162], as observed by scanning electron images. The surface layer is found to have wider bandgap, mainly shifting the valence band down [24], [164]. Overall it leads to a reduced surface recombination [157], which is related to bandgap widening and an enhanced cadmium interdiffusion [25], [157], [160]. Mixed results are reported regarding the effect of the treatment on the doping density. While in some studies an increase in apparent doping is seen in admittance measurements [159] other studies find a decrease in doping after the treatment [157].

The second observation made after an alkali treatment is a strong increase of the alkali metal concentration used for the treatment accompanied by a reduces sodium concentration throughout the layer. This ion exchange mechanism was first reported for low temperature processes [25] but is also observed on high temperature processes [26]. Using a potassium

treatment on selenized precursor stacks likewise shows the ion exchange [165]. In samples only subjected to sodium it was shown that the sodium atoms mainly accumulate at the grain boundaries [77], [128], [166] and are present in much lower concentration within the grains [167]. Whether sodium is only replaced at the grain boundaries or also within the crystal is still under debate. Recent measurements on rubidium fluoride treated samples show a clear accumulation of rubidium at the grain boundaries [168] but also show some regions with increased rubidium content within a grain. Also Würz et al. [169] found rubidium after the treatment within the grains. Independent of the specific location of the ion exchange, it was shown to effect the electrical properties of the bulk. A higher carrier lifetime was determined [159], [170] and as a consequence thereof a higher photoluminescence yield [159], [171]. The enhanced carrier lifetime also facilitates a widening of the effective carrier collection towards the molybdenum back contact as shown by electron beam induced current measurements (EBIC) [71], [80], [159]. Low temperature photoluminescence measurements in addition show a reduction of potential fluctuations after an alkali treatment [146], [170]. All those bulk effects indicate a reduced non-radiative recombination rate and are the basis for the improved open circuit voltage [159], [171].

Beside those two main improvements it has also been observed, that the compositional range in which highest efficiencies can be reached shifts towards higher gallium contents [150]. The shift in [Ga]/([Ga] + [In])-ratio from about 0.30 to roughly 0.37 is facilitated by a larger region in which the V_{OC} follows the bandgap without saturating.

CHAPTER

THREE

POTASSIUM FLUORIDE POST DEPOSITION TREATMENT OF $CuInSe_2$ ABSORBER LAYERS

The treatment of chalcopyrite absorber layers with alkali metals after the growth has lead to tremendous improvements of the device performance, as described in section 2.5. Part of the improvement is related to the formation of a copper deficient surface. This is especially interesting for samples grown with copper excess since large improvements in the efficiency of Cu-rich samples have been reported after the formation of a Cu-poor surface for example by an indium selenide treatment [19]. However, no research efforts in this direction have been made so far. The next chapter closes this gap, presenting two process routes of a potassium fluoride post deposition treatment that can be applied to samples grown with copper excess.

First attempts are done using an ex-situ process, in which the deposition of potassium fluoride (KF) and the annealing is done in two separated steps. Here experimental conditions like temperature, duration, background atmosphere and rinsing procedures are tested. In a second step, the process is done closer to the routine reported in literature [25], with deposition and annealing at the same time. Several annealing temperatures and durations are tested and the effect of the KF treatment is thoroughly investigated by electrical and optical measurements. The results and insights shown in this chapter were gathered in a joint effort together with Hossam Elanzeery. As we both contributed equally to this research the presented results will be also part of his dissertation [172].

3.1 Ex-Situ post deposition treatment

Since it is unknown if the potassium fluoride treatment has any influence on absorbers grown under copper excess, first an ex-situ process is tested. This process has the advantage that the alkali metal can be deposited in an already existing electron beam evaporation tool, without the need to extend the molecular beam epitaxy system used for the growth of the absorber layers. The deposited KF can then be incorporated into the absorber in an annealing step inside a tube furnace. This kind of treatment was reported to improve the V_{OC} on Cu-poor $Cu(In,Ga)Se_2$ solar cells [24] but has not been tested on samples grown with copper excess. The steps of the treatment routine will be discussed below. The usage of a furnace instead of a the growth chamber opens up the possibility to examine the treatment with different background atmospheres and different background pressures. Besides the variation of the treatment conditions, also different rinsing and

etching procedures before the CdS deposition will be tested. At the end of this section the best treated samples will be investigated by electrical measurements. Most of the shown results are also published in [143].

3.1.1 Preparatory steps and alkali deposition

Several steps are needed before a potassium fluoride treatment can be successfully applied, which will be described briefly in the following. In the beginning the processed of the ex-situ KF PDT is described shortly. After that a deposition routine for KF is established to control the amount KF used. This is important as it has been reported that high concentrations of KF reduce the device performance [24]. Besides this the annealing atmosphere and duration are investigated as well as the temperature used. In a last step different rinsing methods after the treatment are compared.

Ex-situ treatment process steps

The ex-situ PDT used consists of the following steps: After growth the sample is cooled down to room temperature and removed from the vacuum growth chamber to conduct a wet chemical etching in potassium cyanide to remove secondary Cu_xSe secondary phases in case of Cu-rich samples (10 wt %, 5 min) and residual oxides in case of Cu-poor samples (5 wt %, 30 s). Afterwards the sample is immediately transferred into the evaporation chamber of the electron beam evaporation tool. At a pressure of below 1×10^{-5} mbar a thin layer of KF is deposited onto the samples at room temperature. In the last step the samples are removed from the evaporation chamber, placed in a graphite box and annealed with a background pressure of 1 mbar under different atmospheres like ambient air, nitrogen, or selenium. A selenium atmosphere is reached by adding 40 mg of selenium powder into the graphite box which starts evaporating at comparable low temperatures ($\sim 250\,^{\circ}$C) leading to high vapour pressure at the temperatures used (~ 0.3 mbar at 350 °C [132]). It should be noted here that for the annealing under selenium the tube furnace is flushed twice with nitrogen before the annealing. It is thus an annealing under selenium and nitrogen. After the annealing process in the tube furnace and before the deposition of CdS, the samples are rinsed with de-ionized water to remove residual fluorides and salts. The CdS and window layer depositions are done in the same manner as non treated samples.

Alkali deposition

The potassium fluoride used within the treatment is evaporated in an electron beam evaporator. First attempts evaporating anhydrous potassium fluoride powders gave unreliable and fluctuating deposition rates. This could be greatly improved by compressing the powder into several pellets. With pellets the deposition of mostly homogenous layers is possible with a stable flux. However, the thickness of the deposited layers could not be measured by a contact profilometer due to the strong hygroscopic behaviour of KF turning the thin layer into watery films. This problem could be avoided by depositing a second layer on top of the KF inside the electron beam evaporator before the sample is exposed to ambient air. NaF was chosen as this second layer because of its overall similar properties but non hygroscopic behaviour. Using NaF is possible since also the deposition of LiF and NaF inside the electron beam evaporator was optimized. Due to the double layer structure the thickness determination is not precise, but it is possible to determine the thickness of the KF layer with an error of about ± 10 nm. When varying the amount

of KF between treatments processes, it was found that best results are achieved with a target thickness of about 10 nm. Using a target thickness of more than 30 nm deteriorates the device parameters.

Variation of annealing conditions

The first reported KF PDT was done in an intermediate step within the cooling process after growth under selenium atmosphere [25]. However, also the deposition of KF at room temperature and the subsequent annealing in vacuum without selenium has been reported [173]. To check the best annealing conditions for the ex-situ process, three identical samples were etched in KCN (10 wt % in water, 5 min) and directly afterwards a thin KF layer was deposited. In three seperate process runs the samples were heated up inside a graphite box in a tube furnace under different atmospheres. The first samples was annealed in ambient air with a background pressure of 1 mbar. The second sample in annealed in nitrogen also at a pressure of 1 mbar. The third one has the same condition as the second one, but a selenium atmosphere was created by placing 40 mg of selenium powder inside the graphite box. Of those three samples, only the sample annealed in selenium atmosphere showed decent power generation under light. The sample annealed in nitrogen exhibited a strongly reduced efficiency and the sample annealed in air was completely shunted. The lower efficiencies are likely due to a loss of selenium from the absorber layers during the annealing. All succeeding treatments are carried out under selenium atmosphere using the same amount of selenium powder each time.

Beside the amount of KF deposited and the atmosphere, also the duration and temperature play an important role on the outcome of the treatment. Temperatures between 250 °C and 400 °C as well as times between 12 min and 45 min were tested. The best results in terms of V_{OC} were achieved using temperatures between 300 °C and 350 °C and durations of below 20 min. For lower temperatures the potassium can likely not be incorporated and using longer times the solar cells are found to be shunted.

Investigation of the rinsing used after PDT

Besides rinsing the sample with de-ionized water [162] after the KF treatment, also rinsing with ammonium hydroxide [165] or etching with hydrochloric acid (HCl) [24], [174] have been reported in literature. To verify what works best for our absorbers, four identical samples have been etched in KCN, covered with KF, and annealed under selenium atmosphere. Before the deposition of CdS each sample is handled differently. Sample 1 is rinsed thoroughly for 30 s with de-ionized water. Sample 2 is etched for 20 s in a weak aqueous KCN solution (5 wt %). Sample 3 and 4 are etched in HCl for 10 s and 2 min, respectively. Both sample 1 and 2 show comparable current voltage characteristics to an untreated reference sample. In direct comparison the open circuit voltage (V_{OC}) is slightly higher for the sample rinsed with de-ionized water compared to the KCN etched one. The samples etched by HCl show lower device performance, mainly driven by a lower V_{OC} (-10 mV and -55 mV) and lower shunt resistance. Both the lower V_{OC} and the higher shunt resistance indicate that the HCl etching at least partly removes the absorber layer. All subsequent samples are rinsed with de-ionized water to remove excessive potassium fluoride and other byproducts before CdS deposition.

3.1.2 Results gathered on the best treated samples

The result of the treatment is rated depending on the change in V_{OC} and efficiency. The best improvements in V_{OC} treating a Cu-rich $CuInSe_2$ sample have been achieved by depositing a KF layer with a target thickness of 15 nm and annealing in selenium atmosphere for 20 min at a temperature of 350 °C. The dark and illuminated current voltage curves of a reference sample and the best sample with KF PDT are plotted for Cu-rich samples on the left of figure 3.1. The treatment has has several effects on the IV curve which are explained in the following. In the reference cell the negative current increases at high reverse voltages. This drop has been investigated recently and was attributed to space charge limited currents originating from defective parts of the interface between absorber and CdS buffer layer [175]. After the treatment this feature is not observed anymore. Besides this, an improvement in the V_{OC} of 36 mV is detected in the treated sample. Detrimental effects are seen in a reduced short circuit density (J_{SC}) and a reduced fill factor. The loss in the latter is mainly driven by an increase in the series resistance as well as an increased diode factor. Overall the efficiency slightly drops from 7.4 % to 7.0 % with the treatment. A summary of the IV parameters which are determined by fitting a one diode model is given in table 3.1.

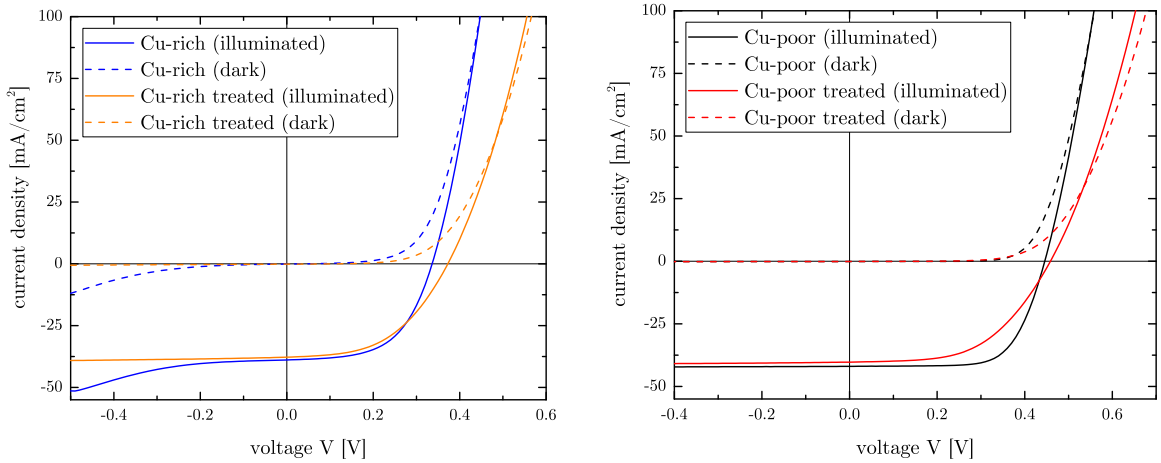

Figure 3.1: Current voltage curves of a Cu-rich (left) and Cu-poor (right) sample with and without ex-situ KF PDT measured in the dark (dashed) and illuminated (solid).

Table 3.1: Average current voltage characteristics of a Cu-rich and a Cu-poor $CuInSe_2$ sample with and without potassium fluoride ex-situ post deposition treatment.

Composition	PDT	V_{OC} [meV]	J_{SC} [mA cm^{-2}]	FF [%]	η [%]	A [1]	R_S [Ω cm^2]
Cu-rich	No	336	38.9	57	7.4	1.4	0.5
	Yes	372	37.8	49	7.0	1.8	0.9
Cu-poor	No	446	42.0	68	12.8	1.3	0.6
	Yes	458	40.3	54	9.9	2.0	1.2

Using the same treatment conditions on a Cu-poor sample similar effects are observed, as shown on the right side of figure 3.1. The open circuit voltage is slightly improved by 10 mV in the treated sample. However, an increase in the series resistance and the

diode factor reduce the fill factor. Besides this also the J_{SC} decreases slightly. In total the efficiency drops from 12.8 % to 9.9 %.

Overall three effects onto the current voltage characteristics are observed which are (1) a reduced fill factor, (2) a reduced J_{SC} and (3) an improved V_{OC}. Possible origins of each effect will be discussed in following. The reduced fill factor (1) originates likely from a combination of two things, namely surface oxidation and too much KF. The hygroscopic nature of the thin KF layer enables the capture of moisture during roughly 4 min long transfer of the samples from the electron evaporation system to the annealing oven leading to the formation of watery films on top of the absorber layers. This likely enhances the oxidation of the surface. This oxidation increases the recombination at the absorber-buffer interface and thus within the space charge region which increases the diode factor. This explanation is supported by results in the literature on Cu-poor Cu(In,Ga)Se_2 samples with an ex-situ KF PDT [24] that also show a reduced fill factor which decreases with increasing air exposure time. The second possibility is a too high amount of KF which can come either from a too thick KF layer deposited or a redistribution of KF on the sample surface. The difficult control of the KF deposition possibly leads to thicker layers than targeted. Also possible is a redistribution of KF at the surface due to the formation of the watery film leading to an inhomogenous amount of KF across the sample with possible accumulations at certain spots.

Either way a too thick KF layer was reported in literature [24], [158] to reduce the fill factor. This is inline with our experiments using different thicknesses of the KF layer. Both the oxidation of the surface and also the too high amount of KF can further increase the series resistance also reducing of the fill factor.

To investigate the changes in J_{SC} (2), the external quantum efficiency is measured for the investigated samples. Details about the measurement technique can be found in [92] and a description about the set up used can be found in [95], [172]. The external quantum efficiency is plotted over the wavelength on the left side of figure 3.2. Both untreated samples show the known shape of a EQE curve [33], [92]. Below 400 nm no signal is detected due to parasitic absorption in the window layers. Between 400 nm and 525 nm a dip in signal is observed due to parasitic absorption in the CdS buffer layer. The wiggles in the signal between 600 nm and 900 nm originate from interferences in the window layer and the drop in the signal above 1200 nm is due to incomplete absorption [33], [92]. The absorption edge is steeper in case of the Cu-rich composition possibly due to lower Urbach tailing [16] and the bandgap evaluated by linear extrapolation is with 0.995 eV about 40 meV higher than the Cu-poor bandgap. The difference in bandgap is in line with findings in literature [43]. After the treatment both compositions exhibit a drop of the EQE in the low wavelength region which is likely due to a thicker CdS layer leading to enhanced parasitic absorption. This interpretation is supported by the findings of Chirila et al. [25] which showed an enhanced CdS growth after a potassium fluoride treatment. Besides this the EQE spectrum of the Cu-rich sample remains mostly unchanged. In case of the treated Cu-poor sample a lower EQE response compared to the untreated sample is observed above 800 nm which is possibly related to a reduced charge carrier collection. The current density of a device can be predicted by integrating the product of the EQE and the AM1.5 sun spectrum [88]. From this a 0.5 mA cm^{-2} lower J_{SC} is expected for the treated Cu-rich device, whereas a loss of 2.5 mA cm^{-2} is expected for the treated Cu-poor device. The values give the right trend of a lower loss in the Cu-rich sample (1.1 mA cm^{-2}) and a higher loss in the Cu-poor sample (1.7 mA cm^{-2}). The loss in J_{SC} can thus be explained by enhanced CdS growth leading to more parasitic absorption and in case of the treated

Cu-poor sample further by a lower EQE response in the long wavelength region.

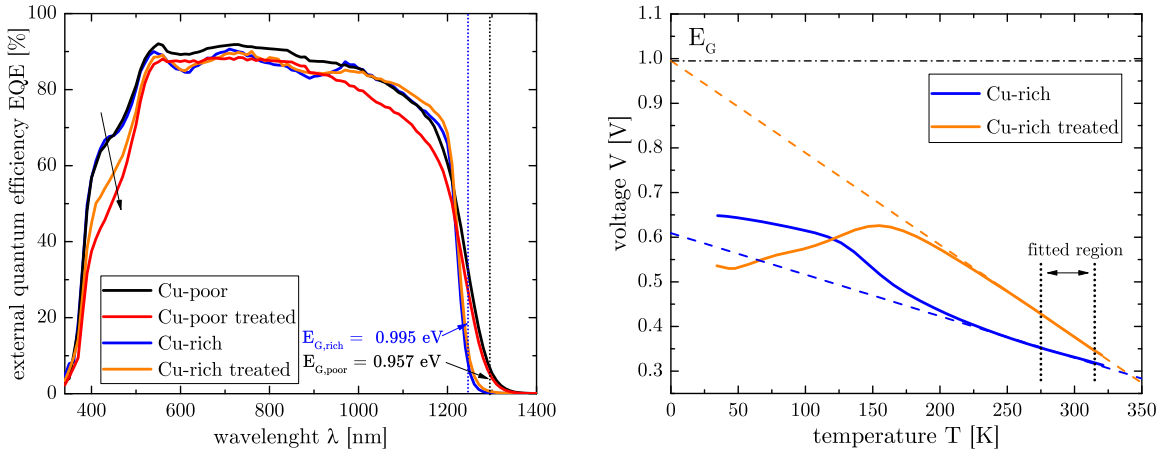

Figure 3.2: Left: External quantum efficiency measured for a Cu-poor (black) and Cu-rich (blue) device or untreated reference devices. Furthermore, the EQE of a Cu-poor (red) and Cu-rich (orange) sample with KF treatment is plotted. Right: Open circuit voltage of the Cu-rich samples with (orange) and without (blue) treatment plotted over the temperature. The data is fitted linearly between 275 K and 315 K to determined the activation energy E_A.

The third observation is an improvement in V_{OC} (3) which is more pronounced in the case of a Cu-rich composition. To investigate the main recombination channel, temperature dependent current voltage measurements are carried out on the finished devices. The open circuit voltage of the Cu-rich cell with and without KF PDT is plotted over the temperature on the right side of figure 3.2. By extrapolating the linear fit of the high temperature region towards 0 K, the activation energy of the main recombination channel can be determined [91] (see also equation (2.14)). For the untreated Cu-rich device an activation energy of 0.61 eV is determined which is well below the bandgap. This means that the device is limited by recombination at the absorber buffer interface or close to this interface [18]. This is in line with previous results on $CuInSe_2$ samples grown with copper excess [19], [176]. After the treatment the activation energy is greatly increased to 0.995 eV and thus equal to the bandgap. This increase in activation energy is interpreted as a shift of the main recombination channel away from the buffer-absorber interface to the absorber bulk. Since recombination close to the interface is detrimental for the V_{OC}, this shift is likely the main reason for the improvement in V_{OC} of the treated Cu-rich sample. In case of the Cu-poor samples, hardly any change is observed in in the temperature dependent IV measurements. For both the treated and untreated sample an activation energy of 0.98 eV is determined which is slightly above the bandgap and thus indicates a limitation by bulk recombination.

In case of the Cu-rich sample most of the gain in V_{OC} can be explained by the shift of the main recombination channel. But also in the Cu-poor sample a small gain in V_{OC} is observed. This could be related to Cu-deficient surface layer which is already hinted in the faster CdS growth. To probe the near surface composition and investigate the formation of a new surface layer, X-ray photo-electron spectroscopy (XPS) measurements are carried out on treated absorber layers. Before the measurement the samples are rinsed with de-ionized water and shortly etched with KCN (5 wt %, 30 s). In figure 3.3 the XPS signals related to the Cu 2p peak (932.6 eV), the In 3d peak (444.5 eV) and the

Se 3d peak (54.1 eV) are plotted for the treated Cu-rich sample (a,b,c) and the treated Cu-poor sample (d,e,f). To investigate the near surface composition also measurements after removing part of the surface by sputtering are conducted. Cumulative sputter times of 0 s, 120 s, 240 s and 720 s are used on the same spot with a final depth of about 50 nm. The curves for the different sputter times are shifted vertically by 0.75 to increase the visibility.

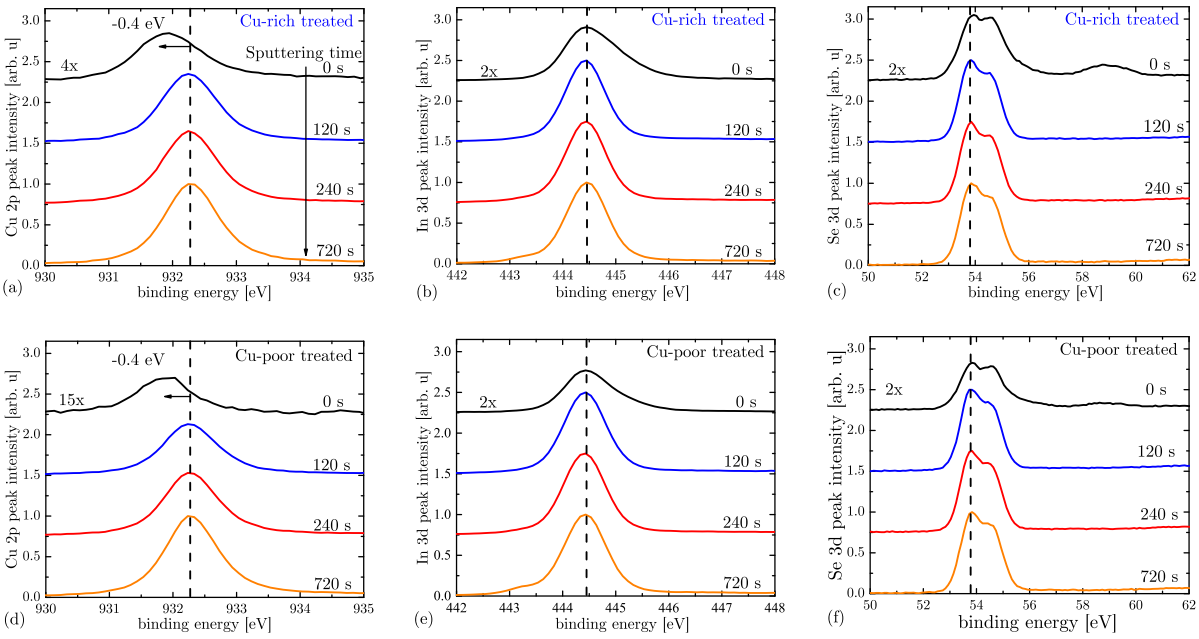

Figure 3.3: XPS measurements of the constituent elements Cu, In and Se after the ex-situ treatment of a Cu-rich (a-c) and a Cu-poor (d-f) $CuInSe_2$ absorber layer. Investigated are the Cu 2p peak, the In 3d peak and the Se 3d peak. Four measurements at different cumulative sputter durations are carried out ranging in depth from the surface to about 50 nm deep into the absorber. The signal at the surface (black) are multiplied by the shown factor to increase the visibility.

Quite surprisingly both composition show the same features and a similar development with sputter duration. The same spectra are detected for sputter times of 120 s, 240 s and 720 s, indicating that only a thin surface layer of below 10 nm is affected by the treatment which is inline with observations in literature [25], [159]. The signal at the surface (0 s) is reduced by a factor of 2 for indium and selenium, likely due to contamination from the short transfer through ambient air after etching and before the introduction into the vacuum chamber for measurements. Comparing the [Cu]/[In]-ratio at the surface (black) to the bulk (orange), a two times lower [Cu]/[In]-ratio is detected at the surface of the Cu-rich grown sample and an eight times lower [Cu]/[In]-ratio in case of the Cu-poor sample. Although the copper content is reduced, both compositions still have considerable amounts of it at the surface.

This is differing from the literature results discussed in section 2.5.2 that show a complete copper depletion [25]. There are at least two possible explanations for this. Firstly the surface layer could be patterned as shown in [158], [159], [162]. This would lead to a super position of measurement signals from the new surface layer and from an untreated surface. This explanation is supported by findings of Khatri et al. [159] reporting a 10x reduced copper content of an in-situ treated $Cu(In,Ga)Se_2$ sample which had patterned surface. Secondly it could be related to the ex-situ post deposition routine

used possibly forming a different surface layer. This is supported by findings of Pistor et al. [24] showing a similar decrease in copper content in an ex-situ treatment. In any case, this strongly reduced copper content at the surface of the Cu-poor sample shows that the ex-situ treatment indeed works at least similar to the in-situ treatment. For the Cu-rich sample the [Cu]/[In]-ratio at the surface reduced by a factor of 2, showing that the goal of a Cu-poor surface was achieved.

Besides the reduction of copper content, also the peak position of the Cu 2p peak is shifted by 0.4 eV towards lower binding energies which means that the copper is in another chemical environment compared to the bulk. Copper could be possible in a compound together with potassium. The shift can be excluded to originate from oxidation, since oxidation would shift the peak to higher binding energies [177]. The In 3d peak shows an asymmetric broadening towards higher binding energies which could be due to oxidation, which would fit to findings showing that mostly indium oxide forms at the surface [145]. The measurement data for the Se 3d peak shows a second peak at 59 eV which is likely related to SeO_2 [159]. Summarized, the ex-situ treatment reduces the [Cu]/[In]-ratio independent of the composition of the sample but also leads to an enhanced surface oxidation.

3.1.3 Interim conclusion

Using an ex-situ post deposition routine it is possible to improve the V_{OC} of Cu-poor but also Cu-rich $CuInSe_2$ solar cells. However, no improvement in the efficiency could be reached due to a strongly reduced fill factor. This lower fill factor is likely due to an enhanced oxidization of the sample surface after KF deposition and before the annealing due to the hygroscopic nature of the KF. Small losses in J_{SC} as well as a reduced EQE response in the low wavelength region indicate a faster CdS growth as reported in literature. XPS measurements show a strongly reduced copper content in case of Cu-poor samples similar to literature [159]. Also for Cu-rich samples a reduction of copper at the surface by 50 % was detected. An ex-situ KF PDT is thus able to form a Cu-poor surface on top of a stoichiometric bulk. This intermediate layer improves the junction formation and shifts the recombination away from the buffer/absorber interface into the bulk, as shown by a strongly improved activation energy of the main recombination channel. The detrimental effects of the surface oxidation during the process routine can not be avoided and another process is needed which does not expose the deposited KF to air during the treatment procedure.

3.2 In-situ post deposition treatment with etching step

Building on the results gathered from the ex-situ KF PDT, a second routine is established in which the KF deposition and annealing take place in the same vacuum chamber to avoid the exposure of the samples to air during the KF treatment. More details about the process and the similarities to the ex-situ process are specified in the beginning of this section. Afterwards a Cu-rich sample series with different treatment durations and fixed annealing temperature is investigated thoroughly. At the end of this section results of this treatment method on Cu-poor samples are presented, confirming the validity of the treatment approach. The publication [148] is based on the findings of this chapter.

3.2.1 Process routine and treatment conditions

The in-situ process is in many steps similar to the previously used ex-situ process. In contrast to the ex-situ treatment where first KF is deposited and the sample then annealed, in the in-situ treatment the KF is deposited to the absorber layer at an elevated temperature for a certain duration. This approach was used to be closer to the routine reported in literature [25]. The potassium fluoride is evaporated from an individual effusion cell that was added to the growth chamber. In details the treatment consists of the following steps:

After the growth process the samples are taken out of the vacuum and etched to remove secondary Cu_xSe phases from the absorber surface in case of Cu-rich samples. Also Cu-poor sample are etched to remove oxides and to have a comparable process to the Cu-rich cells. After the etching the samples are immediately transferred back into the growth chamber before the actual KF PDT is performed. The samples are first rapidly heated up (20 °C/min) and then slower (5 °C/min) to about 380 °C under selenium atmosphere. The selenium flux used is similar to the one used during sample growth. When the annealing temperature is reached, the shutter of the KF sources is opened to evaporate a small flux. After the predefined treatment duration the samples are cooled down rapidly (20 °C/min) to about 250 °C and moved from the growth chamber to the loading chamber, where it cools down to room temperature. Before the deposition of CdS the samples are rinsed with de-ionized water to remove residual fluorides and salts. The CdS and window layer depositions are done in the same manner as for non treated samples. Since the samples are exposed to ambient air during this treatment, it will be called post deposition treatment with etching step to clearly distinguish it from the all-vacuum based methods.

Similar to the ex-situ treatment a double layer structure (KF + Cu) was used to determine the thickness of the evaporated KF. The effusion cell temperature was adjusted to give a flux of 1.5 nm/min which is used in all KF treatments. Several treatment temperatures[1] ranging from 320 °C to 550 °C have been tested as well as treatment durations between 4 min and 20 min. Using temperatures above 425 °C reduces the V_{OC} and the J_{SC} leading to a reduction in device performance. Best results are achieved for treatment conditions below 12 min. Longer treatments lead to a reduction in V_{OC} and fill factor.

3.2.2 Variation of the treatment duration

In the following, a set of four identical Cu-rich $CuInSe_2$ samples is investigated. They are grown with moderate copper excess ([Cu]/[In]-ratio $\sim$ 1.3). From this set one sample is used as a reference, which is only etched and processed to a device. On the three other cells a KF PDT is carried out with an annealing temperature of 380 °C, a fixed KF flux, a fixed Se flux and with varying durations of 4, 8 and 12 min. After treatment, the samples are rinsed with de-ionized water, and finished to devices. In the beginning of this section the current voltage characteristics are described. In the subsequent paragraph, possible influences on the J_{SC} are investigated, followed by a paragraph about influences on the V_{OC}. Afterwards changes on the sample surface are investigated and other effects of the treatment are discussed.

[1] Measured on the sample surface by a pyrometer.

Current-Voltage characteristics

The finished devices are measured in a solar simulator and exemplary current voltage characteristics under illumination are plotted in figure 3.4. The average device parameters of six solar cells determined by fitting a 1 diode model are summarized in table 3.2.

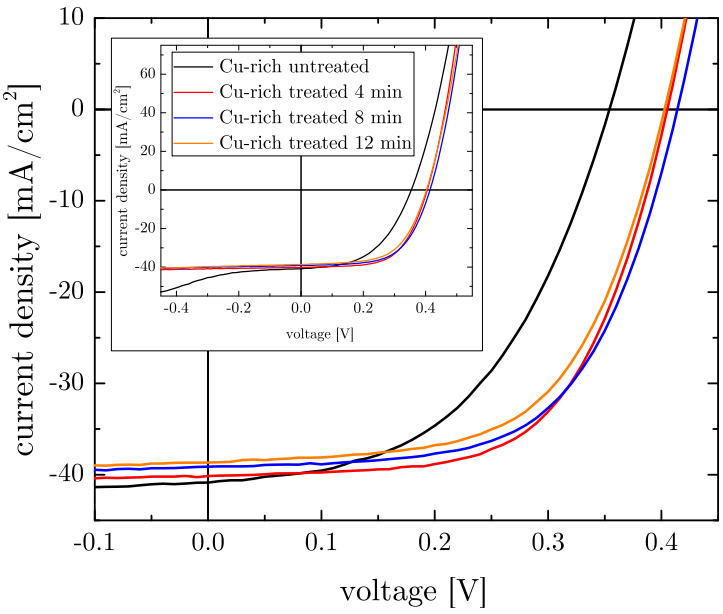

Figure 3.4: Illuminated current voltage curves of an untreated Cu-rich sample (black) and with KF treated cells with varying treatment durations of 4, 8 and 12 min. The inset shows the same plot with a wider voltage and current range.

The treatment has various effects on the IV curve. The most striking one is the improvement in V_{OC} of (50-60) mV which is more prominent than in the ex-situ process investigated previously where the V_{OC} changed by 35 mV. Differing from the ex-situ treatment is also the improvement of the fill factor by up to 10 % absolute. This improvement is driven by an improved shunt resistance ($120\,\Omega\,cm^2 \rightarrow$ above $900\,\Omega\,cm^2$) and a reduced diode factor ($1.9 \rightarrow 1.6$). In contrast to the ex-situ treatment the series resistance only slightly increases ($0.4\,\Omega\,cm^2 \rightarrow 0.5\,\Omega\,cm^2$), not deteriorating the fill factor. In the reference sample a break down current at high negative voltages is observed related to space charge limited currents [175]. This behaviour is not observed in any of the treated samples in the investigated voltage range. The J_{SC} decreases with increasing treatment duration which can be explained by the external quantum efficiency measurements below. Overall, the treated samples show an improved device performance reaching up to 10 % efficiency for the best cell.

Influences on J_{SC} : EQE, reflectance and admittance

To investigate the change in J_{SC} in more detail, external quantum efficiency measurements are carried out on the best cell of each sample which are plotted in figure 3.5. All treated samples show a pronounced drop in the spectral response in the wavelength region from 400 nm to 525 nm as also observed in the ex-situ treatment. This drop is the same in between samples and has been attributed to the enhanced growth of CdS leading to a thicker buffer layer and more parasitic absorption earlier. To verify this, a corner of each devices was split off and cross section SEM images were taken at several spots. Exemplary

Table 3.2: Average current voltage characteristics of a Cu-rich $CuInSe_2$ reference sample as well as samples with different potassium fluoride in-situ post deposition treatments with etching step. Included in brackets are also the values from the best solar cell.

PDT	V_{OC} [meV]	J_{SC} [mA cm^{-2}]	FF [%]	η [%]	A [1]
No	347 (354)	39.5 (40.8)	50.6 (49.9)	7.0 (7.2)	1.9 (1.9)
4 min	398 (405)	41.1 (40.2)	58.0 (61.2)	9.5 (10.0)	1.6 (1.5)
8 min	410 (414)	37.7 (39.1)	60.8 (60.6)	9.4 (9.8)	1.6 (1.6)
12 min	395 (403)	37.0 (38.7)	59.9 (59.6)	8.8 (9.3)	1.6 (1.6)

SEM images are shown in figure D.1 in the appendix. In case of the reference sample the thickness of the CdS layer is (35 ± 2) nm and with this a bit thinner than expected. For the treated samples on average a thickness of (48 ± 3) nm is determined, confirming a thicker CdS layer. The gain in thickness of about 38 % fits considerably well to the roughly 30 % lower EQE response in the short wavelength region.

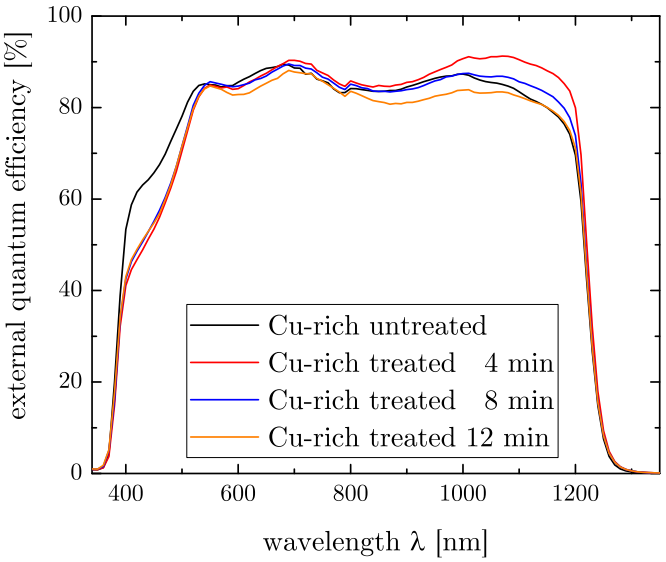

Figure 3.5: External quantum efficiency plotted over the wavelength of an untreated Cu-rich sample (black) and three cells with varying treatment durations of 4, 8 and 12 min.

The response in the long wavelength region (900 nm to 1200 nm) is lower for the 12 min treated sample and enhanced for the 4 min and 8 min treated samples compared to the reference. Since the increase in the latter ones is stronger for the higher wavelengths, it is likely related to an improved carrier collection [92], [178] meaning that also carriers generated closer to the molybdenum back contact are efficiently collected. This improvement could be linked to a better carrier lifetime (widening the collection width as measured in EBIC [159]), to a passivation of the absorber-molybdenum interface, or to a reduced doping widening the space charge region. The latter one will be discussed later.

Integrating the product of the EQE curve and the AM1.5 spectrum, the expected J_{SC} is estimated. The estimated loss in current for the two longer treatment durations matches well with the measured values of 1.8 mA cm^{-2} and 2.5 mA cm^{-2}. However, for the 4 min treatment no change in J_{SC} is predicted from EQE, but a gain of 1.6 mA cm^{-2}

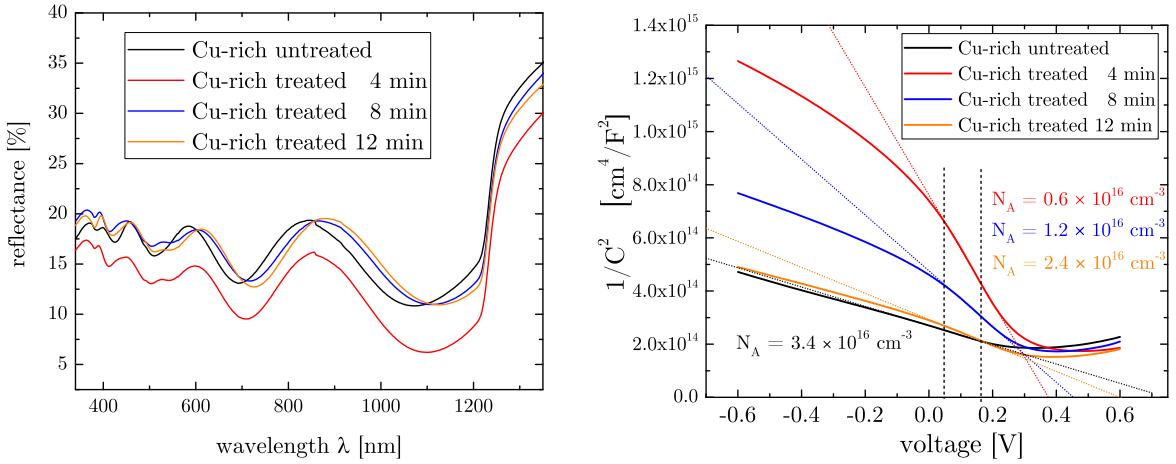

Figure 3.6: Left: Reflectance of an untreated Cu-rich sample (black) and three cells with varying treatment durations of 4, 8 and 12 min measured in the wavelength region of the EQE measurements. Right: Capacitance voltage measurements of the same sample set.

is measured. To investigate this mismatch, reflectance measurements are carried out on all finished devices[2] which are plotted on the left side of figure 3.6. For the reference sample and the two longer treatment durations, similar curves are detected which exhibit interference fringes from the window layer and the absorption edge of the absorber. The shortest duration shows the same features but the reflectance is 7 % lower over the whole relevant wavelength region (400 nm to 1200 nm). This lower reflectance leads to the higher J_{SC} measured in the device. That the lower reflectance is not measured in the EQE measurements might be related to the investigation of two different spots on the device.

A possible explanation for the change of the EQE response in the long wave length region is a wider space charge region width, resulting from a reduced doping density. To investigate this, voltage dependent capacitance measurements are carried out with a frequency of 100 kHz for all devices. The data is plotted in a Mott-Schottky plot on the right in figure 3.6 in which the doping depends on the inverse slope. The reverse bias region is not fitted to avoid influences of deep defects [59]. Also the in-diffusion of CdS leading to a depth depending doping density can influence the result determined here [78], [179]. Fitting is done between 0.03 V and 0.2 V assuming that the value extracted here reflects the doping densities within the space charge region. This doping inside the space charge region is the most interesting one because it directly affects the device performance. Since the investigated devices consist of different layers and interfaces which might contribute to the capacitance [59], [180], [181], the extracted values will be called apparent doping.

The untreated sample shows an apparent doping of $3.4 \times 10^{-16}\,\mathrm{cm}^3$ which is comparable to values measured on Cu-rich samples grown with high selenium overpressure [142], [182]. For 4 min treated sample the doping is decreased down to $0.6 \times 10^{-16}\,\mathrm{cm}^3$. For increasing treatment duration the apparent doping increases but stays below the reference value. The decrease of the doping density in the treated samples can be explained by the removal of a 200 meV deep acceptor type defect observed by admittance measurements [147],

[2]The reflectance is measured on finished devices in a comparable large area (more than one solar cell) which includes contacting grids and mechanical scribing lines. Both have a high reflectivity in the investigated wavelength region leading to an overestimation of the reflectance by a few %. For the comparison between samples this is not relevant, but calculating the internal quantum efficiency will lead to values above 100 % which physically makes no sense.

[172]. Further details about the origin and the removal of this defect can be found in [32], [147], [172] and will not be further discussed here. The increasing doping density with treatment duration is probably linked to the formation of a Cu-poor interface layer on top of the stoichiometric bulk. This additional layer likely introduces a capacitance which increases with treatment duration. Since the capacitance measurements mostly probe the near interface region, this layer influences the measurements and increases the determined doping density. A similar observation of an increasing apparent doping is made on Cu-poor devices as discussed later (section 3.2.3). Due to the addition of a new layer the determined doping densities have to be treated with caution since they might not reflect the doping of the bulk. No efforts are made regarding the interpretation of the built in voltage (V_{bi}) which is determined by the intercept of the linear fit with the voltage axis. This intercept reduces for the treated sample although an increase in the V_{OC} observed. The basic assumption of a one sided abrupt junction may not be applicable to the investigated system, leading to the difference in V_{bi} and V_{OC}.

In summary, the treatment leads to an enhanced CdS growth, shown by SEM images which increases the parasitic absorption in the short wavelength region. This leads to a reduced J_{SC} for treatment durations of 8 min and 12 min. The higher J_{SC} in case of the 4 min treated sample is linked to a reduced reflectance. In EQE measurements an enhanced carrier collection in the long wavelength region is observed for the shorter treatment duration which is likely linked to a longer lifetime or a wider space charge region width. Although the latter one is hinted by a reduced apparent doping, it is argued that the space charge region width has a small influence on the carrier collection. The improvement of the carrier lifetime or the passivation of the backside interface are thus more likely reasons for the improvement.

Influences on V_{OC}: Main recombination channel and qFLs analysis

In the ex-situ treatment the improvement of the V_{OC} can be mostly traced back to a shift of the main recombination channel away from the surface. To investigate the same for the in-situ treatment, temperature dependent current voltage measurements are carried out and the V_{OC} is extracted. The V_{OC} is plotted over the temperature for each sample in figure 3.7. A linear fit close to room temperature (275 °C to 315 °C) is extrapolated to 0 K to extract the activation energy of the main recombination channel.

For the untreated sample an activation energy of 0.64 eV is determined, showing that the device is limited by recombination close to the interface. The activation energy of the treated samples is greatly improved to values between 0.94 eV and 0.97 eV. The highest value is reached for the 4 min treatment. However, all determined values are below the bandgap of 0.995 eV. It should be noted here that this differs form the treatment with In-Se [19] in which the activation energy is increased to values above the bandgap. Nevertheless the clear improvement of E_{A}confirms that the main recombination channel is shifted away from the surface by the treatment. This removal of the recombination close to the interface will likely increase the V_{OC}.

The quasi Fermi level splitting measured on an absorber layer at 1 sun illumination gives an upper limited for the V_{OC} of the finished device. Although the V_{OC} in Cu-rich devices is much lower compared to Cu-poor devices (-100 mV), absorber layers passivated with CdS[3] of both compositions have been shown to have similar quasi Fermi level splitting

[3]The deposition of a CdS layer is needed to prevent the fast degradation of the luminescence signal determined on bare absorber layer [17].

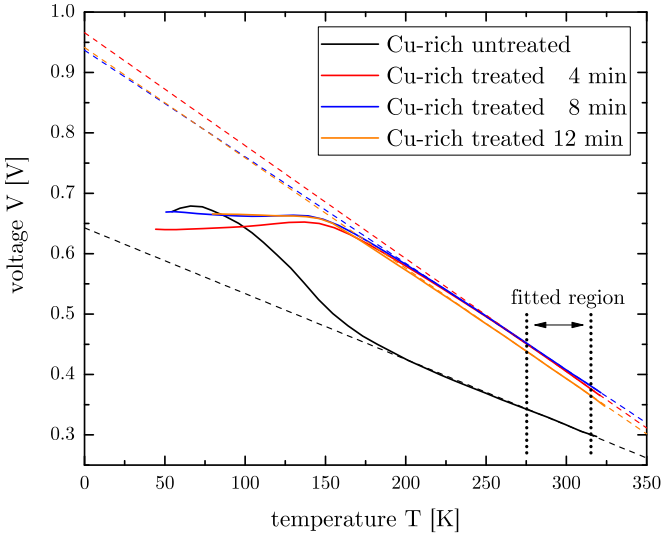

Figure 3.7: Open circuit voltage of the Cu-rich samples with and without treatment plotted over the temperature. The data is fitted linearly between 275 K and 315 K to determined the activation energy E_A of the main recombination channel.

values [17]. From those measurements and other findings [183], it was deduced that the finishing of the cell with the highly doped window layer leads to the recombination losses at the absorber interface.

To investigate in more detail how the treatment affects this upper limit of the V_{OC}, calibrated photoluminescence measurements are carried out from which the quasi Fermi level can be extracted as described in section 2.3.5. The measurements presented in the following are done on a second sample set, since no absorber piece of the sample series discussed so far with treatments of 4 min, 8 min and 12 min duration was covered with only CdS. This second sample set consist of a Cu-rich reference sample and a treated Cu-rich sample both covered with CdS. The KF treatment conditions of this sample are identical to sample presented with the 8 min long treatment. Overall the treatment of the new sample gave similar results as presented before, showing an increase in V_{OC} of 50 mV (343 mV to 393 mV). For the untreated reference sample, a quasi Fermi level splitting of 422 meV is determined and for the KF treated one a value of 441 meV. The gain in quasi Fermi level splitting shows that the treatment reduces non-radiative recombination even before the junction formation by the window layer deposition. Comparing the gain in V_{OC} and in quasi Fermi level splitting, it can thus be deduced that the improvement in V_{OC} observed is a combination of a better bulk (20 mV) and an improved interface (30 mV). The gain at the interface is likely related to the passivation of a 200 meV defect [32], [147].

Already anticipating results from section 3.2.3, it should be noted here that the gain in quasi Fermi level splitting of treated Cu-poor samples is with 20 meV (450 meV to 470 meV) in the same range as in Cu-rich samples. This shows that the treatments acts similar in the bulk for both compositions. However, the gain in V_{OC} is only about 22 mV revealing that only the bulk is improved. The interface does not benefit from the treatment because it is already good.

Investigation of the sample surface: SEM and low temperature PL

The shift of the recombination channel and the improvement in device performance show that the treatment changes the surface. Although no XPS measurements were carried out for this sample set, the change at the surface is still directly observable. After the KF treatment and rinsing with water a small piece of the sample is investigated by SEM together with a KCN etched reference sample. The images of the untreated sample (left) and of the 8 min treated sample (right) are shown in figure 3.8. Both samples show the facets of comparable larger crystals, but the treated sample also shows a distinguishable surface patterning. Although the patterning is not as pronounced as shown in some reports [159], [162], it is interpreted to be the structured surface layer with reduced copper content formed through the treatment. The patterning is less in the other treated samples but still visible, as shown in figure D.3.

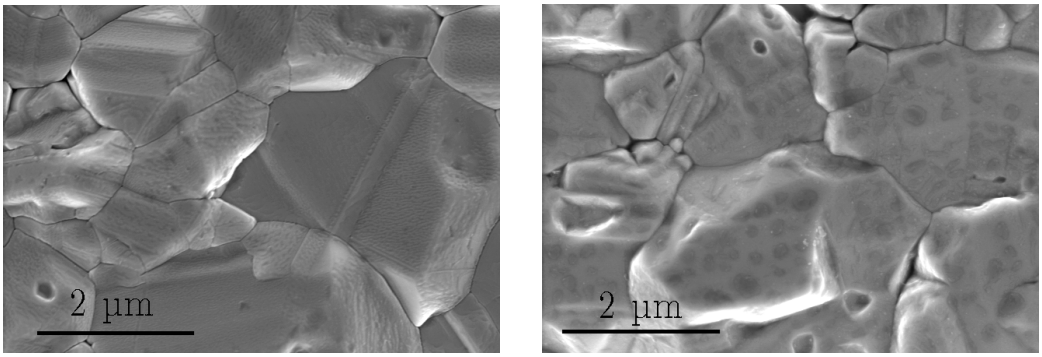

Figure 3.8: Scanning electron microscope image of a $CuInSe_2$ absorber layer grown under copper excess after KCN etching (left) and the sample absorber after 8 min long potassium fluoride treatment.

Low temperature photoluminescence measurements are a great way to investigate the electronic structure on semiconductors as described in section 2.3.3. Distinguishing Cu-rich and Cu-poor $CuInSe_2$ samples in low temperature photoluminescence measurements is simple, since the spectra of Cu-rich samples consist of several well defined peaks whereas the spectra of Cu-poor samples exhibit one broad asymmetric peak which is shifted towards lower energies [12], [15], [96]. In the past those features have been used to investigate the front and back of samples treated with In-Se, showing that the front had Cu-poor behaviour and the back side still had Cu-rich behaviour [19], [176]. The details about the characteristic fingerprints of both compositions are only described briefly in the following, but are discussed in more detail in chapter 4.

The following photoluminescence measurements are carried out at 10 K with several illumination intensities to investigate what happens to the surface after an in-situ KF treatment. The samples measured are bare absorbers and not covered with CdS, since this changes the electronic properties of the surface as shown in [78] and also discussed in section 4.4.2. The normalized photoluminescence spectrum of the untreated sample is shown in figure 3.9 (a). It shows the typical finger print of a Cu-rich sample grown under high copper excess ([Cu]/[In] > 1.3) [12], [15]. The main peak at 0.97 eV is the DA2 transition from a shallow donor (Cu_i or In_{Cu}) to the second shallow acceptor (Cu_{In}), as discussed in section 2.3.4. The peaks towards lower energies at 0.94 eV and 0.91 eV are phonon replica of the DA2-transition. The involved optical phonon is found to have an energy of 27 meV. A weak but distinguishable peak is found at 1.035 eV related to excitonic luminescence.

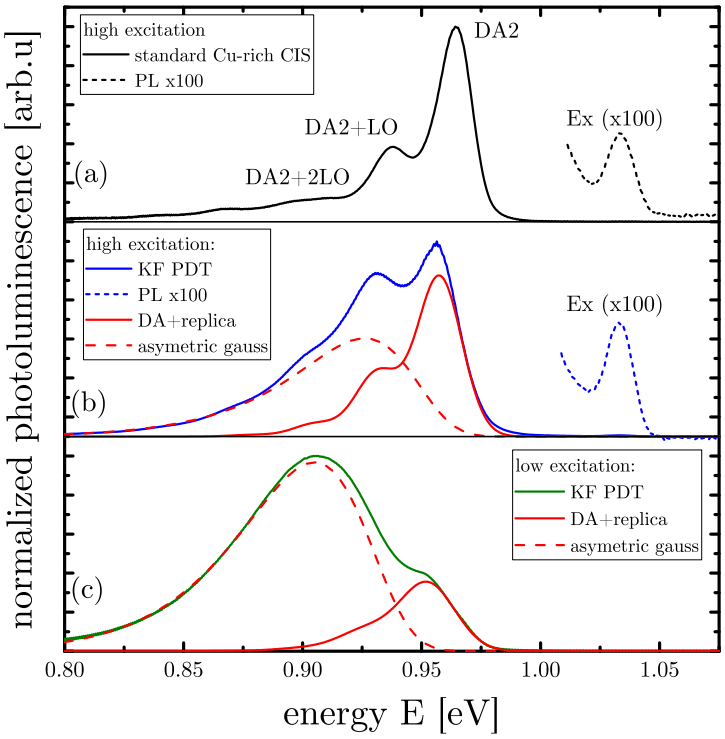

Figure 3.9: Photoluminescence spectra measured at 10 K of a Cu-rich reference sample (a) and an absorber layer with a KF treatment measured at high excitation (b) and low excitation (c). Included in (b) and (c) are red fitting functions depicting an asymmetric Gauss profile (dashed) and a donor-acceptor transition with phonon replica (solid). The luminescence signal at above 1.02 eV is magnified by a factor of 100 to increase the visibility of the excitonic luminescence.

The results of the different treatment durations are similar to each other. Because of this only the results of the sample with the 8 min long treatment will be discussed in the following. The normalized spectra of the treated sample are shown in figure 3.9 at low excitation (b) and at high excitation (c). At low excitation a broad asymmetric peak centered around 0.9 eV is detected. The peak position and the spectral shape fit well to the expected spectral shape of a Cu-poor sample which is broadened and red shifted by potential fluctuations. Also observable is a shoulder at 0.96 eV. This shoulder can be better understood looking at the spectrum at high excitation. The spectral shape differs here since the intensity of the possible transitions types changes differently with excitation.

At high excitation excitonic luminescence is observed at 1.035 eV and the shoulder at 0.96 eV developed into the main peak. The excitonic luminescence is a clear indication that at least part of the photoluminescence comes from a stoichiometric (Cu-rich grown) phase. Considering this, the peak at 0.96 eV is likely to be a DA-transition and the peak at 0.93 eV a phonon replica. Fitting the spectra with a broad asymmetric peak representing a Cu-poor phase and a DA-transition with phonon replica representing a stoichiometric phase works good over the three orders of magnitude shown here[4]. With increasing excitation the broad peak shifts with 14 meV/decade, agreeing well with the strong blue shift expected for the luminescence of a compensated (Cu-poor) material. The DA-transition exhibits a shift below 5 meV/decade agreeing with a DA-transition

[4]The fitting works also over 5 order of magnitude as shown in detail in section D.1 of the appendix for a Cu-rich sample with lower Cu-excess showing a DA1 transition.

in a weakly compensated material as Cu-rich $CuInSe_2$. The growth of both peaks with excitation differs leading a to change in spectral shape and is another indicator that two different transitions are observed. From this it can be deduced that the spectra observed are a superposition of luminescence from a copper poor surface and stoichiometric bulk.

The small shift in the peak position of 10 meV of the DA2 transition from the expected 0.97 eV to 0.96 eV can originate from several things and will discussed in more detail later. Using the absorption coefficient of the absorber taken from [42] for the used laser excitation (660 nm) the absorption profile inside the absorber can be estimated using Beer-Lambert laws. The absorption profile corresponds to the excitation profile of excess charge carriers. At the low temperature used during measurement it can be approximated that the generated carriers do not diffuse and that the recombination takes place at the same place as the excitation. Assuming that the photoluminescence yield of the Cu-poor phase is around 5x higher than the Cu-rich phase[5] and assuming that the integrated photoluminescence of both phases is roughly the same (which it is at high excitation), it can be estimated that the copper deficient layer is below 20 nm thick. This estimate is in agreement with literature values of a few nanometers [159] and the XPS results of the ex-situ treatment.

One more insight can be derived from the above findings. The copper deficient surface layer is commonly assumed to be formed by pushing the copper atoms from the surface into the absorber, slightly increasing the [Cu]/([Ga] + [In])-ratio in the bulk. The samples investigated here have a stoichiometric bulk which is saturated with copper atoms. Since no chalcopyrite phase with excess copper exists [38] (see also figure 2.2), no copper from the surface can diffuse into the absorber. From this consideration, it can be concluded that the new copper deficient surface layer forms by growth during the potassium treatment, combining the K and Se atoms supplied from the gas phase with In and Cu atoms from the absorber. This hypothesis is supported by the observation that in samples with longer treatment durations also the DA1 transition can be observed in low temperature photoluminescence measurements. In the DA1 transition the same donor is involved as in the DA2 transition, but a shallower acceptor A1 which originates from the copper vacancy (V_{Cu}). This means that for longer treatment durations more copper diffuses out of the stoichiometric bulk into the new layer.

Possible performance limitation

Treating Cu-rich absorbers with potassium leads to an improvement in V_{OC} by 60 mV to values up to 410 mV. However, this is still below the V_{OC} values reached with Cu-poor $CuInSe_2$ samples of above 450 mV (or even 490 mV [19]). A possible reason for this might be a deep defect. In figure 3.10 the photoluminescence spectra measured at room temperature of a reference sample and the earlier investigated samples with treatment duration of 4 min, 8 min and 12 min are plotted. The main peak observed at 1.02 eV fits to the band-band transition of a Cu-rich absorber layer. All treated samples show a broadening of this main peak towards lower energies which is likely related to the luminescence of the copper deficient surface layer since Cu-poor absorbers have an about 50 meV lower bandgap. This broadening is thus not worrisome.

However, all curves show a roughly 200 meV broad peak centered around 0.8 eV. This means that there is a defect state which is comparably deep in the bandgap to be not

[5] Investigating Cu-poor and Cu-rich $CuInSe_2$ at 10 K normally a 4x to 20x higher photoluminescence yield was observed for Cu-poor samples.

thermally emptied at room temperature. Furthermore, it has to be present in considerably large quantities, since otherwise it would not be ovservable. The high quantity and high activation energy of this defect level will much likely reduce the open circuit voltage, since it acts as a recombination center. The peak height of this defect transition remains unaffected by the treatment and will thus also after the treatment affect the maximal reachable V_{OC}. A possible origin of this defect transition will be later discussed in section 4.4.3 and it becomes also relevant in section 6.1.2.

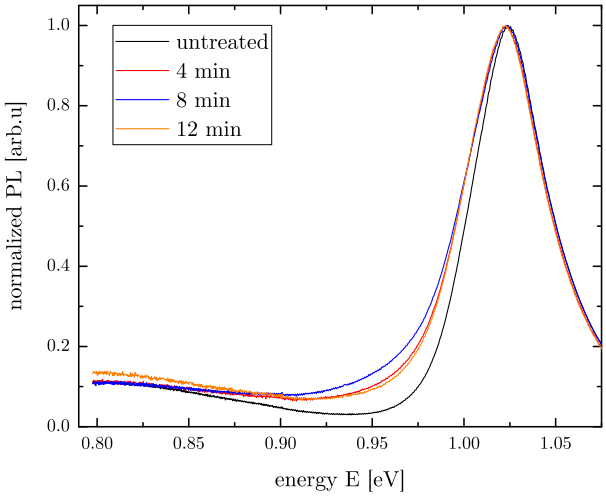

Figure 3.10: Normalized photoluminescence of an untreated Cu-rich $CuInSe_2$ sample and three samples with KF treatments with duration of 4 min, 8 min and 12 min measured at room temperature.

Investigation of the energy shift of the DA2 transition

A broad picture about what and how the KF treatment changes the absorber surface and the device parameters has been discussed on the basis of one sample series with different treatment durations. Discussing the low temperature photoluminescence characteristics of a treated sample, a shift of the DA2 transition from 0.97 eV to 0.96 eV was observed. Although this seem negligible at first glance it is actually observed on all treated samples. In the following also other sample sets are discussed with varying KF treatment conditions to examine this shift further.

The first data set consists of three samples grown in the same process but with different treatments. On the left side of figure 3.11 the photoluminescence spectra of three samples measured at 10 K with similar but comparably high excitation density are shown. The first sample is an untreated Cu-rich reference (black). On the second sample an in-situ KF treatment was applied with a duration of 6 min at 380 °C (blue). The third sample (red) was treated nearly the same. After growth it was etched and reintroduced to the growth chamber. There, it was annealed under selenium atmosphere using the same temperature and heating ramps but not KF was evaporated during the annealing. This process will be called Se treatment in the following.[6]

The reference sample shows all the known features of excitonic luminescence (1.035 eV), a DA1 transition visible as shoulder (0.99 eV), DA2 main peak (0.97 eV) + phonon replica

[6]This process improves the efficiency in a comparable way to the KF treatment. It removes a 200 meV defect and thus improves the surface recombination [147]. More details about the treatment and its effects can be found in [147], [172].

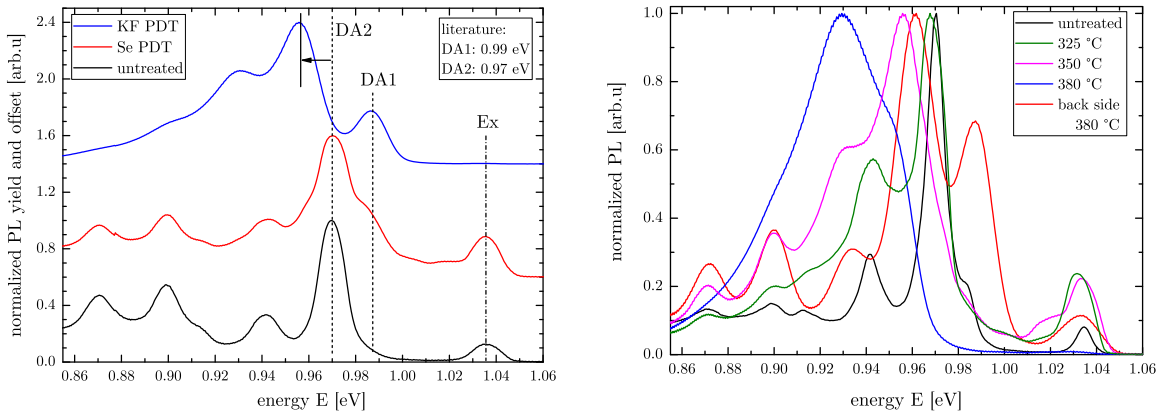

Figure 3.11: Left: Normalized photoluminescence measured at 10 K of an untreated Cu-rich $CuInSe_2$ sample (black), a sample with a Se treatment (red) and a sample with KF treatment (blue). For better visibility the curves are shifted upwards. Right: Normalized photoluminescence measured at 10 K of an untreated Cu-rich $CuInSe_2$ sample (black) and three samples with KF treatments with temperatures of 325 °C, 350 °C and 380 °C. The last sample was additionally physically lifted of the substrate and measured from the backside.

(0.94 eV). Besides this two further peaks at 0.90 eV and 0.87 eV are observed which will be neglected for now but are discussed in detail in chapter 4. Looking at the red curve similar characteristics are observed. The excitonic luminescence is at the same position and even a second excitonic peak at 1.02 eV is observable corresponding to "M6" in [184]. The DA1 peak is now the main peak which is related to the KCN etching removing copper from the surface (see also section 4.4.1). The DA2 transition and its phonon replica are observed and do not shift in energy. The KF treated sample (blue) shows the same features as the other samples. However, the DA2 transition and its replica are shifted towards lower energies as observed previously. The Cu-poor surface layer discussed previously and observed in figure 3.9 (c) is hardly visible due to the high excitation used.

After etching and Se treatment, the different transitions remain unchanged in energetic position and also the intensities do not change much, except for the DA1 transition. This shows that the defect properties stay the same and that likely no defect is related to additional selenium. Looking at the KF treated sample, it can be seen that only the DA2 transition is shifted in energy. Since the exciton does not shift, a change in bandgap can be excluded as a reason for the shift of the DA2. Also the introduction or release of strain can be excluded as it would effect all transitions. The same donor is involved in the DA1 and the DA2 transition which can thus also be assumed to be unchanged. All those findings indicate that the introduction of K to the absorber bulk changes the defect energy of the second acceptor defect A2 which is related to the Cu_{In}-antisite defect.

More information about the shift of the DA2 can be gathered from another sample series, in which the treatment duration was constant (12 min) and the temperature was varied between 325 °C, 350 °C and 380 °C. The normalized photoluminescence spectra measured at 10 K are plotted on the right side of figure 3.11. The reference (black) shows the known fingerprints like exciton, DA1 and DA2 plus replica. The blue curve represents the sample treated at 380 °C and is thus very close to the conditions investigated previously in figure 3.9. A broad asymmetric peak at 0.93 eV is observed which is attributed to the Cu-poor surface layer. The shoulder at 0.95 eV originates from the energetically shifted

DA2 transition of the underlying stoichiometric phase. The existence of the stoichiometric phase is confirmed by the excitonic luminescence which can be seen in logarithmic scale.

Looking at the pink curve (350 °C) it can be seen that the DA2 transition is the main peak and shifted in energy. However, at this temperature the signal from the Cu-poor phase is much lower indicating that this temperature might not be sufficient to form the Cu-poor phase in sufficient quantities. For even lower temperature (325 °C), the DA2 is hardly shifted and the spectrum is similar to the reference besides a considerable broadening of all peaks. This temperature is thus not enough to form the Cu-poor surface and also too low to induce the energy shift of the DA2 transition.

The red curve depicts a measurement from the backside of the sample treated at 380 °C. For this measurement the absorber is physically lifted off the molybdenum back contact with the help of epoxy glue. The spectrum exhibits excitonic luminescence and the DA1 transition at the energy expected from literature [15]. However, the DA2 transition and its phonon replica are shifted, showing that the influence of the potassium is not only at the front but through out the absorber layer.

From those two measurement series, several things can be concluded. The shift of the DA2 transition towards lower energies by 10 meV to 15 meV is not an effect of excitation density or compensation. Since only the DA2 is shifted but not the exciton or the DA1, a change of the involved acceptor A2 (Cu_{In}) is proposed as the origin of the energy shift. The shift only appears when potassium is available during the annealing and also only if the temperature is high enough to incorporate it. At the temperature used for the treatments investigated before the shift is also detected at the backside of the absorber indicating that the whole bulk is changed by the treatment. This findings are the fist measurements indicating a change of the defect spectrum related with the alkali treatment. The exact nature of the shift in defect energy of the A2 (60 meV $\rightarrow \sim$70 meV) remains unknown. It is speculated to be related to K_{In}.

3.2.3 Investigation of Cu-poor $CuInSe_2$ with KF PDT

Several effects and improvements have been observed by the treatment of Cu-rich absorber layers with the in-situ KF treatment with etching step. However, as a proof of concept the process also has to work on Cu-poor samples. Overall a similar process window is determined and a sample treated for 6 min at a temperature of 380 °C will be discussed in the following.

The current voltage characteristics of an exemplary solar cell of the reference sample and the treated sample in the dark and under illumination are shown on the left side of figure 3.12. Averaging six cells, an improvement of the V_{OC} by 22 mV (445 mV → 467 mV) is determined. The gain in V_{OC} is lower to values reached in literature on $Cu(In,Ga)Se_2$ of roughly 50 meV [26], [171] which might be related to the non optimized process or the usage of $CuInSe_2$. The fill factor improves by a few percent (64.0 % → 68.3 %) mainly due to an improved diode factor which is also observed in literature [26]. Similar to all treated samples before, the J_{SC} reduce slightly (41.3 mA cm^{-2} → 40.8 mA cm^{-2}). Shunt and parallel resistance remain within error unchanged. Overall, the efficiency increases on average from 11.8 % to 13.0 %. The loss in J_{SC} can be explained by a drop in the low wavelength region of external quantum efficiency measurements shown on the right side of figure 3.12. The drop is less pronounced compared to the one observed for the Cu-rich treated samples. To determine the thickness of the CdS layer, a corner of the finished absorbers is split off and the cross section investigated by SEM (see figure D.2 on page D.2). A CdS thickness of (34 ± 3) nm is determined for the reference sample and (43 ± 2) nm for the treated sample. The lower drop in EQE can thus be explained by a less pronounced gain in CdS thickness compared to the Cu-rich samples (34 nm → 48 nm).

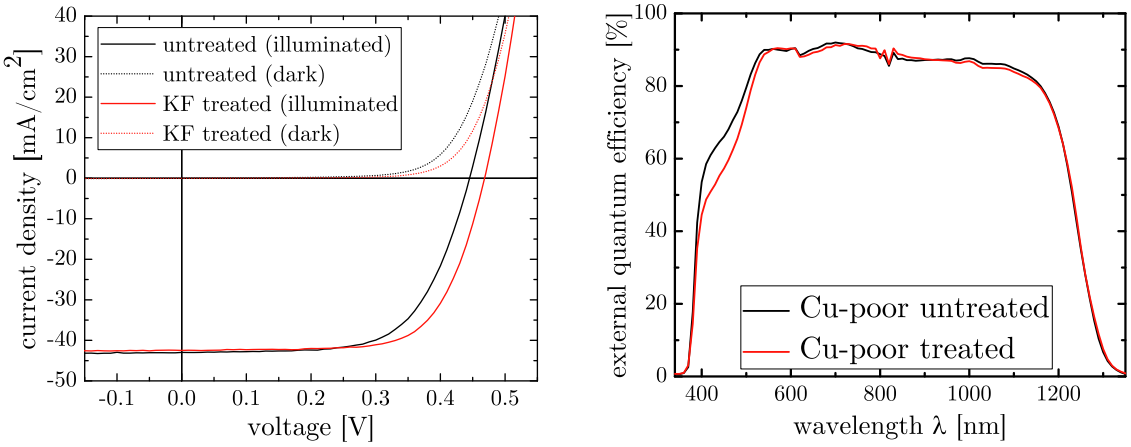

Figure 3.12: Left: Current voltage curves in the dark and illuminated of a Cu-poor $CuInSe_2$ sample with (red) and without (black) 6 min long KF treatment. Right: External quantum efficiency measurements of the same samples.

Hardly any differences between the two samples are observed measuring the current voltage curves temperature dependent. By extrapolating the V_{OC} to 0 K for both samples, the same activation energy of 1.02 eV is determined, as shown on the left in figure 3.13. Those values indicate that both samples are dominated by bulk recombination. For both samples capacitance measurements are carried out and plotted in a Mott-Schottky plot on the right side in figure 3.13. The apparent doping is determined in forward bias as indicated by the vertical lines and in the same region as on the Cu-rich samples. A small increase of the apparent doping from 1.3×10^{-16} cm^3 to 1.5×10^{-16} cm^3 is measured which

is within the error of the method. However, an increase of the apparent doping is seen on all treated Cu-poor samples. It is thus argued that the treatment slightly increases the apparent doping.

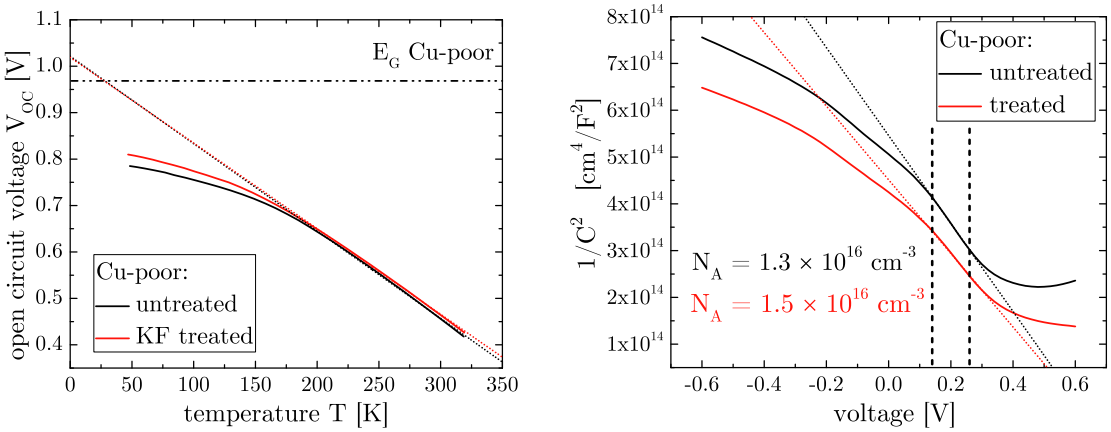

Figure 3.13: Left: Open circuit voltage plotted over the temperature for a Cu-poor $CuInSe_2$ sample with (red) and without (black) KF treatment. Right: Capacitance voltage measurements of the same sample. The vertical dashed lines indicate the region fitted for the extraction of the apparent doping.

The evaluation of low temperature photoluminescence spectra is hampered by the fact that they are strongly distorted by interference fringes. The determination of a peak shape or shifts with excitation is thus not possible and no conclusions can be drawn. However, the high energy side of the photoluminescence spectra used for the determination of the quasi Fermi level splitting are not distorted. From calibrated photoluminescence measurements on a CdS covered reference samples and a CdS covered sample with KF treatment, a gain of 20 meV is determined, as already briefly mentioned in the discussion of the Cu-rich samples. This gain is similar to the gain in V_{OC} and is thus interpreted as an improvement of the bulk properties.

Overall, the treatment can also be used for $CuInSe_2$ samples with a Cu-poor composition leading to improvements in most IV parameters. However, the gain in V_{OC} of 20 meV is lower to values reached in literature on $Cu(In,Ga)Se_2$ of up to 50 meV [26], [171] but this might be related to a not fully optimized process, to the usage of $CuInSe_2$ instead $Cu(In,Ga)Se_2$ as an absorber material or to the air exposure during the treatment routine.

3.3 Summary potassium fluoride treatments

Two different process routes for a KF treatment including an etching step have been presented. In the ex-situ process the deposition of KF and the annealing is done in two separate steps whereas during the in-situ process both steps are done simultaneously. Both routines improve the V_{OC} for Cu-rich and Cu-poor $CuInSe_2$ samples when the treatment is done under selenium atmosphere for 4 to 20 min and temperatures between 320 °C and 400 °C. The many effects that the treatment has onto the absorber properties can be divided into changes within the bulk and changes at the sample surface.

Changes of the bulk

The in-situ treatment with etching step leads to an improvement of the quasi Fermi level splitting measured on passivated absorbers of roughly 20 meV independent of the composition used. This gain originates from a reduced non radiative recombination rate in the bulk, which is likely linked to the incorporation of potassium throughout the whole absorber layer and not only at the surface. A newly found shift in the activation energy of the second acceptor defect (Cu_{In}) is observed at the front as well as on the backside of the treated absorber layer. This finding of the potassium distribution is in line with recent findings detecting rubidium throughout the absorber after the treatment [169]. The gain in quasi Fermi level splitting, which is an upper limit of the open circuit voltage, is identical with the gain in V_{OC} in case of Cu-poor samples meaning that all the gain in voltage is related to a improvement of the bulk. The surface does not benefit from the treatment since it is already good.

Changes at the surface

The treatment leads to a patterned surface layer which from XPS and photoluminescence can be attributed to be copper deficient and below 10 nm thick. This finding is in line with literature observation on Cu-poor samples [25], [159]. Since the copper deficient layer is also observed on Cu-rich samples, it can be deduced that this layer forms by growth and not in-diffusion of copper. In case of Cu-rich samples, the treatment removes a 200 meV deep defect [147] and shifts the main recombination channel away from the surface and more into the bulk. This removal of recombination at the surface explains the higher gain in V_{OC} of ~ 55 mV compared to the gain in quasi Fermi level splitting of 20 meV. For Cu-rich samples the bulk and the surface are improved.

The treatment of Cu-rich absorbers with potassium fluoride has been successfully implemented leading to efficiency gains of more than 2 % absolute. The developed in-situ treatment with etching steps also improves Cu-poor samples proofing the validity of the treatment approach. By comparing the effects on Cu-rich an Cu-poor samples, it was found that the treatment works similar on both compositions, although they exhibit different electronic properties.

CHAPTER

FOUR

IS THERE A THIRD ACCEPTOR IN CI(G)S?

Over the past decades a comprehensive model about intrinsic defects emerged from experiments and theoretical calculations (see section 2.3.4). Besides the verified acceptors V_{Cu} and Cu_{In} as well as donors In_{Cu} and Cu_i, the question of a third acceptor or of the defect level of the selenium vacancy V_{Se} are still under debate. Cathodoluminescence measurements [31] and spatially resolved photoluminescence measurements [30] in $CuGaSe_2$ showed that a peak 1.58 eV is a superposition of a phonon replica of the DA2 transition and another donor acceptor pair transition, likely from the known shallow donor into a third acceptor with an activation energy of 130 meV. Based on this, a third acceptor was also postulated for $CuInSe_2$, but no evidence was found in favor of a third DA-transition at 0.94 eV in epitaxial or polycrystalline $CuInSe_2$ [32] by spatially resolved photoluminescence measurements. However, in the investigated polycrystalline Cu-rich $CuInSe_2$ samples grown with high selenium overpressure another peak is found at 0.9 eV in low temperature photoluminescence measurements. This chapter will deal with the question what kind of transition is observed at 0.9 eV and if the same transition exists in $Cu(In,Ga)Se_2$. Furthermore, a possible link between photoluminescence and admittance measurements will be examined. Moreover, the effect of different surface alteration, which improve the photoluminescence yield, on the low temperature photoluminescence characteristics are investigated. Those measurements facilitate the investigation defect transitions at lower energies with an extended set up. Large parts of the shown results are also published in [32].

4.1 Characteristics of the 0.9 eV peak in $CuInSe_2$

The photoluminescence spectrum of a $CuInSe_2$ grown under high copper excess and high selenium excess during growth at 10 K is depicted in figure 4.1. The transitions described in literature of the exciton (Ex) at 1.035 eV and the donor acceptor pair transition (DA2) at 0.97 eV as well as its phonon replica at about 0.94 eV are detected. The first donor acceptor pair transition (DA1) at 0.99 eV is not observed because of the high copper flux during growth that suppresses the formation of the related A1 defect. Additionally to the known transitions, four clearly distinguishable peaks below 0.91 eV are measured (labeled #1 to #4). The relative intensity of those peak decreases towards lower energies. Moreover a rather broad peak at 1.005 eV is observed, which is likely a bound exciton as shown in [142]. To identify the transition type involved in peaks #1 to #4, excitation and temperature dependent measurements are carried out.

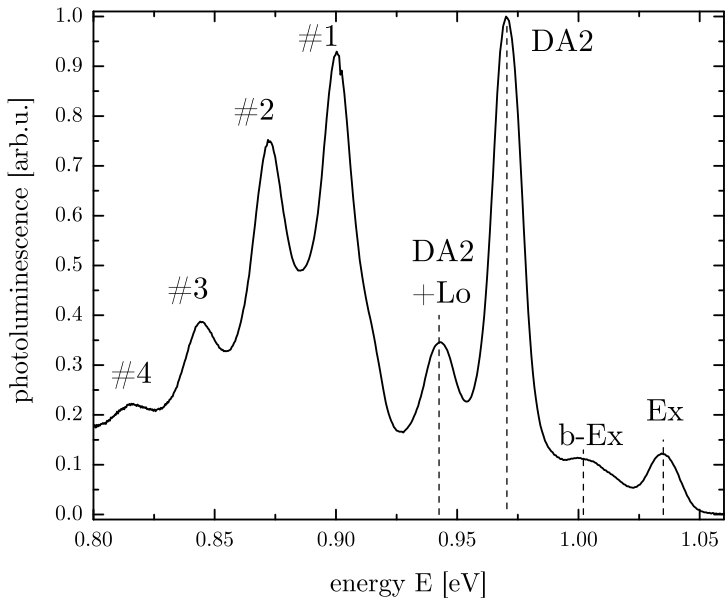

Figure 4.1: Photoluminescence spectra of a polycrystalline $CuInSe_2$ samples grown under high copper excess measured at 10 K.

4.1.1 Excitation dependency

Photoluminescence spectra are recorded at various illumination conditions over the range of two orders of magnitude to distinguish between the different transitions, as described in section 2.3.3. The various peaks are fitted with a Gaussian profile each and the peak position as well as the photoluminescence intensity (area of the Gaussian profile) are determined. The photoluminescence intensity is plotted double-logarithmically over the excitation in figure 4.2 and fitted linearly to extract the power law exponent k according to equation (2.24), which is determined by the linear slope. The k-value for peak #4 to #1 are similar and about 0.75, see table 4.1. The k-value for the DA2 transition and its phonon replica are also similar to each other and are around 0.83. As discussed in section 2.3.3, a k-value below 1 is expected for a free-bound transition or a donor-acceptor pair transition, when fitted in a limited range of 1 or 2 orders of magnitude as done here. For larger fitting areas a shift from 1 to 1/2 would be expected [115]. For excitons a slope between 2 and 1 is expected depending on the excitation density. With a k-value of 1.1, both excitonic peaks are within this range.

In figure 4.2 the peak position of the three main peaks are plotted semi-logarithmically over the excitation density. The other peaks are not plotted to increase the visibility of the low shift with excitation. Although not plotted, peak #4 shows no shift with excitation (β), likely due to a high background at 0.8 eV. The peaks #3, #2 and #1 show all a similar blue shift with excitation of 0.42 meV/decade. The blue shift of the DA2 transition and its phonon replica are comparable to each other and with 0.9 meV/decade about twice as high. Both values are really low even compared to reported values of epitaxial samples [15], [29] showing the low degree of compensation and the good crystal quality. The bound exciton shows no shift, whereas the exciton shows a clear blue shift of 1.1 meV/decade. In this energy region several excitons (bound excitons at 1.005 eV, 1.017 eV, 1.028 eV, 1.034 eV, 1.036 eV, 1.038 eV and free excitons at 1.042 eV and 1.045 eV) have been observed on single crystals [102], [184], [185]. Since excitons do not shift with excitation density, the observed shift is interpreted as the shift from one exciton to another one [186]. This

interpretation also explains the rather broad peak of the excitonic luminescence, which is expected to be narrower than the defect related transitions. The full set of extracted k-values and β-values is shown in table 4.1.

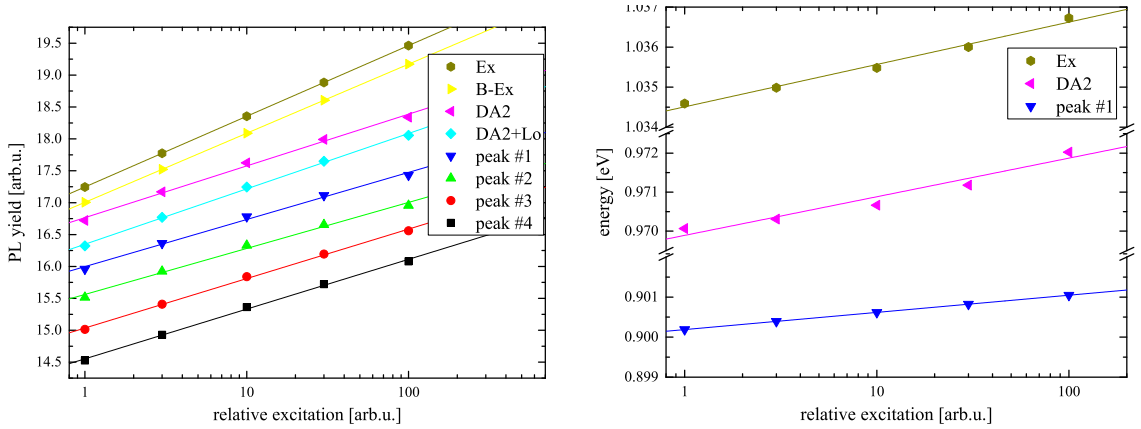

Figure 4.2: Left: Logarithm of the photoluminescence intensity of various transitions of a $CuInSe_2$ absorber plotted logarithmically over the excitation density for the extraction of the k-value. Right: Peak position of selected transitions of a $CuInSe_2$ absorber plotted semi-logarithmically over the excitation density.

Table 4.1: Peak position, k-value and β-value for the different transition observed in a polycrystalline $CuInSe_2$ sample gown under high copper excess.

peak	#4	#3	#2	#1
position [eV]	0.816	0.844	0.873	0.900
k-value	0.80 ± 0.02	0.78 ± 0.02	0.72 ± 0.03	0.74 ± 0.03
β [meV/decade]	0.00 ± 0.05	0.39 ± 0.05	0.43 ± 0.09	0.43 ± 0.05

peak	DA2+Lo	DA2	Bound-Exciton	Exciton
position [eV]	0.942	0.970	1.000	1.035
k-value	0.86 ± 0.02	0.82 ± 0.03	1.08 ± 0.01	1.11 ± 0.01
β [meV/decade]	0.78 ± 0.05	0.99 ± 0.12	0.00 ± 0.05	1.06 ± 0.06

The peaks #4, #3 and #2 show the same behaviour with excitation as peak #1 and are likely phonon replica of peak #1. The energy of the involved phonon determined from the distance between the peaks is 28 meV and in agreement with the energy distance seen in the phonon replica of the DA2 transition. To corroborate the assignment of the different peaks to transitions, the spectrum is fitted as a whole. The two excitonic emissions are described by two independent Gaussian functions. The DA2 transition and its phonon replica are fitted according to known line shape of emissions with phonon interaction [100], as also described in section 2.3.2. This means that the main peak at 0.97 eV is fitted in terms of amplitude and peak width. A second Gaussian profile with the same width is shifted to lower energies by the energy of the involved phonon and the peak amplitude is scaled by the Huang-Rhys factor, as described in equation (2.20). A third Gaussian profile has the same width, is shifted by 2x the energy of the involved phonon and is scaled in amplitude by the same Huang-Rhys factor again. In the used model each zero

phonon line (main peak) has 4 replica peaks. Peak #1 is fitted in the same way as the DA2. Peak width, amplitude and Huang-Rhys factor of peak #1 are independent from the DA2 transition but they share the same phonon energy. To get a good fit below 0.86 eV another broad peak at 0.8 eV has to be added. Evidence that there is such a peak and a possible origin will be discussed later in section 4.4. Fitting the deep luminescence only the amplitude is taken as a free parameter whereas values of the peak position and the width are taken from the measurements shown in section 4.4.

The different emissions and a sum of the fit is shown in figure 4.3. The fitting confirms the derived energy of the involved phonon of 28 meV. For the DA2 transition a Huang-Rhys factor of 0.35 is derived. Both values agree well with literature values of 27 meV to 29 meV and 0.30 ± 0.05 [117], [186]–[188]. For peak #1 a higher Huang-Rhys factor of 0.75 is found, showing a stronger coupling to the lattice than the DA2 transition. Taking those findings into account, it can be concluded that peak #1 and its phonon replica come from a distinct defect level and are related to free-bound transition or a donor-acceptor pair transition.

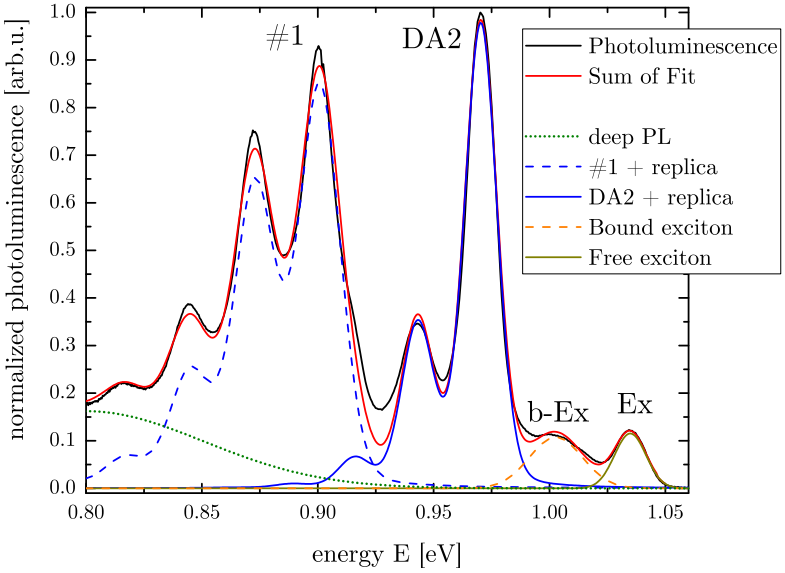

Figure 4.3: Same photoluminescence spectrum of a $CuInSe_2$ samples measured at 10 K as in figure 4.2 fitted with Gaussian functions. For the DA2 and peak#1 the known lineshape for transition with phonon interactions is used.

4.1.2 Evaluation of the activation energy

To gather more information about the transition, temperature dependent measurements under constant illumination are carried out. The recorded spectra are plotted semi-logarithmically in figure 4.4 showing that all transitions quench with increasing temperature. The excitonic peaks vanishes first, as expected due to the small binding energy of the electron hole pairs. The DA2 transitions shows a slower quenching and peak #1 an even slower quenching. All spectra are fitted as a whole as shown previously in figure 4.3 with amplitude, width and peak position as free fitting parameter but with the Huang-Rhys factor and phonon energy fixed to the previously found values. From the model the peak position of each transition as well as the photoluminescence intensity of the main transitions is extracted. For the evaluation of the photoluminescence intensity, the area of

the Gaussian functions is taken and not the amplitude to account for peak broadening with increasing temperature. The quenching model described in [22], [96] (equation (2.22)) is used for the determination of the activation energy of the involved defects, as described in section 2.3.3.

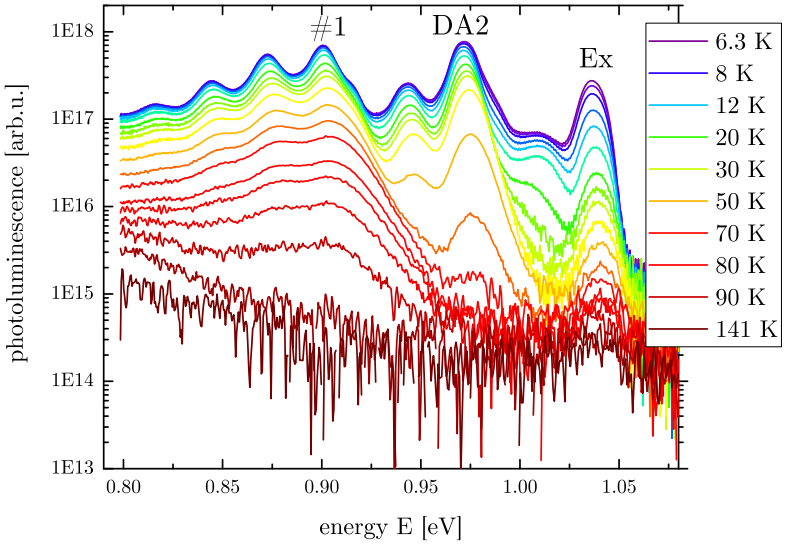

Figure 4.4: Temperature dependent photoluminescence measurements between 6 K and 140 K of a $CuInSe_2$ sample grown under high Cu excess and a high selenium flux. The legend shows only every other temperature used.

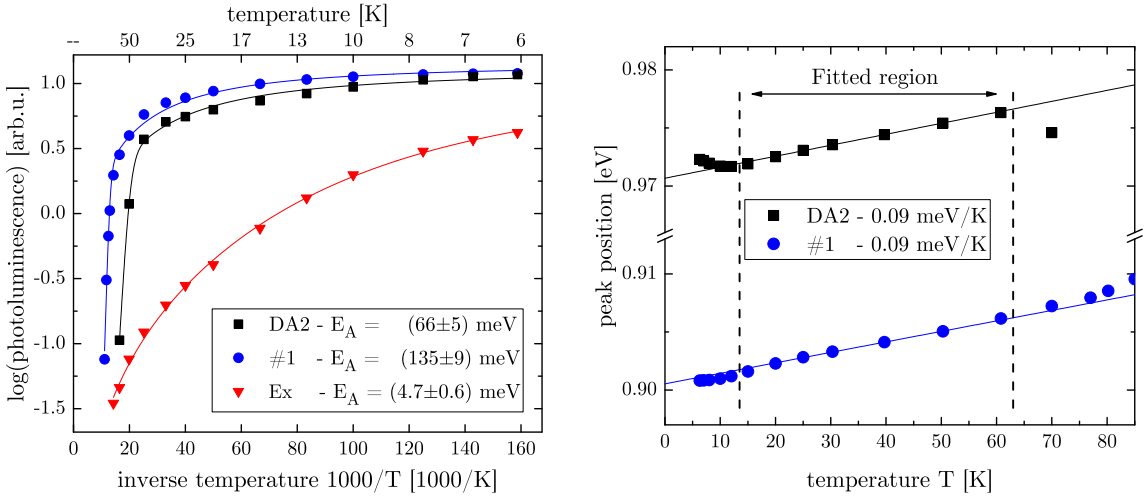

Figure 4.5: Left: Semi-logarithmic plot of the photoluminescence intensity over the inverse temperature for the extraction of the activation energy E_A of DA2 transition (black), peak #1 (blue) and the excitonic luminescence (red). Right: Peak position of peak #1 (black) and DA2 transition (blue) plotted over the temperature.

To fit the quenching, the photoluminescence intensity is plotted semi-logarithmically over the inverse temperature (1000/K) in figure 4.5. Fitting the excitonic luminescence an activation energy of about 5 meV is determined, agreeing to literature values [28], [29], [184]. Fitting the DA2 transition a shallow defect below 8 meV is found and a deeper defect with (66 ± 4) meV. The initial drop of photoluminescence intensity with increasing temperature is due to the thermal depletion of the shallow shallow donor involved in the

DA2 transition. The fitted value for the shallow acceptor of about 66 meV is in good agreement with literature values [15]. For peak #1 a similar shallow defect is found and a higher activation energy of (135 ± 9) meV at higher temperatures for the deeper defect. Plotting the peak position of both the DA2 transition and peak #1 over the temperature, as done in figure 4.5, it is observed that both show the same small blue shift of $0.09\,\mathrm{meV\,K^{-1}}$ (or $1.05 \cdot k_B$). This blue shift fits to the expected small blue shift of a donor-acceptor-pair transition [22], [117] and is higher than the shift of $1/2 \cdot k_\mathrm{B}$ expected for a free-bound-transition (see also table 2.1 p. 33). The blue shift can be interpreted as as the shift from a donor-acceptor pair transition into a free-bound transition from the conduction band to the respective acceptor [15]. Since both transition exhibit the same shift it can be concluded that both transition involve the same shallow donor. From all this data, it is concluded that peak #1 is a donor-acceptor pair transition from the known shallow donor D into a third acceptor A3 and will be called DA3 in the following.

4.1.3 Influence of the growth conditions

To check the influence of the copper excess, several polycrystalline samples are grown varying the copper flux and with a constant high selenium flux. Similar to the previous chapter, illumination and temperature dependent photoluminescence measurement are carried out. The peak position of the DA3 transition remains unchanged with Cu-excess and no clear trend is observed for the relative peak height between the DA3 and the DA2 transition. From the temperature dependent measurements the activation energy of all main transitions are evaluated and shown in table 4.2 for different growth conditions (See figure D.5 and figure D.6 in the appendix for spectra and evaluation). Since the DA1 is only clearly observed in samples grown close to stoichiometry, the activation energy is only determined for one sample.

The found activation energies of the DA1 and DA2 transition fit really well to literature values [15]. The activation energy of the DA2 and DA3 transition scatter a bit in between samples. This is due to the high influence of the data points at high temperatures onto the fitting routine. Small variation here lead to strong changes in the determined activation energy. As a rough estimate the DA3 transition has an activation energy determined from temperature dependent photoluminescence measurements of (130 ± 15) meV. Another way to determined the activation energy of a transition is to measure the energetic distance between the main peak and the excitonic luminescence. This is possible since the exciton and the donor involved in the DA-transitions have a really similar activation energy [15]. The energetic difference between exciton and DA3 of (135 ± 10) meV agrees well in between samples and also agrees with the activation energy from the quenching model. It is thus concluded that the copper excess does not change the defect energy and has no clear effect on the formation likelihood of the defect.

To investigate the influence of the selenium flux, samples grown with various selenium over pressures are investigated. In low temperature photoluminescence measurements the peak height of the DA3 and the DA2 transitions were determined, but no trend is found between the selenium flux and the peak intensities. A trend though is found between old $CuInSe_2$ absorber layers and those deposited recently (within the past 3 years). The old samples show no or low contribution of the DA3 transition in low temperature photoluminescence measurements. The same 1-stage process, as described in section 2.4.2, was used, with the same temperature changes during the co-evaporation of the elements. The only difference is temperature of the cracking head of the valved selenium source. In

Table 4.2: Comparison of the extracted activation energies for various transition in Cu-Rich $CuInSe_2$ layers grown under different copper excess.

		ΔE	PL(T)		
	[Cu]/[In]	DA3	DA3	DA2	DA1
		[meV]	[meV]	[meV]	[meV]
Low Cu-excess	1.0 ± 0.2	138 ± 6	125 ± 7	61 ± 8	46 ± 3
Mid Cu-excess	1.4 ± 0.2	135 ± 4	135 ± 9	66 ± 5	/
High Cu-excess	1.8 ± 0.2	137 ± 5	127 ± 20	56 ± 8	/

the recently made samples it was heated up to 1000 °C whereas earlier the cracking head would be only heated up to 600 °C. The higher temperature is used to split up the most likely gaseous species of Se_6 into smaller clusters to enhance the reactivity [132], [133].

Because of this it is argued that the selenium species and the selenium overpressure has a strong influence on the formation likelihood of the third acceptor. It is likely that this is the reason why it is seen in some samples but not all, depending on the preparation conditions. Additionally to the samples investigated here grown by co-evaporation, the defect transition has been observed in selenized precursor layers [117] and on single crystals annealed in the presence of excess selenium [28]. But it has not been detected on some co-evaporated samples and on epitaxial samples [15], [29]. A reason for the latter could lie in the growth process, where atoms are deposited on the absorber surface when process gases decompose inside the fabrication reactor above certain temperatures. When the target thickness is reached at the end of a fabrication process, the flow of the precursor gases is stopped and the sample is passively cooled down from the growth temperature which is in the range of 500 °C to 600 °C. During this cooling, selenium is probably lost from the sample, because of the high vapour pressure of selenium [135], [136] and since no selenium is supplied (as compared to the growth processes where the DA3 is observed).

From comparison to theoretical calculation, it should be speculated which point defect or defect complex could be the origin of the third acceptor. An overview about recent defect calculations using the screened-exchange hybrid density functional theory of Heyd, Scuseria and Ernzerhof (HSE06) [50]–[54], [189] can be found in Chapter 7 of [101] and in [122]. The calculations agree with experiments on the two known shallow acceptors V_{Cu} and Cu_{In}, although the latter one is with 150 meV to 220 meV normally calculated deeper than found in experiment 60 meV. It should be noted here that the defect levels from calculation are normally given with an error of about 50 meV. Also the activation energy of two known donors Cu_i and In_{Cu} are calculated in agreement with experiment.

Looking into the calculation and looking for an acceptor type defect, there are only few possible candidates. Pohl and Albe [50] calculated V_{Se} as a shallow acceptor, but the formation energy increases from Se-poor to Se-rich conditions contradicting with the observation made for the DA3 which shows the opposite. Furthermore, the defect is also proposed to show metastable properties and might be not detectable in photoluminescence measurements due to this, as discussed in section 2.3.4. Another possible acceptor, the selenium interstitial is not taken into consideration because of its high formation energy (2.5 eV in Cu-poor and >3.2 eV for Cu-rich growth conditions).

A further acceptor defect is the indium vacancy V_{In}, which first charge transition (0/-1) is calculated to be shallow or resonant with the valence band and which second charge transition (-1/-2) is mostly calculated to be a deep acceptor 350 meV to 700 meV [122].

Although the formation energy is comparably high (2.0 eV), it does decrease for Cu-rich condition from low selenium excess to high selenium excess, making the formation more likely and following the observed trend in the experimental findings. It is argued by Pohl and Albe [50] that this defect could occur in case of the right growth conditions despite the high formation energy.

Another possible origin could a defect complex as discussed by Malitckaya et al. [54]. Of the three complexes discussed in [54], the one formed by a copper interstitial Cu_i together with a copper on indium antisite Cu_{In} has the lowest formation energy. However, it is only an acceptor type defect for n-type materials, which is not the case for the here investigated samples. A second complex formed by Cu_i and V_{In}, is an acceptor type defect in p-type material, but has a higher formation energy than V_{In} alone. Because of this it is unlikely that the A3 is related to this complex. The third complex made of Cu_i and 2 V_{Cu} has a low binding energy but it is plausible that it exists because of the high concentration of constituents.This complex is thus the only potential complex candidate for the A3 defect.

Nevertheless, from the current state of knowledge, the indium vacancy V_{In} is proposed as the origin of the third acceptor defect. This attribution is base on the trend of the appearance of the DA3 peak with Se supply and due to the reason that the proposed complex should be also visible in epitaxial samples.

4.2 Comparison to Cu(In,Ga)Se_2

The DA1 transition exist over the whole range of solid solution of Cu(In,Ga)Se_2 [29] (likely also the DA2 transition). To check the same for the newly found DA3, the growth process of the Cu(In,Ga)Se_2 absorbers was adjusted to promote the presence of the DA3, meaning high selenium overpressure and the cracking head heated to 1000 °C. In comparison to the previously analysed $CuInSe_2$ samples grown by a 1-stage process (section 2.4.2), the Cu(In,Ga)Se_2 samples were grown by a 3-stage process (section 2.4.3). The samples grown by this process exhibit a lower variation of the lateral thickness and a lower surface roughness. The combination of both leads to interference effects that distort the photoluminescence spectra especially at low energies [190], [191] and prohibit a quantitative analysis of the data. The first section will thus deal with the detection and removal of those interference effects. Afterwards the low temperature photoluminescence spectrum of a $CuInSe_2$ sample and a Cu(In,Ga)Se_2 samples with a low amount of gallium are compared. Finally a wider range of samples with gallium content up to 0.45 are investigated.

4.2.1 Influence and removal of interference

The grown Cu(In,Ga)Se_2 samples have a low surface roughness and tend to show interference effects. Those can be detected by reflection measurements as shown in red in figure 4.6. To change the reflectivity of the surface and remove the interference effects a scattering layer is added to the surface of the absorber as shown in [192]. The reflectivity of a sample with interference effects before and after deposition of the scattering layer is shown in figure 4.6. After deposition the reflectivity is increased, but the variation is reduced by a factor of three and and the energetic distance between extrema widened from 80 meV to 200 meV.

The photoluminescence spectrum before the deposition (black) has three distinct peaks at low energies (0.84 eV, 0.90 eV, 0.96 eV), corresponding to minima in the reflectance

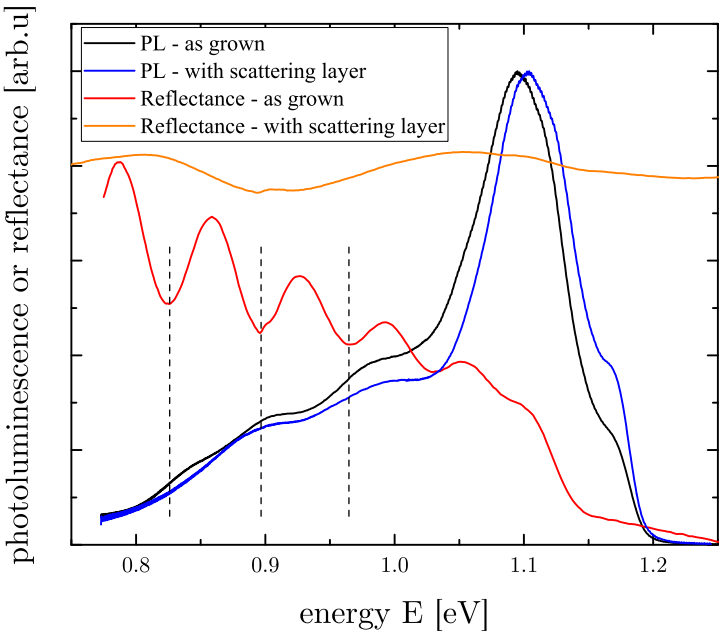

Figure 4.6: Reflectance and low temperature photoluminescence measurement of a Cu(In,Ga)Se$_2$ sample before and after the deposition of a scattering layer.

measurement (red) as indicated by the vertical dashed lines. With a scattering layer on top (blue) only two peaks are visible at 0.9 eV and 1.0 eV. Therefore the interpretation of the measurement data from samples without the addition of a scattering layer would have been incorrect. All Cu(In,Ga)Se$_2$ samples investigated in the next two sub-chapters are thus covered with such a layer to avoid wrong interpretations.

4.2.2 Low gallium concentration

The photoluminescence spectra of a CuInSe$_2$ sample and a Cu(In,Ga)Se$_2$ sample with a low amount of gallium ([Ga]/([Ga] + [In])≈ 0.08) at low temperature are shown in figure 4.7. Both spectra exhibit the same features only shifted in energy. Furthermore, all peaks are broadened in the Cu(In,Ga)Se$_2$ sample. The broadening stems from local variations of the indium and gallium atoms on the cation sub-lattice. This statistical distribution leads to local bandgap fluctuations which do not exist in the ternaries CuInSe$_2$ and CuGaSe$_2$ and are the strongest for a GGI of 0.5.

To identify the different peaks, intensity dependent measurements are carried out for the Cu(In,Ga)Se$_2$ sample. The peak at 1.075 eV shows a power law exponent of about 1.1 and a shift of 1.4 meV/decade, making it likely that the peak originates from an excitonic transition. The peak at 1.005 eV has an exponent of 0.7 and a shift of 1.3 meV/decade. In logarithmic scale also another transition can be seen as a shoulder at 1.02 eV. From the energy difference, the peak position and the intensity dependance it is concluded that the main peak originates from the DA2 transition and the shoulder from the DA1 transition.

The peak at 0.93 eV shows similar intensity dependance as the DA2 peak (exponent of 0.6 and shift 1.2 meV/decade). It is likely that this peak originates from the DA3 transition and that the peak at lower energies are phonon replicas. Fitting the whole spectrum with the known line shape for DA-transition and their replicas as shown in figure 4.3, it is possible to determine the Huang-Rhys factor of the transitions. For both the DA2 (0.4) and the DA3 (0.78) they are within error the same as in CuInSe$_2$, also confirming

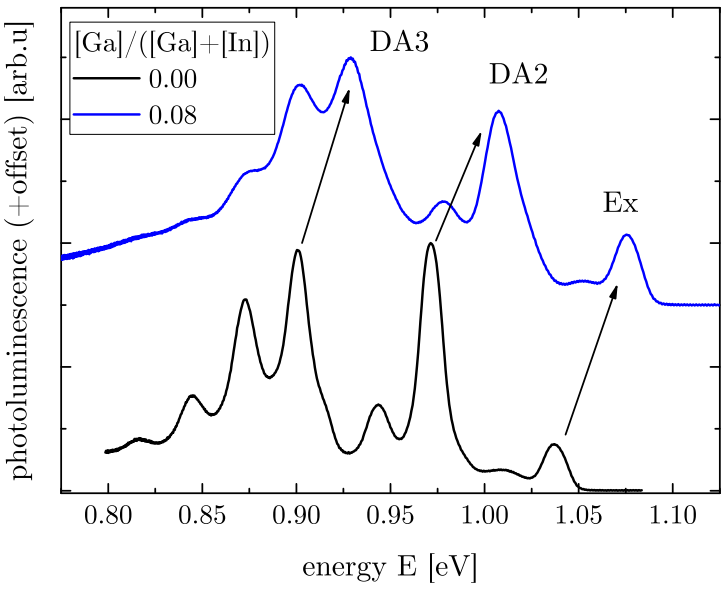

Figure 4.7: Photoluminescence at 10 K of a $CuInSe_2$ sample and a $Cu(In,Ga)Se_2$ sample with low gallium content.

the attribution of the different peaks to the respective transition. This measurement shows that the DA3 exists also in $Cu(In,Ga)Se_2$ and that it shifts together with the other DA-transitions to higher energies with increasing gallium content.

4.2.3 Various gallium content

To investigate the shift of the DA3 transition, samples with various gallium content are grown with similar copper excess. The recorded low temperature photoluminescence spectra are plotted in figure 4.8. It is observed that all peaks shift with the addition of gallium and the broadening increases further. From intensity dependent measurements the peak at high energies marked with vertical dashed lines, is identified as excitonic luminescence. The presence of it in all samples indicates the good crystal structure of the $Cu(In,Ga)Se_2$ samples. Due to the broadening of the peaks it is complicated to distinguish between the DA1 and DA2 transition for GGI values above 0.3 . The peak of the DA3 transition reduces relative in intensity to the DA1 and DA2 transition but is observable in all samples. The position of the DA3 is sketched with the dotted purple line. For GGI values above 0.1 a second peak peak at low energies is detected. The second deep peak is difficult to spot in the linear plot, but clearly observable in the semi-logarithmic plot on the right side of figure 4.8 showing the three samples with the highest GGI. Since interference effects can be excluded and the peak is detected in all samples, it is assumed that two independent transition are observed at low energies.

All spectra are fitted as a whole with Gaussian profiles and the known line shape for the phonon replicas [100] as in figure 4.3. The extracted positions of the respective peaks are plotted over the position of the excitonic luminescence in figure 4.9. The energetic position of the excitonic luminescence is chosen as the x-axis value since it is a good indicator for the local GGI of the probed sample, whereas the values determined by EDX (energy dispersive X-ray spectroscopy) are averaged over a bigger area and have a larger error. For comparison the data of a $CuGaSe_2$ sample is added, taken from reference [14]. All peaks shift towards higher energies with the addition of gallium. A linear fit through

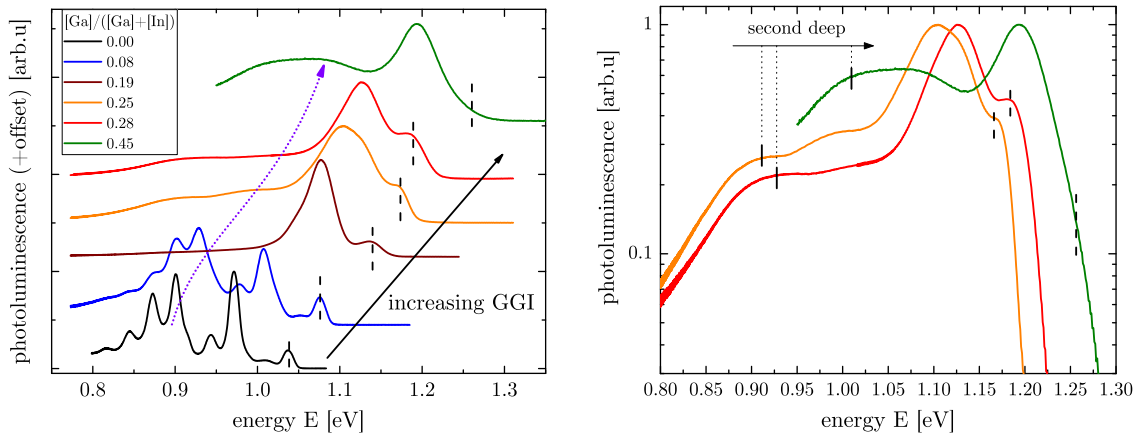

Figure 4.8: Left: Photoluminescence at 10 K of Cu(In,Ga)Se$_2$ samples with various gallium contents. The black dashed lines indicate the position of the excitonic luminescence. The dotted purple line indicates the position of the DA3 transition. Right: Semi-logarithmic plot of selected curves.

the data points of the DA1 and DA2 transition yields a good fit over the whole GGI range, indicating that also the DA2 transition shifts monotonic over the whole compositional range. The shift of the DA3 transition to higher energies with the addition of gallium is weaker compared to the DA1 transition and DA2 transition, increasing its activation energy and moving it deeper into the bandgap. For the second deep peak, the opposite trend is measured. It shifts stronger with gallium content, moving it closer to the main transitions DA1 and DA2. If those trends continue for both transitions, they will presumably merge together and will be not distinguishable anymore for GGI values between 0.5 (1.35 eV) and 0.9 (1.63 eV).

The DA3 is proposed to originate from the V_{In} point defect in $CuInSe_2$ and Cu(In,Ga)Se$_2$. For Cu(In,Ga)Se$_2$ it would be straight forward to discuss the second deep peak as the gallium vacancy (V_{Ga}). But indium and gallium share the same position in the lattice of Cu(In,Ga)Se$_2$ and are known to be without any order. Whether an indium or gallium atom is missing, does not play a role and the related defect is V_{III}, which energetic defect level is defined by the next neighboring group III atoms (indium and gallium). There are 5 possible configurations of In and Ga around a vacancy (4xIn, 3xIn and 1xGa, 2xIn and 2xGa, 1xIn and 3xGa, 4xGa). With increasing gallium content the most likely configuration presumably change more or less linear, leading to one broad transition (due to statistical variation of the configuration as well as bandgap fluctuations) that shifts with increasing Ga content. This would also explain the stronger broadening of the DA3 transition compared to the DA1 and DA2 transition. From this considerations it can be excluded that the second peak is related to the III vacancy. The origin of the second deep peak and its nature remains unknown, but is speculated to be related to a defect complex [54].

Added in figure 4.9 is also a DA-transition found in $CuGaSe_2$ by spatially resolved low temperature photoluminescence [30] as well as by cathodoluminescence [31]. In the case of photoluminescence, a peak at 1.58 eV was detected, which intensity is uncorrelated with the intensity of the DA2 transition at 1.62 eV. The measurements were done on epitaxial samples grown close to stoichiometry with low copper excess. For samples with higher copper excess, in which the DA2 transition is dominating, the third DA3 could not ambiguously identified. It is argued in in the work of Larsen [30], that the DA3 is either

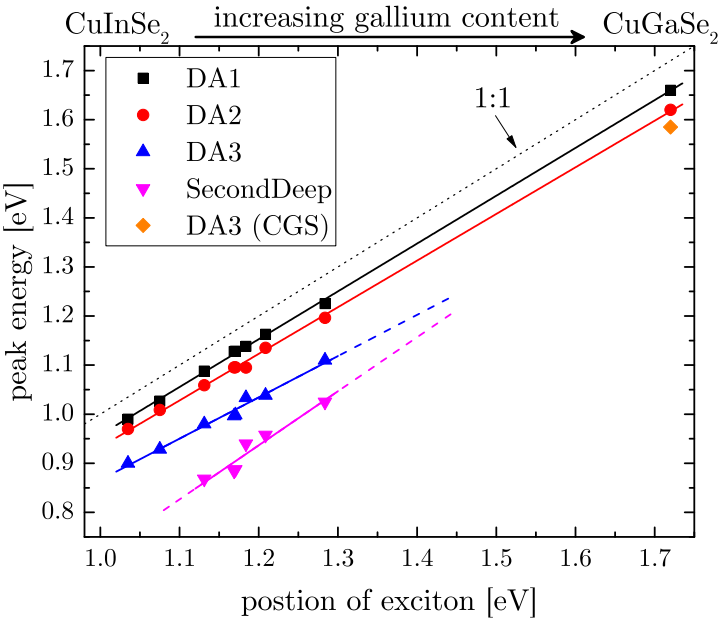

Figure 4.9: Peak position of the different transitions observed in Cu(In,Ga)Se_2 with various GGI plotted over the peak position of the exciton as a measure of gallium content. The data for $CuGaSe_2$ is taken from reference[14]. The solid lines depict linear fits through the data. The dashed lines estimate the peak shift of the two peaks at low energies with high gallium content.

not observed or super imposed with a phonon replica of the DA2 transition, which has the same energetic position for samples with higher copper excess. Meaning that this third acceptor state in $CuGaSe_2$ only exist in a very limited range of preparation conditions. The DA3 found here in $CuInSe_2$, however exist over a wide range of [Cu]/[In]-ratios in polycrystalline samples as shown in section 4.1.3 as well as singly crystals [28] and samples selenized after precursor sputtering [117]. Furthermore, extrapolating the found activation energy of the DA3 to an exciton energy of 1.7 eV, yields an activation energy of above 200 meV and is thus much larger than the 130 meV determined for the DA3(CGS) [30]. From this consideration, it is speculated that the origin of the third acceptor A3 found in $CuInSe_2$ and Cu(In,Ga)Se_2 is different from the defect involved in the third acceptor in $CuGaSe_2$.

4.3 Comparison to admittance measurements

Beside low temperature photoluminescence measurements also other methods can be used to probe the electronic defect structure of semiconductor layers. For finished devices or Schottky contacts, capacitance measurements at various temperatures and various frequencies can be used to get more insights about electronic defects or barriers. Since admittance is not one of the main characterization techniques used for sample analysis within the manuscript, the approach for the measurement technique and the evaluation of the data will only be described briefly. Before continuing it should be made clear that all admittance measurements are carried out and evaluated by Hossam Elanzeery and are not my own effort. An overview about this method is given by Heath and Zabierowski [59].

The previously investigated Cu(In,Ga)Se_2 samples are etched and an aluminum layer

is deposited to form a Schottky contact. A typical admittance spectrum is plotted semi-logarithmically on the left side of figure 4.10. The spectra are dominated by one capacitance step. By taking the derivative, the inflection points (marked by the black dots) are determined. On the right side of figure 4.10 the inflection frequencies are plotted in an Arrhenius plot. From the slope of the linear fit, the apparent activation energy is determined. The $CuInSe_2$ samples are annealed under selenium atmosphere before the deposition of the front contact to remove a defect close to the surface, possibly caused by the strong potassium cyanide etching [147], [148]. This defect has an activation energy of 200 meV and would otherwise dominate the admittance spectrum.

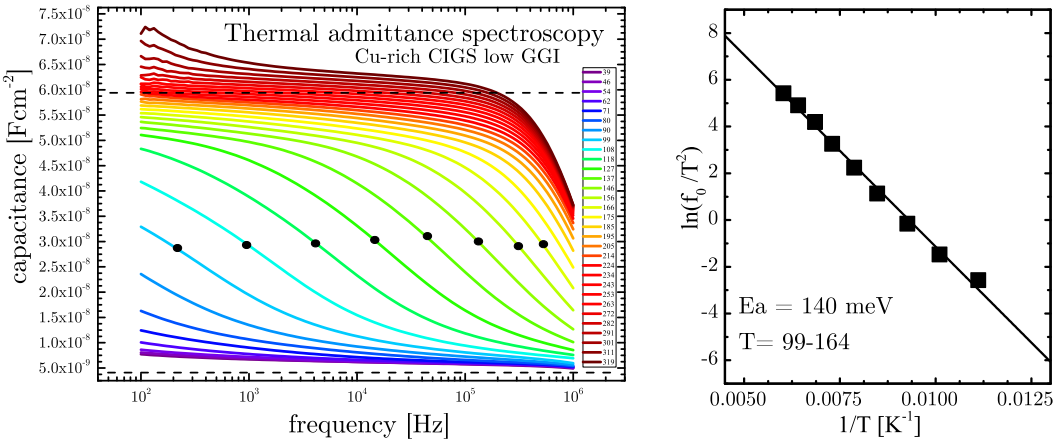

Figure 4.10: Left: Capacitance plotted semi-logarithmically over the frequency for temperatures from 40 K to 320 K. The black circles mark the inflection point of the main step. Left: Arrhenius plot of the inflections points and linear fit for the extraction of the activation energy.

In figure 4.11 the activation energies of the three acceptor levels A1, A2 and A3 found by low temperature photoluminescence measurements and the activation energy of the main step of admittance measurements are plotted over the energetic position of the respective excitonic luminescence. For $CuInSe_2$, an activation energy of 125 meV is extracted in admittance measurements, agreeing within error with the 135 meV activation energy of the A3 defect. Both methods give similar values and show the same trend for low gallium contents. Therefore it is concluded that the same defect is observed in photoluminescence and admittance measurements, linking optical and electrical measurement techniques. For GGI values above 0.15 the values from admittance decrease, whereas the values from photoluminescence keep increasing. The drop in admittance is presumably, due to the reason that the defect moves too deep into the bandgap and does not dominate the capacitance measurements anymore. The admittance is then dominated by the shallower defects and moves close to the activation energy of the second acceptor A2.

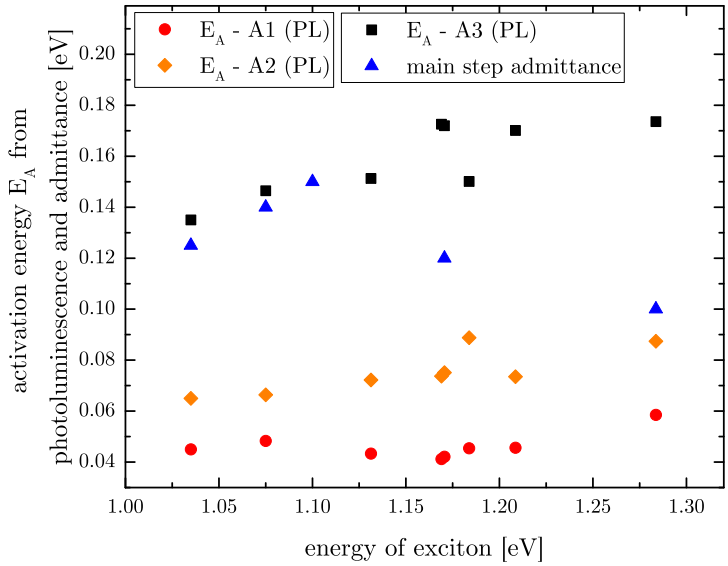

Figure 4.11: Activation energy of the three acceptor defects A1, A2 and A3 from photoluminescence measurements at 10 K as well as the activation energy of the main capacitance step from admittance measurements plotted over the energy position of the excitonic luminescence.

4.4 Effect of surface modification on low temperature photoluminescence spectra and deep luminescence

Epitaxial and polycrystalline $CuInSe_2$ samples are known to degrade in ambient air and under illumination as shown by Regesch et al. [17]. Similar effects are observed in polycrystalline $Cu(In,Ga)Se_2$ samples as shown in section 6.1. This degradation increases the surface recombination velocity and with this the non-radiative recombination. This leads to a decrease of the radiative recombination, meaning that the overall photoluminescence yield drops. Since it is not feasible to measure all samples directly after growth, etching in aqueous KCN solution is used to remove oxides from the surface before measurement or the absorber layers are covered with a thin CdS layer. Both methods normally do not change the shape of photoluminescence spectra measured at room temperature. However, this does not prove that the absorber is not changed. To check if the defect structure changes, photoluminescence spectra before and after the surface modification are measured. In the end the found findings are used to interpret measurements towards low energies ($<$0.8 eV) and to check for deep luminescence.

4.4.1 Effect of potassium cyanide etching

A $CuInSe_2$ absorber layer grown with a final composition of [Cu]/[In] of 1.3, which corresponds to the standard Cu-Rich process used, is once measured at 10 K after growth with the Cu_xSe secondary phase still on the absorber surface and once measured after etching in KCN (10 %, 5 minutes). The spectra measured under similar illumination conditions are shown in figure 4.12. The spectrum of the as grown sample (black) shows the known characteristics of a sample grown under high copper excess consisting of some excitonic luminescence, a dominating DA2 transition as well as the DA3 transition with their phonon replica. After etching, the spectrum (blue) changes quite a bit. The DA1

transition barely seen before becomes the dominant peak. The DA2 transition is still observed together with its phonon replica. The DA3 transition is still visible but the peak intensity relative to the DA2 transition strongly decreased. The excitonic luminescence remains nearly unchanged. In both spectra, the luminescence signal at the detection edge of 0.8 eV does not drop to zero.

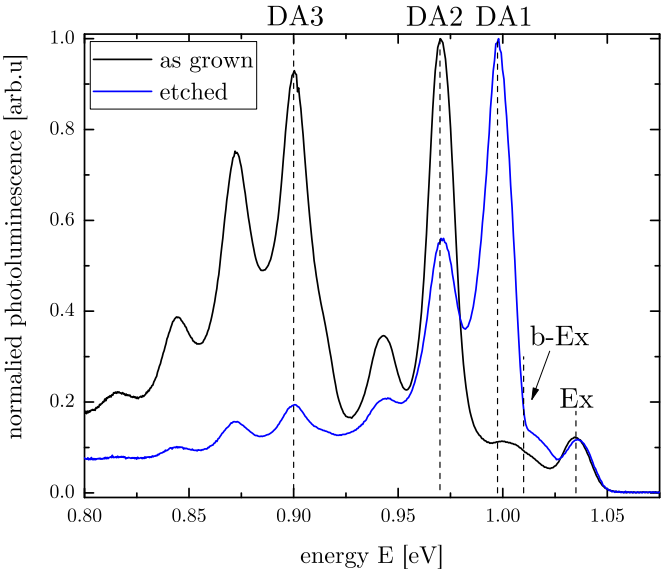

Figure 4.12: Photoluminescence spectra measured at 10 K of a $CuInSe_2$ sample grown with moderate copper excess measured "as grown" (black) and after KCN etching (blue).

It is not possible to conclude from the relative peak heights onto the absolute defect concentration. However, from the clear increase of the DA1 transition it can be assumed that the concentration of copper vacancies V_{Cu}, the responsible point defect of the A1, increased. Hashimoto et al. [82] reported that the copper content of Cu-rich samples at the surface (<9 nm) is reduced after KCN etching, whereas it is stoichiometric in the bulk. Additionally it can be calculated that most charge carriers are excited within the first 65 nm in the photoluminescence experiment. Combining these findings, the strong increase of the DA1 transition can be explained by the removal of Cu from the surface by the etching and by the emission of the detected luminescence from near the surface.

4.4.2 Effect of CdS deposition

A way to passivate the surface against oxidation and preserve the room temperature photoluminescence signal (the quasi Fermi level splitting) is to deposit a thin CdS layer on top of the absorber layer, as it is done during devices processing described in section 2.2.2. This passivates the surface for polycrystalline $CuInSe_2$ samples [17] as well as $Cu(In,Ga)Se_2$ [193] as also shown later in section 6.1. Before the CdS deposition, all samples are commonly etched to remove the Cu_xSe layer and residual oxides. This leads to the changes in the low temperature photoluminescence spectra described before, like the gain in DA1 in samples grown under copper excess. The $CuInSe_2$ sample discussed earlier (see figure 4.12) is covered with CdS and measured intensity dependent at 10 K. The normalized spectra measured over six orders of magnitude excitation are plotted on the left side of figure 4.13. The measurement down to low excitation densities like (OD4, 1mW) is possible due to the strongly enhanced photoluminescence signal. For a broad range of excitation densities only one broad asymmetric peak is observed which differs from the multiple defined peaks before. This peak shows a strong blue shift with excitation (β) of above 14 meV/decade (compared to <1 meV/decade of the defined peaks of the sample before CdS deposition). Only for very high excitation densities (that also heat up the sample above 40 K) excitonic luminescence dominates the spectrum and the DA1 and DA2 are observable. In logarithmic scale also the DA3 transition can be seen.

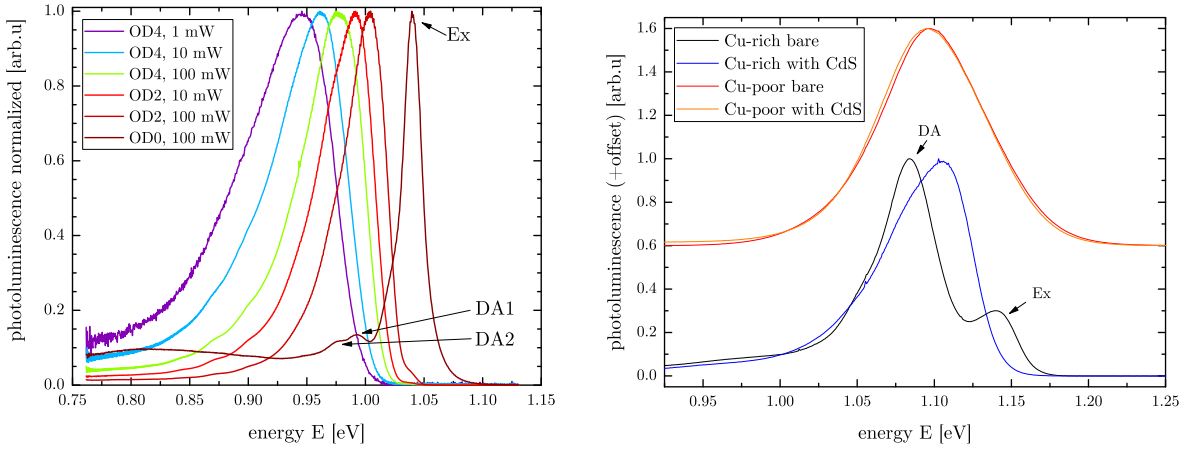

Figure 4.13: Left: Normalized low temperature photoluminescence spectra with various excitation densities of a Cu-rich grown $CuInSe_2$ absorber after KCN etch and CdS deposition plotted over the energy. Right: Low temperature photoluminescence spectra of a $Cu(In,Ga)Se_2$ samples as grown and after etching plus CdS deposition for a Cu-rich sample and Cu-poor sample (+0.6 offset) with similar GGI.

The broadening of the peak and the strong blue shift are typical signatures of potential fluctuations, as described in section 2.3.3. They are commonly observed in samples with Cu-poor composition. Those potential fluctuations occur when the a significant amount of donors is introduced into the originally strongly p-type doped absorber layer. The compensation of donors and acceptors leads to strong local electrostatic fluctuations [14], [96] and reduces the net doping as well. The donor type defects are possibly related to the in-diffusion of cadmium into the absorber layer. Abou-Ras et al. [194] showed that there is no abrupt interface between the absorber layer but instead an intermixing of buffer and absorber layer over a width of about 40 nm. Atom probe tomography measurements also show an intermixing at the interface, but to a smaller extend (5 nm) [195]. The similar

ionic radius of Cd^{+2} (0.97 Å) and of Cu^{+} (0.96 Å) [196] make it likely that Cd diffuses onto the copper vacancies formed by KCN etching. The Cd on Cu antisite is assumed to be a shallow donor [197]. Also recent Hall measurements show the change of the apparent doping after CdS deposition [78]. The interface region dominated by potential fluctuations stretches likely below a few 10 nm into absorber. However, this is also the region where most of the excess charge carrier are generated in the photoluminescence experiment. Combining this two findings with the low mobility of the free carriers at 10 K [120], [198], [199] impeding a diffusion into absorber, can explain the potential fluctuations observed in the photoluminescence spectra. In the shown photoluminescence measurements, it is only possible with very high excitation to screen part of the potential fluctuations and see the underlying properties of the Cu-rich bulk. Possibly due to the increase temperature and thus higher charge carrier mobility.

On the right side of figure 4.13 the photoluminescence spectra of a Cu-poor and a Cu-rich Cu(In,Ga)Se_2 sample are plotted as grown and after KCN etching + CdS deposition. Before CdS deposition the Cu-rich samples shows excitonic luminescence as well as a main peak consisting of the DA1 and DA2 transition. After CdS deposition, the sample only shows one asymmetric peak, as already seen in $CuInSe_2$. The shift of the main peak with excitation increases form below 4 meV/decade to above 10 meV/decade. Peak shape and shift with excitation indicate again the introduction of potential fluctuations. The behaviour for Cu-rich $CuInSe_2$ and Cu-rich Cu(In,Ga)Se_2 are similar in this regard. In contrast, the deposition of CdS has no influence on the peak shape or position in case of the Cu-poor sample. This can be explained by the fact that already before etching and CdS deposition the luminescence is defined by potential fluctuations due to the high degree of compensation [14], [200]. After CdS deposition β increases slightly, but since the sample is already highly compensated the addition of CdS only has a small effect. Low temperature measurements of samples grown under Cu-excess and covered with CdS should thus be treated carefully.

4.4.3 Deep luminescence in $CuInSe_2$

The low temperature measurements of $CuInSe_2$ samples grown under copper excess presented in the previous chapters always exhibit a photoluminescence signal at 0.8 eV which is higher than the noise level. To check if there is another transition at this energy or if this signal is a measurement artifact, measurements towards lower energies are needed. For this purpose detectors with narrow bandgaps have to be used. Unfortunately with decreasing bandgap the inherent signal-to-noise ratio decreases drastically. To measure down to low energies a well luminescent sample and high laser powers are need. An extended InGaAs detector array with a bandgap of 0.56 eV was used to measure an etched $CuInSe_2$ absorber. In figure 4.14 on the left side the photoluminescence spectra measured with the same excitation density by the extended detector (black) and by the standard detector (InGaAs $E_G \approx 0.78$ eV) in blue are plotted semi-logarithmically over the energy.

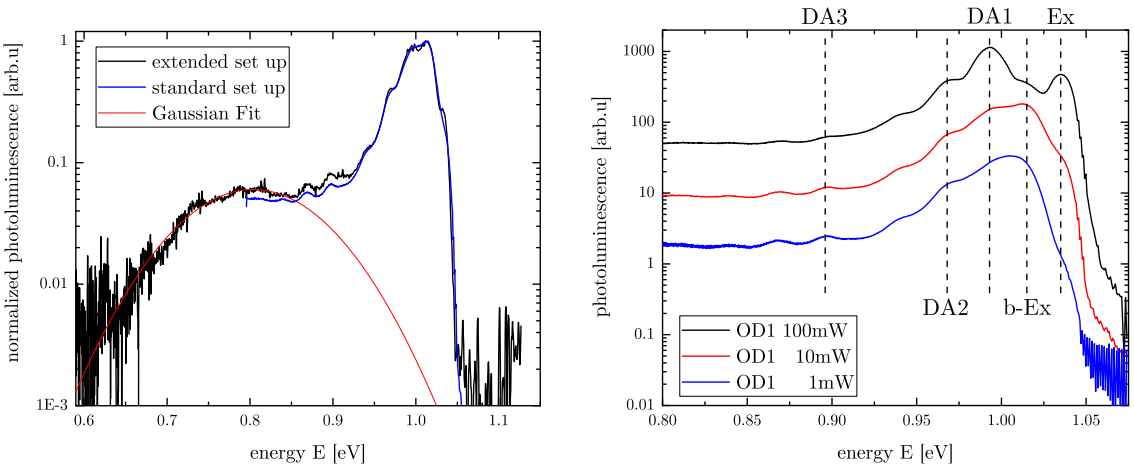

Figure 4.14: Left: Photoluminescence spectra measured at 10 K of a $CuInSe_2$ sample after KCN etching with the standard set up (black) and with the extended InGaAs detector (blue) in linear scale. Right: Illumination dependent measurement of the same sample with the standard set up.

Both curves agree over the whole range supporting the proper calibration of both set ups. In the high energy range distinct peaks at 1.035 eV, 1.01 eV, 0.99 eV, 0.97 eV, 0.94 eV and 0.9 eV are observed, related to the known excitonic transitions and donor-acceptor pair transitions plus replica. After etching, the bound exciton at 1.01 eV is the dominant peak for certain illumination conditions in this sample, as can be seen by illumination dependent measurements on the right side in figure 4.14.

Besides the know peaks, the extended spectra also exhibits a broad peak centered at 0.8 eV with a peak width of about 190 meV. This peak is likely related to the second charge transition of the Cu_{In} antisite defect, which first charge transition is the acceptor type defect of the DA2 transition [101]. It is observed in almost all polycrystalline $CuInSe_2$ grown under copper excess studied during during this work. The peak position and width known from these measurements are used to improve the fitting done in section 4.1.1 and section 4.1.2.

4.5 Summary and new defect picture

The defect model derived over the last decades for Cu(In,Ga)Se_2 chalcogenides, was extended by the measurements presented in this chapter. Figure 4.16 shows an overview of defect model for Cu(In_{1-x}, Ga_x)Se_2, based on Rega et al. [29].

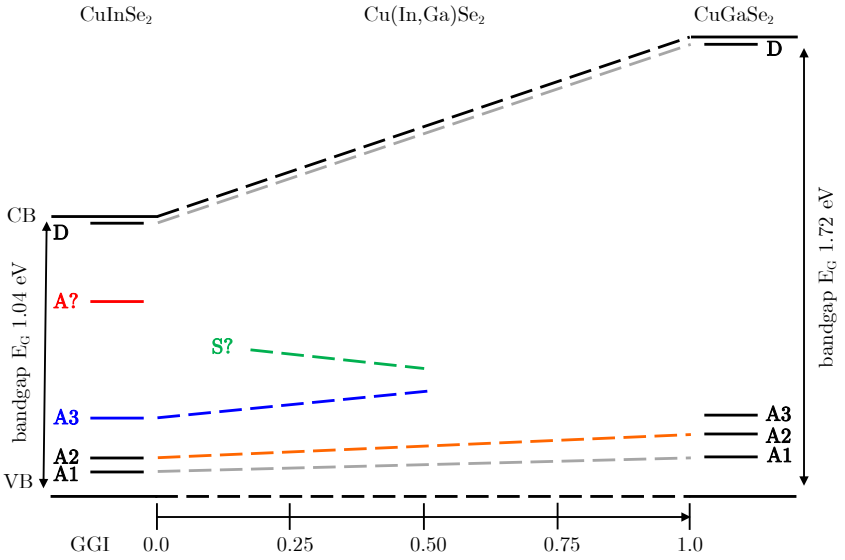

Figure 4.15: Defect model based on Rega et. al [29] updated with the found DA3 transition in $CuInSe_2$ and Cu(In,Ga)Se_2 as well as the deep luminescence in Cu(In,Ga)Se_2 and and the peak at 0.8 eV in $CuInSe_2$.

For the ternary $CuInSe_2$ a third acceptor with an activation energy of (135 ± 5) meV could be determined (shown in blue), which is proposed to be originating from the indium vacancy V_{In}. The defect was also found in Cu(In,Ga)Se_2 (dashed blue line) and moves deeper into the bandgap with increasing gallium content. In Cu(In,Ga)Se_2 it is assumed that the involved defect originates from the cation vacancy V_{III}, which is defined by the occupation of the next cation shell around it. In the defect picture the A3 found in $CuInSe_2$ and Cu(In,Ga)Se_2 is not extrapolated to the A3 found in $CuGaSe_2$ by Larsen [30]. From the different photoluminescence characteristics with compositional changes it is presumed that the both defect levels originate from different defects in the crystal, as discussed in section 4.2.3. Both should be denoted differently in the future to avoid misconceptions.

A second deep peak was observed for Cu(In,Ga)Se_2 samples with an GGI above 0.2. From the energy distance to the exciton a possible activation energy of (260 ± 20) meV was determined, which is constant within the probed gallium range. But this is only a rough indicator, since the nature of the transition is unknown (FB, DA) and it is unclear whether the deep defect involved is an acceptor or a donor. Due to this, it was added to the defect picture as unknown state (S) which needs further investigation. Low temperature photoluminescence measurement towards low energies, reveal a broad transition at 0.8 eV in $CuInSe_2$ which was also added to the picture. This transition is likely due to a deep acceptor state (shown in red) related to the second charge transition of the copper on indium antisite defect Cu_{In} or Cu_{Ga} respectively [101]. Lastly, the investigations show that the DA2 shifts monotonically at least until a GGI of 0.45, making it likely that it shifts monotonically over the full range (orange line). Not included are two deep defects bands recently found in $CuGaSe_2$ [124] which lie roughly 380 meV and 530 meV below the conduction band.

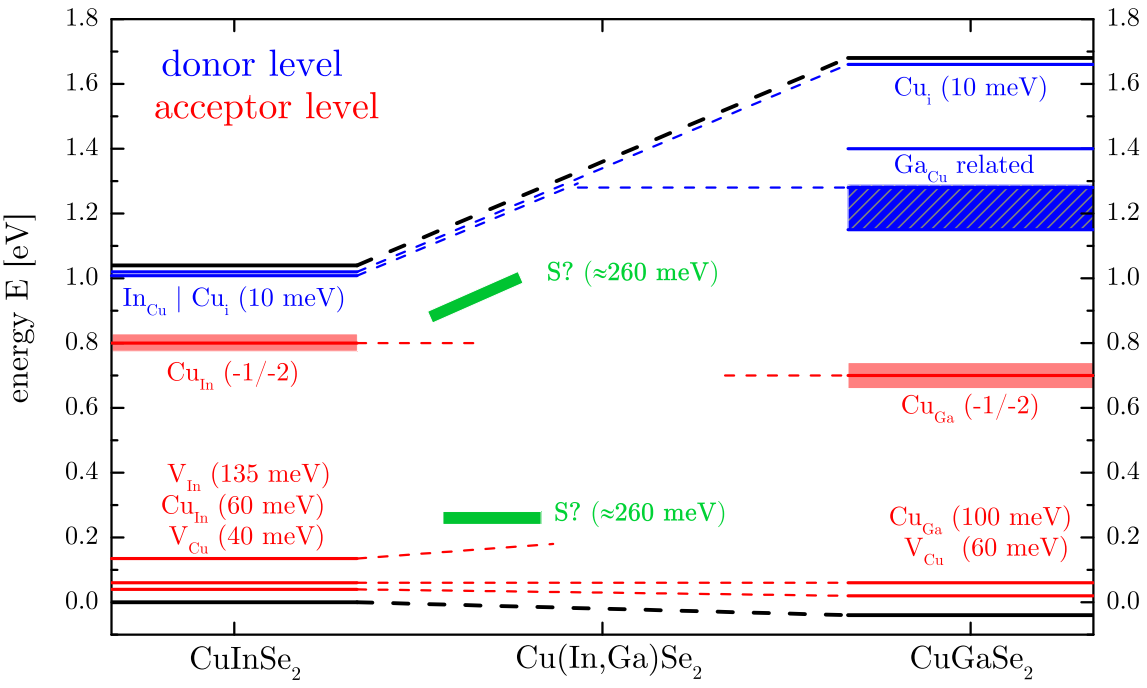

Figure 4.16: Defect model based on Rega et. al [29] and Spindler et. al [101] updated with the found DA3 transition in $CuInSe_2$ and $Cu(In,Ga)Se_2$ as well as the deep luminescence in $Cu(In,Ga)Se_2$.

CHAPTER

FIVE

THE OPTICAL DIODE FACTOR

The diode factor (or diode ideality factor) is a quantity introduced to the Shockley equation (2.10) to account for non idealities in a device. In the ideal case of a homo junction with recombination taking place only in the quasi neutral region by Shockley-Read-Hall or radiative recombination a diode factor of 1 would be determined. However, in real devices recombination and losses occur also at other places leading to larger diode factors, as briefly described in section 2.2.2. The diode factor is thus an important quantity to characterize the quality of a solar cell device. It is commonly determined by fitting current voltage curves [92]. But this method is prone to a number of effects that influence the result as will be discussed in the beginning of this chapter. A second method for the determination of the diode factor are SunsVoc measurements which will be explained afterwards. They are useful since the series resistance has no influence on the measurement. Although it is possible to determine the ideality factor reliable with this method it is still linked to complete device structure. Since the completion of solar cells takes time, it would be advantageous to predict the device performance already from the absorber layer alone. For the V_{OC} this can be done by optical measurements of the quasi Fermi level splitting. Since the diode factor and V_{OC} are linked, and the former can be deduced from illumination dependent measurements of the latter, it makes sense to assume that from illumination dependent measurement of the quasi Fermi level splitting a related quantity can be derived. In section 5.2 such link between the diode factor and the power law exponent will be derived theoretical and empirical. Afterwards, this link will be experimentally investigated using Cu-poor and Cu-rich Cu(In,Ga)Se_2 absorber layers and solar cell. Finally, it will be demonstrated how this method can be used to unveil defective interfaces and potential for improvements in the device structure. The content of this chapter is published in [201].

5.1 Diode factor of devices

As mentioned before the diode factor is initially introduced to the Shockley equation (2.10) (page 21) to describe the main recombination path. In the classical model by Shockley [202] minority charge carriers are injected through the space charge region. They then diffused and recombine in the quasi neutral region. If the recombination is radiative or non-radiative does not matter and the diode factor is 1 in this case. In the second example a defect state is located in the middle of the bandgap within the space charge region. If it is present in sufficient quantity it will be an efficient recombination center causing Shockley-Read-Hall recombination. This dominating recombination channel within the space charge region divides the voltage drop of the electron and of the holes in half, leading to a diode factor of 2 [36].

For hetero junctions, as used within the manuscript, recombination via surface states can occur and dominate. A brief overview is given in the following and a more detailed discussion can be found in [36]. If both quasi Fermi levels are not pinned, the diode factor depends on the ratio of the voltage drops on both sides [203] and ranges between 1 and 2. If only one quasi Fermi level is pinned, the other one will move resulting in one side voltage drop and thus a diode factor of 1. If tunneling of charge carriers between states is taken into consideration the diode factor can also have values above 2. In a complex device even more things can influence the diode factor (eg. recombination via coupled defects or fluctuations of the activation energy of the dominating recombination process $E_{\mathrm{A,rec}}$ [36]). For certain cases the diode factor even becomes illumination dependent or temperature dependent.

5.1.1 Classical determination from IV

As discussed briefly in section 2.2.3, the diode factor is commonly derived from dark current voltage measurements. When the current is plotted logarithmically over the applied voltage, the diode factor can be extracted from the slope of a linear fit [36], [204]. However, the diode factor becomes voltage dependent when a defect level is crossed by the Fermi level [36], [92], [205]. Furthermore, this method is influenced by the series resistance at high forward bias [206]–[208] and the shunt resistance at low forwards bias. Mainly, the bias dependence and the influence of the series resistance strongly limit the range, in which the diode factor can be fitted without their influence [36]. The IV curve measured in the dark for an exemplary sample is plotted semi-logarithmic over the voltage in figure 5.1 in black (shifted up by J_0). The inverse of the local slope divided by $k_{\mathrm{B}}T$ gives the diode ideality factor as plotted in blue. The influence of the voltage onto the extracted diode factor as discussed above is clearly observable. Only in the marked red circle a realistic value can be determined. A more advanced method is to fit the whole IV curve with a one or two diode equation, making sure to use an orthogonal regression like the ECN ivfit program [90] discussed in section 2.2.3. A fit with the Shockley equation including resistances (equation (2.11)) of the same IV curve as well as the illuminated IV curve (shifted by J_{SC}) is shown on the right side of figure 5.1. The extracted value for the ideality factor of about 1.6 is in good agreement with the value from the local slope derived by linear fitting (1.57 ± 0.05). To account for the voltage dependence of the diode factor, a second diode could be added to the equivalent circuit and with this to the Shockley equation. If non-ohmic shunts are included, possibly caused by space charge limited currents [175], the model gets even more complex [209]. Although physically

justified, this leads to more ambiguities in the fitting and not always to better physical insights. Since both the fitting in the semi-logarithmic plot and the fitting of the diode equation have their drawbacks, another measurement technique will be used to circumvent the ambiguities.

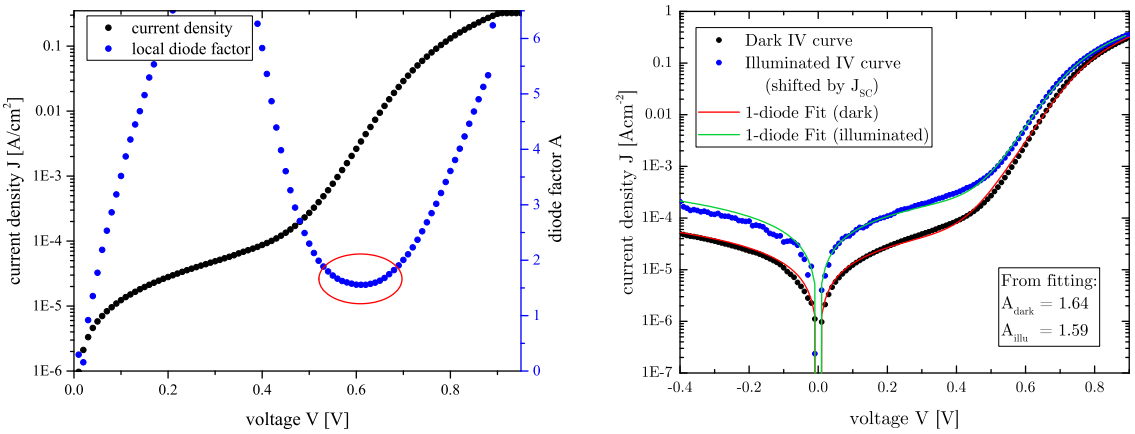

Figure 5.1: Left: Current density J measured in the dark plotted semi-logarithmically over the voltage (black). The blue curve shows the local diode ideality factor calculated from the inverse of the slope. Right: Same dark IV curve the same sample measured illuminated (shifted up by J_{SC}) fitted with ECN IVfit.

5.1.2 Determination by SunsVoc

Beside the commonly used way to apply a voltage and measure the current, the IV curve can also be determined by a J_{SC}-V_{OC} measurement. Here the V_{OC} and J_{SC} are measured for several illumination conditions and then plotted against each other giving a pseudo IV curve. The advantage of this method is, that it is not affected by the effect of the series resistance [206]. But this method is quite time consuming and the data acquisition not straight forward. Therefore, it never became a standard measurement technique. However, this measurement technique can be varied to simplify the data acquisition in two steps. In a first step the J_{SC} is not measured anymore. Instead a calibrated diode is used to determine the illumination intensity and then calculate the respective J_{SC}. Implementing the measurement like this a fast tracking of illumination condition (J_{SC}) and V_{OC} is possible. In a second step the illumination source is changed to a flash lamp. The illumination can now be changed over more than two orders of magnitude within ten milliseconds, as shown exemplary in figure 5.2. It is important though that the illumination does not decay too fast ($\tau > 3\,\mathrm{ms}$) to make sure that the solar cell voltage is in quasi-steady-state with the excitation [210]. This method is called quasi-steady-state V_{OC} (QssV_{OC}) or SunsVoc in literature. A more generalized background for the measurement technique can be found in [211] and [212]. From those measurements, the diode factor can be determined by a linear fit of the V_{OC} plotted semi-logarithmic over the illumination (or J_{SC}). The region where the correct diode factor can be extracted is now much larger compared to standard IV measurements (red circle in figure 5.1), since the series resistance has no influence. This measurement technique is well known in the silicon community and has also been successfully employed for kesterite and Cu(In,Ga)Se_2 cells [213]. For the measurements a system like depicted in figure 5.2 from the company Sinton instruments was used at the DLR Institute of Networked Energy Systems (formerly EWE Next Energy) in Oldenburg.

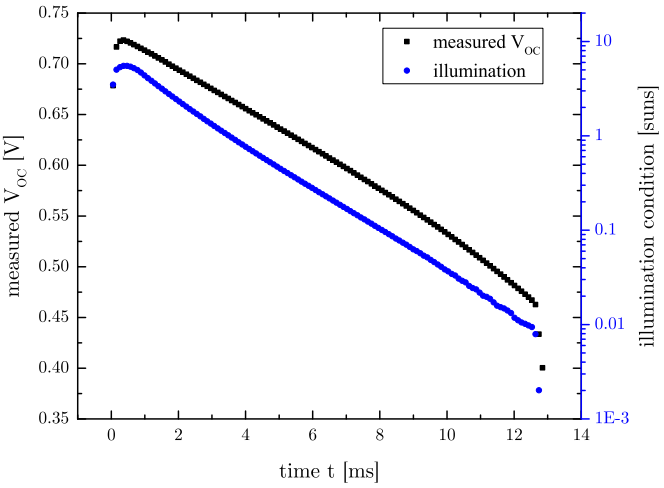

Figure 5.2: Left: Illumination conditions (plotted logarithmic) and open circuit voltage (plotted linear) measured over time during a SunsVoc measurement. Right: Picture of the measurement set up used.

5.2 Theoretical derivation of the link between diode factor and k value

As discussed in section 5.1, the diode factor depends on the location and the type of recombination happening in the device. Although photoluminescence probes the radiative recombination, it is possible to obtain information about the non-radiative recombination by investigating the absolute yield and the dependence with excitation. The luminescence yield I_{PL} usually follows a power law dependency and is proportional to the excitation I_{Exc} to the power of k, as shown in equation (5.1).

$$I_{\mathrm{PL}} \propto I_{\mathrm{Exc}}^{k} \tag{5.1}$$

In low temperature photoluminescence measurement the power law exponent k can give insight onto the transition type observed, as used in section 4.1.1. At room temperature in general band-to-band transition dominated the radiative luminescence, where free electrons from the conduction band recombine with free holes from the valence band, as described in section 2.3.2. If this is the only recombination channel the photoluminescence yield increases linearly and thus $k = 1$, as recently discussed by Spindler et al. [115]. If however competing recombination channels exist, especially those involving deep defects, the exponent will be larger than 1 [113], [114].

The luminescence spectrum and its yield is described by Planck's generalized law (equation (2.16)). The equation can be simplified to equation (5.2) when the quasi Fermi level splitting μ is much larger than the thermal voltage $k_{\mathrm{B}}T/q$. In the equation R_0 describes the recombination rate at thermal equilibrium $\left[R_0 = \frac{n}{\pi^2\hbar^3c^2} \cdot \frac{A(E)E^2}{\exp\left(\frac{E}{k_{\mathrm{B}}T}\right)-1}\right]$, as derived in [214].

$$I_{\mathrm{PL}} \propto R^{\mathrm{rad}} = R_0 \exp(q\mu/k_{\mathrm{B}}T) \tag{5.2}$$

Assuming radiative recombination from band to band is the only recombination path ($R = R^{\mathrm{rad}}$) and taking into consideration that the recombination has to balance the

generation ($G = R$), equation (5.3) can be written. Which is the same as equation (5.1) with $k = 1$.

$$I_{\mathrm{PL}} \propto R^{\mathrm{rad}} = R = G \propto I_{\mathrm{Exc}} \tag{5.3}$$

In case competing recombination channels exist, equation (5.4) is derived.

$$G^k \propto R^{\mathrm{rad}} = R_0 \exp(q\mu / k_{\mathrm{B}} T) \tag{5.4}$$

To relate this to the current voltage characteristics, the Shockley equation (2.10) is taken into consideration in open circuit condition without the influence of parasitic resistances. When rearrange for the photo current J_{SC}, equation (5.5) is derived.

$$J_{\mathrm{SC}} = J_0 \left[\exp\left(\frac{q V_{\mathrm{OC}}}{A\, k_{\mathrm{B}} T} \right) - 1 \right] \approx J_0 \exp\left(\frac{q V_{\mathrm{OC}}}{A\, k_{\mathrm{B}} T} \right) \tag{5.5}$$

The photo current is proportional to the illumination and thus to the generation rate ($J_{\mathrm{SC}} \propto G$). Inserting this into equation (5.4) it is possible to derive equation (5.6).

$$J_{\mathrm{SC}}^k \propto G^k \propto \exp(e\mu / k_{\mathrm{B}} T) \rightarrow J_{\mathrm{SC}} \propto \exp\left(\frac{q\mu}{k\, k_{\mathrm{B}} T} \right) \tag{5.6}$$

By comparing equation (5.5) and equation (5.6), it can be directly seen that the diode ideality factor A of a finished device is directly linked to the power law exponent k of the luminescence of an absorber layer. This relationship should hold true if the quasi Fermi level splitting μ can be equated with the open circuit voltage V_{OC} and if no further recombination channels are added during device finishing by layers, interfaces or contacts. The former is usually the case if the quasi Fermi level splitting is measured as a spatial average [215]. Cu-poor and Cu-rich Cu(In,Ga)Se_2 samples are a good model system to test the derived relation. For Cu-poor samples the relationship should hold true, since no new recombination channel is introduced during device finishing. On the other side, Cu-rich devices are known to be limited by recombination close to the interface and thus the relationship should not hold true, since a new recombination channel is added.

5.2.1 Relationship in measurements

The direct link between the power law exponent k and the diode factor A can also be derived in more empirical way. In section 5.1.1 and 5.1.2 the possibility to determine the diode factor from the slope of the V_{OC} plotted semi-logarithmically over the illumination or the photo current is discussed (see also equation (2.13)). The slope r is thereby defined by equation (5.7) and depends on the temperature T and the diode factor A. In general the decadic logarithm (or common logarithm) with base 10 is used for semi-logarithmic plotting. A factor of 2.3 is introduced to account for the switch from natural logarithm to the decadic logarithm.

$$r = (k_{\mathrm{B}} T / q) \cdot A \cdot 2.3 \tag{5.7}$$

For the evaluation of the quasi Fermi level splitting from luminescence measurements, Planck's generalized law (equation (2.16)) is used in a simplified way, like shown in equation (2.25). If this equation is rearranged for the qFLs, equation (5.8) is derived, where C summarizes some constants and is $\approx 10^{23}$.

$$\mu = \frac{k_\mathrm{B}T}{q} \ln\left(\frac{I_\mathrm{PL}}{C\,E^2}\right) - E \tag{5.8}$$

If the power law dependency from equation (5.1) is added with the proportionality constant C_2, it can be rewritten to equation (5.9).

$$\mu = \frac{k_\mathrm{B}T}{q} \ln\left(\frac{C_2\, I_\mathrm{Exc}^{k}}{C\,E^2}\right) - E \tag{5.9}$$

$$= \frac{k_\mathrm{B}T}{q}\, k\, \ln\left(I_\mathrm{Exc}\right) + \frac{k_\mathrm{B}T}{q} \ln\frac{C_2}{C\,E^2} - E \tag{5.10}$$

From this it can be seen that the slope (s) of the quasi Fermi level splitting plotted semi-logarithmically over the illumination is defined by equation (5.11). Again a factor of 2.3 is introduced to account for the switch of the logarithm base used.

$$s = k_\mathrm{B}T/q \cdot k \cdot 2.3 \tag{5.11}$$

Comparing equation (5.7) and equation (5.11) it is observed that the slope of the qFLs and of the V_OC have the same link to the power law exponent and the diode factor, respectively. Assuming that qFLs and V_OC are the same, both equation can be equated giving the same relationship $A = k$.

5.3 Experimental Validation

In the following the derived link between the diode factor and the power law exponent k will be investigated experimentally. Therefore the connection between the power law exponent and the change of the quasi Fermi level splitting with illumination is reviewed to verify equation (5.11). In a second step, the power law exponent of absorber layers will be compared to the diode factor for a set of Cu-rich and for a set of Cu-poor Cu(In,Ga)Se_2 samples.

5.3.1 Relationship of the power law exponent k to the slope of the excitation dependency of the quasi Fermi level splitting

In section 5.2.1 it was shown that the increase of the quasi Fermi level splitting depends directly on the power law exponent. To verify this this relationship, the quasi Fermi level splitting was measured intensity dependent on a broad range of Cu(In,Ga)Se_2 samples. The sample set included Cu-poor and Cu-rich samples with varying copper content ($0.8 < [\mathrm{Cu}]/([\mathrm{Ga}] + [\mathrm{In}]) < 1.4$). The gallium content varied between from 0.4 down to no gallium ($0 < [\mathrm{Ga}]/([\mathrm{Ga}] + [\mathrm{In}]) < 0.4$). The majority of the samples measured was covered with CdS, but additionally complete devices were measured. Absorbers without any passivation could not be measured due to the strong degradation of the photoluminescence signal when exposed to ambient air and light, as discussed in section 6.1. The quasi Fermi level splitting is plotted over the illumination in figure 5.3 for an exemplary Cu-poor (black) and a Cu-rich (blue) absorber layer which were etched and covered with CdS. Both data sets are linear over the probe illumination range and the slope s is determined by a linear fit.

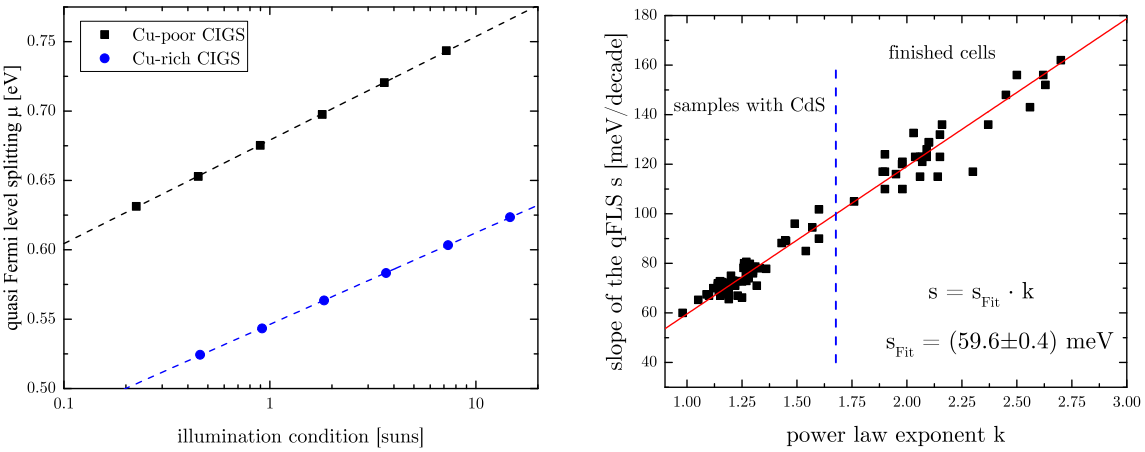

Figure 5.3: Left: quasi Fermi level splitting of a Cu poor and a Cu-rich sample both passivated with a CdS layer plotted over the equivalent suns illumination condition. Right: Measured slope of the quasi Fermi level splitting with illumination plotted over the k-value for absorbers covered with CdS and finished solar cells. The red line depicts a linear Fit through the origin.

The same measurements used for the extraction of the qFLs are used for the determination of the power law exponent. To do this, the photoluminescence signal is integrated and plotted double-logarithmically over the excitation. The slope of a linear fit defines the k value [96]. The determined slope of the qFLs s is plotted over the power law exponent k on the right side of figure 5.3. It should be noted here that the determination of the power law exponent yields an at least 10 time smaller error compared to the error in the determination of s, leading to an error mainly in the direction of the s-axis. A linear increase of s is observed and a linear fit with a fixed y-intercept at 0 yields a slope of $(59.6 \pm 0.4)\,\mathrm{meV/decade}$. This is in good agreement with the slope of $(57.7 \pm 0.6)\,\mathrm{meV/decade}$ expected for the measured room temperature of $(296 \pm 3)\,\mathrm{K}$ according to equation (5.11). This confirms the derived relation between s and k. Within the graph no difference between Cu-rich and Cu-poor samples are observable. However, samples which are covered only with CdS exhibit in general a lower slope and k value than samples with a full device stack. The increased power law exponent might be an artifact caused by a separation of the generated charge carriers, due to the finished junction.

5.3.2 Comparison of power law exponent and diode factor

To verify the assumption that the diode factor and the power law exponent are the same in certain circumstances, a smaller set of samples is investigated. In total 4 Cu-poor and 4 Cu-rich absorbers layers from different processes but with similar gallium content (GGI ≈ 0.3) are compared. For each absorber layer a piece is split off, etched and covered with CdS for the photoluminescence measurements. The rest of the inch by inch absorber piece is finished into a device for SunsVoc measurements, as described in section 2.2.2, with 6 solar cells with an area of about $0.5\,\mathrm{cm}^2$ each.

The intensity dependent photoluminescence measurements for the Cu-poor absorber layers yield on average a power law exponent k of (1.25 ± 0.05) and slope in qFLs s of $(75 \pm 3)\,\mathrm{meV/decade}$. Compared to this, the values for the Cu-rich absorbers are slightly lower with $k = (1.16 \pm 0.05)$ and $s = (69 \pm 3)\,\mathrm{meV/decade}$. Both data sets fulfill the derived relation of equation (5.11).

For each of the 6 solar cell of a finished device, a SunsVoc measurement is carried out as discussed in section 5.1.2. An exemplary SunsVoc curve is plotted for a Cu-poor (black) and a Cu-rich (blue) sample in figure 5.4. The curve of the Cu-poor device is linear over a wide illumination range. Only for illumination intensities below 0.1 suns the curve slightly bends of towards lower values. The measured V_{OC} of the Cu-rich sample lies well below the Cu-poor curve and exhibits a higher slope at 1 suns illumination. Furthermore, a strong drop towards low illumination conditions is observed.

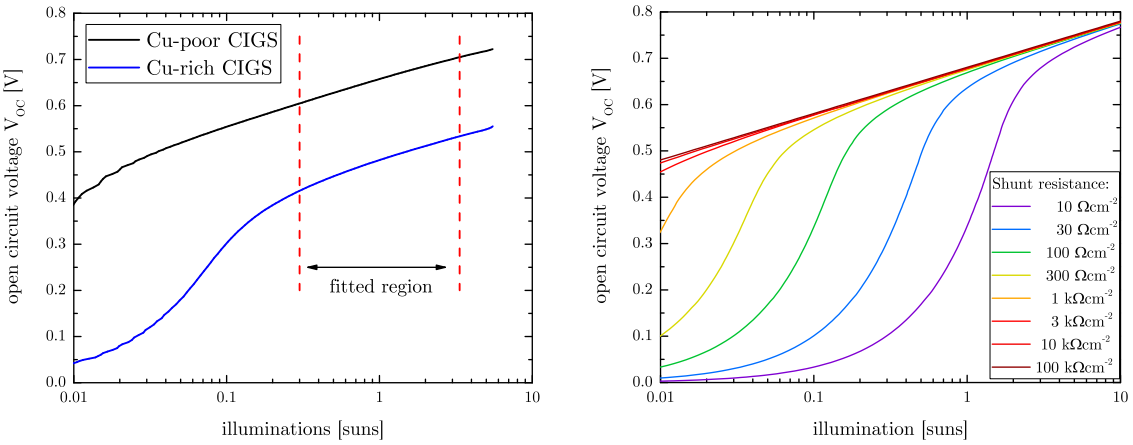

Figure 5.4: Left: Measured open circuit voltage plotted over the illumination intensity for an exemplary Cu-poor and a Cu-rich Cu(In,Ga)Se_2 solar cell during a SunsVoc measurement. Right: Calculated illumination dependence of V_{OC} according to equation (5.12) for varying shunt resistances R_{Sh}

This drop originates in the low shunt resistance of Cu-rich devices [216], [217], which are generally below $300\,\Omega\,cm^2$ whereas Cu-poor samples have a shunt resistance above $1000\,\Omega\,cm^2$. For such low values the term V_{OC}/R_{Sh} in equation (2.13) (page 26) can not be neglected. In this case equation (5.12) including a Lambert W function has to be used to describe the V_{OC} as a function of illumination (J_{SC}) and shunt resistance (R_{Sh}) [216].

$$V_{OC} = (J_0 + J_{SC})R_{Sh} - \frac{A\,k_B T}{q} \cdot W\left[\frac{q}{A\,k_B T} J_0 R_{Sh} \cdot \exp\left(\frac{q}{A\,k_B T} J_{SC} R_{Sh}\right)\right] \tag{5.12}$$

On the right side of figure 5.4 the influence of the shunt resistance is depicted. Here empirical parameters of a Cu-poor cell were used to calculate the illumination dependency of the V_{OC} assuming a fixed diode factor of $A = 1.42$, a saturation current density of $J_0 = 1 \times 10^{-9}\,mA\,cm^{-2}$ and a short circuit current density J_{SC} of $33.2\,mA\,cm^{-2}$ for various shunt resistances. The break down of the V_{OC} shifts towards higher illumination conditions for decreasing shunt resistances. The value of about $3000\,\Omega\,cm^2$ describes the bending of the Cu-poor curve quite well and also the measured Cu-rich curve can be nicely explained by a shunt resistance of about $100\,\Omega\,cm^2$.

The measured SunsVoc curves are fitted from 0.3 suns to 3 suns to be symmetrical around 1 suns to extract the slope r of the V_{OC} with illumination. Averaging 29 solar cells with a Cu-poor composition, a slope r of $(80 \pm 12)\,meV/decade$ and calculated from this using equation (5.7) a diode factor A of (1.3 ± 0.2) is determined. The determined diode factor is in good agreement with the previously determined power law exponent k of (1.25 ± 0.05), confirming the direct relationship of the two parameters. The power law

exponent k can thus be defined as an optical diode factor, which can be used to predict the diode factor of finished devices.

To determine the power law exponent absolute calibrated measurements were used, since also the quasi Fermi level splitting was determined. However, for the determination of k, relative measurements without proper calibration of the measured photon flux or/and without a defined excitation density are sufficient. Both calibrations are multiplicative factors and have no influence on the slope in the double logarithmic plot which is used for the determination of k. This makes the determination of this property rather easy and can be done in all photoluminescence set ups in which the excitation density can be varied.

For the samples grown under Cu-excess an average slope of $(112 \pm 9)\,\mathrm{meV/decade}$ and an average diode factor A of (1.9 ± 0.2) is determined. Hence the diode factor is well above the power law exponent value of (1.16 ± 0.05). The higher diode factor in the devices fits to values commonly observed for Cu-rich $CuInSe_2$ and $Cu(In,Ga)Se_2$ solar cells ranging from 1.9 to 2.8[1] [20], [142], [183] and can be explained by recombination close to the interface [12], [18]. A way to determine this is the extrapolation of the V_{OC} from temperature dependent IV measurements towards 0 K. For an exemplary investigated sample, this measurement was carried out (shown in figure 6.7 on page 113). The V_{OC} extrapolates to a value well below the bandgap confirming the limitation of the device by recombination close to the interface. The higher diode factor compared to the power law exponent can thus be explained by the introduction of a new recombination channel during device finishing.

The finding can be used to unveil cell performance limitations by interfaces. The measured quasi Fermi level splitting inside the bare absorber is essentially a bulk property. If no recombination channels are added, the measured bulk quasi Fermi level splitting and the open circuit voltage at the terminals will be the same, as depicted on the left side of figure 5.5. For the case when a recombination path is added, for instance by interface defects with a high recombination velocity, the diode factor will increase but also the qFLs will decrease towards the interface. Leading to a considerable loss in V_{OC}. The comparison of the optical diode factor and the electrical diode factor can thus be used reveal problems with interfaces which limit the V_{OC}.

5.4 Summary

This chapter covered the relationship of optical determined parameters of bare absorbers and electrical parameters of finished devices. It was shown that the diode factor A of a finished solar cell can be directly linked to the power law exponent k of an absorber layer. An empirical way to look at this is linking the diode factor to the intensity dependence of the V_{OC} and the power law exponent to the intensity dependence of the qFLs and then to equate V_{OC} and qFLs , as shown in equation (5.13) with $c = q/(k_B T \cdot 2.3)$.

$$k = c \cdot \frac{d\mu}{d(\ln I_{Exc})} \overset{\mu = V_{OC}}{\longleftrightarrow} c \cdot \frac{dV_{OC}}{d(\ln I_{Exc})} = A \tag{5.13}$$

This relationship was verified using intensity dependent quasi Fermi level splitting as well as SunsVoc measurements on Cu-rich and Cu-poor $Cu(In,Ga)Se_2$ absorber layer.

[1] It should be noted here that diode factor values determined by fitting IV curves are in general slightly above values determined by SunsVoc. The diode factor for the same set of samples from IV measurements range from 1.9 to 2.4

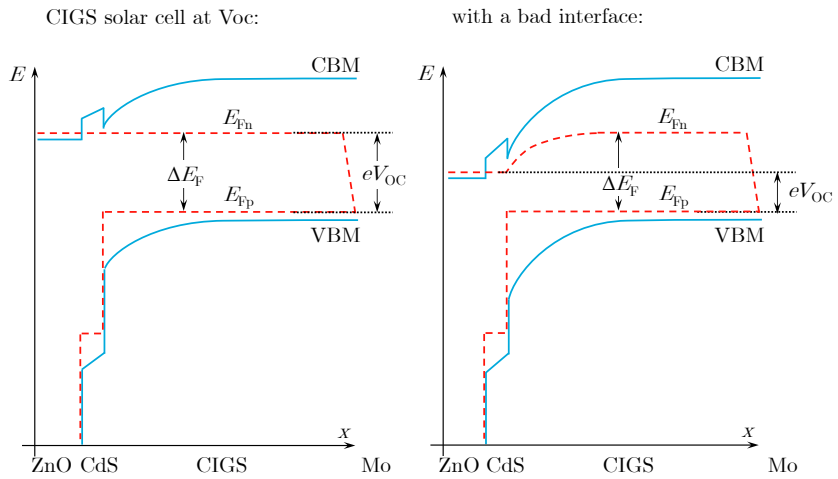

Figure 5.5: Schematic band diagram of a Cu(In,Ga)Se_2 solar cell depicted at open circuit conditions. The left side shows the ideal situation without detrimental interfaces, whereas the right side shows the influence of an efficient recombination center formed at the interface. The open circuit voltage in this case is considerably lower compared to the quasi Fermi level splitting of the absorber itself. It should be noted here that for simplicity reason it is assumed that the interface has not influence on quasi Fermi level splitting in the bulk, although this could be the case for devices with high charge carrier mobilities.

Table 5.1: Comparison of the power law exponent k, the slope of the quasi Fermi level splitting over excitation s, the slope of the open circuit voltage over excitation r, and the diode factor A of Cu-rich and Cu-poor Cu(In,Ga)Se_2 samples

	exponent k	slope qFLs s [mV/decade]	slope Voc r [meV/decade]	diode factor A
Cu-poor	1.25 ± 0.05	75 ± 3	80 ± 12	1.3 ± 0.2
Cu-rich	1.16 ± 0.05	69 ± 3	112 ± 9	1.9 ± 0.2

Using Cu(In,Ga)Se_2 solar cells has the advantage that by changing only the composition of the absorber layer and thus using the same cell architecture, different recombination channels are present.

In case of Cu-poor samples, where the device is dominated by recombination in bulk, the power law exponent and the diode factor agree well with each other, as summarized in table 5.1. In case of Cu-rich samples an additional recombination channel is introduced and the device is limited by recombination close to the interface. The diode factor is thus larger than the power law exponent.

For the determination of the power law exponent k any photoluminescence set up can be used and no absolute calibration of excitation density or photoluminescence yield is needed. The shown method is thus a quick and easy way to estimate the diode factor and can be used for the screening of new materials for solar cells based on the photoluminescence of the absorber alone. Furthermore, it is relevant for the development of new materials into solar cells as it indicates whether the limitations of the solar cell stem from the absorber or from the interface and thus give an indication where the solar cell can still be optimized.

CHAPTER

SIX

QUASI FERMI LEVEL SPLITTING OF $Cu(In,Ga)Se_2$ LAYERS WITH VARIOUS BANDGAPS

The quasi Fermi level splitting (qFLs) is an upper boundary of the open circuit voltage [21], [55], [96], [218] and is thus an important indicator of the absorber quality. It can be determined from calibrated room temperature measurements by using Planck's generalized law (equation (2.16)), as discussed in section 2.3.5. However, accessing the photoluminescence properties of bare absorbers is hindered by the fact that $CuInSe_2$ and $Cu(In,Ga)Se_2$ absorber layers degrade in the presence of ambient air [17], [219]. An exponential decay of the quasi Fermi level splitting was shown for epitaxial and polycrystalline $CuInSe_2$ samples [17]. In the following chapter similar studies are carried out for $Cu(In,Ga)Se_2$. In the beginning the evaluation method is presented and the degradation in ambient air under constant illumination is investigated. With this method $Cu(In,Ga)Se_2$ samples with Cu-rich and Cu-poor composition are investigated and compared to check if the large difference in V_{OC} ($> 175\,mV$) can be linked to the quasi Fermi level splitting of the absorber layers. Since the quasi Fermi level splitting of bare absorbers degrades within minutes (see section 2.4.4 or [17]) measurements from freshly etched absorbers and absorbers covered with CdS are compared to simplify the accessibility of the quasi Fermi level splitting. In the end, the quasi Fermi level splitting of $Cu(In,Ga)Se_2$ absorbers with Cu-rich and Cu-poor composition will be compared to the open circuit voltage of the respective finished devices. The content of the first half of this chapter is published in [216]. The second half of the chapter is part of [122].

6.1 Time dependent qFLs measurement

Strong differences in the degradation of the qFLs have been found between polycrystalline Cu-poor and Cu-rich $CuInSe_2$ samples, showing a 10 to 20 times faster decay as well as a four times stronger drop in case of a Cu-poor composition compared to Cu-rich composition [17]. Since the decrease is mostly driven by the oxidation of indium in $CuInSe_2$, this behaviour might be different in $Cu(In,Ga)Se_2$ and will be thus investigated in the following. For this purpose polycrystalline absorbers grown on molybdenum coated soda lime glass by a 3-stage process, as described in section 2.4.3, are used. The good crystal quality of the grown samples can be seen in the high efficiencies of about 16 % in case of the Cu-poor samples and by the excitonic luminescence observed in low temperature photoluminescence measurements in case of the samples grown Cu-rich.

6.1.1 Evaluation of the qFLs after etching

For the evaluation of the qFLs from room temperature photoluminescence measurements, a calibration factor is needed to convert the spectrum from relative intensity into absolute numbers of photons/(cm^2eVs). A new calibration is done before each measurement day as described in the appendix in section C.1. For the evaluation of the qFLs, the high energy slope of the photoluminescence peak is fitted about 0.1 eV above the bandgap in a logarithmic scale. The slope depends on the temperature and the Y-intercept gives the quasi Fermi level splitting. The evaluation is straight forward but prone to noise and background signals since only the lower 5 % of a peak are fitted. Small background signals lead to a deviation of the linear drop of the high energy wing decreasing the slope. Therefore the temperature evaluated by the linear fit artificially increases to values above 330 K for moderate excitation densities. This decreases the extracted qFLs value by about 75 meV compared to the qFLs evaluated with the measured room temperature in the laboratory (2.47 meV K^{-1} as discussed in section C.2 in the appendix). Although it is possible to correct for background signals, see section C.2, it is easier to measure the room temperature externally and eliminated this free variable. This is possible since the later used excitation densities do not heat up the illuminated spot, as verified by a thermal camera.

To evaluate the qFLs after etching the excitation density, accumulation time, number of measurements and position of the sample are adjusted before the sample is etched to start the measurement as soon as possible after the etching. The illumination density is tuned to be equivalent to the illumination of 3x the standard AM 1.5 suns spectrum, details can be found in section C.2 in the appendix. After the KCN etching the sample is directly transferred back to the photoluminescence set up and the measurement is started. The raw data is saved by means of single measurements of two seconds each. To access the time development those measurements are averaged in different time intervals ranging from 30 s up to 20 min. Those larger time intervals are needed to increase the signal to noise ratio of the later measurements because of the decreasing photoluminescence yield. The different data points are corrected as described in section C in the appendix and the qFLs is extracted using the measured room temperature of (296 ± 2) K. The extracted qFLs are plotted over the time for the different time intervals in figure 6.1. The first value is plotted at 2.4 min, taking the transfer process of the sample to the photoluminescence set up and the start of the measurement into consideration. To get the initial value after etching the first 10 data points (~ 20 s) are averaged and the qFLs is extracted. The difference in qFLs between the data of the first seconds and averaging 2 minutes is in the range of 5 meV to 14 meV.

In total, six samples with a Cu-poor composition ([Cu]/([Ga] + [In]) ≈ 0.9) with different gallium concentration ranging from 0.25 to 0.38 and eight samples grown Cu-rich ([Cu]/([Ga] + [In]) $\approx 1{,}2$) with [Ga]/([Ga] + [In]) from 0.25 to 0.45 are measured over time after etching. The decay curves for some exemplary samples are shown in figure 6.2. Each sample shows a decay of the quasi Fermi level splitting with time. The absolute drop in qFLs is with about 100 meV higher for the Cu-poor samples compared to the 40 meV of Cu-rich ones and are comparable with values observed in $CuInSe_2$ (≈ 120 meV and ≈ 35 meV) [17]. To evaluate the decay time τ, mono-exponential decay curves with an offset [$\mu(t) = \mu_0 + A \cdot \exp(-t/\tau)$] are fitted to the data, as shown by the solid lines in figure 6.2.

However, the mono-exponential fit does not describe the data well. Plotting the qFLs semi-logarithmically over the time, as shown on the right figure 6.2, more than one linear

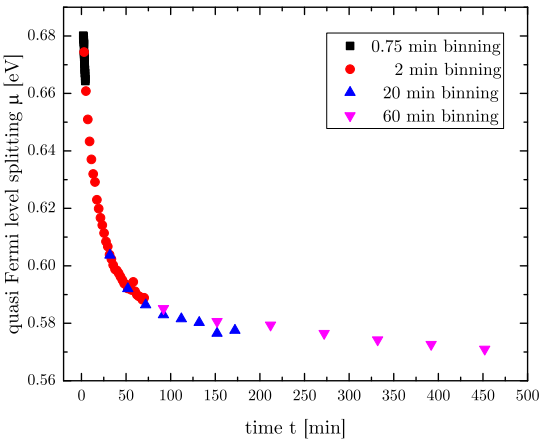

Figure 6.1: Exemplary curve of the quasi Fermi level splitting after KCN etching plotted over time. Different data point binning values are shown for comparison.

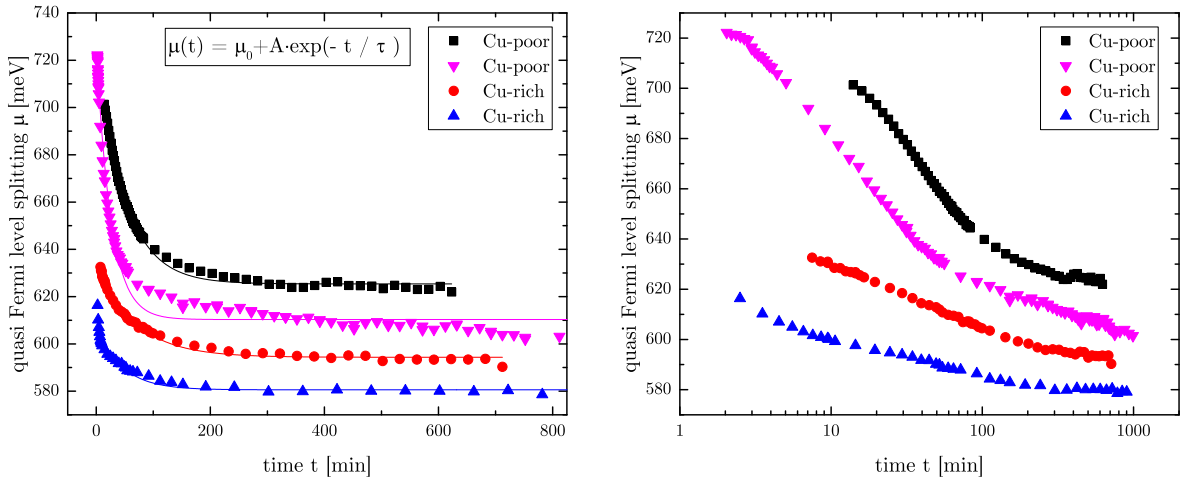

Figure 6.2: Exemplary curve of the quasi Fermi level splitting after KCN etching plotted linear (left) and semi-logarithmic (right) over time. The green laser line 514 nm is used for excitation with a power density of 3x equivalent suns.

part is observed, indicating a bi-exponential or worse decay behaviour. Shifting the data linear in time to lower values, assuming a slower degradation without laser illumination during the sample transfer, does not change this. The evaluated decay times can thus only be taken as a rough indicator. Averaging the values for the different samples shows that the decay for the Cu-poor sample (25 min) is about twice as fast as for the Cu-rich samples (40 min), see also table 6.1. The very strong difference as seen in polycrystalline $CuInSe_2$ of a factor of 20 (35 min and 650 min) is not observed in $Cu(In,Ga)Se_2$. Nevertheless all in all, the same trends are found in both materials. The degradation of the qFLs is less pronounced and slower in absorber layers grown with a Cu-rich composition.

6.1.2 Comparison of the initial qFLs

Looking at the first data point of each curve, representing the first 20 s of a measurement series, it is observed that the quasi Fermi level splitting values of the Cu-rich samples lay below the Cu-poor ones. Since different [Ga]/([Ga] + [In])-ratios are studied, the different bandgaps of the samples have to be taken into account. To evaluate the bandgap a second

Table 6.1: Average decay time and average absolute drop of the quasi Fermi level splitting after KCN etching for Cu-poor and Cu-rich $CuInSe_2$ and $Cu(In,Ga)Se_2$. Data for $CuInSe_2$ taken from [17].

	$Cu(In,Ga)Se_2$		$CuInSe_2$	
Composition	Cu-poor	Cu-rich	Cu-poor	Cu-rich
$\Delta\mu$ [meV]	$\approx$ 100	$\approx$ 40	$\approx$ 120	$\approx$ 35
τ [min]	$\approx$ 25	$\approx$ 40	$\approx$ 30	$\approx$ 650

piece of each absorber layer is finished into a solar cell. For each device external quantum efficiency measurements are performed and the bandgap is extracted by linear extrapolation of the high wavelength slope. The initial qFLs splitting value is plotted for each Cu-poor (black) and Cu-rich (blue) absorber layer over the bandgap in figure 6.3. All data points for Cu-rich samples lay well below the Cu-poor ones. This is fundamentally different from what has been observed for the ternary $CuInSe_2$, where the qFLs of freshly etched Cu-rich absorber layers was determined to be the same or even a bit higher compared to Cu-poor samples [16], [17]. Possible reasons for the difference between materials will be discussed later.

The absolute difference is determined to be 120 meV from a linear fit with a fixed slope of 0.92. The slope is below 1 since the qFLs cannot directly follow the bandgap due to thermodynamic and other unavoidable losses. A detailed discussion about fundamental losses in solar cells can be found in [220]. In the perfect solar cell qFLs and V_{OC} are the same and the change with bandgap can numerically approximated with $V_{OC,max} = 0.918 \cdot E_G - 0.152$ according to [89]. For the fit over the limited range of 100 meV in bandgap change, it is legitimate to assume no changes in device physics and to take the slope of the maximum qFLs reachable.

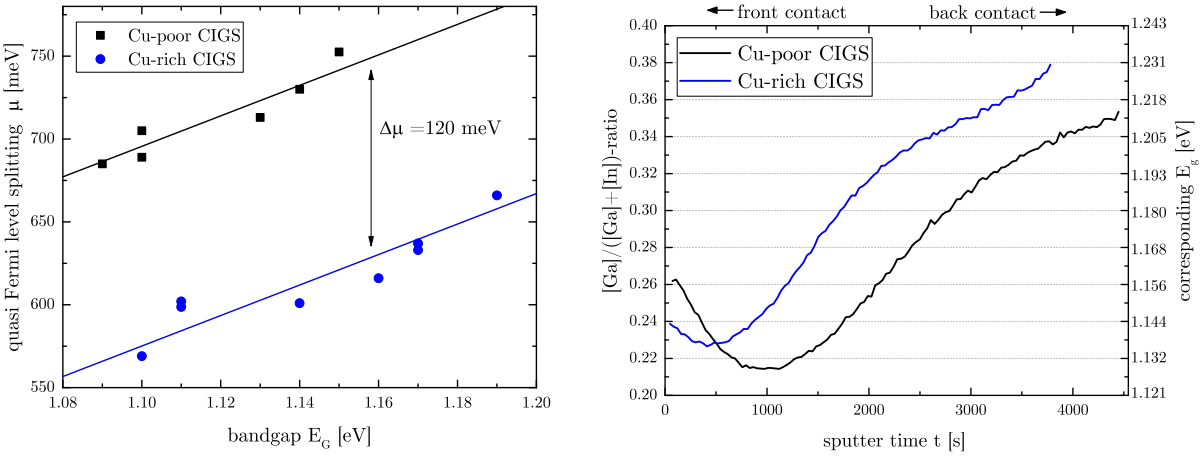

Figure 6.3: Left: Initial quasi Fermi level splitting of Cu-poor (black) and Cu-rich (blue) $Cu(In,Ga)Se_2$ absorber layers after KCN etching plotted over the bandgap. Right: [Ga]/([Ga] + [In]) profile of a Cu-poor and a Cu-rich $Cu(In,Ga)Se_2$ absorber determined SIMS plotted over the sputter duration. The right Y-axis shows the corresponding bandgap.

This large difference in qFLs between the compositions could be explained by the difference in gallium gradient or by a fundamentally different recombination process. Both options will be discussed in the following.

The 3-stage process used for the absorber preparation commonly induces a gallium double gradient [138]. The [Ga]/([Ga] + [In])-ratio (GGI) throughout the absorber thickness might be different for both compositions, since the length of the third stages is varied to achieve different final copper contents. To check this assumption, secondary ion mass spectrometry (SIMS) is carried out on some exemplary samples. This measurement technique can measure relative counts for each element analysed [221]. For the data evaluation the relative GGI is calculated. By assuming that the bandgap measured by external quantum efficiency corresponds to the bandgap minimum and linking this to the bandgap change with gallium, this relative GGI can be scaled to a meaningful value. The bandgap in $Cu(In_{1-x}, Ga_x)Se_2$ does not change completely linear with gallium content but with a small bowing, as discussed in section 2.1.3. Equation (2.1) was used with a bowing factor of 1.67 [42] to calculate the bandgap from the GGI and vice versa. This is an approximation since the bowing was determined for stoichiometric materials. Using this formula, possible bandgap differences between Cu-rich and Cu-poor composition, as seen in $CuInSe_2$, are neglected. The scaled GGI values of a Cu-rich and a Cu-poor sample with similar gallium content are shown in figure 6.3.

Both composition types show indeed the characteristic double gallium gradient observed in co-evaporated 3-stage samples [72], [138]. Copper is the fastest diffusing element in $CuInSe_2$ [222]–[224] and $CuGaSe_2$ [222] as found by ab initio calculation. Experiments indicate the same behaviour [225]–[227]. Calculations of the migration barrier for copper vacancy mediated indium and gallium diffusion shows that indium is more mobile than gallium over the whole solid solution of $Cu(In,Ga)Se_2$ [72]. Taking those findings into consideration, the formation of the double gallium gradient can be explained. After the formation of the $(In,Ga)Se_x$ precursor layer in the first stage, the copper supplied in the second stage diffuses into the precursor and indium migrates stronger to the surface than gallium, leading to an gallium enrichment at the back contact. In the beginning of the third stage the process is more or less the opposite. The supplied indium is more mobile than gallium and is diffusing faster through the Cu_xSe layer that forms at the end of the second stage on the absorber surface. This process leads to gallium enrichment at the sample surface. The double gallium gradient is intentionally and widely used in literature since it reduces the recombination at the molybdenum back contact as well as the CdS interface, leading to higher efficiencies [72], [140].

In the measured samples shown in figure 6.3 the gallium gradient towards the back is similar for both compositions. The front gradient is less pronounced in the Cu-rich sample than in the Cu-poor sample. This is related to the growth process in which the length of the third stage is used to control the final copper content of the absorber. Thus, the Cu-rich sample has a shorter third stage leading to less enrichment of gallium at the surface. The difference of the bandgap between the front and in the bandgap minimum (notch) is about 40 meV in case of the Cu-poor sample and 10 meV for the Cu-rich sample. If the measured photoluminescence used for the determination of the qFLs is assumed to originate from the notch of the gallium grading, then a stronger grading to the front could possibly reduce recombination at the front surface. That the emitted photons originate from the notch is supported by the fact that photoluminescence measurements with different excitation wavelengths and thus different penetration depths give the same results without any shift of the peak position which would indicate a change in bandgap. Also photoluminescence spectra measured from the backside of an absorber that was physically lifted of the molybdenum substrate, exhibit a peak at the same energy [171]. Besides this a recent study investigating different GGI profiles also concludes that the

emission originates from the bandgap notch [228].

Summarized, a double gallium gradient is found for both compositions, but a stronger pronounced gradient towards the front is detected in case of Cu-poor samples. Since the luminescence comes from the bandgap notch, this higher grading will likely reduce the effect of possible surface states with a high recombination velocity. However, this passivation is estimated to give an at most 50 meV higher splitting and can thus at most partly explained the strong difference of 120 meV in quasi Fermi level splitting found.

A second possible explanation for the lower quasi Fermi level splitting in Cu-rich samples could be a fundamental difference in the recombination process between Cu-rich $CuInSe_2$ and Cu(In,Ga)Se_2. One possibility would be a gallium related (deep) defect, which is not present in the ternary. The gallium on copper antisite (Ga_{Cu}) forms a defect band about 500 meV below the conduction band in $CuGaSe_2$, as found in experiment [101], [124] and theory [50]. This defect would be also in the samples Cu-poor compositions, but there it would likely form a complex with the abundant copper vacancies (Ga_{Cu}-$2V_{Cu}$) which is calculated to be shallower, reducing its detrimental effect. But with decreasing gallium content the defect level gets shallower and is proposed to be resonant with the conduction band for GGI-ratios below 0.45 [101], [122]. It should be thus not affect the investigated samples.

Another defect related possibility could be a defect present in $CuInSe_2$ that moves deeper into the bandgap with increasing gallium content. A possible candidate for this would be the second charge transition of the Cu_{In} antisite defect. In samples grown under high copper excess, as the investigated ones, this defect is the dominating acceptor in low temperature photoluminescence measurements as seen in section 4.2. The second charge transition is proposed to have an acceptor state about (700 ± 100) meV above the valence band in $CuInSe_2$ from theoretical calculation [50], [53], [54], [189] and a similar position is calculated in $CuGaSe_2$ [50]. Experimentally, a peak in the right region was found in $CuGaSe_2$ samples [101], [122] and also in $CuInSe_2$ a deep luminescence peak was measured in this energy region in section 4.4.3. The second charge transition of Cu_{III} would be thus a good candidate to explain the difference in qFLs between Cu-rich and Cu-poor Cu(In,Ga)Se_2 samples.

Since the defect moves closer to the conduction band with decreasing gallium content, it could be suspected that it does not influence the quasi Fermi level splitting in Cu-rich $CuInSe_2$ samples. This would explain why the same quasi Fermi level splitting was found for samples with Cu-rich and Cu-poor composition in literature [17]. However, the defect is present in such a high quantity that it is detected in low temperature and room temperature measurements (see section 3.2.2 and section 4.4.3). It should should thus affect the quasi Fermi level splitting. Preceding the results of the next section, actually a lower qFLs is found in Cu-rich samples compared to Cu-poor samples when taking the bandgap into consideration.

6.2 Measurements on passivated absorber layers

To access the qFLs of bare absorber layers after etching is complex and time consuming. Furthermore, it yields only a limited accuracy of the qFLs since the first measured data point has to be taken as the "real" qFLs of the sample, not taking any degradation process in the transfer time of about 2 min and the time under laser illumination before the first measurement of about 30 s into account. Additionally, it is not possible to measure the qFLs dependent on the excitation density, since every measurement takes a few minutes in

which the photoluminescence yield decreases. To avoid those problems and make the qFLs more accessible, measurements on passivated samples are preferable. For epitaxial and polycrystalline $CuInSe_2$ absorber layer it has been shown that a thin CdS layer effectively passivates the absorber surface preserving the qFLs for several months [17]. In the following the passivation properties of a CdS will be examined for polycrystalline $Cu(In,Ga)Se_2$ samples and the qFLs values compared to values obtained on bare samples. Afterwards the limited sample set studied in the previous section is extended to higher and lower gallium contents. In the end, the measured qFLs values are compared to the open circuit voltage of finished devices made from the investigated absorber layers.

6.2.1 Comparison of qFLs on bare and CdS covered samples

A possible way to stop the degradation of the photoluminescence yield for months on $CuInSe_2$ is to deposit a thin layer of CdS [17]. To verify this for $Cu(In,Ga)Se_2$ the previously investigated samples were etched in KCN and thin layer of CdS was deposited by chemical bath deposition. The luminescence yield was measured for some exemplary samples over the course of several hours but no change in the signal was detected. This holds true for Cu-rich and Cu-poor samples. Measuring some exemplary samples after 14 months results within error in the same qFLs. Therefore, it is concluded that the passivation of the absorber surface by a CdS layer works the same in $Cu(In,Ga)Se_2$ as in $CuInSe_2$. The qFLs of the etched absorbers (first 20 s) (closed symbols) is plotted over the bandgap on the left in figure 6.4 together with the values determined for absorber layers covered with CdS (open symbols). The qFLs value measured on CdS covered samples is with (4 ± 8) meV on average slightly higher than the value from the bare absorber. This difference possibly originates from the fast initial decay of the qFLs after etching, that starts after etching and is likely accelerated by the laser light after mounting the sample in the set up. Thus the value from the etched absorbers is likely to be degraded slightly even before the first measurement. Some data points are also found to be below their counterpart. A possible explanation for this are inhomogeneities across the absorber layer leading to fluctuations of the photoluminescence yield. In general, it is concluded that the determined qFLs values of bare and CdS covered absorbers agree well with each other.

A second problem to assess the measured qFLs is the bandgap of the absorber layer. Contrary to $CuInSe_2$ samples where there is one bandgap for Cu-poor composition and one bandgap for Cu-rich composition, every $Cu(In,Ga)Se_2$ sample will have a different bandgap due to the different gallium content. Previously the bandgap was taken from external quantum efficiency measurements of finished devices. This procedure has two drawbacks. First, you need finished devices for the comparison of absorbers. Secondly, especially Cu-rich $Cu(In,Ga)Se_2$ absorber layer tend to be slightly inhomogeneous in terms of composition across the inch by inch absorber layer. This compositional fluctuations are mostly in copper content but also a bit in gallium content. The bandgap measured on the finished solar cell might thus be different to the bandgap of the spot measured by photoluminescence. Another way to determine the bandgap is to fit the peak position of the main peak in room temperature photoluminescence measurements.

Since the absorption edge of $Cu(In,Ga)Se_2$ absorber layers is known to be broadened by tail states, the energy position of luminescence peak will not be $k_B T/2$ above the real bandgap as expected for an ideal semiconductor [44]. However, the value extracted by linear extrapolation of the external quantum efficiency also does not represent the real bandgap since it is also affected by the tail states [98]. The bandgap value from photoluminescence

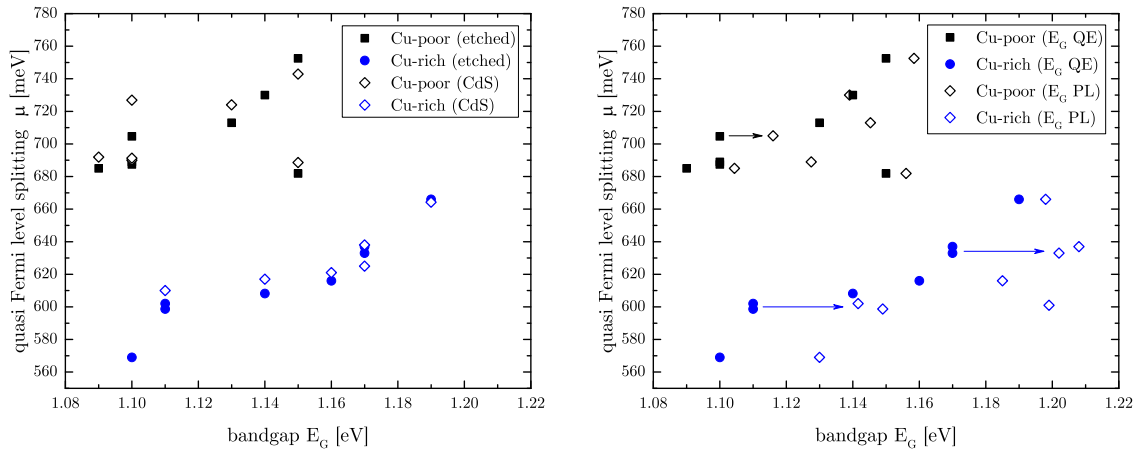

Figure 6.4: Left: Quasi Fermi level splitting after etching of bare absorbers (closed symbols) and absorber layer covered with CdS (open symbols) plotted over the bandgap form external quantum efficiency. Right: qFLs of bare absorbers after etching once plotted over the bandgap from external quantum efficiency (closed symbols) and plotted over the bandgap from photoluminescence(open symbols).

is expected to be slightly higher compared to the value from the linear extrapolation of external quantum efficiency. To verify this, the measured qFLs after etching are once plotted over the bandgap from external quantum efficiency (closed symbols) and once over the bandgap from photoluminescence (open symbol) on the right side of figure 6.4. All data points shift to higher energies as expected. The shift is on average smaller for Cu-poor samples ($\approx$ 20 meV) than in the Cu-rich samples ($\approx$ 30 meV) because of the less steep edge at high wavelengths in external quantum efficiency measurements compared to Cu-rich samples [20] leading to stronger underestimation of the bandgap value [98]. Plotting the data over the bandgap from photoluminescence will thus increase the difference between Cu-rich and Cu-poor samples by about 10 meV compared to the previous extracted 120 meV but not change anything in the interpretation.

The third and last change towards the broadening of the data set is the change of laser excitation source. Previously the 514 nm laser line of an argon ion laser was used for excitation because of its nearly perfect Gaussian laser profile and its stable long term power output needed for the time dependent measurements. All the previously shown photoluminescence measurements used to determine quasi Fermi level splitting values were done with this laser. However, using this laser sometimes artificial background signals hinder the evaluation of the data (as shown in figure C.3 p. 130). Those problems with background signals are most of the time worse for samples covered with CdS compared to bare absorber layers. Although a fixed temperature is used for fitting, the background changes the quasi Fermi level splitting by a few meV. To avoid this the excitation source is changed to a solid state laser with a wavelength of 660 nm. The laser profile is also nearly Gaussian shaped and only solely an artificial background in the luminescence signal is observed.

6.2.2 Enlargement of the data set

Evaluating the bandgap from photoluminescence measurements and using passivated absorber layers enables to access the qFLs of a variety of absorber layers in shorter

time. Also excitation dependent measurements are now possible, not being constrained to measurements at 3x equivalent suns as before. The qFLs is measured for a range of Cu(In,Ga)Se_2 absorber layers with Cu-poor and Cu-rich composition with GGI-ratios ranging from 0 to 0.45. All measurements are carried out with an excitation wavelength of 660 nm and with illumination condition ranging from 0.2 to 20 equivalent suns. The qFLs is extracted for each excitation density and plotted semi-logarithmically over the excitation intensity, like shown in section 5.3.1 in figure 5.3 (page 99). The value at 1 sun equivalent illumination is extracted from a linear fit through the data. The measured qFLs are plotted over the bandgap from photoluminescence in figure 6.5. Also polycrystalline $CuInSe_2$ are included for comparison (within the magenta dashed box).

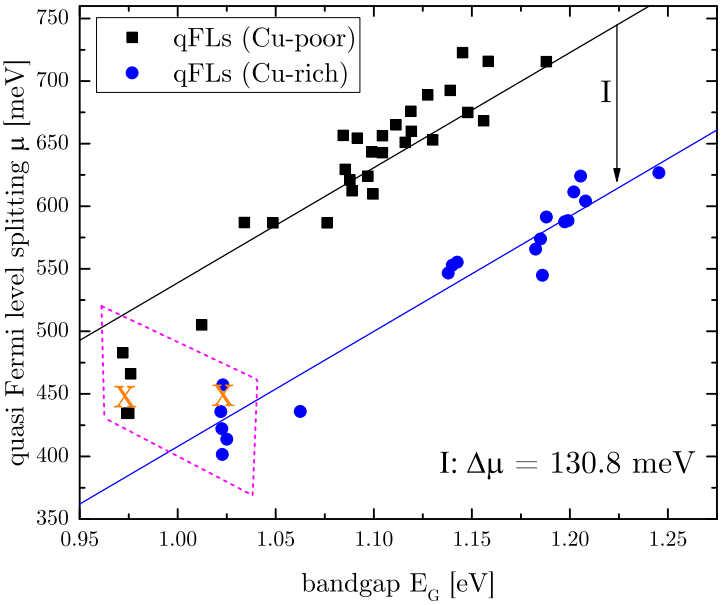

Figure 6.5: Quasi Fermi level splitting of CdS covered Cu-rich (blue) and Cu-poor (black) Cu(In,Ga)Se_2 absorber layers at 1 sun equivalent illumination. The linear Fit is done with a fixed slope of 0.92. The orange crosses mark the data determined by Regesch et al. [17].

Overall the same pattern as before is determined where the qFLs values of Cu-rich samples are well below the ones of Cu-poor samples, but the bandgap range probed was increased from about 80 meV to above 200 meV. With the inclusion of more samples, also more scattering is observed. This is not surprising since the crystal quality also varies between samples with the same GGI. The orange crosses (X) mark the quasi Fermi level splitting values found by Regesch et al. [17] on CdS passivated absorbers. For direct comparison the values measured at 5 suns equivalent illumination in the reference were shifted down by 48 meV using equation (5.11) assuming a k-value of 1.2, to represented the qFLs at 1 sun illumination. Furthermore, an error in the calibration procedure formerly used, leading to an overestimation of the calibration factor by a factor about 5 to 6, was taken into account shifting the data further down using the formula shown in figure C.2 (page 129).

The linear fit with a slope of 0.92 gives a difference in qFLS between Cu-rich and Cu-poor samples of about 130 meV, as also indicated by arrow I. The increase of the 10 meV relative to the previous value of 120 meV comes from the bandgap value used for plotting which was determined from photoluminescence and not from external quantum efficiency measurements. When looking closely at the linear fit, it is observed that all

qFLs values for Cu-poor $CuInSe_2$ lie below the fitting line. This can be explained by the introduction of the double gallium gradient, as shown in figure 6.3, that is not present in the ternary and is assumed to reduce the recombination at the front and back interface thus increasing the qFLs. A similar gallium double gradient is found in the Cu-rich samples, but the determined qFLs values of $CuInSe_2$ lie on the fitting line, although scattering quite a bit. This means that although the recombination at back and front interface is reduced by the gallium double gradient, the quasi Fermi level splitting does not improve stronger than predicted. This behaviour could be explained by a defect or recombination center moving deeper into the bandgap with increasing gallium content, which counter acts the improvements of the gallium grading. As discussed before this deep defect (possibly Cu_{III} as discussed in section 6.1.2) could also be the reason for the overall lower qFLs. The qFLs values measured for $CuInSe_2$ agree with the literature data (X) [17]. However, for the Cu-rich composition the literature data lies on the upper end of the value range determined, whereas the Cu-poor literature value lies on the lower end of the qFLs range determined. It is thus speculated that in the study [17] very good Cu-rich absorber were used, but that the process for the Cu-poor layers was not fully optimized. Furthermore, in the previous study the bandgap difference was not taken into account. Derived from the presented data it is argued that there is a difference in quasi Fermi level splitting of about 75 meV between Cu-rich and Cu-poor $CuInSe_2$, including the difference in bandgap of about 50 meV.

6.2.3 Comparison of the qFLs and V_{OC}

A second piece of absorber from each absorber layer studied in the previous chapter was made into a finished device as described in section 2.2.2. Each samples has six to eight solar cells and the current voltage characteristics were measured under a solar simulator or a halogen cold mirror lamp for each one. In both illumination conditions the incoming flux is adjusted to 100 mW cm^{-2} using a silicon reference solar cell, corresponding to 1 sun illumination. The average V_{OC} is plotted together with the qFLs determined at 1 sun equivalent illumination in figure 6.6. The V_{OC} of the Cu-poor samples (red) lie below the measured qFLs (black). On average a difference of (30 ± 14) meV is determined, as indicated by arrow II, making the qFLs a good predictor of the achievable V_{OC}. Moreover, it reveals that there might be further improvements possible in the baseline process used.

For the Cu-rich samples an about (90 ± 21) mV lower V_{OC} compared to the qFLs is determined over the whole GGI range, as indicated by arrow III. Since this loss is higher than the observed loss in the Cu-poor samples it is likely that the V_{OC} is reduced because of enhanced recombination close to the buffer interface due to interface defects or to stronger band bending [12], [18], [142]. To verify this, the current voltage characteristics of a Cu-rich and a Cu-poor sample are measured temperature dependent. The extracted V_{OC} is plotted over the temperature on the left side of figure 6.7. The linear fit of the data between 250 K and 320 K is extrapolated to 0 K as described in equation (2.14) and compared to the bandgap. For the Cu-poor sample the activation energy of the main recombination channel is slightly above the bandgap, indicating that the sample is limited by bulk recombination [18], [92]. The extrapolated activation energy of the Cu-rich sample is well below the bandgap, showing that the sample is dominated by recombination close to the absorber buffer interface. Another evidence for this is found by plotting the diode ideality factor over the temperature, as shown on the right side of figure 6.7. The ideality factor increases only slightly for the Cu-poor sample whereas it increases strongly

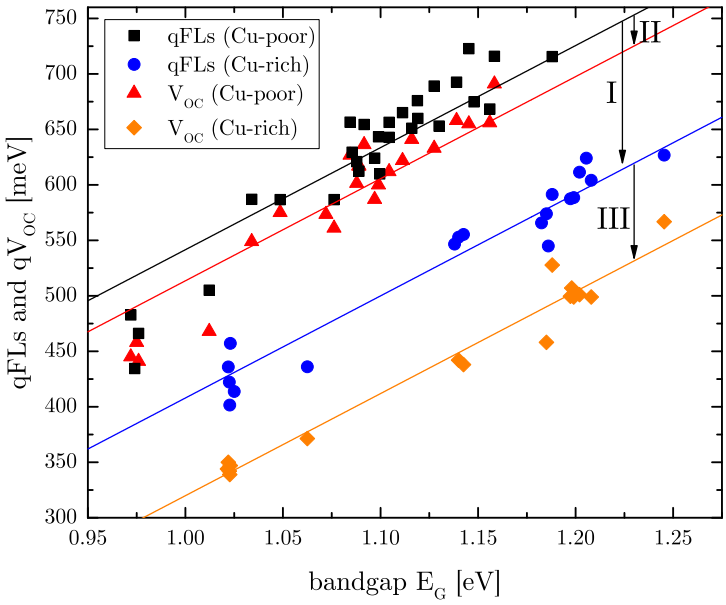

Figure 6.6: Quasi Fermi level splitting of CdS covered Cu-rich (blue) and Cu-poor (black) $Cu(In,Ga)Se_2$ absorber layers and the open circuit voltage (rich - orange, poor -red) for different gallium content both quantities measured at 1 sun equivalent illumination.

from 1.9 at room temperature to 3.6 at 200 K to for the Cu-rich sample. This strong temperature dependence can be explained by tunnel enhanced recombination or a multi-step recombination process [229]. Thus temperature dependent V_{OC} and ideality factor measurements both indicate an additional recombination channel close to the interface leading to a reduction of the V_{OC}.

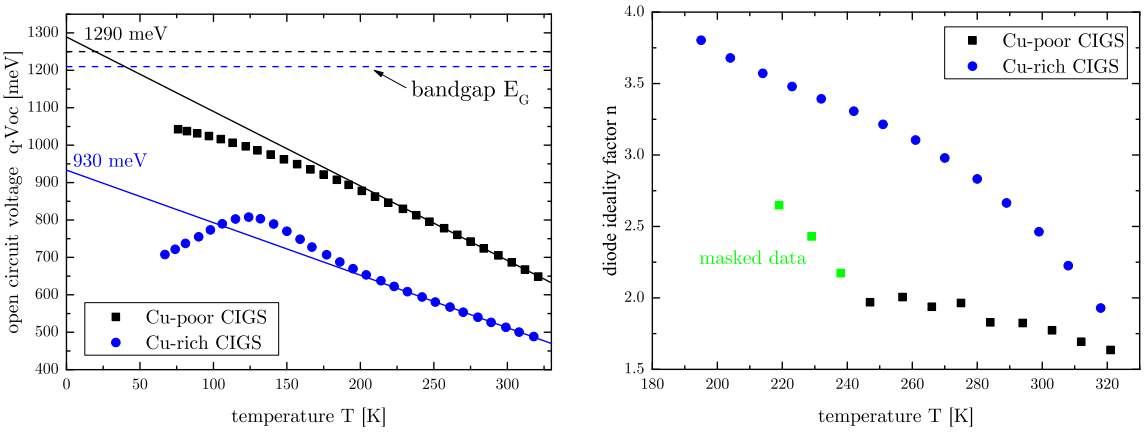

Figure 6.7: Left: Open circuit voltage of a Cu-poor (black) and a Cu-rich (blue) $Cu(In,Ga)Se_2$ device plotted over the temperature. The dashed lines indicate the respective bandgap determined from external quantum efficiency measurements. Right: Diode ideality factor for the same samples plotted over the temperature.

6.3 Summary

The comprehensive photoluminescence study of Cu(In,Ga)Se_2 samples with gallium content ranging from 0 to 0.4 in this chapter shows that the quasi Fermi level splitting of absorber layers grown with Cu-rich composition is about 120 meV lower compared to absorber layers with Cu-poor composition. This difference increases with gallium content but is still considerably high 75 meV for the ternary $CuInSe_2$. The deviation to literature [17], where the same quasi Fermi level splitting for both composition was reported, can be explained the quality of the investigated samples and by the fact that for the present study the bandgap was taken into consideration, which differs by about 50 meV between both compositions.

This difference between Cu-rich composition and Cu-poor composition can be explained by a fundamentally different recombination process between the absorber types. A possible defect fitting to this explanation is the second charge transition of the copper on indium antisite defect. The first charge transition of this point defect is the dominating acceptor defect (A2) in samples grown with high copper excess. It is proposed to be a deep acceptor about 800 meV above the valence band for the whole GGI range from theory [50] and was also possibly found in experiments in $CuGaSe_2$ layers [124] and in the investigated $CuInSe_2$ absorber layers (see section 4.4.3). This defect would act as a recombination center and reduce the quasi Fermi level splitting in $CuInSe_2$ samples grown with Cu-rich composition. With increasing gallium content the defect state moves deeper into the bandgap, increasing the detrimental influence on the quasi Fermi level splitting.

Comparing the quasi Fermi level splitting to the open circuit voltage of the finished device a drop of 30 meV is found for Cu-poor samples, showing that the qFLs is a good indicator for the absorber quality. The V_{OC} of the Cu-rich samples is about 90 meV lower than the respective qFLs. Temperature dependent current voltage measurements and the analysis of the V_{OC} and diode ideality factor reveal that this loss is related to recombination close to the absorber/buffer interface. The origin of this recombination is speculated to be a defect related to selenium, which is caused by the strong etching with KCN before the buffer layer deposition [147]. If the same strong etching is used for samples with Cu-poor composition a similar loss in V_{OC} can be observed [147].

Using this result it is possible to explain the findings of the In-Se treatment on $CuInSe_2$ samples [19], [176] and the Ga-Se treatment on Cu(In,Ga)Se_2 samples [20]. In case of the ternary $CuInSe_2$, the qFLs of the absorbers are at least similar between compositions and the lower V_{OC} in finished Cu-rich devices originates from recombination close to the interface. The treatment with In-Se forms a Cu-poor surface and removes the recombination close to the interface, leading to efficiencies close to Cu-poor $CuInSe_2$ samples [230]. In Cu(In,Ga)Se_2 samples the V_{OC} is also lowered by recombination close to the absorber-buffer interface in samples grown under copper excess. Using a Ga-Se treatment, also here a Cu-poor surface is formed removing most of the recombination close to the interface and improving the V_{OC} by up to 150 mV. However, the V_{OC} is still about 100 mV lower than in Cu-poor samples. Photoluminescence measurements show a 120 meV lower quasi Fermi level splitting in the as grown samples, likely caused by a deep defect. This additional recombination process is not changed with the treatment, leading to the difference in V_{OC} also observed after the treatment. It can further be concluded that the efficiency of treated Cu-rich Cu(In,Ga)Se_2 absorbers will not reach the efficiency of Cu-poor absorbers, if the deep recombination center is not removed.

Besides this, the degradation of the quasi Fermi level splitting of bare absorber layers exposed to air and light was studied. An overall about half as slow degradation has been found for Cu(In,Ga)Se_2 samples grown under copper excess ($\tau \approx 40\,\mathrm{min}$) compared to Cu-poor samples ($\tau \approx 25\,\mathrm{min}$). However, the strong difference of a factor of x20 found in polycrystalline $CuInSe_2$ samples [17] could not be verified. The absolute loss in qFLs is higher in Cu-poor samples (100 meV) than in Cu-rich samples (40 meV) similar to what has been observed in $CuInSe_2$. Depositing a thin layer of CdS passivates the surface preventing any degradation of the qFLs for several months or even years. The initial qFLs values after a KCN etch and of a sample covered with CdS are within error the same, with slightly higher values (5 meV) for passivated samples.

All in all, the knowledge about the quasi Fermi level splitting of chalcopyrites could be advanced from $CuInSe_2$ [17] to Cu(In,Ga)Se_2, also published in [193]. The different degradation behaviour for Cu-rich and Cu-poor compositions could be partly confirmed, but lower quasi Fermi level splitting values for Cu-rich samples were found for the whole GGI range investigated.

CHAPTER

SEVEN

SUMMARY

$CuInSe_2$ and $Cu(In,Ga)Se_2$ absorbers are an interesting and versatile material for the fabrication of solar cells. Especially absorber layers which are grown with a final Cu-rich composition exhibit advantageous material properties. However, they can not live up to the expectations when made into devices showing a low open circuit voltage and high diode factors. Within this work different aspects of efficiency limitations of $CuInSe_2$ and $Cu(In,Ga)Se_2$ solar cells grown under copper excess have been investigated.

In the first part, an alkali treatment with potassium fluoride, which on Cu-poor samples leads to strong improvements in device performance, was adapted to Cu-rich grown samples by adding an etching step. The alkali treatment has been found to work similarly on both Cu-rich and Cu-poor samples, although both compositions exhibit different electronic properties. In line with reported findings in literature, the open circuit voltage and fill factor are improved by the treatment. Furthermore, a few nanometer thick and patterned surface layer is formed with lower copper content. The photoluminescence characteristics of Cu-rich samples consisting of several defined peaks allows to conclude that this new surface layer grows on top of the absorber layer and not by pushing copper into the absorber. Those photoluminescence fingerprints also show a change of the defect structure. In detail, the activation energy of the second acceptor is changed after the treatment (60 meV $\rightarrow$ $\sim$70 meV) which is observed throughout the whole absorber layer.

For Cu-poor samples, the gain in V_{OC} is the same as the gain in quasi Fermi level splitting, showing that only the bulk profits from the treatment since the surface is already good. However, the gain is less than half compared to values reported in literature [26], [171] which might be due to the usage of $CuInSe_2$ instead of $Cu(In,Ga)Se_2$, the addition of an etching step, or due to a non optimized process. In case of Cu-rich samples, the gain in V_{OC} is higher and originates roughly equally from an improvement of the bulk and the removal of a 200 meV defect close to the interface. However, a deep defect is observed in room temperature photoluminescence measurements of Cu-rich $CuInSe_2$ samples independent of the treatment. This defect gives a broad peak centered around 0.8 eV in photoluminescence measurements and is proposed to originate from the second charge transition of the Cu_{In} antisite defect [Cu_{In}(-1/-2)]. The first charge transition of this defect is the main acceptor (A2) for samples grown with high copper excess ([Cu]/([Ga] + [In]) $>$ 1.2). The second charge transition is predicted to be an acceptor 0.6 eV to 0.8 eV above the valence band from calculations for the whole [Ga]/([Ga] + [In])-range and was recently observed in $CuGaSe_2$ [115].

This defect is also a possible explanation for the lower quasi Fermi level splitting of

130 meV observed in Cu-rich Cu(In,Ga)Se_2 samples compared to Cu-poor samples. In contrast to previous studies [17], also in $CuInSe_2$ a difference of 75 meV was observed. The mismatch stems mainly from taking the difference in bandgap into consideration ($\Delta E_G \sim 50$ meV), but also from better Cu-poor samples. The gap in quasi Fermi level splitting values between Cu-poor and Cu-rich in Cu(In,Ga)Se_2 increases with gallium content. This increasing difference matches the 0.8 eV defect [Cu_{In}(-1/-2)] which stays constant above the valence band and thus moves deeper into the bandgap, increasing its detrimental effect. It is likely that this is also the reason why the treatment of $CuInSe_2$ with In-Se [19] works better than the treatment of Cu(In,Ga)Se_2 with Ga-Se [20]. Removing or passivating this defect will be a key objective to improve the efficiency of Cu-rich grown chalcopyrites.

On the positive side, no difference in the optical diode factor, determined on passivated absorber layers, between Cu-rich and Cu-poor composition is found. This newly introduced property is essentially the power law exponent determined in intensity dependent photoluminescence measurements at room temperature. A direct link between optical diode factor of absorber layers and the diode factor of finished devices was shown and verified using Cu-poor Cu(In,Ga)Se_2 samples. For Cu-rich layers, the diode factor of the device is above the optical diode factor due to the addition of a recombination channel during device finishing. This channel is likely related to a defect caused by the strong etching with potassium cyanide [147].

During the investigation of the deep defect, additionally a peak at 0.9 eV is detected and attributed to a DA-transition. A third acceptor, beyond the two well established acceptors A1 and A2, is determined which is (135 ± 10) meV above the valence band and is proposed to originate from the indium vacancy (V_{In}). The defect was also detected in admittance measurements and in Cu(In,Ga)Se_2 samples with low gallium content.

In summary using the underlying scientific questions, this thesis can be consolidated:
(**i**) Do alkali treatments also work on Cu-rich absorber layers?
- Yes, it works similar and additionally removes a surface defect.
(**ii**) Is the V_{OC} limited by deep defects?
- Yes, the defect is likely Cu_{In}(-1/-2), also a new acceptor (A3) was found.
(**iii**) Is the diode factor intrinsically higher in Cu-rich samples?
- No, the optical diode factor is the same in both compositions.
(**iv**) Is the qFLs of Cu-rich and Cu-poor Cu(In,Ga)Se_2 absorber layers comparable?
- No, lower qFLs in Cu-rich films are observed also limiting the gains in V_{OC} possible with surface treatments.

Within this work, some new findings regarding Cu-rich chalcopyrites have been presented. With the optical diode factor, a method has been developed and presented which possibly can be used for the screening of new photovoltaic materials. Further research on photovoltaic materials and renewable energies in general are a key component to make the energy revolution happen. And this revolution is sorely needed as the world which is already warmed up by 1 °C is heading towards a global warming of above 3 °C until 2100 [231], [232] with its current policies, missing the objective of the Paris agreement of 1.5 °C to 2 °C big time.

CHAPTER

EIGHT

OUTLOOK

Within this work, many open questions could be answered and the knowledge about $Cu(In,Ga)Se_2$ solar cells was expanded. However, not all topics could be investigated thoroughly in their full extend. Furthermore, new questions and possible aspects of investigation arose over time. A few of those things will be outlined within the next paragraphs.

Applying the developed in-situ treatment with etching step to Cu-rich $CuInSe_2$ absorbers shows promising results and also works on Cu-poor samples. However, the gain in V_{OC} is much lower compared to literature values on treated $Cu(In,Ga)Se_2$. The reason for this remains unknown but could be related to the material (no gallium), a not optimized process, or the exposure to air during the process. To clarify this the alkali treatment with KF has to be optimized and performed on Cu-poor $Cu(In,Ga)Se_2$ with and without etching step. Furthermore, a KF treatment on Cu-rich $Cu(In,Ga)Se_2$ as well as the combination of different surface treatments (like first Ga-Se and then KF PDT) are interesting topics. The treatment with In or Ga has been shown to change mainly the sample surface whereas the treatment with KF as well improves the bulk. Combining the results of this thesis and from Aida et al [19], for a Cu-rich $CuInSe_2$ sample after etching a deposition of indium for 1 min to 2 min at 300 °C with subsequent annealing and KF deposition at 380 °C for 4 min is proposed.

A broad defect band observed around 0.8 eV in photoluminescence measurements likely limits the device performance of Cu-rich solar cells. Removing this defect state should thus facilitate strong improvements in the quasi Fermi level splitting and V_{OC}. For the time being this defect is attributed to the second charge transition of the Cu_{In} antisite. The relative acceptor concentration of A1 (V_{Cu}) and A2 (Cu_{In}) changes with Cu-excess [15]. It is thus interesting to check if the efficiency and the photoluminescence signal of the 0.8 eV peak changes when investigating a narrow region of Cu-excess just above the stoichiometric point. To investigate this topic in greater detail, [Cu]/([Ga] + [In])-ratios between 1 and 1.1 would be a good starting point. Furthermore, $CuInSe_2$ should be used instead of $Cu(In,Ga)Se_2$ to avoid effects of bandgap grading, bandgap fluctuations, and inhomogeneities across the sample. Additionally, the influence of sodium on the defect formation might be interesting to look at. First result gathered on two absorber layers grown in the same process, once on a standard substrate SLG/Mo and once with a sodium blocking layer between SLG and molybdenum, show that the presence of sodium during growth reduces the defect formation.

Within this work a new acceptor state was found and attributed to the indium vacancy V_{In}. However, from the author's point of view this attribution is not strongly evidenced and might be subject to change when more data is available. So far it has been observed that the temperature of the cracking tube and thus the selenium species available during growth has a strong influence on the formation likelihood of this defect state. A more detailed study in this area might clarify things here. Besides this, the defect state has been observed in $CuInSe_2$ and $Cu(In,Ga)Se_2$ with low gallium content. It should thus be also observable in $CuGaSe_2$. To verify this low temperature photoluminescence measurements of polycrystalline $CuGaSe_2$ samples grown with high selenium over pressure and activated cracking tube are needed.

To complement the defect picture derived from photoluminescence also more research about the second deep peak observed in the $Cu(In,Ga)Se_2$ samples has to be conducted. The nature of this defect so far remains unknown (FB, DA) and it is unclear whether the deep defect involved is an acceptor or a donor state.

The optical diode factor was introduced and derived within this work. A follow up study is needed to test the method on other materials like perovskites, kesterites, GaAs, CdTe, or silicon. Together with quasi Fermi level splitting measurements, it is proposed to be a good screening technique for new materials.

Overall, there are always more topics to investigate and more questions to be answered. A considerable amount of knowledge was added with this work, but there are still various ways to improve the understanding and the efficiency of chalcopyrites even further.

APPENDIX

A

ACKNOWLEDGMENTS

In the making of this thesis, I received a lot of support, not only while writing it, but also while gathering the data, sharing my results, or processing solar cells.

First of all, I want to thank my supervisor Prof. Dr. Susanne Siebentritt for the opportunity to work at the Laboratory for Photovoltaics in Luxemburg and the chance to work in the field of renewable energies. I am grateful for her guidance in the last four years. From endless hours of discussing results over the opportunities to share my results at conference all over the world, her supervision was always fuelled by the desire to advance the research on solar cells and to help me to become a better scientist every day through my work.

Furthermore, I want to thank Andreas Michels, Jürgen Christen, Stephan Bücheler, Daniele Brida and Susanne Siebentritt for being part of the dissertation defence committee.

Additionally, I want to thank all my colleagues from LPV and LEM – not only for their scientific support, but also for making me feel welcome and at home at my time in Luxembourg. I am leaving with many fond memories, half happy about what is to come, but also half blue looking back at the last four years. A special thanks goes to Thomas Schuler for the technical support and his never ending help with repairing the PVD. Also, I want to thank Patricia Ramoa for organizing so many things behind the scenes, like paper work and placing orders. I want to thank Michele Melchiorre as well, for the countless KCN etches and baseline processes he has done for me. At last but not least, I want to thank Hossem Elanzeerey for the great team work and the joint effort regarding the KF PDT. Moreover, I want to thank Conrad Spindler, Max **H.** Wolter, Alberto Lomuscio, David Regesch and Jan Sendler for all those productive PL discussions.

I also want to thank my friends and family, especially my parents, for their support during my PhD. My last thanks go to Britta Ingwersen – the only person I know who can kick my ass in such a loving way that I achieved things I never thought I would even dare to try. Thank you for your never ending support in all aspects of my life.

In the end, I want to thank every one, who is not mentioned on this page. A doctor thesis is such an enormous task that it cannot be done by one person alone. So if you have supported me, helped me or just gave me something to laugh about within the last four years – thank you for your contribution to this doctor thesis.

The presented measurement data and results were not gathered alone by the author. Following people contributed substantially to the presented work.

- **Hossam Elanzeery** - all results regarding the KF PDT (chapter 3) were gathered in a joint effort with Hossam, which includes the sample growth as well as the treatment routine. Also current voltage measurements at room temperature (3.1/3.4/3.12) and temperature dependent (3.2/3.7/3.13/6.7), external quantum efficiency measurements (3.2/3.5/3.12), and capacitance measurements (3.6/3.13) were performed by Hossam. The admittance measurements (4.10/4.11) used for comparison in chapter 4.3 were done and evaluated by him.

- **Michele Melchiorre** - did all baseline processing which includes washing of substrates, molybdenum deposition, KCN etching after growth, CdS deposition, window layer deposition, and application of grids. Also the KCN etchings needed to study the degradation behaviour of the quasi Fermi level splitting of absorber layers exposed to air were done by him. Michele furthermore supplied all scanning electron microscopy images shown in this work (2.6/3.8/D1/D2/D3) and supplied energy-dispersive X-ray spectroscopy (EDX) data to study the elemental composition of the absorber layers.

- **Leo Choubrac** - grew most of the Cu(In,Ga)Se_2 samples investigated in chapter 5 and made the IV measurements shown in Fig. 5.1. Those Cu(In,Ga)Se_2 samples are also analysed in chapter 6 and account for about 1/3 of the data set. The open circuit voltage data used in Fig. 6.6 was mostly gathered by Hossam, but also partly by Leo.

- **Nathalie Valle** - performed the secondary ion mass spectroscopy measurements shown in Fig. 6.3.

- **Jerome Guillot** - performed the X-ray photo-electron spectroscopy measurements shown in Fig. 3.3.

- **Max H. Wolter** - deposited a scattering layer onto some Cu(In,Ga)Se_2 samples to remove interference effects disturbing the photoluminescence spectra (Fig. 4.6/4.8)

- **David Regesch** - supplied a self written software which greatly simplifies the evaluation measured photoluminescence spectra which therefore was widely used.

- **DLR Institute of Networked Energy Systems** - supplied the setup used for SunsVoc measurements (Fig. 5.2/5.4).

APPENDIX

B

GLOSSARY

Table B.1: Abbreviations used in the manuscript.

AM	air mass (1.5)
BFM	beam flux monitor
CdS	cadmium sulfide buffer layer
EDX	energy dispersive X-ray diffraction
EIES	electron impact emission spectroscopy
EQE	external quantum efficiency
HSE	Heyd, Scuseria and Ernzerhof
IV	current voltage (measurement)
IV(T)	temperature dependent current voltage measurement
MBE	molecular beam epitaxy
PDT	post deposition treatment
PL	photoluminescence
PV	photovoltaics
PVD	physical vapour deposition
QCM	quartz crystal micro balance
SCR	space charge region
SEM	scanning electron microscope
SIMS	secondary ion mass spectrometry
TCO	transparent conductive oxide
XPS	X-ray photo-electron spectroscopy

Table B.2: Commonly used symbols and acronyms.

symbol	unit	description
E	eV	energy
E_{V}	eV	valence band energy
E_{C}	eV	conduction band energy
E_{G}	eV	band gap
E_{A}	eV	activation energy
E_{F}	eV	fermi energy
$E_{\mathrm{h}\nu}$ or E_{Ph}	eV	photon energy
Dn or Dp	$\mathrm{cm^2\,s^{-1}}$	diffusion constant
μ or $\Delta\mu$	eV	quasi Fermi level splitting (qFLs)
m_e	g	electron mass
m_e	g	hole mass
m_r	g	reduced electron-hole mass
N_{A}	$\mathrm{cm^3}$	doping concentration of acceptors
N_{D}	$\mathrm{cm^3}$	doping concentration of donors
N_{V}	$\mathrm{eV\,cm^{-3}}$	density of states at the valence band
N_{C}	$\mathrm{eV\,cm^{-3}}$	density of states at the conduction band
V_{bi}	V	built in voltage
x_{SCR}	m	space charge region width
λ	nm	wavelength
T	K	temperature
S	1	Huang-Rhys factor
η	%	(power conversion) efficiency
FF	%	fill factor
V_{OC}	eV	open circuit voltage
J_{SC}	$\mathrm{mA\,cm^{-2}}$	short circuit current density
A	1	diode (ideality) factor
R_{S}	$\Omega\,\mathrm{cm^2}$	series resistance
R_{Sh}	$\Omega\,\mathrm{cm^2}$	shunt resistance
J_0	$\mathrm{mA\,cm^{-2}}$	saturation current density

Table B.3: Constants.

symbol	value	description
e	$1.602 \times 10^{-19}\,\mathrm{C}$	elemental charge
ϵ_0	$8.85 \times 10^{-12}\,\mathrm{F\,m^{-1}}$	dielectric permittivity
ϵ_r	13.6	dielectric constant [103]
h	$4.135 \times 10^{-15}\,\mathrm{meV\,s^{-1}}$	Planck constant
$\hbar$	$6.582 \times 10^{-16}\,\mathrm{meV\,s^{-1}}$	reduced Planck constant
k_B	$8.617 \times 10^{-3}\,\mathrm{meV\,K^{-1}}$	Boltzmann constant
R_y	13.6 eV	Rydberg energy

APPENDIX

C

CALIBRATION METHODS FOR PL MEASUREMENTS AND QUASI FERMI LEVEL SPLITTING ANALYSIS

C.1 Calibration of the measurement set up

Photoluminescence measurements are a versatile tool and widely used within this thesis. To convert the raw data into something useful, several correction steps have to be done. Each measurement consist of a "illuminated" and a "dark" measurement. For the latter, a shutter inside the monochromator is closed and a measurement with the same duration and detector settings is done. This dark spectrum accounts for the detector signal without any input and is subtracted from the illuminated spectrum. This process is automatically done within the measurement software. The result is a spectrum which only consists of the signal from the sample. All spectra are measured in the nanometer regime.

To correct for the spectral sensitivity of the camera, the transmission properties of the optical fiber, the transmission properties of the long-pass filter as well as the spectrally dependent reflection of the two off-axis collection mirrors, a reference spectrum with a halogen lamp with a known spectrum is taken. For the reference spectrum the light of the halogen lamp is guided onto a spectralon surface positioned at the sample position, which has a Lambertian emission profile and a flat reflection curve close to one over the whole wavelength range studied. The former one is needed to simulated to photoluminescence emission from a semiconductor surface, which also has a Lambertian profile. To calculate the correction function $\Gamma_{\mathrm{corr}}(\mathrm{nm})$, the known lamp spectrum in (photons/s/cm^2/nm) is divided by the measured spectrum in (counts/s/nm). After multiplying the measured photoluminescence spectrum with the correction function it has the same unit as the lamp spectrum. Important to note here is that all shown spectra have this unit and never $\mathrm{W\,cm^{-2}\,nm^{-1}}$. All data are treated in energy space later on. To transform the spectra every wavelength value is calculated into the respective energy ($E = hc/\lambda$) with Planck constant h and the speed of light c. The corresponding ordinates are transformed using the Jacobian transformation to account for different energy spacing, as shown in equation (C.1).

$$y[\mathrm{photons/s/cm^2/nm}] \rightarrow y \cdot hc/x^2[\mathrm{photons/s/cm^2/eV}] \tag{C.1}$$

For absolute calibrated photoluminescence measurements, a calibration factor has to be determined and multiplied to the data to convert the data from relative values into

absolute ones. The basic idea behind the calibration method is to link the known photon flux of a laser beam with the measurement signal of the photoluminescence set up.

In the first step the incoming photon flux density is quantified. To do this three things have to be known, the beam shape, the power at the sample position and the wavelength of the emitted photons. The shape of the laser beam can be directly accessed by measuring it with a CCD camera at the sample position. Both, the argon ion and the diode laser have a nearly Gaussian shape in X and Y dimension, which is fitted to determine the radius. A power meter is used to determined the power of the laser at the sample position. In general, about 40 % of the output power of the laser is lost on the optical path to the sample position in the system due to scattering or non perfect reflection. The information about the wavelength can be taken from the manual or measured with the monochromator.

For the extraction of the qFLs, Planck's generalized law (equation (2.16)) is used, which is only valid for homogenous excitation. Since the spot from which we collect light from inside the PL setup is only about 370 µm wide in diameter (depending on the optical fiber used) and with this much smaller than the radius of the laser spot $r \approx 1.3\,\mathrm{mm}$, we have a laterally flat excitation in first approximation. Knowing this, the photon flux at the peak of the Gaussian profile can be calculated using equation (C.2). With the measured power P, the elemental charge e, the area of the laser beam A and the energy per photon E_{Ph}. The 2 in front accounts for the fact that the power at the peak of a Gaussian profile is twice as high as the average power measured by the power meter.

$$\Phi[\mathrm{photons/s/cm^2}] = \frac{2 \cdot P}{A \cdot E_{\mathrm{Ph}}} \tag{C.2}$$

In a second step the known laser spot is reflected from a spectralon and measured with the photoluminescence set up. The raw data is spectrally corrected and converted into energy space. Although the laser beam consist of only one wavelength, a several meV wide peak will be observed in the measured data. The broadening of the signal originates from the fiber and the monochromator grating used. Integrating this peak, gives a relative photon flux in photons/s/cm^2. Dividing the calculated flux of the laser spot by the relative photon flux measured by the PL setup, gives the calibration factor. Multiplying this to measured photoluminescence spectra gives the spectrum in the desired unit of photons/s/cm^2/nm in absolute numbers.

C.2 Evaluation of the qFLs

To evaluate the quasi Fermi level splitting, room temperature photoluminescence spectra are recorded after the calibration of the set up and the determination of the calibration factor. For the evaluation, Planck's generalized law (equation (2.16)) is simplified using a Boltzmann approximation and setting the absorptivity to unity, as described in section 2.3.5. Rearranging the equation afterwards gives equation (C.3), in which the term 10^{23} summarizes the constant in the equation. Evaluating the high energy slope above the bandgap in a semi-logarithmic plot should give a linear behaviour which's slope is defined by $1/k_{\mathrm{B}}T$. The intercept with the Y-axis divided by $k_{\mathrm{B}}T$ defines the quasi Fermi level splitting.

$$\ln\left(\frac{Y_{\mathrm{PL}}(E)}{10^{23}\,E^2}\right) = \frac{\mu}{k_{\mathrm{B}}T} - \frac{E}{k_{\mathrm{B}}T} \tag{C.3}$$

On the left of figure C.1 the calibrated photoluminescence spectra of a passivated absorber is plotted over the energy for several illumination conditions. On the right side of figure C.1 the spectrum was divided by $10^{23} \cdot E^2$ and the logarithm of the whole term was calculated. Above the bandgap a linear decreases of the measurements data is observed which can be fitted according to equation (C.3). The photoluminescence yield increases with excitation power and thus also the quasi Fermi level splitting, which is directly observed by an upward shift of the data. The data is in general fitted about 0.1 eV above the peak maximum to ensure that the absorptivity can be assumed to be unity. The lowest curve (black) was only measured with the InGaAs-detector array, which strongly limits the range that can be used for fitting. Above 1.47 eV only noise is measured, since the long-pass laser filter blocks the light above this energy. For samples with lower luminescence yield (eg. Cu-rich samples) the fitting region occasionally has to be shifted closer to the peak maximum.

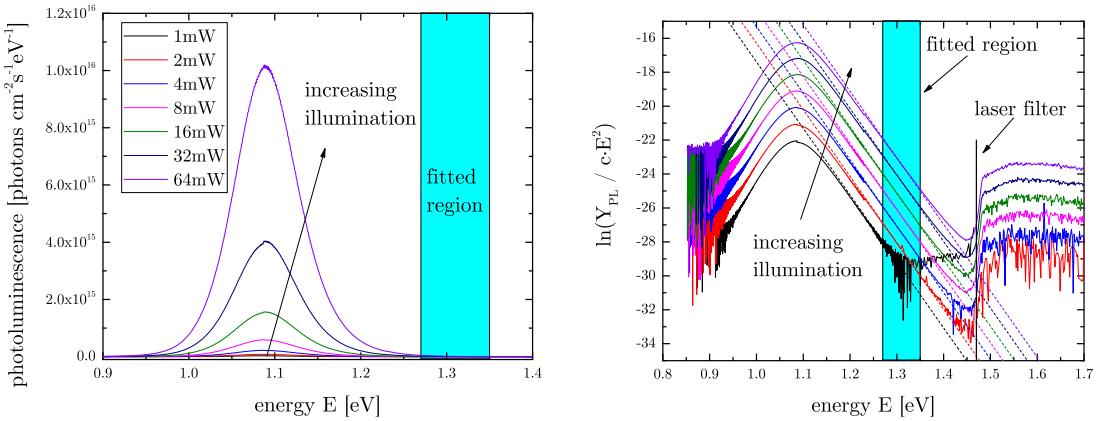

Figure C.1: Left: Photoluminescence spectrum of a Cu-poor Cu(In,Ga)Se_2 sample measured at various illumination condition equivalent to 0.2 to 13 suns. Right: Logarithm of the photoluminescence yield plotted over the energy. The quasi Fermi level splitting is fitted in the cyan region.

The linear fit generally gives temperature values between 300 K and 320 K. Those values are thus slightly above the room temperature of 296 K measured by a thermometer. This offset in the temperature likely comes from a small background noise that bends the curve in the semi-logarithmic plot. If not stated otherwise, a fitting temperature of 296 K is used for analysis. That this assumption is correct was verified using a thermal camera. Until illumination condition equivalent to 10 suns no raise in temperature in the illuminated spot is detected.

Error assessment

The evaluation of the quasi Fermi level splitting uses only the lower 5 % of the recorded photoluminescence peak and is thus prone to background noise, leading to the overestimation of the temperature. To estimate the influence of the temperature, an error analysis is carried out. The left side of figure C.2 shows the change of the evaluated qFLs with artificially changing fitting temperature in the evaluation of the same spectrum. The qFLs decreases linear with about 2.5 meV K^{-1} with increasing fitting temperature. An overestimation of the temperature due to background noise, easily leading to 10 K difference, has

a strong influence of 25 meV. To avoid this, in most cases a fixed temperature of 296 K corresponding to the measured room temperature is used.

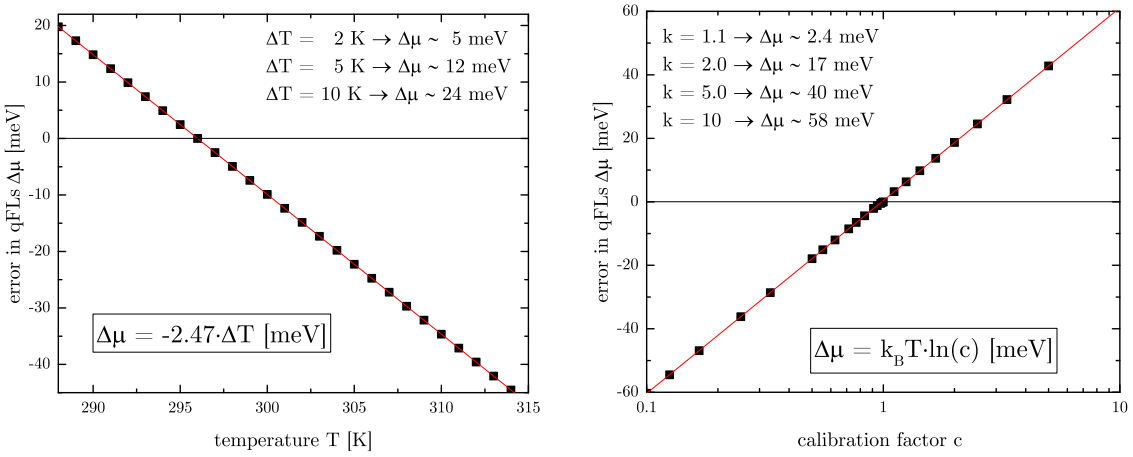

Figure C.2: Left: Error of the quasi Fermi level splitting depending on the temperature. Right: Error of the quasi Fermi level splitting depending on a multiplicative error of the calibration factor.

The determination of the calibration factor depends on several quantities which are all experimentally determined and thus have small errors. To investigate the error in calibration factor onto the evaluated qFLs, a factor c was artificially multiplied to the calibration factor. On the right side of figure C.2 the change of the qFLs is plotted semi-logarithmically over the multiplicative factor c. The error in qFLs changes logarithmically with the calibration factor and can be calculated by the formula shown in figure C.2.

The error in calibration factor estimated to be below 20 % leading to an maximal error in qFLs of 4.7 meV. The overall error in qFLs including temperature, calibration factor and spatial variation on a sample is estimated to be ±12 meV

Background correction methods

As seen in figure C.1 only a small part of the high energy wing is fitted in a logarithmic scale for the evaluation of the qFLs. This is problematic when the luminescence signal from the sample is low and small background signals slightly distort the spectra. An example for this is shown on the left side of figure C.3 in which the photoluminescence spectrum at room temperature of a Cu-rich Cu(In,Ga)Se_2 sample is plotted with the dark count correction but without a spectral correction, as described in section C. In the range from 350 nm to 550 nm the data scatters randomly around zero, showing that the dark count correction works and that there is only noise in the signal. Above 550 nm and thus above the long pass filter the data points scatter around a value of 50, which corresponds to about 0.5 % of the peak maximum. Even with some effort, the source of this background signal could not clearly identified. It varies between samples and is mainly seen when using the 514 nm laser line of the argon ion laser.

The background signal leads to a deviation of the linear drop of the high energy slope above 1.4 eV as seen on the right side of figure C.3 in the black curve. This artificially increases the temperature evaluated by the linear Fit to values above 330 K for moderate excitation densities. This higher temperature decreases the extracted qFLs value by about 75 meV compared to the qFLs evaluated with the measured room temperature

(2.47 meV K^{-1} as discussed earlier). Since the background signal differs for every sample and even differs for different positions on one sample, various ways have been tested to correct for this background signal. The most robust way to correct for it, is to subtract the mean value of the background noise (shown in red in figure C.3) in the raw data before the spectral correction is multiplied. As a result the bending of the high energy slope in the semi-logarithmic plot (blue data) is greatly reduced, increasing the fitted slope and thus decreasing the extracted temperature to a more realistic value of 304 K at 1 sun.

A constant offset in the nanometer regime leads to an exponentially decaying signal in the eV-regime due to the non equidistant energy intervals in the transformation. Therefore, a second method was tested in which an exponentially decaying curve was subtracted from the photoluminescence data in the eV-regime before the qFLs evaluation. With this exponential correction (green curve) even better results can be achieved, meaning a lower error in the slope and in qFLs as well as a lower temperature value. However, the correction is more ambiguous and less robust. The spectra in chapter 6 are fitted with a fixed temperature, strongly limiting the effect of background noise onto the derived qFLs values. In the rare cases with severe background contributions, a linear correction is used to improve the fitting.

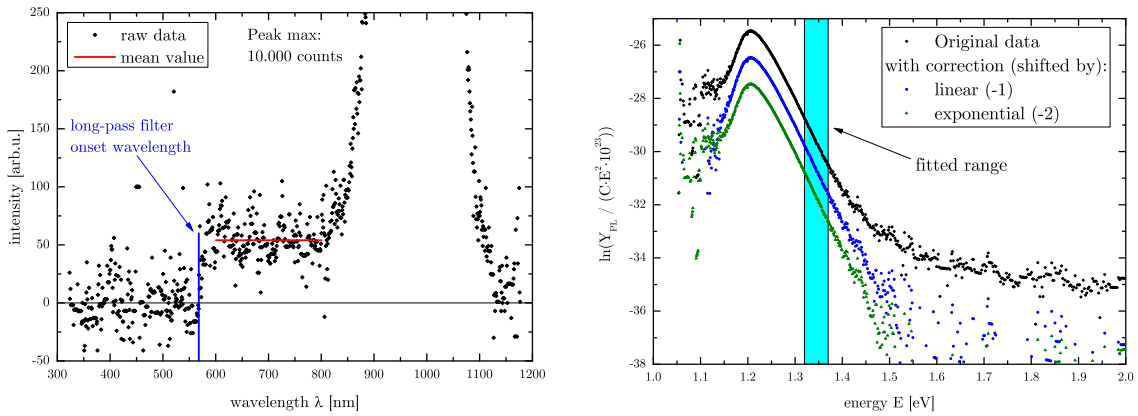

Figure C.3: Left: Spectrally uncorrected photoluminescence measurement of a Cu(In,Ga)Se_2 sample at room temperature. A clear background (600 nm to 800 nm) is observed after the long pass filter, that is different from the observed noise (350 nm to 550 nm). Right: semi-logarithmic plot of the converted photoluminescence plotted over the energy. Different correction methods are applied to correct for the background signal. The spectra for the corrections are shifted downwards for better differentiation.

Determination illumination condition

For the evaluation of the qFLs, room temperature photoluminescence measurements are used, where the absorber layer is excited with monochromatic light. Although this is already a good indicator for the quality of the absorber, a direct comparison to the open circuit voltage is desirable. For this purpose the illumination conditions in the photoluminescence measurement have to match the illumination conditions during current voltage measurements, which uses the AM1.5 solar spectrum from a solar simulator. Since it is not practical to make photoluminescence measurements under the illumination of a solar simulator, the number of photons that the semiconductor can absorb from the solar spectrum and from the laser excitation are compared. For the laser spot the photon

flux can be calculated depending on the power with equation (C.2). Since the photon energy of the lase excitaton is way above the bandgap, it is assumed that all photons are absorbed. In the current voltage measurements the number of absorbed photons depend on the bandgap, since lower bandgaps absorb a wider part of the spectrum. The left side of figure C.4 shows the number of photons absorbed form the AM1.5 solar spectrum for different bandgap energies. For the calculation a complete absorption above the bandgap is assumed. For nearly all evaluations a bandgap of 1.1 eV was taken leading to a flux of $2.76 \times 10^{15}\,\mathrm{s^{-1}\,cm^{-2}}$. The measured flux of the laser at the sample position divided by this flux will be called equivalent flux within this thesis. For the evaluation of the qFLs at 1 sun equivalent flux, the photoluminescence is measured for several laser output powers between 1 mW and 100 mW, corresponding to roughly 0.2 to 20 suns. Only in the evaluation step later on the exact numbers of suns per output power is determined and the qFLs at 1 sun determined by a linear fit through the data.

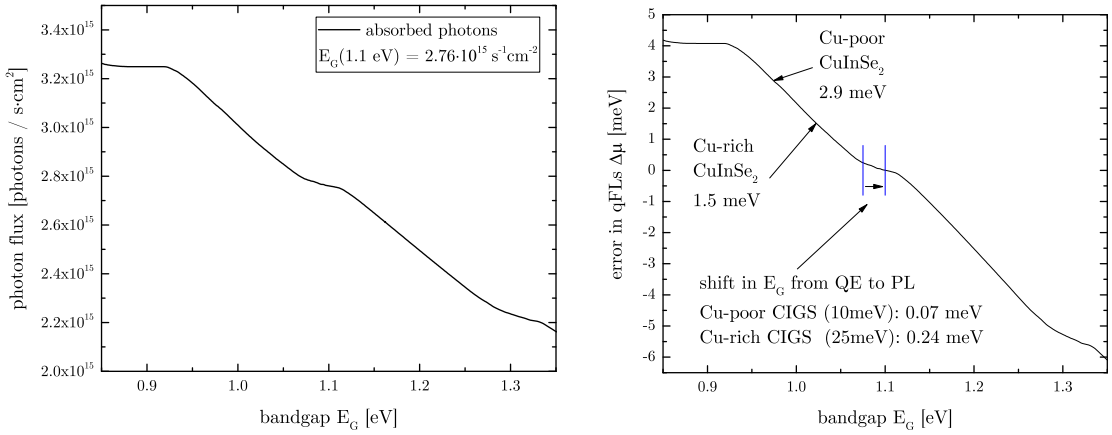

Figure C.4: Number of photons absorbed from an AM1.5 solar spectrum calculated for different bandgaps (left). Difference in qFLs if not the correct bandgap is chosen for the equivalent suns determination (right).

Using the same bandgap for the calculation of the 1 sun equivalent illumination causes errors in the final qFLs. To get an idea about how large this error is, the already known relationship of the error in the calibration factor can be used (right side of figure C.2). On the right side of figure C.4 the change in qFLs depicted when a wrong bandgap is used to calculated the 1 sun equivalent illumination conditions. Using the example of Cu-poor $CuInSe_2$ with a bandgap of 0.995 eV, the qFLs will be overestimated by only 3 meV. For Cu-rich $CuInSe_2$ a difference of 1.5 meV is estimated. In this case the introduced error in qFLs is negligible. For $Cu(In,Ga)Se_2$ samples with high gallium content an under erstimation of up to 5 meV is possible.

In section 6.2.1, the bandgap determination is switched from the determination by external quantum efficiency to the evaluation of the photoluminescence peak maximum. This correspond to a change in bandgap of up to 25 meV. The error in qFLs arising from this bandgap change onto the determination of the equivalent illumination condition to 1 sun is merely 0.3 meV. All these small errors in the qFLs do not change any of the interpretations made in chapter 6.

APPENDIX

D

ADDITIONAL INFORMATION AND DATA

D.1 KF post deposition treatment of $CuInSe_2$

To determine the thickness of the CdS buffer layer of treated and untreated samples, cross section scanning electron images are taken at several spots. Exemplary SEM pictures of a Cu-rich sample without (top) and with KF PDT (bottom) are shown in in figure D.1. The same is shown for a Cu-poor sample in figure D.2.

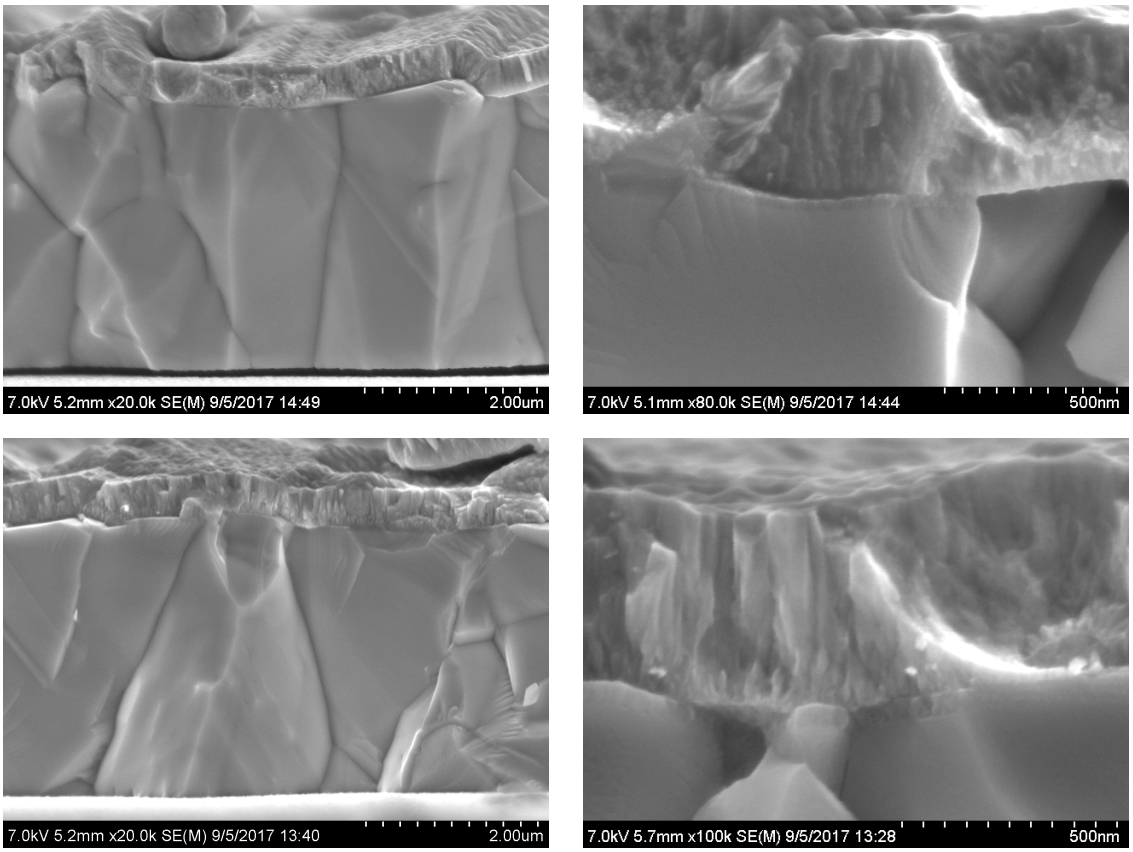

Figure D.1: Top: Cross-section scanning electron images of a Cu-rich sample without treatment. Bottom: Cross-section SEM images of a Cu-rich sample with in-situ KF PDT.

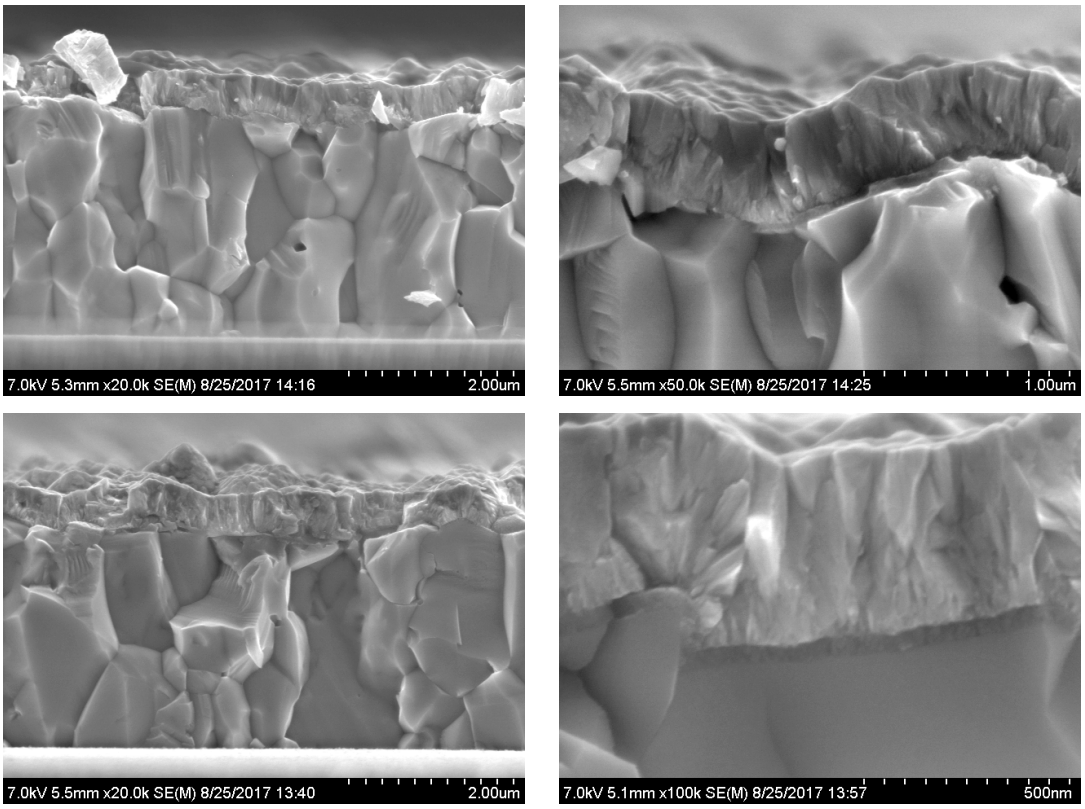

Figure D.2: Top: Cross-section scanning electron images of a Cu-poor sample without treatment. Bottom: Cross-section SEM images of a Cu-poor sample with in-situ KF PDT.

Figure D.3 shows the surface of a Cu-rich $CuInSe_2$ sample with a 4 min (left) and a 12 min (right) long post potassium treatment. The patterning of the surface is less compared to the 8 min treated sample in figure 3.8 (page 63) but is still observable.

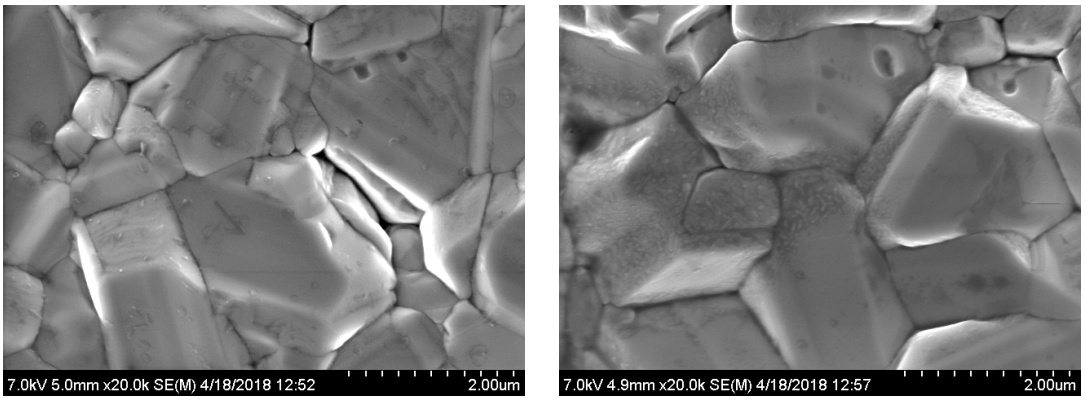

Figure D.3: Left: Top view scanning electron images of a Cu-rich sample with a 4 min in-situ KF treatment. Right: Top view scanning electron images of a Cu-rich sample with a 12 min in-situ KF treatment (right).

Additional low temperature PL on KF treated Cu-rich samples

The treatment of Cu-rich $CuInSe_2$ absorber layer leads to a change in the low temperature photoluminescence spectra as discussed in section 3.2.2 (page 64). Figure D.4 shows the normalized low temperature photoluminescence measurements of a Cu-rich sample with KF PDT measured over five orders of magnitude (each picture shows a 10x higher excitation). The measurement signal is shown in blue, the fitting curves in green, and the sum of the fit in red. Fitted are a asymmetric Gauss curve (representing the Cu-poor surface layer), the DA2 transition plus phonon replica (0.96 eV), and the DA1 transition (0.99 eV).

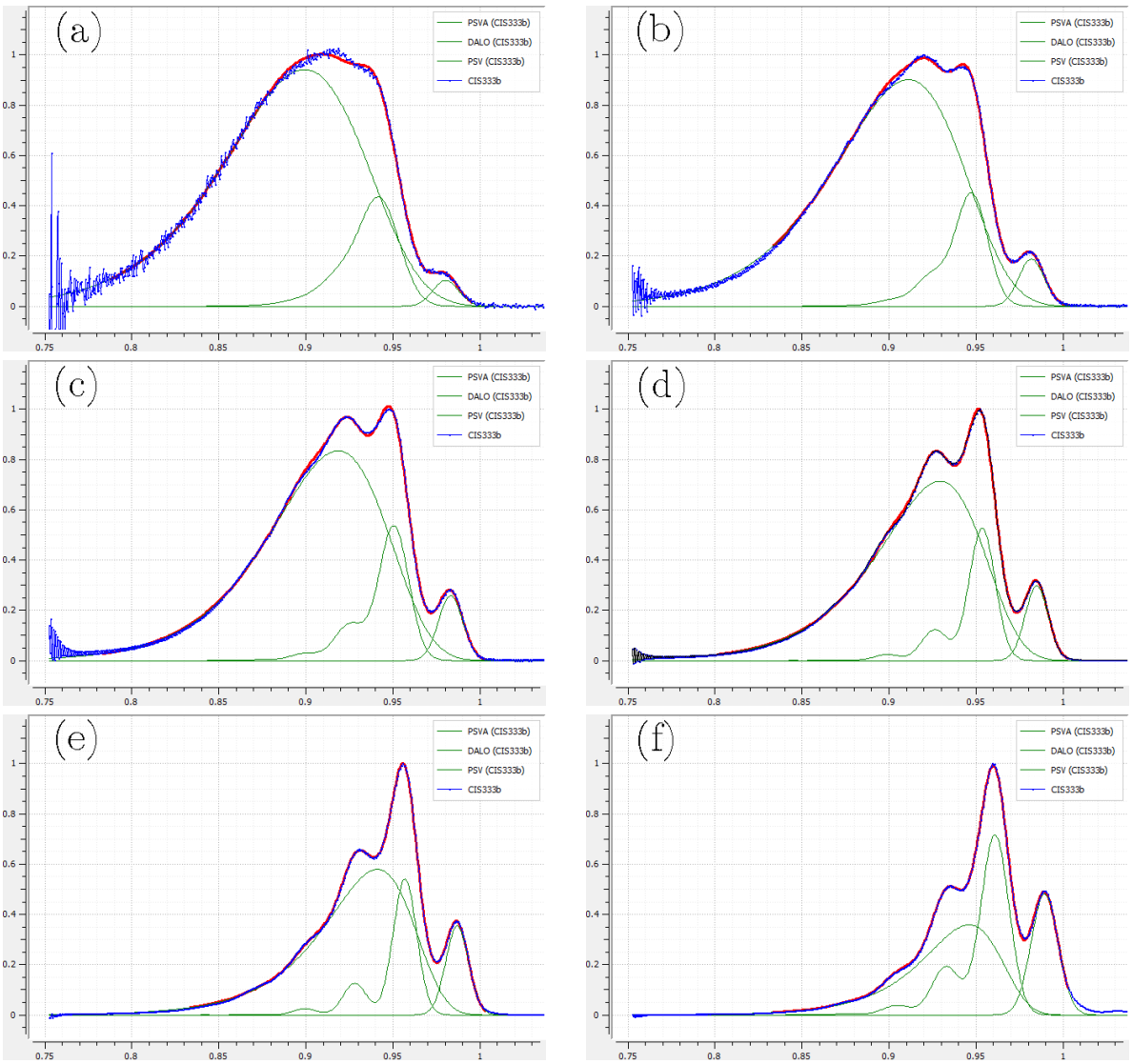

Figure D.4: The blue curves show low temperature photoluminescence spectra of a Cu-rich $CuInSe_2$ samples with KF PDT (6 min, 380 °C) measured over five orders of magnitude excitation. The green lines are fitting curves of a Cu-poor phase (0.90 eV to 0.95 eV), of the DA2 transition (0.96 eV) with phonon replica, and of the DA1 transition (0.99 eV).

D.2 Third Acceptor in $CuInSe_2$

Temperature dependent photoluminescence measurement data of a sample with low (figure D.5) and high (figure D.6) copper content used for the extraction of the activation energy of the observed transitions.

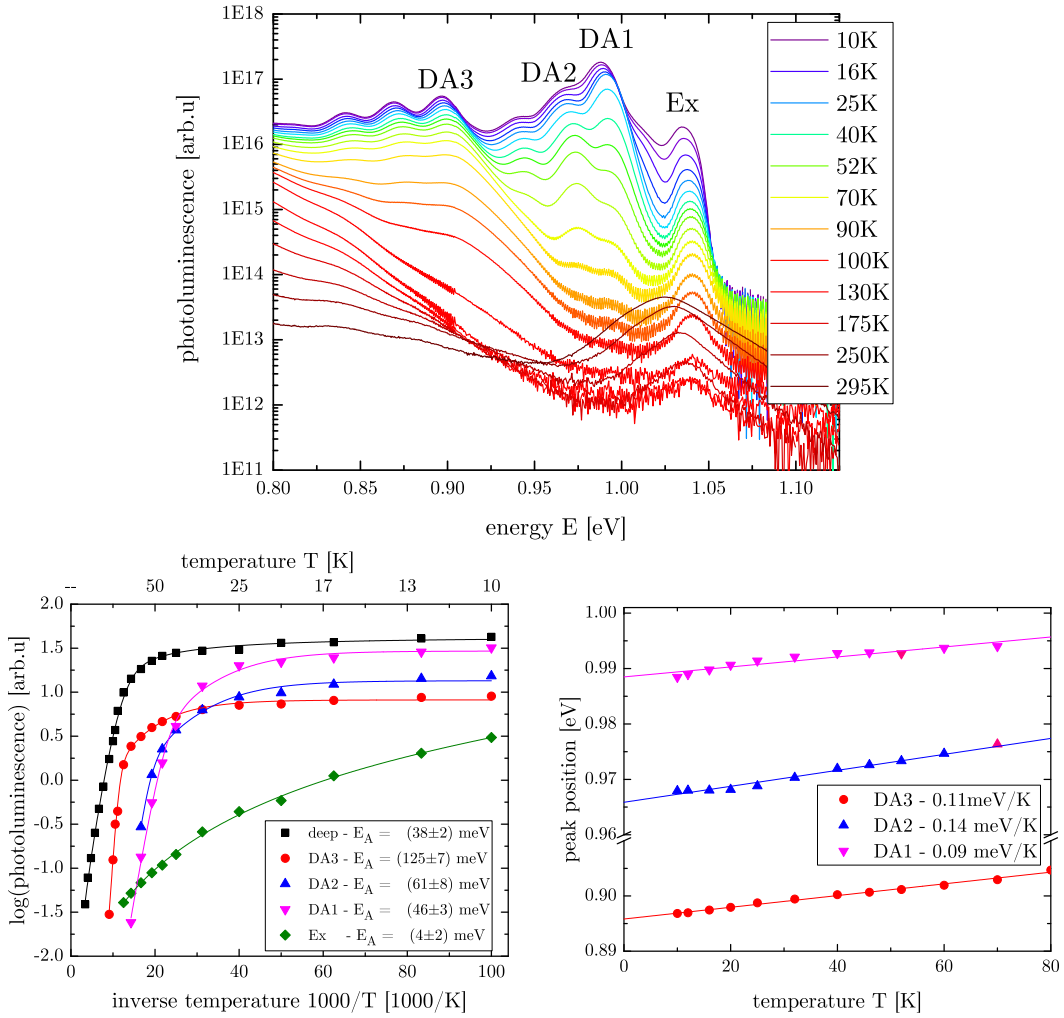

Figure D.5: Top: Temperature dependent photoluminescence measurements between 10 K and 295 K of a $CuInSe_2$ sample grown under low Cu excess ([Cu]/[In] $\approx$ 1.0) and a high selenium flux. The legend shows only every other temperature used. The increase of the band to band transition above 130 K is likely due to the thermal emptying of the deep defect. Bottom left: Photoluminescence signal of the different transitions plotted over the inverse temperature for the evaluation of the activation energy. Bottom right: Peak position of the different DA-transitions plotted over the temperature, showing a small blue shift indicating the shift from a DA to a FB transition.

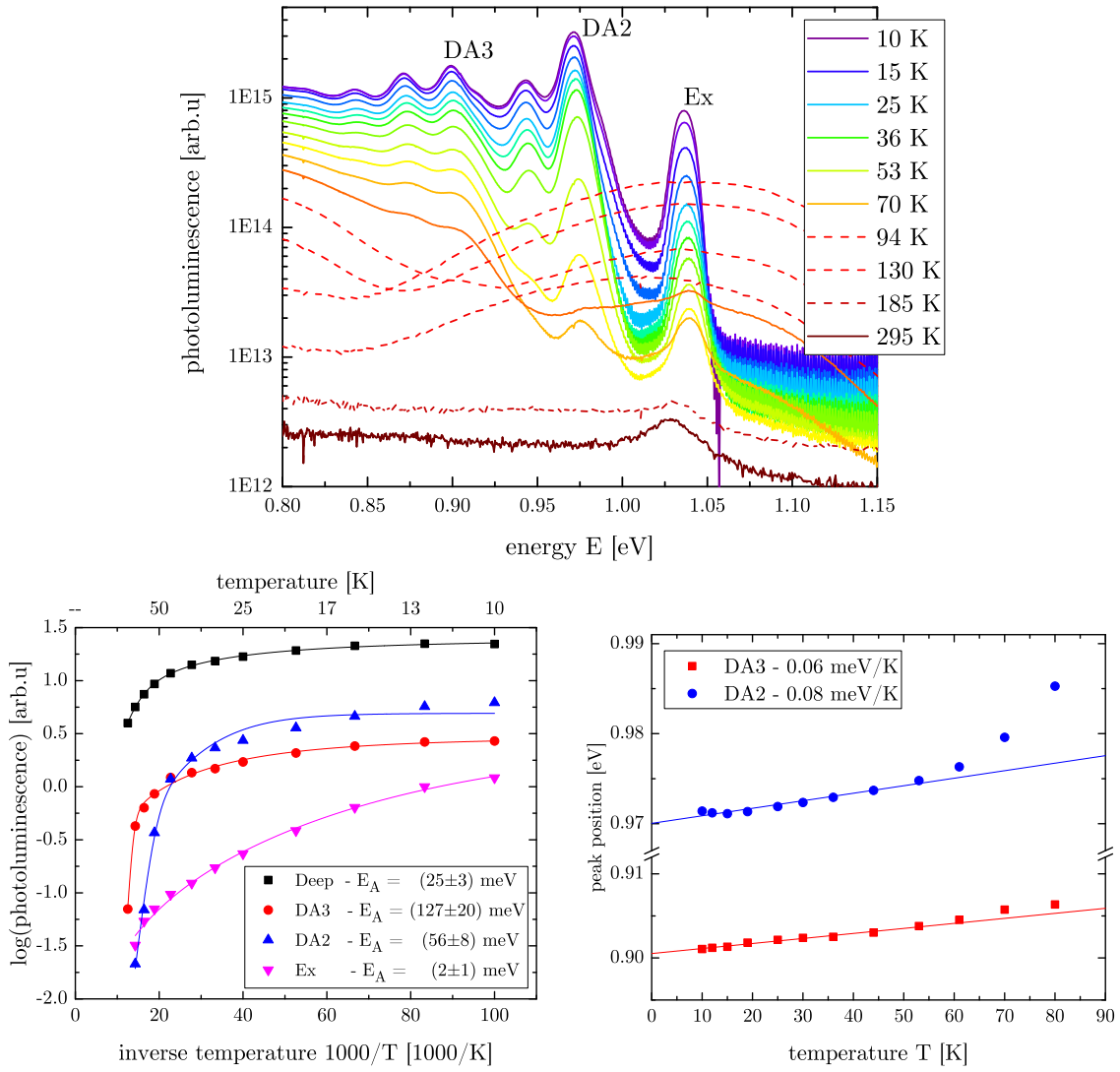

Figure D.6: Top: Temperature dependent photoluminescence measurements between 10 K and 295 K of a $CuInSe_2$ sample grown under high Cu excess ([Cu]/[In] ≈ 1.8) and a high selenium flux. The legend shows only every other temperature used. The dashed lines show a broad peak around 1.05 eV which is a measurement artifact and is not linked to the sample luminescence. Bottom left: Photoluminescence signal of the different transitions plotted over the inverse temperature for the evaluation of the activation energy. Bottom right: Peak position of the different DA-transitions plotted over the temperature, showing a small blue shift.

D.3 Reversibility of surface degradation

The photoluminescence signal and thus the quasi Fermi level splitting degrades over time on bare absorber layers, as discussed in section 6.1 and shown in [17]. Commonly a nearly exponential drop of the intensity is observed over time, as shown on the right in figure D.7. The original photoluminescence yield can be restored by etching the sample with potassium cyanide which removes the formed oxides. However, this can also be done by exposing the samples to ultra high vacuum.

For the experiment a sample is exposed to air and light to degrade it on purpose. After degradation the sample is fixed in a glass vial and the photoluminescence is measured, giving a comparable low luminescence intensity, as shown on the left of figure D.7 (orange). After this the sample is put into the LoadLock of the PVD system and is exposed to vacuum ($\sim 1 \times 10^{-7}$ torr) for about 16 hours. After this the sample is directly transferred into a nitrogen filled glove box, where the glass vial is sealed. The sample is then measured in nitrogen atmosphere giving much higher photoluminescence intensity (dashed), which is constant over time. As soon as the vial is opened the photoluminescence intensity drops as shown on the right in figure D.7[1]. After 3 hours the photoluminescence intensity (red) is the same level as before the vacuum treatment. In another experiment it was shown that the photoluminescence intensity after vacuum treatment is the same as after KCN etching. From this it can be derived that the vacuum treatment restores the photoluminescence intensity as good as a KCN etch. This means that the degradation is likely not due to the formation of real oxides at the surface since those would be stable in vacuum.

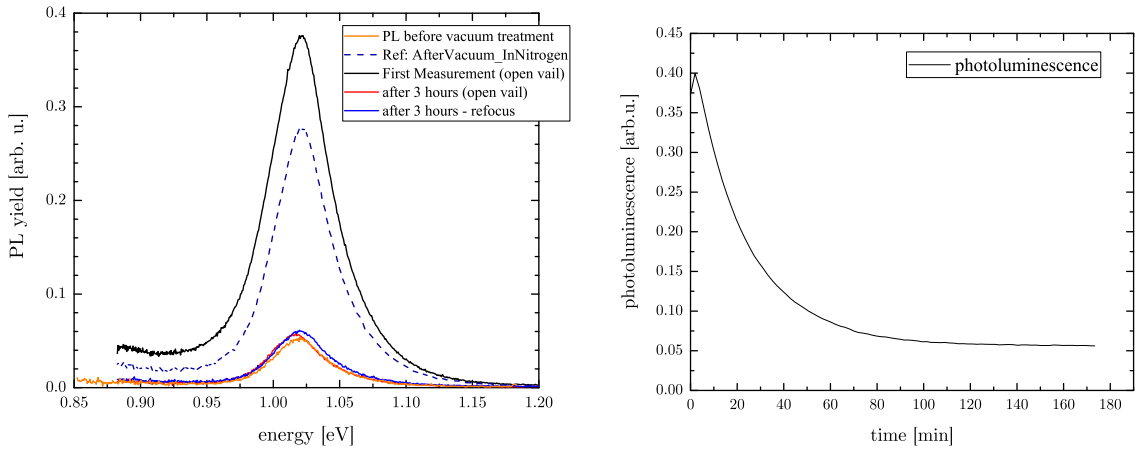

Figure D.7: Left: Room temperature photoluminescence spectra of a sample which is degraded (orange), after vacuum treatment in nitrogen (dashed), after opening the vail and refocusing (black) and after degradation (blue,red). Right: Photoluminescence intensity plotted over time during the degradation.

In other experiments more insight were gathered. (i) The vacuum treatment can be done several times, always restoring the same photoluminescence intensity. (ii) Similar to observations in [17], samples exposed to light degrade faster than samples in the dark. But samples in the dark definitely show degradation, in contrast to observations in [144]. (iii) Samples sealed in nitrogen do not degraded even under illumination (one exception was observed for this).

[1] It should be noted here that after opening the vial the PL intensity is higher due to a better focus in the PL set up and not due to the exposure to ambient air.

APPENDIX

E

LIST OF PUBLICATIONS AND CONFERENCES

Publications

First author

F. Babbe, L. Choubrac, and S. Siebentritt, "Quasi Fermi level splitting of Cu-rich and Cu-poor Cu(In,Ga)Se 2 absorber layers", *Appl. Phys. Lett.*, vol. 109, no. 8, p. 82105, 2016.

F. Babbe, H. Elanzeery, M. Melchiore, A. Zelenina and S.Siebentritt, "Potassium fluoride post deposition treatment with etching step on both Cu-rich and Cu-poor CuInSe2 thin film solar cells", *Phys. Rev. Mater.*, vol. 2, p. 105405, 2018.

F. Babbe, L. Choubrac, and S. Siebentritt, "The Optical Diode Ideality Factor Enables Fast Screening of Semiconductors for Solar Cells", *Solar RRL*, 1800248, 2018.

F. Babbe, H. Elanzeery, M. H. Wolter, K. Santosh, and S. Siebentritt, "The hunt for the third acceptor in CIGS", under review at *Phys. Rev. Applied*, 2019.

Co-author

A. Vetter, **F. S. Babbe**, B. Hofbeck, P. Kubis, M. Richter, S. J. Heise, J. Ohland, I. Riedel, and C. J. Brabec, "Visualizing the performance loss of solar cells by IR thermography - an evaluation study on CIGS with artificially induced defects", *Prog. Photovoltaics Res. Appl.*, vol. 24, no. 7, pp. 1001–1008, 2016.

G. Rey, **F. Babbe**, T. P. Weiss, H. Elanzeery, M. Melchiorre, N. Valle, B. El Adib, and S. Siebentritt, "Post-deposition treatment of $Cu_2ZnSnSe_4$ with alkalis", *Thin Solid Films*, vol. 633, pp. 162–165, 2016.

T. M. Ng, M. T. Weller, G. P. Kissling, L. M. Peter, P. Dale, **F. Babbe**, J. de Wild, B. Wenger, H. J. Snaith, and D. Lane, "Optoelectronic and spectroscopic characterization of vapour-transport grown Cu_2ZnSnS_4 single crystals", *J. Mater. Chem. A*, vol. 5, no. 3, pp. 1192–1200, 2017.

H. Elanzeery, **F. Babbe**, M. Melchiorre, A. Zelenina, and S. Siebentritt, "Potassium Fluoride Ex Situ Treatment on Both Cu-Rich and Cu-Poor $CuInSe_2$ Thin Film Solar Cells," *IEEE J. Photovoltaics*, vol. 7, no. 2, pp. 684–689, 2017.

J. de Wild, **F. Babbe**, E. V. C. Robert, A. Redinger, and P. J. Dale, "Silver-Doped Cu_2SnS_3 Absorber Layers for Solar Cells Application", *IEEE J. Photovoltaics*, vol. 8, no. 1, pp. 299–304, 2018.

M. Liu, D. M. Berg, P.-Y. Hwang, C.-Y. Lai, K. H. Stone, **F. Babbe**, K. D. Dobson, and D. R. Radu, "The promise of solution-processed Fe_2GeS_4 thin films in iron chalcogenide photovoltaics", *J. Mater. Sci.*, vol. 53, no. 10, pp. 7725–7734, 2018.

E. V. C. Robert, R. Gunder, J. de Wild, C. Spindler, **F. Babbe**, H. Elanzeery, B. El Adib, R. Treharne, H. P. C. Miranda, L. Wirtz, S. Schorr, and P. J. Dale, "Synthesis, theoretical and experimental characterisation of thin film $Cu_2Sn_{1-x}Ge_xS_3$ ternary alloys (x = 0 to 1): Homogeneous intermixing of Sn and Ge", *Acta Materialia*, vol. 151, no. 7, pp. 125–136, 2018.

H. Elanzeery, **F. Babbe**, M. Melchiorre, F. Werner, and S. Siebentritt, "High-performance low bandgap thin film solar cells for tandem applications", *Progress in Photovoltaics: Research and Applications*, 26(7), 437–442, 2018

G. Rey, C. Spindler, **F. Babbe**, W. Rachad, S. Siebentritt, M. Nuys, R. Carius, S. Li, and C. Platzer-Björkman, "Absorption Coefficient of a Semiconductor Thin Film from Photoluminescence", *Phys. Rev. Appl.*, vol. 9, no. 6, p. 064008, 2018.

F. Werner, **F. Babbe**, J. Burkhart, C. Spindler, H. Elanzeery, and S. Siebentritt, "Interdiffusion and Doping Gradients at the Buffer/Absorber Interface in Thin-Film Solar Cells", *ACS Appl. Mater. Interfaces*, p. acsami.8b08076, 2018.

Conference contribution

Oral Presentation

F. Babbe, L. Choubrac and S. Siebentritt, "Study on the quasi Fermi level splitting of $Cu(In, Ga)Se_2$ absorber layers with Cu-rich and Cu-poor composition", 43th IEEE PVSC, Portland, 2016, extended talk 25 minutes.

F. Babbe, L. Choubrac, C. Spindler and S. Siebentritt, "Expanding the Theory of the Diode Factor from Devices towards Semiconductor Layers Using the Example of $Cu(In, Ga)Se_2$", MRS Spring Meeting and Exhibit, Phoenix, 2017.

F. Babbe, H. Elanzeery, M. H. Wolter, K. Santhosh and S. Siebentritt, "The hunt for the third acceptor in $Cu(In, Ga)Se_2$", E-MRS Spring meeting, Strasbourg, 2018.

Poster Presentation

F. Babbe, H. Elanzeery, M. Melchiorre and S. Siebentritt, "$CuInSe_2$ absorber layer grown under copper excess with a copper poor surface formed by a KF post deposition treatment", 44th IEEE PVSC, Washington, 2017.

BIBLIOGRAPHY

[1] United Nations. (2015). Paris Agreement, [Online]. Available: https://unfccc.int/process-and-meetings/the-paris-agreement/the-paris-agreement (visited on 03/12/2018) (see p. 9).

[2] U.S. Energy Information Administration. (2018). How much of U.S. carbon dioxide emissions are associated with electricity generation?, [Online]. Available: https://www.eia.gov/tools/faqs/faq.php?id=77&t=11 (visited on 10/12/2018) (see p. 9).

[3] B. Everett, B. Godfrey, S. Peake, and J. Ramage, *Energy Systems and Sustainability - Power for a Sustainable Future*, 2nd. Oxford University Press, 2011, p. 672 (see p. 9).

[4] International Energy Agency. (2011). Solar energy perspectives, [Online]. Available: https://webstore.iea.org/solar-energy-perspectives (visited on 03/12/2018) (see p. 9).

[5] Fraunhofer ISE. (2015). Current and Future Cost of Photovoltaics. Long-term Scenarios for Market Development, System Prices and LCOE of Utility-Scale PV Systems. Study on behalf of Agora Energiewende., [Online]. Available: https://www.ise.fraunhofer.de/content/dam/ise/de/documents/publications/studies/AgoraEnergiewende_Current_and_Future_Cost_of_PV_Feb2015_web.pdf (visited on 08/11/2018) (see p. 9).

[6] C. Kost, S. Shammugam, V. Jülch, H.-T. Nguyen, and T. Schlegl. (2018). Levelized cost of electricity renewable energy technologies, [Online]. Available: https://www.ise.fraunhofer.de/content/dam/ise/en/documents/publications/studies/EN2018_Fraunhofer-ISE_LCOE_Renewable_Energy_Technologies.pdf (see p. 9).

[7] BP. (2018). BP - Statistical Review of World Energy, [Online]. Available: https://www.bp.com/content/dam/bp/en/corporate/pdf/energy-economics/statistical-review/bp-stats-review-2018-full-report.pdf (visited on 03/12/2018) (see p. 9).

[8] S. Wagner, J. L. Shay, P. Migliorato, and H. M. Kasper, "CuInSe 2 /CdS heterojunction photovoltaic detectors", *Applied Physics Letters*, vol. 25, no. 8, pp. 434–435, 1974 (see pp. 9, 13).

[9] S. Frontier. (2017). Solar Frontier Achieves World Record Thin-Film Solar Cell Efficiency of 22.9%, [Online]. Available: http://www.solar-frontier.com/eng/news/2017/1220_press.html (visited on 10/08/2018) (see pp. 9, 10, 43–45).

[10] M. A. Green, Y. Hishikawa, E. D. Dunlop, D. H. Levi, J. Hohl-Ebinger, and A. W. Ho-Baillie, "Solar cell efficiency tables (version 52)", *Progress in Photovoltaics: Research and Applications*, vol. 26, no. 7, pp. 427–436, 2018 (see p. 9).

[11] N. R. E. Laboratory. (2018). Best Research-Cell Efficiencies, [Online]. Available: `https://www.nrel.gov/pv/assets/pdfs/pv-efficiencies-07-17-2018.pdf` (visited on 10/12/2018) (see p. 9).

[12] S. Siebentritt, L. Gütay, D. Regesch, Y. Aida, and V. Deprédurand, "Why do we make Cu(In,Ga)Se2 solar cells non-stoichiometric?", *Solar Energy Materials and Solar Cells*, vol. 119, pp. 18–25, 2013 (see pp. 10, 24, 32, 43, 44, 63, 101, 112).

[13] F. Werner, D. Colombara, M. Melchiorre, N. Valle, B. El Adib, C. Spindler, and S. Siebentritt, "Doping mechanism in pure CuInSe 2", *Journal of Applied Physics*, vol. 119, no. 17, p. 173 103, 2016 (see pp. 10, 16, 34, 43).

[14] A. Bauknecht, S. Siebentritt, J. Albert, and M. C. Lux-Steiner, "Radiative recombination via intrinsic defects in CuxGaySe2", *Journal of Applied Physics*, vol. 89, no. 8, pp. 4391–4400, 2001 (see pp. 10, 34, 35, 43, 82, 84, 88, 89).

[15] S. Siebentritt, N. Rega, A. Zajogin, and M. C. Lux-Steiner, "Do we really need another PL study of CuInSe2?", *physica status solidi (c)*, vol. 1, no. 9, pp. 2304–2310, 2004 (see pp. 10, 11, 34, 35, 43, 63, 68, 74, 78, 79, 119).

[16] D. Regesch, "Photoluminescence and solar cell studies of chalcopyrites. Comparison of Cu-rich vs. Cu-poor and polycrystalline vs. epitaxial material", PhD thesis, 2014, http://hdl.handle.net/10993/16441 (see pp. 10, 44, 53, 106).

[17] D. Regesch, L. Gütay, J. K. Larsen, V. Deprédurand, D. Tanaka, Y. Aida, and S. Siebentritt, "Degradation and passivation of CuInSe2", *Applied Physics Letters*, vol. 101, no. 11, p. 112 108, 2012 (see pp. 10, 11, 23, 44, 61, 62, 86, 88, 103, 104, 106, 108, 109, 111, 112, 114, 115, 118, 138).

[18] M. Turcu, O. Pakma, and U. Rau, "Interdependence of absorber composition and recombination mechanism in Cu(In,Ga)(Se,S)2 heterojunction solar cells", *Applied Physics Letters*, vol. 80, no. 14, pp. 2598–2600, 2002 (see pp. 10, 26, 43, 54, 101, 112).

[19] Y. Aida, V. Depredurand, J. K. Larsen, H. Arai, D. Tanaka, M. Kurihara, and S. Siebentritt, "Cu-rich CuInSe 2 solar cells with a Cu-poor surface", *Progress in Photovoltaics: Research and Applications*, vol. 23, no. 6, pp. 754–764, 2015 (see pp. 10, 11, 44, 49, 54, 61, 63, 65, 114, 118, 119).

[20] L. Choubrac, T. Bertram, H. Elanzeery, and S. Siebentritt, "Cu(In,Ga)Se 2 solar cells with improved current based on surface treated stoichiometric absorbers", *physica status solidi (a)*, vol. 214, no. 1, p. 1 600 482, 2017 (see pp. 10, 11, 43, 44, 101, 110, 114, 118).

[21] P. Wurfel, "The chemical potential of radiation", *Journal of Physics C: Solid State Physics*, vol. 15, no. 18, pp. 3967–3985, 1982 (see pp. 10, 27, 29, 103).

[22] U. Rau and S. Siebentritt, *Wide-Gap Chalcopyrites*, S. Siebentritt and U. Rau, Eds., ser. Springer Series in Materials Science. Berlin/Heidelberg: Springer-Verlag, 2006, vol. 86 (see pp. 10, 27, 32–35, 77, 78).

[23] P. Jackson, D. Hariskos, E. Lotter, S. Paetel, R. Wuerz, R. Menner, W. Wischmann, and M. Powalla, "New world record efficiency for Cu(In,Ga)Se2 thin-film solar cells beyond 20%", *Progress in Photovoltaics: Research and Applications*, vol. 19, no. 7, pp. 894–897, 2011 (see pp. 10, 44).

[24] P. Pistor, D. Greiner, C. a. Kaufmann, S. Brunken, M. Gorgoi, A. Steigert, W. Calvet, I. Lauermann, R. Klenk, T. Unold, and M. C. Lux-Steiner, "Experimental indication for band gap widening of chalcopyrite solar cell absorbers after potassium fluoride treatment", *Applied Physics Letters*, vol. 105, no. 6, p. 063 901, 2014 (see pp. 10, 46, 49–51, 53, 56).

[25] A. Chirilă, P. Reinhard, F. Pianezzi, P. Bloesch, A. R. Uhl, C. Fella, L. Kranz, D. Keller, C. Gretener, H. Hagendorfer, D. Jaeger, R. Erni, S. Nishiwaki, S. Buecheler, and A. N. Tiwari, "Potassium-induced surface modification of Cu(In,Ga)Se2 thin films for high-efficiency solar cells", *Nature Materials*, vol. 12, no. 12, pp. 1107–1111, 2013 (see pp. 10, 43–46, 49, 51, 53, 55, 57, 71).

[26] P. Jackson, R. Wuerz, D. Hariskos, E. Lotter, W. Witte, and M. Powalla, "Effects of heavy alkali elements in Cu(In,Ga)Se 2 solar cells with efficiencies up to 22.6%", *physica status solidi (RRL) - Rapid Research Letters*, vol. 10, no. 8, pp. 583–586, 2016 (see pp. 10, 22, 23, 43–46, 69, 70, 117).

[27] C. Rincón, C. Bellabarba, J. González, and G. Sánchez Pérez, "Optical properties and characterization of CuInSe2", *Solar Cells*, vol. 16, no. C, pp. 335–349, 1986 (see p. 11).

[28] A. V. Mudryi, I. V. Bodnar, V. F. Gremenok, I. A. Victorov, A. I. Patuk, and I. A. Shakin, "Free and bound exciton emission in CuInSe2 and CuGaSe2 single crystals", *Solar Energy Materials and Solar Cells*, vol. 53, no. 3-4, pp. 247–253, 1998 (see pp. 11, 32, 77, 79, 84).

[29] N. Rega, S. Siebentritt, J. Albert, S. Nishiwaki, A. Zajogin, M. C. Lux-Steiner, R. Kniese, and M. J. Romero, "Excitonic luminescence of Cu(In,Ga)Se2", *Thin Solid Films*, vol. 480-481, pp. 286–290, 2005 (see pp. 11, 34, 35, 74, 77, 79, 80, 91, 92).

[30] J. K. Larsen, "Inhomogeneities in epitaxial chalcopyrites studied by photoluminescence", PhD thesis, University of Luxembourg, http://hdl.handle.net/10993/15580, 2011 (see pp. 11, 35, 73, 83, 84, 91).

[31] S. Siebentritt, I. Beckers, T. Riemann, J. Christen, A. Hoffmann, and M. Dworzak, "Reconciliation of luminescence and Hall measurements on the ternary semiconductor CuGa Se2", *Applied Physics Letters*, vol. 86, no. 9, pp. 1–3, 2005 (see pp. 11, 34, 35, 73, 83).

[32] F. Babbe, H. Elanzeery, M. H. Wolter, K. Santosh, and S. Siebentritt, "The hunt for the third acceptor in CIGS", *submitted to Physical Review Applied*, 2018 (see pp. 11, 35, 61, 62, 73).

[33] W. N. Shafarman, S. Siebentritt, and L. Stolt, "Cu(InGa)Se2 Solar Cells", in *Handbook of Photovoltaic Science and Engineering*, 2, A. Luque and S. Hegedus, Eds., vol. 13, Chichester, UK: John Wiley & Sons, Ltd, 2011, pp. 546–599 (see pp. 13, 21, 22, 53).

[34] H. G. Grimm and A. Sommerfeld, "Über den. Zusammenhang des Abschlusses der Elektronengruppen im Atom mit den chemischen Valenzzahlen", *Zeitschrift für Physik*, vol. 36, no. 1, pp. 36–59, 1926 (see p. 14).

[35] H. W. Spiess, U. Haeberlen, G. Brandt, A. Räuber, and J. Schneider, "Nuclear Magnetic Resonance in IB–III–VI2 Semiconductors", *physica status solidi (b)*, vol. 62, no. 1, pp. 183–192, 1974 (see p. 14).

[36] R. Scheer and H.-W. W. Schock, *Chalcogenide Photovoltaics*. Weinheim, Germany: Wiley-VCH Verlag GmbH & Co. KGaA, 2011 (see pp. 14, 17, 20, 21, 26, 27, 94).

[37] S. B. Zhang, S.-H. Wei, and A. Zunger, "Stabilization of Ternary Compounds via Ordered Arrays of Defect Pairs", *Physical Review Letters*, vol. 78, no. 21, pp. 4059–4062, 1997 (see p. 14).

[38] T. Gödecke, T. Haalboom, and F. Ernst, "Phase equilibria of Cu-In-Se I. The In2Se3-Se-Cu2Se subsystem", *Zeitschrift für Metallkunde*, vol. 91, no. 8, pp. 622–634, 1948 (see pp. 15, 65).

[39] D. Schmid, M. Ruckh, and H. Schock, "Photoemission studies on Cu(In, Ga)Se2 thin films and related binary selenides", *Applied Surface Science*, vol. 103, no. 4, pp. 409–429, 1996 (see pp. 15, 22).

[40] J. C. Mikkelsen, "Ternary phase relations of the chalcopyrite compound CuGaSe2", *Journal of Electronic Materials*, vol. 10, no. 3, pp. 541–558, 1981 (see p. 15).

[41] L. L. Kazmerski, M. Hallerdt, P. J. Ireland, R. A. Mickelsen, and W. S. Chen, "Optical properties and grain boundary effects in CuInSe 2", *Journal of Vacuum Science & Technology A: Vacuum, Surfaces, and Films*, vol. 1, no. 2, pp. 395–398, 1983 (see p. 15).

[42] M. I. Alonso, M. Garriga, C. A. Durante Rincón, E. Hernández, and M. León, "Optical functions of chalcopyrite CuGaxIn1-xSe2 alloys", *Applied Physics A: Materials Science and Processing*, vol. 74, no. 5, pp. 659–664, 2002 (see pp. 15, 65, 107).

[43] L. Gütay, D. Regesch, J. K. Larsen, Y. Aida, V. Deprédurand, A. Redinger, S. Caneva, S. Schorr, C. Stephan, J. Vidal, S. Botti, and S. Siebentritt, "Feedback mechanism for the stability of the band gap of CuInSe 2", *Physical Review B - Condensed Matter and Materials Physics*, vol. 86, pp. 1–5, 2012 (see pp. 15, 53).

[44] P. Y. Yu and M. Cardona, *Fundamentals of Semiconductors*, ser. Graduate Texts in Physics. Berlin, Heidelberg: Springer Berlin Heidelberg, 2010 (see pp. 16, 27, 31, 109).

[45] S. Siebentritt, M. Igalson, C. Persson, and S. Lany, "The electronic structure of chalcopyrites-bands, point defects and grain boundaries", *Progress in Photovoltaics: Research and Applications*, vol. 18, no. 6, pp. 390–410, 2010 (see p. 16).

[46] M. Richter, I. Riedel, C. Schubbert, P. Eraerds, J. Parisi, T. Dalibor, and J. Palm, "Simulation study of the impact of interface roughness and void inclusions on Cu(In,Ga)(Se,S) 2 solar cells", *physica status solidi (a)*, vol. 212, no. 2, pp. 298–306, 2015 (see p. 16).

[47] R. Noufi, R. Axton, C. Herrington, and S. K. Deb, "Electronic properties versus composition of thin films of CuInSe 2", *Applied Physics Letters*, vol. 45, no. 6, pp. 668–670, 1984 (see p. 16).

[48] S. B. Zhang, S.-H. Wei, A. Zunger, and H. Katayama-Yoshida, "Defect physics of the CuInSe2 chalcopyrite semiconductor", *Physical Review B*, vol. 57, no. 16, pp. 9642–9656, 1998 (see p. 16).

[49] J. Heyd, G. E. Scuseria, and M. Ernzerhof, "Hybrid functionals based on a screened Coulomb potential", *Journal of Chemical Physics*, vol. 118, no. 18, pp. 8207–8215, 2003 (see pp. 17, 34).

[50] J. Pohl and K. Albe, "Intrinsic point defects in CuInSe2 and CuGaSe2 as seen via screened-exchange hybrid density functional theory", *Physical Review B*, vol. 87, no. 24, p. 245 203, 2013 (see pp. 17, 34, 35, 79, 80, 108, 114).

[51] L. E. Oikkonen, M. G. Ganchenkova, A. P. Seitsonen, and R. M. Nieminen, "Formation, migration, and clustering of point defects in CuInSe 2 from first principles", *Journal of Physics: Condensed Matter*, vol. 26, no. 34, p. 345 501, 2014 (see pp. 17, 34, 35, 79).

[52] J. Bekaert, R. Saniz, B. Partoens, and D. Lamoen, "Native point defects in CuIn1-xGaxSe2: Hybrid density functional calculations predict the origin of p- and n-type conductivity", *Physical Chemistry Chemical Physics*, vol. 16, no. 40, pp. 22 299–22 308, 2014 (see pp. 17, 34, 79).

[53] Y. S. Yee, B. Magyari-Köpe, Y. Nishi, S. F. Bent, and B. M. Clemens, "Deep recombination centers in Cu2ZnSnSe4 revealed by screened-exchange hybrid density functional theory", *Physical Review B*, vol. 92, no. 19, p. 195 201, 2015 (see pp. 17, 34, 79, 108).

[54] M. Malitckaya, H.-P. Komsa, V. Havu, and M. J. Puska, "First-Principles Modeling of Point Defects and Complexes in Thin-Film Solar-Cell Absorber CuInSe2", *Advanced Electronic Materials*, vol. 3, no. 6, p. 1 600 353, 2017 (see pp. 17, 34, 35, 79, 80, 83, 108).

[55] P. Würfel, *Physics of Solar Cells*, P. Wurfel, Ed. Weinheim, Germany: Wiley-VCH Verlag GmbH, 2005 (see pp. 17, 27, 29, 103).

[56] S. Sze and K. K. Ng, *Physics of Semiconductor Devices*, 3rd. Hoboken, NJ, USA: John Wiley & Sons, Inc., 2006, pp. 7–75 (see pp. 17, 19).

[57] A. Luque and S. Hegedus, Eds., *Handbook of Photovoltaic Science and Engineering*. Chichester, UK: John Wiley & Sons, Ltd, 2011 (see pp. 17, 24).

[58] J. Keller, "Charakterisierung und Simulation von sequentiell prozessierten CIGSSe-Solarzellen mit chemisch gradierter Absorberschicht Möglichkeiten und Einschränkungen eines eindimensionalen Ansatzes", PhD thesis, 2012, oops.uni–oldenburg.de/1386/ (see pp. 18, 21).

[59] J. Heath and P. Zabierowski, "Capacitance Spectroscopy of Thin-Film Solar Cells", in *Advanced Characterization Techniques for Thin Film Solar Cells*, D. Abou-Ras, T. Kirchartz, and U. Rau, Eds., Weinheim, Germany: Wiley-VCH Verlag GmbH & Co. KGaA, 2011, pp. 81–105 (see pp. 19, 60, 84).

[60] W. Van Roosbroeck, "Theory of the Flow of Electrons and Holes in Germanium and Other Semiconductors", *Bell System Technical Journal*, vol. 29, no. 4, pp. 560–607, 1950 (see p. 20).

[61] J. L. Gray, "The Physics of the Solar Cell", in *Handbook of Photovoltaic Science and Engineering*, Chichester, UK: John Wiley & Sons, Ltd, 2011, pp. 82–129 (see p. 20).

[62] T. M. Friedlmeier, P. Jackson, A. Bauer, D. Hariskos, O. Kiowski, R. Menner, R. Wuerz, and M. Powalla, "High-efficiency Cu(In,Ga)Se 2 solar cells", *Thin Solid Films*, vol. 633, pp. 13–17, 2017 (see p. 21).

[63] N. Naghavi, D. Abou-Ras, N. Allsop, N. Barreau, S. Buecheler, A. Ennaoui, C.-H. Fischer, C. Guillen, D. Hariskos, J. Herrero, R. Klenk, K. Kushiya, D. Lincot, R. Menner, T. Nakada, C. Platzer-Björkman, S. Spiering, A. N. Tiwari, and T. Törndahl, "Buffer layers and transparent conducting oxides for chalcopyrite Cu(In,Ga)(S,Se)2 based thin film photovoltaics: Present status and current developments", *Progress in Photovoltaics: Research and Applications*, vol. 18, no. 6, pp. 411–433, 2010 (see pp. 21–23).

[64] U. P. Singh and S. P. Patra, "Progress in Polycrystalline Thin-Film Cu(In,Ga)2 Solar Cells", *International Journal of Photoenergy*, vol. 2010, pp. 1–19, 2010 (see p. 21).

[65] W. Witte, S. Spiering, and D. Hariskos, "Substitution of the CdS buffer layer in CIGS thin-film solar cells", *Vakuum in Forschung und Praxis*, vol. 26, no. 1, pp. 23–27, 2014 (see pp. 21, 22).

[66] T. Feurer, P. Reinhard, E. Avancini, B. Bissig, J. Löckinger, P. Fuchs, R. Carron, T. P. Weiss, J. Perrenoud, S. Stutterheim, S. Buecheler, and A. N. Tiwari, "Progress in thin film CIGS photovoltaics - Research and development, manufacturing, and applications", *Progress in Photovoltaics: Research and Applications*, vol. 25, no. 7, pp. 645–667, 2017 (see p. 21).

[67] L. Stolt, J. Hedström, J. Kessler, M. Ruckh, K. Velthaus, and H. Schock, "ZnO/CdS/CuInSe2 thin-film solar cells with improved performance", *Applied Physics Letters*, vol. 62, no. 6, pp. 597–599, 1993 (see pp. 21, 35, 44).

[68] K. Granath, M. Bodegård, and L. Stolt, "The effect of NaF on Cu(In,Ga)Se2 thin film solar cells", *Solar Energy Materials and Solar Cells*, vol. 60, no. 3, pp. 279–293, 2000 (see p. 21).

[69] A. Chirilă, S. Buecheler, F. Pianezzi, P. Bloesch, C. Gretener, A. R. Uhl, C. Fella, L. Kranz, J. Perrenoud, S. Seyrling, R. Verma, S. Nishiwaki, Y. E. Romanyuk, G. Bilger, and A. N. Tiwari, "Highly efficient Cu(In,Ga)Se2 solar cells grown on flexible polymer films", *Nature Materials*, vol. 10, no. 11, pp. 857–861, 2011 (see pp. 21, 44).

[70] R. Matson, O. Jamjoum, A. Buonaquisti, P. Russell, L. Kazmerski, P. Sheldon, and R. Ahrenkiel, "Metal contacts to CuInSe2", *Solar Cells*, vol. 11, no. 3, pp. 301–305, 1984 (see p. 21).

[71] K. F. Tai, R. Kamada, T. Yagioka, T. Kato, and H. Sugimoto, "From 20.9 to 22.3% Cu(In,Ga)(S,Se) 2 solar cell: Reduced recombination rate at the heterojunction and the depletion region due to K-treatment", *Japanese Journal of Applied Physics*, vol. 56, no. 8S2, p. 08MC03, 2017 (see pp. 22, 23, 47).

[72] W. Witte, D. Abou-Ras, K. Albe, G. H. Bauer, F. Bertram, C. Boit, R. Brüggemann, J. Christen, J. Dietrich, A. Eicke, D. Hariskos, M. Maiberg, R. Mainz, M. Meessen, M. Müller, O. Neumann, T. Orgis, S. Paetel, J. Pohl, H. Rodriguez-Alvarez, R. Scheer, H. W. Schock, T. Unold, A. Weber, and M. Powalla, "Gallium gradients in Cu(In,Ga)Se 2 thin-film solar cells", *Progress in Photovoltaics: Research and Applications*, vol. 23, no. 6, pp. 717–733, 2015 (see pp. 22, 25, 41, 107).

[73] M. Bär, S. Nishiwaki, L. Weinhardt, S. Pookpanratana, W. N. Shafarman, and C. Heske, "Electronic level alignment at the deeply buried absorber/Mo interface in chalcopyrite-based thin film solar cells", *Applied Physics Letters*, vol. 93, no. 4, p. 042 110, 2008 (see p. 22).

[74] N. Neugebohrn, "Electronic Transport and Potential Barriers at the MoSe 2 -Mo Back Contact in Cu (In , Ga) Se 2 Solar Cells", PhD thesis, University of Oldenburg, 2016, http://oops.uni–oldenburg.de/2859/ (see p. 22).

[75] M. A. Contreras, M. J. Romero, B. To, F. Hasoon, R. Noufi, S. Ward, and K. Ramanathan, "Optimization of CBD CdS process in high-efficiency Cu(In,Ga)Se2-based solar cells", *Thin Solid Films*, vol. 403-404, pp. 204–211, 2002 (see pp. 22, 23).

[76] D. Liao and A. Rockett, "Cd doping at the CuInSe2/CdS heterojunction", *Journal of Applied Physics*, vol. 93, no. 11, pp. 9380–9382, 2003 (see p. 22).

[77] O. Cojocaru-Mirédin, P.-P. Choi, R. Wuerz, and D. Raabe, "Exploring the p-n junction region in Cu(In,Ga)Se2 thin-film solar cells at the nanometer-scale", *Applied Physics Letters*, vol. 101, no. 18, p. 181 603, 2012 (see pp. 22, 47).

[78] F. Werner, F. Babbe, J. Burkhart, C. Spindler, H. Elanzeery, and S. Siebentritt, "Interdiffusion and Doping Gradients at the Buffer/Absorber Interface in Thin-Film Solar Cells", *ACS Applied Materials & Interfaces*, vol. 10, no. 34, pp. 28 553–28 565, 2018 (see pp. 22, 60, 63, 89).

[79] C. H. Huanga, S. S. Lia, L. Riethb, A. Halani, M. L. Fisher, J. Songa, T. J. Anderson, and P. H. Hollowayb, "Buffer Layer for CIS-based Solar Cells", pp. 696–699, 2000 (see p. 22).

[80] R. Kamada, T. Yagioka, S. Adachi, A. Handa, K. F. Tai, T. Kato, and H. Sugimoto, "New world record Cu(In, Ga)(Se, S)2 thin film solar cell efficiency beyond 22%", in *2016 IEEE 43rd Photovoltaic Specialists Conference (PVSC)*, IEEE, 2016, pp. 1287–1291 (see pp. 22, 45, 47).

[81] U. Rau and M. Schmidt, "Electronic properties of ZnO/CdS/Cu(In,Ga)Se2 solar cells - aspects of heterojunction formation", *Thin Solid Films*, vol. 387, no. 1-2, pp. 141–146, 2001 (see p. 22).

[82] Y. Hashimoto, N. Kohara, T. Negami, M. Nishitani, and T. Wada, "Surface Characterization of Chemically Treated C u(In,Ga)Se2 Thin Films", *Japanese Journal of Applied Physics*, vol. 35, no. Part 1, No. 9A, pp. 4760–4764, 1996 (see pp. 23, 87).

[83] B. Canava, J.-F. Guillemoles, J. Vigneron, D. Lincot, and A. Etcheberry, "Chemical elaboration of well defined Cu(In,Ga)Se2 surfaces after aqueous oxidation etching", *Journal of Physics and Chemistry of Solids*, vol. 64, no. 9-10, pp. 1791–1796, 2003 (see p. 23).

[84] M. Hála, H. Kato, M. Algasinger, Y. Inoue, G. Rey, F. Werner, C. Schubbert, T. Dalibor, and S. Siebentritt, "Improved environmental stability of highly conductive nominally undoped ZnO layers suitable for n-type windows in thin film solar cells", *Solar Energy Materials and Solar Cells*, vol. 161, pp. 232–239, 2017 (see p. 23).

[85] R. Herberholz, V. Nadenau, U. Rühle, C. Köble, H. Schock, and B. Dimmler, "Prospects of wide-gap chalcopyrites for thin film photovoltaic modules", *Solar Energy Materials and Solar Cells*, vol. 49, pp. 227–237, 1997 (see p. 24).

[86] A. Niemegeers, M. Burgelman, and A. De Vos, "On the CdS/CuInSe2 conduction band discontinuity", *Applied Physics Letters*, vol. 67, no. 1995, p. 843, 1995 (see p. 24).

[87] A. Klein, "Energy band alignment in chalcogenide thin film solar cells from photoelectron spectroscopy", *Journal of Physics: Condensed Matter*, vol. 27, no. 13, p. 134 201, 2015 (see p. 24).

[88] "American Society for Testing and Materials (ASTM) G-173-03, International standard ISO 9845-1, 1992.", Tech. Rep. (see pp. 25, 53).

[89] A. Polman, M. Knight, E. C. Garnett, B. Ehrler, and W. C. Sinke, "Photovoltaic materials: Present efficiencies and future challenges", *Science*, vol. 352, no. 6283, aad4424–aad4424, 2016 (see pp. 26, 106).

[90] A. Burgers, J. Eikelboom, A. Schonecker, and W. Sinke, "Improved treatment of the strongly varying slope in fitting solar cell I-V curves", in *Conference Record of the Twenty Fifth IEEE Photovoltaic Specialists Conference - 1996*, IEEE, 1996, pp. 569–572 (see pp. 26, 94).

[91] S. S. Hegedus and W. N. Shafarman, "Thin-film solar cells: device measurements and analysis", *Progress in Photovoltaics: Research and Applications*, vol. 12, no. 23, pp. 155–176, 2004 (see pp. 26, 54).

[92] T. Kirchartz, K. Ding, and U. Rau, "Fundamental Electrical Characterization of Thin-Film Solar Cells", in *Advanced Characterization Techniques for Thin Film Solar Cells*, Weinheim, Germany: Wiley-VCH Verlag GmbH & Co. KGaA, 2011, pp. 33–60 (see pp. 26, 27, 53, 59, 93, 94, 112).

[93] R. Scheer, "Activation energy of heterojunction diode currents in the limit of interface recombination", *Journal of Applied Physics*, vol. 105, no. 10, p. 104 505, 2009 (see p. 27).

[94] T. P. Weiss, "Electrical characterization of kesterite thin film absorbers and solar cells", PhD thesis, 2015, http://orbilu.uni.lu/handle/10993/23357 (see p. 27).

[95] T. Bertram, "Doping, Defects And Solar Cell Performance Of Cu-rich Grown CuInSe2", PhD thesis, 2016, http://orbilu.uni.lu/handle/10993/28325 (see pp. 27, 39, 53).

[96] T. Unold and L. Gütay, "Photoluminescence Analysis of Thin-Film Solar Cells", in *Advanced Characterization Techniques for Thin Film Solar Cells*, D. Abou-Ras, T. Kirchartz, and U. Rau, Eds., vol. 1-2, Weinheim, Germany: Wiley-VCH Verlag GmbH & Co. KGaA, 2011, pp. 151–175 (see pp. 27, 32–34, 63, 77, 88, 99, 103).

[97] J. K. Katahara and H. W. Hillhouse, "Quasi-Fermi level splitting and sub-bandgap absorptivity from semiconductor photoluminescence", *Journal of Applied Physics*, vol. 116, no. 17, p. 173 504, 2014 (see pp. 28, 36).

[98] S. Siebentritt, G. Rey, A. Finger, D. Regesch, J. Sendler, T. P. Weiss, and T. Bertram, "What is the bandgap of kesterite?", *Solar Energy Materials and Solar Cells*, vol. 158, pp. 126–129, 2016 (see pp. 28, 109, 110).

[99] D. G. Thomas, J. J. Hopfield, and W. M. Augustyniak, "Kinetics of Radiative Recombination at Randomly Distributed Donors and Acceptors", *Physical Review*, vol. 140, no. 1A, A202–A220, 1965 (see p. 30).

[100] A. Alkauskas, M. D. McCluskey, and C. G. Van de Walle, "Tutorial: Defects in semiconductors—Combining experiment and theory", *Journal of Applied Physics*, vol. 119, no. 18, p. 181 101, 2016 (see pp. 31, 75, 82).

[101] C. Spindler, "Optical detection of deep defects in Cu(In,Ga)Se2", PhD thesis, University of Luxembourg, 2018, http://hdl.handle.net/10993/37016 (see pp. 31, 35, 38, 79, 90–92, 108).

[102] M. V. Yakushev, R. W. Martin, A. Babinski, and A. V. Mudryi, "Effects of magnetic fields on free excitons in CuInSe 2", *physica status solidi (c)*, vol. 6, no. 5, pp. 1086–1088, 2009 (see pp. 32, 74).

[103] P. Li, R. Anderson, and R. Plovnick, "Dielectric constant of CuInSe2 by capacitance measurements", *Journal of Physics and Chemistry of Solids*, vol. 40, no. 4, pp. 333–334, 1979 (see pp. 32, 125).

[104] S. Niki, H. Shibata, P. J. Fons, A. Yamada, A. Obara, Y. Makita, T. Kurafuji, S. Chichibu, and H. Nakanishi, "Excitonic emissions from CuInSe 2 on GaAs(001) grown by molecular beam epitaxy", *Applied Physics Letters*, vol. 67, no. 9, pp. 1289–1291, 1995 (see p. 32).

[105] S. Chichibu, T. Mizutani, K. Murakami, T. Shioda, T. Kurafuji, H. Nakanishi, S. Niki, P. J. Fons, and A. Yamada, "Band gap energies of bulk, thin-film, and epitaxial layers of CuInSe2 and CuGaSe2", *Journal of Applied Physics*, vol. 83, no. 7, pp. 3678–3689, 1998 (see p. 32).

[106] J. R. Haynes, "Experimental Proof of the Existence of a New Electronic Complex in Silicon", *Physical Review Letters*, vol. 4, no. 7, pp. 361–363, 1960 (see p. 32).

[107] H. Atzmüller and U. Schröder, "Theoretical Investigations of Haynes' Rule", *Physica Status Solidi (b)*, vol. 89, no. 2, pp. 349–356, 1978 (see p. 32).

[108] A. P. Levanyuk and V. V. Osipov, "Edge luminescence of direct-gap semiconductors", *Soviet Physics Uspekhi*, vol. 24, no. 3, pp. 187–215, 1981 (see p. 32).

[109] J. Krustok, H. Collan, and K. Hjelt, "Does the low-temperature Arrhenius plot of the photoluminescence intensity in CdTe point towards an erroneous activation energy?", *Journal of Applied Physics*, vol. 81, no. 3, p. 1442, 1997 (see p. 33).

[110] M. A. Reshchikov, "Temperature dependence of defect-related photoluminescence in III-V and II-VI semiconductors", *Journal of Applied Physics*, vol. 115, no. 1, p. 012 010, 2014 (see p. 33).

[111] E. Zacks and A. Halperin, "Dependence of the Peak Energy of the Pair-Photoluminescence Band on Excitation Intensity", *Physical Review B*, vol. 6, no. 8, pp. 3072–3075, 1972 (see p. 34).

[112] S. Shirakata, K. Ohkubo, Y. Ishii, and T. Nakada, "Effects of CdS buffer layers on photoluminescence properties of Cu(In,Ga)Se2 solar cells", *Solar Energy Materials and Solar Cells*, vol. 93, no. 6-7, pp. 988–992, 2009 (see p. 34).

[113] T. Schmidt, K. Lischka, and W. Zulehner, "Excitation-power dependence of the near-band-edge photoluminescence of semiconductors", *Physical Review B*, vol. 45, no. 16, pp. 8989–8994, 1992 (see pp. 34, 96).

[114] W. Grieshaber, E. F. Schubert, I. D. Goepfert, R. F. Karlicek, M. J. Schurman, and C. Tran, "Competition between band gap and yellow luminescence in GaN and its relevance for optoelectronic devices", *Journal of Applied Physics*, vol. 80, no. 8, pp. 4615–4620, 1996 (see pp. 34, 96).

[115] C. Spindler, G. Rey, T. Galvani, L. Wirtz, and S. Siebentritt, "Excitation-intensity dependence of shallow and deep-level photoluminescence transitions in semiconductors", *submitted to Phys. Rev. B*, 2018 (see pp. 34, 74, 96, 117).

[116] J. Sendler, M. Thevenin, F. Werner, A. Redinger, S. Li, C. Hägglund, C. Platzer-Björkman, and S. Siebentritt, "Photoluminescence studies in epitaxial CZTSe thin films", *Journal of Applied Physics*, vol. 120, no. 12, p. 125 701, 2016 (see p. 34).

[117] M. Wagner, I. Dirnstorfer, D. M. Hofmann, M. D. Lampert, F. Karg, and B. K. Meyer, "Characterization of CuIn(Ga)Se2 Thin Films I. Cu-Rich Layers", *physica status solidi (a)*, vol. 167, no. 1, pp. 131–142, 1998 (see pp. 34, 76, 78, 79, 84).

[118] A. Krysztopa, M. Igalson, Y. Aida, J. K. Larsen, L. Gütay, and S. Siebentritt, "Defect levels in the epitaxial and polycrystalline CuGaSe2 by photocurrent and capacitance methods", *Journal of Applied Physics*, vol. 110, no. 2011, 2011 (see pp. 34, 35).

[119] A. Gerhard, W. Harneit, S. Brehme, A. Bauknecht, U. Fiedeler, M. C. Lux-Steiner, and S. Siebentritt, "Acceptor activation energies in epitaxial CuGaSe2 grown by MOVPE", *Thin Solid Films*, vol. 387, pp. 67–70, 2001 (see p. 34).

[120] S. Schuler, S. Siebentritt, S. Nishiwaki, N. Rega, J. Beckmann, S. Brehme, and M. C. Lux-Steiner, "Self-compensation of intrinsic defects in the ternary semiconductor CuGaSe2", *Physical Review B*, vol. 69, no. 4, p. 045 210, 2004 (see pp. 34, 89).

[121] P. M. Gorley, V. V. Khomyak, Y. V. Vorobiev, J. González-Hernández, P. P. Horley, and O. O. Galochkina, "Electron properties of n- and p-CuInSe2", *Solar Energy*, vol. 82, no. 2, pp. 100–105, 2008 (see p. 34).

[122] C. Spindler, F. Babbe, M. H. Wolter, F. Ehre, K. Santosh, P. Hilgert, F. Werner, and S. Siebentritt, "Electronic Defects in Cu(In,Ga)Se2 – towards a comprehensive model", 2018 (see pp. 35, 79, 103, 108).

[123] S. Wasim, "Transport properties of CuInSe2", *Solar Cells*, vol. 16, pp. 289–316, 1986 (see p. 35).

[124] C. Spindler, D. Regesch, and S. Siebentritt, "Revisiting radiative deep-level transitions in CuGaSe 2 by photoluminescence", *Applied Physics Letters*, vol. 109, no. 3, p. 032 105, 2016 (see pp. 35, 91, 108, 114).

[125] B. Huang, S. Chen, H.-X. Deng, L.-W. Wang, M. A. Contreras, R. Noufi, and S.-H. Wei, "Origin of Reduced Efficiency in Cu(In,Ga)Se2 Solar Cells With High Ga Concentration: Alloy Solubility Versus Intrinsic Defects", *IEEE Journal of Photovoltaics*, vol. 4, no. 1, pp. 477–482, 2014 (see p. 35).

[126] D. Rudmann, A. F. Da Cunha, M. Kaelin, F. Kurdesau, H. Zogg, a. N. Tiwari, and G. Bilger, "Efficiency enhancement of Cu(In,Ga)Se2 solar cells due to post-deposition Na incorporation", *Applied Physics Letters*, vol. 84, no. 7, pp. 1129–1131, 2004 (see pp. 35, 44, 45).

[127] Z.-K. Yuan, S. Chen, Y. Xie, J.-S. Park, H. Xiang, X.-G. Gong, and S.-H. Wei, "Na-Diffusion Enhanced p-type Conductivity in Cu(In,Ga)Se 2 : A New Mechanism for Efficient Doping in Semiconductors", *Advanced Energy Materials*, vol. 6, no. 24, p. 1 601 191, 2016 (see p. 35).

[128] E. Cadel, N. Barreau, J. Kessler, and P. Pareige, "Atom probe study of sodium distribution in polycrystalline Cu(In,Ga)Se2 thin film", *Acta Materialia*, vol. 58, no. 7, pp. 2634–2637, 2010 (see pp. 36, 47).

[129] F. Couzinie-Devy, E. Cadel, N. Barreau, L. Arzel, and P. Pareige, "Atom probe study of Cu-poor to Cu-rich transition during Cu(In,Ga)Se 2 growth", *Applied Physics Letters*, vol. 99, pp. 97–100, 2011 (see p. 36).

[130] C. P. Muzzillo, "Review of grain interior, grain boundary, and interface effects of K in CIGS solar cells: Mechanisms for performance enhancement", *Solar Energy Materials and Solar Cells*, vol. 172, no. December, pp. 18–24, 2017 (see pp. 36, 45, 46).

[131] J. Mooney and P. Kambhampati, "Correction to "Get the Basics Right: Jacobian Conversion of Wavelength and Energy Scales for Quantitative Analysis of Emission Spectra"", *The Journal of Physical Chemistry Letters*, vol. 5, no. 20, pp. 3497–3497, 2014 (see p. 38).

[132] H. Rau, "Vapour composition and critical constants of selenium", *The Journal of Chemical Thermodynamics*, vol. 6, no. 6, pp. 525–535, 1974 (see pp. 39, 50, 79).

[133] R. Viswanathan, R. Balasubramanian, D. Darwin Albert Raj, M. Sai Baba, and T. Lakshmi Narasimhan, "Vaporization studies on elemental tellurium and selenium by Knudsen effusion mass spectrometry", *Journal of Alloys and Compounds*, vol. 603, pp. 75–85, 2014 (see pp. 39, 79).

[134] N. Kohara, S. Nishiwaki, Y. Hashimoto, T. Negami, and T. Wada, "Electrical properties of the Cu(In,Ga)Se2/ MoSe2/Mo structure", *Solar Energy Materials and Solar Cells*, vol. 67, no. 1-4, pp. 209–215, 2001 (see p. 40).

[135] H. Rau and A. Rabenau, "Vapour pressure measurements in the copper-selenium system", *Journal of Solid State Chemistry*, vol. 1, no. 3-4, pp. 515–518, 1970 (see pp. 41, 79).

[136] S. C. Jackson, B. N. Baron, R. E. Rocheleau, and T. W. F. Russell, "A chemical reaction model for physical vapor deposition of compound semiconductor films", *AIChE Journal*, vol. 33, no. 5, pp. 711–721, 1987 (see pp. 41, 79).

[137] V. Deprédurand, T. Bertram, and S. Siebentritt, "Influence of the Se environment on Cu-rich CIS devices", *Physica B: Condensed Matter*, vol. 439, pp. 101–104, 2014 (see p. 41).

[138] A. M. Gabor, J. R. Tuttle, D. S. Albin, M. A. Contreras, R. Noufi, and A. M. Hermann, "High-efficiency CuInxGa1-xSe2 solar cells made from (Inx,Ga1-x)2Se3 precursor films", *Applied Physics Letters*, vol. 65, pp. 198–200, 1994 (see pp. 41, 107).

[139] E. Avancini, D. Keller, R. Carron, Y. Arroyo-Rojas Dasilva, R. Erni, A. Priebe, S. Di Napoli, M. Carrisi, G. Sozzi, R. Menozzi, F. Fu, S. Buecheler, and A. N. Tiwari, "Voids and compositional inhomogeneities in Cu(In,Ga)Se 2 thin films: evolution during growth and impact on solar cell performance", *Science and Technology of Advanced Materials*, vol. 19, no. 1, pp. 871–882, 2018 (see p. 41).

[140] T. Dullweber, O. Lundberg, J. Malmström, M. Bodegård, L. Stolt, U. Rau, H.-W. Schock, and J. H. Werner, "Back surface band gap gradings in Cu(In,Ga)Se2 solar cells", *Thin Solid Films*, vol. 387, no. 1, pp. 11–13, 2001 (see pp. 41, 107).

[141] H. Rodriguez-Alvarez, N. Barreau, C. Kaufmann, A. Weber, M. Klaus, T. Painchaud, H.-W. Schock, and R. Mainz, "Recrystallization of Cu(In,Ga)Se2 thin films studied by X-ray diffraction", *Acta Materialia*, vol. 61, no. 12, pp. 4347–4353, 2013 (see p. 42).

[142] V. Deprédurand, T. Bertram, D. Regesch, B. Henx, and S. Siebentritt, "The influence of Se pressure on the electronic properties of CuInSe 2 grown under Cu-excess", *Applied Physics Letters*, vol. 105, no. 17, p. 172 104, 2014 (see pp. 43, 60, 73, 101, 112).

[143] H. Elanzeery, F. Babbe, M. Melchiorre, A. Zelenina, and S. Siebentritt, "Potassium Fluoride Ex Situ Treatment on Both Cu-Rich and Cu-Poor CuInSe2 Thin Film Solar Cells", *IEEE Journal of Photovoltaics*, vol. 7, no. 2, pp. 684–689, 2017 (see pp. 43, 50).

[144] T. Hölscher, S. Förster, T. Schneider, M. Maiberg, W. Widdra, and R. Scheer, "Light induced degradation of Cu(In,Ga)Se 2 thin film surfaces", *Applied Physics Letters*, vol. 111, no. 1, p. 011 604, 2017 (see pp. 44, 138).

[145] A. J. Nelson, S. Gebhard, L. L. Kazmerski, E. Colavita, M. Engelhardt, and H. Höchst, "Characterization of the native oxide of CuInSe 2 using synchrotron radiation photoemission", *Applied Physics Letters*, vol. 57, no. 14, pp. 1428–1430, 1990 (see pp. 44, 56).

[146] M. H. Wolter, S. Siebentritt, *et al.*, "Link between urbach tailing and quasi Fermi level splitting", *in preperation*, (see pp. 44, 47).

[147] H. Elanzeery, M. Melchiorre, M. Sood, F. Babbe, F. Werner, G. Brammertz, and S. Siebentritt, "Challenge in Cu-rich Thin Film Solar Cells: Defect Caused by Etching", *submitted to Energy & Environmental Science*, 2018 (see pp. 44, 60–62, 66, 71, 85, 114, 118).

[148] F. Babbe, H. Elanzeery, M. Melchiorre, A. Zelenina, and S. Siebentritt, "Potassium fluoride postdeposition treatment with etching step on both Cu-rich and Cu-poor CuInSe2 thin film solar cells", *Physical Review Materials*, vol. 2, no. 10, p. 105 405, 2018 (see pp. 44, 56, 85).

[149] M. Contreras, B. Egaas, P. Dippo, J. Webb, J. Granata, K. Ramanathan, S. Asher, A. Swartzlander, and R. Noufi, "On the role of Na and modifications to Cu(In,Ga)Se2 absorber materials using thin-MF (M=Na, K, Cs) precursor layers", in *Conference Record of the Twenty Sixth IEEE Photovoltaic Specialists Conference - 1997*, IEEE, 1997, pp. 359–362 (see p. 44).

[150] P. Jackson, D. Hariskos, R. Wuerz, W. Wischmann, and M. Powalla, "Compositional investigation of potassium doped Cu(In,Ga)Se2 solar cells with efficiencies up to 20.8%", *Physica Status Solidi - Rapid Research Letters*, vol. 8, no. 3, pp. 219–222, 2014 (see pp. 45–47).

[151] P. Jackson, D. Hariskos, R. Wuerz, O. Kiowski, A. Bauer, T. M. Friedlmeier, and M. Powalla, "Properties of Cu(In,Ga)Se 2 solar cells with new record efficiencies up to 21.7%", *physica status solidi (RRL) - Rapid Research Letters*, vol. 9, no. 1, pp. 28–31, 2015 (see p. 45).

[152] P. Salomé, H. Rodriguez-Alvarez, and S. Sadewasser, "Incorporation of alkali metals in chalcogenide solar cells", *Solar Energy Materials and Solar Cells*, vol. 143, pp. 9–20, 2015 (see p. 45).

[153] P. Salomé, V. Fjällström, A. Hultqvist, and M. Edoff, "Na Doping of CIGS Solar Cells Using Low Sodium-Doped Mo Layer", *IEEE Journal of Photovoltaics*, vol. 3, no. 1, pp. 509–513, 2013 (see p. 45).

[154] P. M. P. Salome, A. Hultqvist, V. Fjallstrom, M. Edoff, B. G. Aitken, K. Zhang, K. Fuller, and C. Kosik Williams, "Incorporation of Na in Cu(In,Ga)Se2 Thin-Film Solar Cells: A Statistical Comparison Between Na From Soda-Lime Glass and From a Precursor Layer of NaF", *IEEE Journal of Photovoltaics*, vol. 4, no. 6, pp. 1659–1664, 2014 (see p. 45).

[155] D. Guttler, A. Chirila, S. Seyrling, P. Blosch, S. Buecheler, X. Fontane, V. Izquierdo-Roca, L. Calvo-Barrio, A. Perez-Rodriguez, J. Morante, A. Eicke, and A. N. Tiwari, "Influence of NaF incorporation during Cu(In,Ga)Se2 growth on microstructure and photovoltaic performance", in *2010 35th IEEE Photovoltaic Specialists Conference*, IEEE, 2010, pp. 003 420–003 424 (see p. 45).

[156] A. Laemmle, R. Wuerz, T. Schwarz, O. Cojocaru-Mirédin, P.-P. Choi, and M. Powalla, "Investigation of the diffusion behavior of sodium in Cu(In,Ga)Se2 layers", *Journal of Applied Physics*, vol. 115, no. 15, p. 154 501, 2014 (see p. 45).

[157] F. Pianezzi, P. Reinhard, A. Chirilă, B. Bissig, S. Nishiwaki, S. Buecheler, and A. N. Tiwari, "Unveiling the effects of post-deposition treatment with different alkaline elements on the electronic properties of CIGS thin film solar cells", *Physical Chemistry Chemical Physics*, vol. 16, no. 19, p. 8843, 2014 (see pp. 45, 46).

[158] T. Kodalle, M. D. Heinemann, D. Greiner, H. A. Yetkin, M. Klupsch, C. Li, P. A. van Aken, I. Lauermann, R. Schlatmann, and C. A. Kaufmann, "Elucidating the Mechanism of an RbF Post Deposition Treatment in CIGS Thin Film Solar Cells", *Solar RRL*, vol. 2, no. 9, p. 1 800 156, 2018 (see pp. 46, 53, 55).

[159] I. Khatri, H. Fukai, H. Yamaguchi, M. Sugiyama, and T. Nakada, "Effect of potassium fluoride post-deposition treatment on Cu(In,Ga)Se 2 thin films and solar cells fabricated onto sodalime glass substrates", *Solar Energy Materials and Solar Cells*, vol. 155, pp. 280–287, 2016 (see pp. 46, 47, 55, 56, 59, 63, 65, 71).

[160] B. Ümsür, W. Calvet, A. Steigert, I. Lauermann, M. Gorgoi, K. Prietzel, D. Greiner, C. A. Kaufmann, T. Unold, and M. C. Lux-Steiner, "Investigation of the potassium fluoride post deposition treatment on the CIGSe/CdS interface using hard X-ray photoemission spectroscopy – a comparative study", *Physical Chemistry Chemical Physics*, vol. 18, no. 20, pp. 14 129–14 138, 2016 (see p. 46).

[161] P. Reinhard, B. Bissig, F. Pianezzi, E. Avancini, H. Hagendorfer, D. Keller, P. Fuchs, M. Döbeli, C. Vigo, P. Crivelli, S. Nishiwaki, S. Buecheler, and A. N. Tiwari, "Features of KF and NaF Postdeposition Treatments of Cu(In,Ga)Se 2 Absorbers for High Efficiency Thin Film Solar Cells", *Chemistry of Materials*, vol. 27, no. 16, pp. 5755–5764, 2015 (see p. 46).

[162] P. Reinhard, B. Bissig, F. Pianezzi, H. Hagendorfer, G. Sozzi, R. Menozzi, C. Gretener, S. Nishiwaki, S. Buecheler, and A. N. Tiwari, "Alkali-Templated Surface Nanopatterning of Chalcogenide Thin Films: A Novel Approach Toward Solar Cells with Enhanced Efficiency", *Nano Letters*, vol. 15, no. 5, pp. 3334–3340, 2015 (see pp. 46, 51, 55, 63).

[163] E. Handick, P. Reinhard, R. G. Wilks, F. Pianezzi, T. Kunze, D. Kreikemeyer-Lorenzo, L. Weinhardt, M. Blum, W. Yang, M. Gorgoi, E. Ikenaga, D. Gerlach, S. Ueda, Y. Yamashita, T. Chikyow, C. Heske, S. Buecheler, A. N. Tiwari, and M. Bär, "Formation of a K-In-Se Surface Species by NaF/KF Postdeposition Treatment of Cu(In,Ga)Se 2 Thin-Film Solar Cell Absorbers", *ACS Applied Materials & Interfaces*, vol. 9, no. 4, pp. 3581–3589, 2017 (see p. 46).

[164] E. Handick, P. Reinhard, J.-H. Alsmeier, L. Köhler, F. Pianezzi, S. Krause, M. Gorgoi, E. Ikenaga, N. Koch, R. G. Wilks, S. Buecheler, A. N. Tiwari, and M. Bär, "Potassium Postdeposition Treatment-Induced Band Gap Widening at Cu(In,Ga)Se 2 Surfaces – Reason for Performance Leap?", *ACS Applied Materials & Interfaces*, vol. 7, no. 49, pp. 27 414–27 420, 2015 (see p. 46).

[165] L. M. Mansfield, R. Noufi, C. P. Muzzillo, C. DeHart, K. Bowers, B. To, J. W. Pankow, R. C. Reedy, and K. Ramanathan, "Enhanced Performance in Cu(In,Ga)Se2 Solar Cells Fabricated by the Two-Step Selenization Process With a Potassium Fluoride Postdeposition Treatment", *IEEE Journal of Photovoltaics*, vol. 4, no. 6, pp. 1650–1654, 2014 (see pp. 47, 51).

[166] O. Cojocaru-Mirédin, T. Schwarz, and D. Abou-Ras, "Assessment of elemental distributions at line and planar defects in Cu(In,Ga)Se 2 thin films by atom probe tomography", *Scripta Materialia*, vol. 148, pp. 106–114, 2018 (see p. 47).

[167] O. Cojocaru-Mirédin, T. Schwarz, P.-P. Choi, M. Herbig, R. Wuerz, and D. Raabe, "Atom Probe Tomography Studies on the Cu(In,Ga)Se2 Grain Boundaries", *Journal of Visualized Experiments*, no. 74, pp. 1–8, 2013 (see p. 47).

[168] P. Schöppe, S. Schönherr, R. Wuerz, W. Wisniewski, G. Martínez-Criado, M. Ritzer, K. Ritter, C. Ronning, and C. S. Schnohr, "Rubidium segregation at random grain boundaries in Cu(In,Ga)Se2 absorbers", *Nano Energy*, vol. 42, pp. 307–313, 2017 (see p. 47).

[169] R. Wuerz, W. Hempel, and P. Jackson, "Diffusion of Rb in polycrystalline Cu(In,Ga)Se 2 layers and effect of Rb on solar cell parameters of Cu(In,Ga)Se 2 thin-film solar cells", *Journal of Applied Physics*, vol. 124, no. 16, p. 165 305, 2018 (see pp. 47, 71).

[170] S. A. Jensen, S. Glynn, A. Kanevce, P. Dippo, J. V. Li, D. H. Levi, and D. Kuciauskas, "Beneficial effect of post-deposition treatment in high-efficiency Cu(In,Ga)Se2 solar cells through reduced potential fluctuations", *Journal of Applied Physics*, vol. 120, no. 6, p. 063 106, 2016 (see p. 47).

[171] M. H. Wolter, B. Bissig, E. Avancini, R. Carron, S. Buecheler, P. Jackson, and S. Siebentritt, "Influence of Sodium and Rubidium Postdeposition Treatment on the Quasi-Fermi Level Splitting of Cu(In,Ga)Se2 Thin Films", *IEEE Journal of Photovoltaics*, vol. 8, no. 5, pp. 1320–1325, 2018 (see pp. 47, 69, 70, 107, 117).

[172] H. Elanzeery, "Electrical characterization of alkali treated chalcogenides", PhD thesis, University of Luxembourg, 2019, add link (see pp. 49, 53, 60, 61, 66).

[173] A. Laemmle, R. Wuerz, and M. Powalla, "Investigation of the effect of potassium on Cu(In,Ga)Se2 layers and solar cells", *Thin Solid Films*, 2014 (see p. 51).

[174] ——, "Efficiency enhancement of Cu(In,Ga)Se2 thin-film solar cells by a post-deposition treatment with potassium fluoride", *Physica Status Solidi - Rapid Research Letters*, vol. 7, no. 9, pp. 631–634, 2013 (see p. 51).

[175] A. Zelenina, F. Werner, H. Elanzeery, M. Melchiorre, and S. Siebentritt, "Space-charge-limited currents in CIS-based solar cells", *Applied Physics Letters*, vol. 111, no. 21, p. 213 903, 2017 (see pp. 52, 58, 94).

[176] V. Depredurand, Y. Aida, J. Larsen, T. Eisenbarth, A. Majerus, and S. Siebentritt, "Surface treatment of CIS solar cells grown under Cu-excess", in *2011 37th IEEE Photovoltaic Specialists Conference*, IEEE, 2011, pp. 000 337–000 342 (see pp. 54, 63, 114).

[177] M. C. Biesinger, B. P. Payne, A. P. Grosvenor, L. W. Lau, A. R. Gerson, and R. S. Smart, "Resolving surface chemical states in XPS analysis of first row transition metals, oxides and hydroxides: Cr, Mn, Fe, Co and Ni", *Applied Surface Science*, vol. 257, no. 7, pp. 2717–2730, 2011 (see p. 56).

[178] A. Nakane, H. Tampo, M. Tamakoshi, S. Fujimoto, K. M. Kim, S. Kim, H. Shibata, S. Niki, and H. Fujiwara, "Quantitative determination of optical and recombination losses in thin-film photovoltaic devices based on external quantum efficiency analysis", *Journal of Applied Physics*, vol. 120, no. 6, p. 064 505, 2016 (see p. 59).

[179] F. Werner, T. Bertram, J. Mengozzi, and S. Siebentritt, "What is the dopant concentration in polycrystalline thin-film Cu(In,Ga)Se 2 ?", *Thin Solid Films*, vol. 633, pp. 222–226, 2017 (see p. 60).

[180] T. Eisenbarth, T. Unold, R. Caballero, C. A. Kaufmann, and H.-W. Schock, "Interpretation of admittance, capacitance-voltage, and current-voltage signatures in Cu(In,Ga)Se2 thin film solar cells", *Journal of Applied Physics*, vol. 107, no. 3, p. 034 509, 2010 (see p. 60).

[181] G. Sozzi, M. Lazzarini, R. Menozzi, R. Carron, E. Avancini, B. Bissig, S. Buecheler, and A. N. Tiwari, "A numerical study of the use of C-V characteristics to extract the doping density of CIGS absorbers", in *2016 IEEE 43rd Photovoltaic Specialists Conference (PVSC)*, IEEE, 2016, pp. 2283–2288 (see p. 60).

[182] T. Bertram, V. Depredurand, and S. Siebentritt, "Electrical Characterization of Defects in Cu-Rich Grown CuInSe 2 Solar Cells", *IEEE Journal of Photovoltaics*, vol. 6, no. 2, pp. 546–551, 2016 (see p. 60).

[183] V. Deprédurand, D. Tanaka, Y. Aida, M. Carlberg, N. Fèvre, and S. Siebentritt, "Current loss due to recombination in Cu-rich CuInSe 2 solar cells", *Journal of Applied Physics*, vol. 115, no. 4, p. 044 503, 2014 (see pp. 62, 101).

[184] F. Luckert, M. V. Yakushev, C. Faugeras, a. V. Karotki, A. V. Mudryi, and R. W. Martin, "Excitation power and temperature dependence of excitons in CuInSe 2", *Journal of Applied Physics*, vol. 111, no. 2012, 2012 (see pp. 67, 74, 77).

[185] A. V. Mudriy, I. V. Bodnar, I. A. Viktorov, V. F. Gremenok, M. V. Yakushev, R. D. Tomlinson, A. E. Hill, and R. D. Pilkington, "Optical properties of high-quality CuInSe2 single crystals", *Applied Physics Letters*, vol. 77, no. 16, pp. 2542–2544, 2000 (see p. 74).

[186] N. Rega, "Photolumineszenz epitaktischer Cu(In,Ga)Se2-Schichten", PhD thesis, Freie Universität Berlin, 2004, https://refubium.fu–berlin.de/handle/fub188/10480 (see pp. 74, 76).

[187] S. Niki, Y. Makita, A. Yamada, A. Obara, S. Misawa, O. Igarashi, K. Aoki, and N. Kutsuwada, "Sharp Optical Emission from CuInSe2 Thin Films Grown by Molecular Beam Epitaxy", *Japanese Journal of Applied Physics*, vol. 33, no. Part 2, No. 4A, pp. L500–L502, 1994 (see p. 76).

[188] I. Dirnstorfer, D. M. Hofmann, D. Meister, B. K. Meyer, W. Riedl, and F. Karg, "Postgrowth thermal treatment of CuIn(Ga)Se2: Characterization of doping levels in In-rich thin films", *Journal of Applied Physics*, vol. 85, no. 3, pp. 1423–1428, 1999 (see p. 76).

[189] R. Saniz, J. Bekaert, B. Partoens, and D. Lamoen, "Structural and electronic properties of defects at grain boundaries in CuInSe 2", *Phys. Chem. Chem. Phys.*, vol. 19, no. 22, pp. 14 770–14 780, 2017 (see pp. 79, 108).

[190] J. K. Larsen, S.-Y. Li, J. J. S. Scragg, Y. Ren, C. Hägglund, M. D. Heinemann, S. Kretzschmar, T. Unold, and C. Platzer-Björkman, "Interference effects in photoluminescence spectra of Cu2ZnSnS4 and Cu(In,Ga)Se2 thin films", *Journal of Applied Physics*, vol. 118, no. 3, p. 035 307, 2015 (see p. 80).

[191] M. H. Wolter, B. Bissig, P. Reinhard, S. Buecheler, P. Jackson, and S. Siebentritt, "Correcting for interference effects in the photoluminescence of Cu(In,Ga)Se2 thin films", *Physica Status Solidi (C) Current Topics in Solid State Physics*, vol. 14, no. 6, 2017 (see p. 80).

[192] M. H. Wolter, D. Siopa, P. Thiele, A. Lomuscio, F. Babbe, B. Bissig, E. Avancini, R. Carron, S. Buecheler, P. Jackson, W. Witte, and S. Siebentritt, "Removal of interference effects in thin semiconductors for quantatative photoluminescence analysis", *in preperation*, 2018 (see p. 80).

[193] F. Babbe, L. Choubrac, and S. Siebentritt, "Quasi Fermi level splitting of Cu-rich and Cu-poor Cu(In,Ga)Se 2 absorber layers", *Applied Physics Letters*, vol. 109, no. 8, p. 082 105, 2016 (see pp. 88, 115).

[194] D. Abou-Ras, G. Kostorz, A. Romeo, D. Rudmann, and A. N. Tiwari, "Structural and chemical investigations of CBD- and PVD-CdS buffer layers and interfaces in Cu(In,Ga)Se2-based thin film solar cells", *Thin Solid Films*, vol. 480-481, pp. 118–123, 2005 (see p. 88).

[195] O. Cojocaru-Mirédin, P.-P. Choi, R. Wuerz, and D. Raabe, "Atomic-scale characterization of the CdS/CuInSe2 interface in thin-film solar cells", *Applied Physics Letters*, vol. 98, no. 10, 2011 (see p. 88).

[196] K. Ramanathan, R. Noufi, J. Granata, J. Webb, and J. Keane, "Prospects for in situ junction formation in CuInSe2 based solar cells", *Solar Energy Materials and Solar Cells*, vol. 55, no. 1-2, pp. 15–22, 1998 (see p. 89).

[197] C. Persson, Y.-J. Zhao, S. Lany, and A. Zunger, "n-type doping of CuInSe2 andCuGaSe2", *Physical Review B*, vol. 72, no. 3, p. 035 211, 2005 (see p. 89).

[198] S. Siebentritt and S. Schuler, "Defects and transport in the wide gap chalcopyrite CuGaSe2", *Journal of Physics and Chemistry of Solids*, vol. 64, pp. 1621–1626, 2003 (see p. 89).

[199] F. Werner, "Hall measurements on low-mobility thin films", *Journal of Applied Physics*, vol. 122, no. 13, p. 135 306, 2017 (see p. 89).

[200] I. Repins, L. Mansfield, A. Kanevce, S. A. Jensen, D. Kuciauskas, S. Glynn, T. Barnes, W. Metzger, J. Burst, C.-s. Jiang, P. Dippo, S. Harvey, G. Teeter, C. Perkins, B. Egaas, A. Zakutayev, J.-h. Alsmeier, T. Lusky, L. Korte, R. G. Wilks, M. Bar, Y. Yan, S. Lany, P. Zawadzki, J.-s. Park, and S.-H. Wei, "Wild band edges: The role of bandgap grading and band-edge fluctuations in high-efficiency chalcogenide devices", in *2016 IEEE 43rd Photovoltaic Specialists Conference (PVSC)*, IEEE, 2016, pp. 0309–0314 (see p. 89).

[201] F. Babbe, L. Choubrac, and S. Siebentritt, "The Optical Diode Ideality Factor Enables Fast Screening of Semiconductors for Solar Cells", *Solar RRL*, vol. 1800248, p. 1 800 248, 2018 (see p. 93).

[202] W. Shockley, "The Theory of p-n Junctions in Semiconductors and p-n Junction Transistors", *Bell System Technical Journal*, vol. 28, no. 3, pp. 435–489, 1949 (see p. 94).

[203] U. Dolega, "Theorie des pn-Kontaktes zwischen Halbleitern mit verschiedenen Kristallgittern", *Zeitschrift für Naturforschung A*, vol. 18, no. 5, pp. 653–666, 1963 (see p. 94).

[204] H. Bayhan and M. Bayhan, "A simple approach to determine the solar cell diode ideality factor under illumination", *Solar Energy*, vol. 85, no. 5, pp. 769–775, 2011 (see p. 94).

[205] Z. Hameiri, K. McIntosh, and G. Xu, "Evaluation of recombination processes using the local ideality factor of carrier lifetime measurements", *Solar Energy Materials and Solar Cells*, vol. 117, pp. 251–258, 2013 (see p. 94).

[206] M. Wolf and H. Rauschenbach, "Series resistance effects on solar cell measurements", *Advanced Energy Conversion*, vol. 3, no. 2, pp. 455–479, 1963 (see pp. 94, 95).

[207] K. R. Mcintosh and C. B. Honsberg, "The influence of edge recombination on a solar cells I-V curve", *16th PVSEC*, no. August, pp. 1651–1654, 2000 (see p. 94).

[208] O. Breitenstein, J. Bauer, A. Lotnyk, and J. M. Wagner, "Defect induced non-ideal dark I-V characteristics of solar cells", *Superlattices and Microstructures*, vol. 45, no. 4-5, pp. 182–189, 2009 (see p. 94).

[209] B. L. Williams, S. Smit, B. J. Kniknie, K. J. Bakker, W. Keuning, W. M. M. Kessels, R. E. I. Schropp, and M. Creatore, "Identifying parasitic current pathways in CIGS solar cells by modelling dark J-V response", *Progress in Photovoltaics: Research and Applications*, vol. 23, no. 11, pp. 1516–1525, 2015 (see p. 94).

[210] R. A. Sinton and A. Cuevas, "A Quasi-Steady-State Open-Circuit Voltage Method for Solar Cell Characterization", in *16th European Photovoltaic Solar Energy Conference*, 2000, pp. 1152–1155 (see p. 95).

[211] M. J. Kerr, A. Cuevas, and R. A. Sinton, "Generalized analysis of quasi-steady-state and transient decay open circuit voltage measurements", *Journal of Applied Physics*, vol. 91, no. 1, p. 399, 2002 (see p. 95).

[212] M. Kerr and A. Cuevas, "Generalized analysis of the illumination intensity vs. open-circuit voltage of solar cells", *Solar Energy*, vol. 76, no. 1-3, pp. 263–267, 2004 (see p. 95).

[213] O. Gunawan, T. Gokmen, and D. B. Mitzi, "Suns- V OC characteristics of high performance kesterite solar cells", *Journal of Applied Physics*, vol. 116, no. 8, p. 084 504, 2014 (see p. 95).

[214] W. van Roosbroeck and W. Shockley, "Photon-Radiative Recombination of Electrons and Holes in Germanium", *Physical Review*, vol. 94, no. 6, pp. 1558–1560, 1954 (see p. 96).

[215] A. Delamarre, M. Paire, J.-F. Guillemoles, and L. Lombez, "Quantitative luminescence mapping of Cu(In, Ga)Se 2 thin-film solar cells", *Progress in Photovoltaics: Research and Applications*, vol. 23, no. 10, pp. 1305–1312, 2015 (see p. 97).

[216] F. Babbe, "Masterarbeit - Systematische Untersuchung von definiert präparierten Shunts auf CIGSSe-Solarzellen mit Hilfe der Lock-In Thermographie", 2014 (see pp. 100, 103).

[217] F. W. Fecher, A. Pérez Romero, C. J. Brabec, and C. Buerhop-Lutz, "Influence of a shunt on the electrical behavior in thin film photovoltaic modules – A 2D finite element simulation study", *Solar Energy*, vol. 105, pp. 494–504, 2014 (see p. 100).

[218] L. Gütay and G. Bauer, "Local fluctuations of absorber properties of Cu(In,Ga)Se2 by sub-micron resolved PL towards "real life" conditions", *Thin Solid Films*, vol. 517, no. 7, pp. 2222–2225, 2009 (see p. 103).

[219] W. K. Metzger, I. L. Repins, and M. A. Contreras, "Long lifetimes in high-efficiency Cu(In,Ga)Se2 solar cells", *Applied Physics Letters*, vol. 93, no. 2, p. 022 110, 2008 (see p. 103).

[220] L. C. Hirst and N. J. Ekins-Daukes, "Fundamental losses in solar cells", *Progress in Photovoltaics: Research and Applications*, vol. 19, no. 3, pp. 286–293, 2011 (see p. 106).

[221] P. van der Heide, *Secondary Ion Mass Spectrometry*. Hoboken, NJ, USA: John Wiley & Sons, Inc., 2014 (see p. 107).

[222] J. Pohl and K. Albe, "Thermodynamics and kinetics of the copper vacancy in CuInSe2, CuGaSe2, CuInS2, and CuGaS2from screened-exchange hybrid density functional theory", *Journal of Applied Physics*, vol. 108, no. 2, 2010 (see p. 107).

[223] ——, "Erratum: Thermodynamics and kinetics of the copper vacancy in CuInSe 2 , CuGaSe 2 , CuInS 2 , and CuGaS 2 from screened-exchange hybrid density functional theory", *Journal of Applied Physics*, vol. 110, no. 10, p. 109 905, 2011 (see p. 107).

[224] L. E. Oikkonen, M. G. Ganchenkova, a. P. Seitsonen, and R. M. Nieminen, "Mass transport in CuInSe 2 from first principles", *Journal of Applied Physics*, vol. 113, no. 13, p. 133 510, 2013 (see p. 107).

[225] H. J. von Bardeleben, "Selenium self-diffusion study in the 1-3-6 2 semiconductor: CuInSe 2", *Journal of Applied Physics*, vol. 56, no. 2, pp. 321–326, 1984 (see p. 107).

[226] K. Gartsman, L. Chernyak, V. Lyahovitskaya, D. Cahen, V. Didik, V. Kozlovsky, R. Malkovich, E. Skoryatina, and V. Usacheva, "Direct evidence for diffusion and electromigration of Cu in CuInSe2", *Journal of Applied Physics*, vol. 82, no. 9, pp. 4282–4285, 1997 (see p. 107).

[227] S. Wißmann and K. Becker, "Tracer diffusion of indium in CuInS2", *Solid State Ionics*, vol. 101-103, pp. 539–545, 1997 (see p. 107).

[228] Y. Ando, S. Ishizuka, S. Wang, J. Chen, M. M. Islam, H. Shibata, K. Akimoto, and T. Sakurai, "Relationship between bandgap grading and carrier recombination for Cu(In,Ga)Se 2 -based solar cells", *Japanese Journal of Applied Physics*, vol. 57, no. 8S3, 08RC08, 2018 (see p. 108).

[229] T. Kirchartz, A. Helbig, B. E. Pieters, and U. Rau, "Electroluminescence Analysis of Solar Cells and Solar Modules", in *Advanced Characterization Techniques for Thin Film Solar Cells*, D. Abou-Ras, T. Kirchartz, and U. Rau, Eds., Weinheim, Germany: Wiley-VCH Verlag GmbH & Co. KGaA, 2011, pp. 61–80 (see p. 113).

[230] T. Bertram, V. Depredurand, and S. Siebentritt, "In-Se surface treatment of Cu-rich grown CuInSe2", in *2014 IEEE 40th Photovoltaic Specialist Conference (PVSC)*, IEEE, 2014, pp. 3633–3636 (see p. 114).

[231] Climate Action Tracker. (2018). Warming projections global update - Decemeber 2018, [Online]. Available: `https://climateactiontracker.org/documents/507/CAT_2018-12-11_Briefing_WarmingProjectionsGlobalUpdate_Dec2018.pdf` (visited on 12/12/2018) (see p. 118).

[232] The Intergovernmental Panel on Climate Change. (2018). Global Warming of 1.5 °C, [Online]. Available: `https://www.ipcc.ch/sr15/` (see p. 118).